

Development of
Mixed Quantum-Classical Methods
for Coherent Control and Ultrafast
Spectroscopy in Complex Systems

Dissertation

zur Erlangung des akademischen Grades

Doctor rerum naturalium

(Dr. rer. nat.)

im Fach Physik

eingereicht am

Fachbereich Physik

der Freien Universität Berlin

von Dipl.-Chem. Jens Petersen

geb. in Berlin

Juni 2013

Die Arbeiten für die vorliegende Dissertation wurden zwischen Juli 2008 und Mai 2013 unter der Betreuung von Prof. Dr. Dr. h.c. Vlasta Bonačić-Koutecký an der Humboldt-Universität zu Berlin und unter der Betreuung von Prof. Dr. Roland Mitrić an der Freien Universität Berlin durchgeführt.

Gutachter:

1. Prof. Dr. Roland Mitrić
2. Prof. Dr. Dr. h.c. Vlasta Bonačić-Koutecký
3. Prof. Dr. Dr. h.c. Wolfgang Domcke

Tag der Einreichung: 05.06.2013

Tag der Disputation: 12.07.2013

Danksagung

Diese Dissertation hätte nicht erarbeitet und abgeschlossen werden können ohne ein großes Maß an wissenschaftlicher und moralischer Unterstützung. Zuallererst möchte ich mich bei meinen Betreuern, Prof. Vlasta Bonačić-Koutecký und Prof. Roland Mitrić für die Bereitstellung des Themas und der Möglichkeit, die Dissertationsarbeiten an der Humboldt-Universität und der Freien Universität Berlin abzufassen, bedanken. Darüber hinaus haben die in vielen Diskussionen mit beiden entstandenen wissenschaftlichen Impulse maßgeblich dazu beigetragen, diese Arbeit voranzubringen. Insbesondere möchte ich die beständige Energie hervorheben, mit der Prof. Bonačić-Koutecký interessante Fragestellungen eingegrenzt und Kooperationen angestoßen hat, aber auch die Beharrlichkeit, die manches Mal dem wankenden Durchhaltevermögen des Doktoranden den nötigen neuen Schub zu geben vermochte. Mindestens ebenso bedeutsam war der kontinuierliche wissenschaftliche Dialog mit Prof. Mitrić, der vor allem maßgebliche Grundlagen für die theoretisch-methodologischen Ergebnisse dieser Arbeit gelegt hat, und dem ich tiefe Einsichten in viele Bereiche der theoretischen Physik auch über unser eigentliches Fachgebiet hinaus verdanke.

Darüber hinaus hat für die Themenbereiche dieser Dissertation auch der Austausch mit externen experimentellen und theoretischen Kollegen eine entscheidende Rolle gespielt. Dafür danke ich insbesondere Prof. Ludger Wöste, Prof. Joshua Jortner, Prof. Herschel Rabitz, Dr. Jonathan Roslund, Prof. Jean-Pierre Wolf, Dr. Bernhard Sellner und Prof. Hans Lischka.

Allen früheren und jetzigen Mitgliedern der beiden Arbeitsgruppen Bonačić-Koutecký und Mitrić danke ich für die angenehme und kollegiale Atmosphäre sowie vielerlei technische, wissenschaftliche und, Gott sei Dank!, auch nichtwissenschaftliche Gespräche. In loser Reihenfolge seien daher aufgeführt: Merle Röhr, Matthias Wohlgemuth, Polina Lisinetskaya, Dr. Gaia Tomasello, Alexander Humeniuk, Dr. Ute Werner, Dr. Alexander Kulesza, Lars Gell, Dr. Melanie Nößler und Dr. Christian Bürgel. Besonderer Dank gilt Matthias Wohlgemuth für die Unterstützung bei allerlei programmiertechnischen Fragen und Problemen, sowie die ständige Bereitschaft, auf Zuruf Ergänzungen und Verbesserungen der gruppeneigenen Programmpakete vorzunehmen, zu denen er maßgeblich beigetragen hat und die bei der Entstehung von Teilen dieser Arbeit sehr nützliche Werkzeuge waren.

Schließlich sei auch die tatkräftige Unterstützung beim Korrekturlesen dieses Werkes hervorgehoben, geduldig durchgeführt von Merle Röhr und Ute Werner; nochmals ganz herzlichen Dank dafür.

Ebenso ist den finanziellen Unterstützern dieser Arbeiten im Rahmen von Drittmitteln zu danken, insbesondere dem Verband der Chemischen Industrie, der zwei Jahre

Förderung durch ein Chemiefonds-Stipendium bereitstellte, sowie der Deutschen Forschungsgemeinschaft, die im Rahmen der Forschergruppe 1282 für die verbleibende Zeit die Finanzierung meiner Stelle übernahm.

Ganz wesentlich für den Erfolg dieser Arbeit und das konsequente Durchhalten auch über einige Durststrecken war nicht zuletzt der Zuspruch außerhalb des Wissenschaftsbereichs. Insbesondere meinen Eltern und Anverwandten möchte ich daher für stetige Ermutigung und Unterstützung Danke sagen.

Contents

Introduction	1
I Theoretical Methodology	9
1 Coupled Electron-Nuclear Molecular Dynamics	11
1.1 Quantum molecular dynamics and classical approximations	11
1.1.1 Quantum nuclear dynamics	13
1.1.2 Classical nuclear dynamics	15
1.2 Nonadiabatic dynamics	17
1.2.1 Ehrenfest dynamics	18
1.2.2 Trajectory surface hopping	19
1.2.3 Nonadiabatic dynamics with semiclassical propagation of the nuclei	23
2 Multistate Molecular Dynamics Simulations	27
2.1 Algorithms for solving the classical equations of motion	27
2.2 Electronic structure calculations	30
2.2.1 Electronic energies	30
2.2.2 Molecular Properties	42
2.2.3 Quantum mechanical/molecular mechanical (QM/MM) approach for inclusion of the environment	47
2.2.4 Choice of electronic structure methods employed in this thesis . . .	47
3 Field-Induced Surface Hopping Method (FISH)	49
3.1 Semiclassical time evolution of a molecular system	49
3.2 Introduction of classical trajectories	51
3.3 Surface hopping procedure in FISH	53
3.4 Simulation procedure	57
3.5 Scope of FISH	58
4 Formal Aspects and Validation of FISH	63
4.1 Forbidden hops and internal consistency	63
4.2 Quantum coherence in FISH	64
4.3 Field-induced excitation and distribution of vibronic energy	71
4.4 Conclusions	74

II	FISH simulation of ultrafast observables	77
5	Ultrafast spectroscopy	79
6	Time-resolved photoelectron spectroscopy (TRPES)	83
6.1	Introduction	83
6.2	Time-resolved photoelectron spectra within the FISH method	86
6.2.1	Discretized continuum approximation for photoionization	86
6.2.2	Role of vibrational quantum states	91
7	TRPES study of the nonadiabatic relaxation in small clusters	95
7.1	Introduction	95
7.2	Computational Procedures	97
7.3	Results and discussion	99
7.3.1	Excited state dynamics and TRPES of Ag_3	99
7.3.2	Excited state dynamics and TRPES of Au_7^-	110
7.4	Conclusions	113
III	Coherent control in complex systems using FISH	115
8	Concepts and applications of coherent control in molecular systems	117
9	Validation of FISH:	
	Coherent control of selective excited state population in K_2	123
9.1	Introduction	123
9.2	Computational Procedures	124
9.2.1	Ab initio potential energy curves and transition dipole moments	124
9.2.2	Quantum dynamics simulations	124
9.2.3	FISH simulations	125
9.2.4	Pulse optimization	125
9.3	Results and discussion	126
9.4	Conclusions	138
10	Coherent control in the condensed phase: Laser pulse trains for manipulating the photodynamics of solvated adenine	139
10.1	Introduction	139
10.2	Theoretical Approach	141
10.2.1	Combination of FISH with the QM/MM approach	142
10.2.2	Design of laser pulse trains	142
10.3	Computational Procedures	143

10.4 Results and Discussion	145
10.5 Conclusions	154
11 Revealing experimental control mechanisms:	
Optimal dynamic discrimination of flavins	157
11.1 Introduction	157
11.2 Photophysical properties of flavins	159
11.3 Experimental ODD of RBF and FMN	162
11.4 Simulation of ODD using experimentally shaped laser pulses	164
11.4.1 Computational	164
11.4.2 Results and Discussion	166
11.4.3 Conclusions	171
Conclusion and Outlook	175
IV Appendix	179
A Computational details and supplementary material for the model studies of Chapter 4	181
A.1 Forbidden hops and internal consistency (Sec. 4.1)	181
A.2 Quantum coherence in FISH (Sec. 4.2)	182
A.2.1 General settings	182
A.2.2 Model system for studying the influence of coherence magnitude . .	182
A.2.3 Model system for studying the influence of coherence phase	183
A.2.4 Model system for studying pump-probe excitation	184
A.3 Field-induced excitation and distribution of vibronic energy (Sec. 4.3) . . .	185
B Field-induced surface hopping with decoherence correction	187
C Electronic coherences in K_2	189
D FISH dynamics of adenine with electrostatic embedding	191
E Electronic structure of RBF and FMN	193
Bibliography	197
Summary	213
Zusammenfassung	215

Vorveröffentlichungen	217
Lebenslauf und Publikationsliste	218
Selbstständigkeitserklärung	221

Introduction

Since the discovery of the microscopical structure of matter, the idea to observe the motion of the smallest particles in real time has attracted large interest of the scientific community. However, in the early days of exact sciences, the limitations of experimental capabilities prevented any insight into the course of molecular processes and only allowed for determining the velocities of slow chemical reactions, initially at most on time scales of seconds, and later down to milliseconds using sophisticated flow tube techniques [1,2]. These data were complemented by empirical theories relating the reaction velocities to external parameters such as temperature, as pioneered by Arrhenius more than 120 years ago [3,4]. With the discovery of quantum mechanics [5–7], the basic laws governing the motion at the molecular level became essentially known [8], but for a long time their application to realistic molecular systems remained computationally intractable. Instead, the concepts of quantum mechanics were utilized to refine the empirical kinetic theories, notably by the invention of transition state theory accomplished by Eyring and others [9,10]. In the meantime, the experimental limits of resolving increasingly shorter time scales were pushed forward, most notably by the work of Eigen, Norrish and Porter, who developed techniques based on the impulsive interruption of a previously equilibrated system, followed by measuring the system’s relaxation. This could be achieved e.g. by sudden changes of temperature, pressure, or electric fields [11], or, alternatively, by an intensive light flash, as performed in the technique of flash photolysis [12,13]. In this way, investigations of dynamical processes on the microsecond time scale became possible.

The advent of laser technology capable to generate light of very high intensity and precisely adjusted frequency represented a further major advancement. In particular, the possibility to produce very short laser pulses with durations from the nanosecond to the sub-picosecond time regime opened fascinating opportunities for following the course of radiative and nonradiative processes [14]. Entering the realm of femtosecond time resolution [15] eventually allowed for the study of chemical reactions in real time, which was pioneered by Zewail more than 20 years ago [16]. Since then, the experimental resolution was further pushed downwards to shorter times, ultimately reaching the attosecond time scale in which even the electronic motion can be followed [17,18]. Typically, time-resolved measurements are nowadays performed by employing time-delayed laser pulse sequences, in which the first pulse excites the system to a superposition of quantum states in which dynamics is initiated, while the second one maps the dynamical evolution onto the detection signal. In this way, a plethora of experiments has been successfully conducted, providing insights into processes like structural rearrangement (isomerization, proton or electron transfer), redistribution of vibrational energy, electronic relaxation, excitation energy transfer, molecular dissociation, or ionization, or chemical reactions [19].

Moreover, not only techniques for mere observation have been advanced, but also the active manipulation of molecular processes has become an active area of research. Stimulated by several strategies theoretically proposed by Tannor and Rice [20] as well as by Brumer and Shapiro [21, 22], molecular quantum control has been experimentally realized for a wide variety of processes. A major advancement in this context was the steadily improved capability to create very complex shaped pulse forms, and to employ such pulses in iterative optimization procedures [23–26], as proposed by Judson and Rabitz [27]. This has allowed for obtaining specifically tailored pulses, best adapted to achieve a given control objective without the need to know the intrinsic properties of the studied system in all details [28–34].

However, notwithstanding the increasing capabilities to successfully design and perform ultrafast experiments, a major challenge has been always posed by the task of connecting the measured data to the underlying molecular-level processes. Generally, it has been realized that based on experiments and simple empirical models alone, the opportunities to extract information from the measurements are limited. Therefore, already in the early stages of ultrafast science, attempts were made from the theoretical side to provide more refined models and simulations that help interpret the experimental data. For this purpose, the quantum mechanical time evolution equations for the studied systems have to be solved, frequently also including the laser fields used in the experiments for observation and control. In this context, a milestone in the quantum mechanical description of molecules that can hardly be overestimated is the separation of electronic and nuclear motion formulated by Born and Oppenheimer [35], which has led to the concept of an electronic potential energy surface on which the nuclear motion takes place [36, 37]. The characterization of such surfaces in terms of minima or saddle points provides the basis for the common chemical notions of molecular structures or of transition states traversed during a reaction. Moreover, the quantum dynamics of the nuclei can be formulated to take place on these surfaces. While several decades ago the computational capabilities available still largely prevented sophisticated dynamics simulations of realistic molecules, restricting the theoretical efforts to simplified models, the extraordinary progress of computational technology has up to now enabled such studies for increasingly complex systems.

In spite of these achievements, the treatment of polyatomic molecules in their full dimensional complexity is still not possible on the basis of a full quantum mechanical formulation, and therefore simulation techniques which approximate the nuclear motion classically, are of large significance. This idea can be traced back to the early finding of Ehrenfest that, in the dynamics of quantum mechanical systems, the mean values of the observables evolve according to classical-like equations of motion [38]. Within the concept of potential energy surfaces, the classical forces on the nuclei in molecules can

be obtained from the gradients of the energy. In the beginning, the calculation of energy surfaces, and even more of their gradients, was much too demanding for realistic systems, and thus empirical model potentials were used instead, allowing nevertheless for pioneering studies of collisional dynamics in simple systems, cf. e.g. Refs. [39,40]. Nowadays, this situation has largely changed, and the calculation of accurate electronic energies and gradients has become possible for a multitude of systems. Moreover, the erstwhile most commonly employed procedure of globally precalculating the energy surfaces prior to the simulation of nuclear dynamics has become outperformed by the development of molecular dynamics “on the fly” techniques [41–44], in which the energies and gradients are only calculated for the current nuclear configurations during the course of the dynamics. This has provided the opportunity to extend the scope of dynamics simulations to complex molecules accounting for all degrees of freedom [45,46].

Combining these methods with an approximate description of nonadiabatic electronic transitions, occurring when the Born-Oppenheimer separation of electronic and nuclear motion breaks down, has also been an active research area since the very beginning of quantum mechanics. Early contributions for calculating nonadiabatic transition probabilities go back to Landau and others in the 1930s [47–49]. The combination of their approach with classical molecular dynamics paved the way for the development of surface-hopping techniques [50,51], which have been advanced and generalized since [52,53], and thus have found widespread application for the simulation of coupled electron-nuclear nonadiabatic dynamics. Yet the applicability of this class of methods for the theoretical simulation of ultrafast laser experiments has so far been rather limited, as the interaction between molecule and laser field is not accounted for. Despite that, important insights into the intrinsic molecular processes occurring in excited states, such as internal conversion or excited state isomerization, could be gained using this approach, thus providing important hints as to which processes may happen following the laser-induced photoexcitation [54]. However, phenomena induced by moderately strong laser fields, such as Rabi cycling of electronic populations or the competing excitation of different electronic states, which also represent the key to various strategies for optimal control, cannot be described within this framework. This gap could be closed by the development of our field-induced surface hopping method (FISH) [55], which introduces explicitly the matter-field interaction into nonadiabatic molecular dynamics simulations. In this way, it could be demonstrated that excitation induced by moderately intense laser fields can be described with high accuracy, opening the perspective for performing simulations that are much more comparable to the experimental situation. Thus, the FISH method represents a highly valuable means for the simulation of laser-induced dynamical processes accounting for the full system complexity.

In the present thesis, the theoretical foundation of FISH is elaborated, and the accuracy of the method is validated by comparison with exact numerical quantum dynamics. In particular, the role of electronic quantum coherence in FISH simulations is investigated in depth, and the conditions for the accurate treatment of electronic coherences in this mixed quantum-classical framework are determined. In addition, the implications of the classical approximation to the nuclear degrees of freedom on the accurate description of vibronic (i.e. simultaneous electronic and vibrational) excitation are carefully assessed. Furthermore, the general scope of the FISH method is significantly advanced by extending it for systems in the condensed phase, such as molecules in solution. Consequently, the present thesis provides, based on the FISH method, a general theoretical methodology for the simulation of laser-driven multistate dynamics in complex systems. This will be utilized for application-oriented studies in the context of ultrafast spectroscopy and optimal control. It will be shown that this involves two complementary aspects: The simulation and interpretation of available experiments, providing a molecular-level understanding of the experimental observations, and the theoretical prediction of molecular processes, eventually stimulating novel investigations.

With regard to ultrafast spectroscopy, the focus has been put on the time-resolved photoelectron spectroscopy (TRPES), since this technique represents a particularly convenient approach to the observation of coupled electron-nuclear dynamics in molecular systems [56–58]. It involves the creation of a quantum wavepacket in an excited electronic state by a pump laser pulse, and subsequent probing of the dynamically evolving system by photoionization due to a time-delayed probe pulse. The broad applicability of this technique is due to the fact that a TRPES signal can always be recorded if ionization is energetically possible (e.g. no dark states are present), and the detection of photoelectrons can be performed with high sensitivity. Moreover, the energetic and angular distribution of the photoelectrons carries a wealth of information about the character of the electronic and nuclear quantum states. In order to enable the simulation of TRPES based on field-induced multistate dynamics, a major extension of the FISH method has been devised and elaborated in this thesis, as outlined in Chapter 6. The scope of this methodology for the simulation of TRPES has been illustrated by studies of the photodynamics in small noble-metal clusters. Since these systems are characterized by strongly non-scalable properties, the investigation of their ultrafast dynamics is of fundamental importance for establishing the relation between structure, size, optical properties, and the time scales of nonradiative processes determining their photoemission. The specific systems selected in this thesis serve to illustrate the aforementioned two applicational aspects of simulations based on the FISH method. First, the nonadiabatic relaxation dynamics after photoexcitation and the associated TRPES signals are studied for the silver trimer (Ag_3) [59, 60]. While the ground state dynamics of this system has been already

extensively investigated, studies of the dynamics in excited electronic states have not been performed so far. Consequently, the present investigations, which established the lifetimes of nonradiative relaxation as well as the structural dynamics occurring during this process, attempt to fill this gap theoretically and also aim to stimulate comparative experimental studies. Conversely, the choice of the second example, the relaxation dynamics of the anionic gold heptamer (Au_7^-) after photoexcitation [61], was motivated by previously obtained experimental TRPES. For this case, the simulation of the TRPES signal and the analysis of the underlying dynamics permitted the interpretation of the experimental data by a bulk-like electronic relaxation behaviour accompanied by only small structural fluctuations. Contrary to that, previous studies in a lower excitation energy regime have found a molecular-like relaxation involving large structural deformations [62]. These results reveal the presence of distinctly different relaxation mechanisms in one and the same system, only depending on the energy regime of electronic excitation.

Beyond the simulation of observables, the main emphasis of the present thesis lies on the extension of the FISH approach to the coherent control in complex molecular systems interacting with their environment. As mentioned above, the use of optimally shaped laser fields allows for the manipulation of a wide variety of processes. However, the gap between experimental observation and the molecular-level interpretation is even larger in optimal control than in purely analytical spectroscopic applications. To a major part, this is caused by the usually very complex pulse forms arising in iterative optimization procedures, which prevent a straightforward connection to the underlying processes. Therefore, the mutual interaction between experiments and theoretical simulations is highly desirable. In this context, the FISH method, due to the explicit inclusion of the laser field in the dynamics, provides a unique opportunity to simulate the laser-driven processes occurring in optimal control. In particular, the combination of FISH with pulse shaping in the spectral domain, as introduced in this thesis, allows for the construction of control fields analogous to the experimental procedure. This opens the possibility to employ arbitrarily shaped fields, which can be either theoretically optimized in an iterative fashion, or, alternatively, directly taken from the experiment. Moreover, also the ability to achieve a given control target can be assessed as a function of the pulse parameters, thus entire control landscapes can be theoretically explored. Hence, for the first time the connection between experimental pulses and intrinsic dynamical processes in coherent control can be established for realistic molecules accounting for their full complexity, eventually including their environment. These opportunities are utilized in this thesis for the investigation of selected applications of optimal control.

At the outset, the applicability of the FISH method for the precise control of electronic excitation processes is benchmarked in Chapter 9 against exact quantum dynamical simulations on the example of selective population transfer to energetically close-lying excited

states in the potassium dimer molecule (K_2) [63]. This represents an example of strong-field control involving complete population inversion, which is of interest if close-lying excited states are present that exhibit differences, for instance, in the initiated nuclear motion after excitation, in fluorescence efficiency, coupling mechanisms to other states, possible onset of molecular dissociation, etc. The comparison of the results obtained by FISH with those from quantum dynamics simulations allows for establishing the accuracy of FISH for simulating coherent control processes, which provides a basis for applying the method to the much more complex molecular systems discussed in the subsequent chapters.

The first of these, presented in Chapter 10, is inspired by the idea to theoretically design simplified laser pulses based on an analytic parameterization of the electric field, thus avoiding the time-consuming iterative optimization procedure. This approach will be illustrated on a challenging application of coherent control in the condensed phase, namely the suppression of ultrafast nonradiative relaxation in the nucleobase adenine interacting with water environment [64]. Adenine represents an example of a biomolecule characterized by very efficient radiationless electronic relaxation processes following photoexcitation. This phenomenon is prominently seen in a number of molecules related to the genetic material of living cells. It has been surmised that this represents an evolutionary adaptation aiming to ensure the stability of the genetic information under solar irradiation [65]. In the context of optimal control, the question can be raised if the ultrafast radiationless decay can be counteracted by adequately tailored laser pulses such that the excited state lifetimes are extended. It could be shown that this is indeed possible by utilizing the dynamical processes in different excited electronic states, thereby hindering the system to directly advance towards conical intersections to the ground state. This might ultimately open a route to invoke fluorescence in intrinsically non-fluorescent systems, which can be of considerable interest in the context of biosensing applications.

Due to the direct inclusion of the electric field in the dynamics simulations within the FISH method, also the straightforward application of experimentally obtained laser pulses in theoretical simulations is feasible. In this way, a real-time picture of the dynamics at the molecular level can be obtained in direct connection to experimental observations. This approach is utilized in Chapter 11 to study the optimal dynamic discrimination of nearly identical molecules using shaped laser fields, which represents a sophisticated variant of optimal control in which the optimization goal is at the same time to maximize the response of one, and to minimize that of a second system. Specifically, two flavin molecules, riboflavin and flavin mononucleotide, will be studied, which share the same chromophore and differ only by a phosphate residue at the tail of a side group. These molecules have virtually indistinguishable absorption and fluorescence spectra, which prevents their discrimination using stationary spectroscopic techniques. However, it has been

demonstrated experimentally that the use of optimized laser fields enables the generation of experimental signals (in this case the fluorescence depletion induced by an ionizing laser pulse) which differ for the two molecules [66]. Since the experimental data alone do not allow one to deduce the molecular mechanism underlying this finding, FISH simulations provide a unique means to directly investigate the influence of the experimental pulses on the system dynamics. In this way, it could be revealed that the shaped pulses take advantage of minute transient differences of the dynamics in the two molecules to steer them to slightly different regions on their potential energy surfaces, in which for one of the molecules the ionization probability is enhanced, while for the other one it is diminished [67]. This finding might represent a general clue to the spectroscopic distinction between very similar analytes, thus offering promising application potential in analytical sciences.

Altogether, the present thesis is structured as follows: The first part is concerned with the methodological foundations. Therefore, in the introductory Chapter 1, the quantum mechanical basis of the dynamics in molecules is outlined, and an overview of mixed quantum-classical and semiclassical approximations to the coupled electron-nuclear dynamics is provided. Subsequently, in Chapter 2 the basic computational tools needed to carry out multistate nonadiabatic molecular dynamics simulations are presented, in particular algorithms for solving the classical equations of motion as well as methods for the calculation of the molecular electronic structure. Thereafter, the FISH method is elaborated in Chapter 3, followed by an analysis and validation of several formal aspects of this method in Chapter 4, which concludes the methodological part.

The second part is devoted to the extension and application of the FISH method to ultrafast spectroscopic observables. To this end, in Chapter 5 a general introduction to ultrafast spectroscopy is provided, followed by the description of a broadly applicable approach to the simulation of TRPES based on FISH dynamics in Chapter 6. Applications of this method to the simulation of TRPES in noble-metal clusters are presented in Chapter 7.

The ensuing third part of the thesis focuses on applications of FISH dynamics to optimal control. After the introductory Chapter 8 providing the basic theoretical strategies of optimal control as well as an overview of applications, three chapters presenting applications follow, each aiming to point out particular aspects of the scope of FISH simulations for quantum control. The first of these, Chapter 9, presents the strong-field control in the potassium dimer molecule. This study serves to illustrate the applicability of FISH for controlling strong-field excitation phenomena and in addition provides a thorough validation against exact numerical quantum dynamics calculations. Subsequently, in Chapter 10, the predictive power of FISH simulations to design optimal control fields will be addressed in the context of manipulating the excited state dynamics in the nucle-

obase adenine. This study also represents an illustration of control in a complex system including solvent environment. Finally, in Chapter 11, the opportunities of FISH control to provide interpretation and molecular-level understanding of experimental results are presented on the example of optimal dynamic discrimination of two nearly identical flavin molecules. Ultimately, conclusions and outlook are given.

Part I

Theoretical Methodology

1 Coupled Electron-Nuclear Molecular Dynamics

Dynamical processes in molecules are characterized by the interplay of electronic and nuclear motion. Frequently, due to the large mass difference of electrons and nuclei (the lightest nucleus, the proton, is 1836 times heavier than an electron), these two types of motion can be treated separately, but under certain circumstances, this is not possible due to strong coupling between electronic and nuclear motion. A comprehensive theoretical description of these phenomena is possible in the framework of quantum mechanics. However, for the numerical simulation of the dynamics occurring in realistic molecules, the large computational demand of solving the quantum mechanical equations of motion often prevents their direct use, and a variety of approximate approaches have been devised. A large number of them are based on introducing a purely or partially classical description of the nuclear motion, giving rise to the mixed quantum-classical or semiclassical methods. The following chapter serves to provide a general overview of the theoretical approaches to coupled electron-nuclear dynamics in molecular systems, beginning with the exact quantum mechanical formulation and successively introducing classical approximations to the nuclear motion. In the first Section 1.1, this is performed for the case of purely adiabatic nuclear dynamics without changes of the electronic state, while thereafter in Section 1.2, approaches to the nonadiabatically coupled electron-nuclear dynamics will be presented.

1.1 Quantum molecular dynamics and classical approximations

In the framework of quantum mechanics, motion in the molecular size regime can be described by the time-dependent Schrödinger equation,

$$i\hbar|\dot{\Psi}\rangle = \hat{H}|\Psi\rangle, \quad (1.1)$$

with the Hamiltonian operator \hat{H} and the quantum state vector $|\Psi\rangle$ [5–7]. In the particular case of a molecular system, composed of electrons and nuclei, the Hamiltonian can, in the absence of relativistic effects, be split into the nuclear kinetic energy and an electronic part as $\hat{H}_0 = \frac{1}{2}\hat{\mathbf{p}} \cdot \mathbf{M}^{-1}\hat{\mathbf{p}} + \hat{H}_{el}$, with $\hat{\mathbf{p}}$ as the Cartesian nuclear momentum operator and \mathbf{M}^{-1} as the inverse of the diagonal matrix of the nuclear masses¹. The electronic Hamiltonian \hat{H}_{el} is defined here as the sum of the kinetic energy of the electrons plus the Coulomb interaction among the electrons, among the nuclei, as well as between electrons and nuclei, and reads, with atomic units for the interaction terms ($e = 1$ and $1/4\pi\epsilon_0 = 1$),

$$\hat{H}_{el} = \frac{1}{2m_e} \sum_i^{el.} \hat{\mathbf{p}}_i^2 + \sum_{i<j}^{el.} \frac{1}{r_{ij}} + \sum_{A<B}^{nuc.} \frac{Z_A Z_B}{R_{AB}} - \sum_A^{nuc.} \sum_i^{el.} \frac{Z_A}{r_{Ai}}, \quad (1.2)$$

¹Bold-faced variables in lower case stand for vectorial quantities, those in upper-case for matrices.

where $\hat{\mathbf{p}}_i$ is the momentum operator for electron i , Z_A is the charge of nucleus A , and the r_{ij} , R_{AB} , and r_{Ai} indicate the distance of two electrons, two nuclei, and pairs of nuclei and electrons, respectively. Considering the large difference in masses between electrons and nuclei, it is sensible to introduce as a basis the eigenstates of \hat{H}_{el} at fixed value \mathbf{q} of the nuclear coordinate, which are solutions of

$$\hat{H}_{el}(\mathbf{q})|i; \mathbf{q}\rangle = E_i(\mathbf{q})|i; \mathbf{q}\rangle, \quad (1.3)$$

where eigenenergies $E_i(\mathbf{q})$ and eigenstates $|i; \mathbf{q}\rangle$ are parametrically dependent on the nuclear coordinates. Assuming completeness of the set of electronic eigenstates $|i; \mathbf{q}\rangle$, the total electron-nuclear wavefunction can, according to Born [68, 69], be expressed as a linear combination of the electronic eigenstates,

$$|\Psi(\mathbf{q}, t)\rangle = \sum_i \chi_i(\mathbf{q}, t)|i; \mathbf{q}\rangle, \quad (1.4)$$

with the nuclear-coordinate-dependent coefficients $\chi_i(\mathbf{q})$ being interpreted as nuclear wavefunctions². Insertion of the wavefunction (1.4) into the time-dependent Schrödinger equation (1.1) followed by projection on the electronic eigenstates yields a set of coupled equations of motion for the nuclear wavefunctions $\chi_i(\mathbf{q})$:

$$\begin{aligned} i\hbar\dot{\chi}_i(\mathbf{q}, t) &= \left(-\frac{\hbar^2}{2}\nabla_{\mathbf{q}} \cdot \mathbf{M}^{-1}\nabla_{\mathbf{q}} + E_i(\mathbf{q}) \right) \chi_i(\mathbf{q}, t) \\ &\quad - \frac{\hbar^2}{2} \sum_j \left(2\mathbf{d}_{ij} \cdot \mathbf{M}^{-1}\nabla_{\mathbf{q}}\chi_j(\mathbf{q}, t) + \tilde{d}_{ij}\chi_j(\mathbf{q}, t) \right). \end{aligned} \quad (1.5)$$

Here, $\mathbf{d}_{ij} = \langle i; \mathbf{q} | \nabla_{\mathbf{q}} | j; \mathbf{q} \rangle$ and $\tilde{d}_{ij} = \langle i; \mathbf{q} | \nabla_{\mathbf{q}} \cdot \mathbf{M}^{-1}\nabla_{\mathbf{q}} | j; \mathbf{q} \rangle$ denote the first- and second-order nonadiabatic coupling, respectively. These terms arise owing to the interdependence of nuclear and electronic motion. However, due to the aforementioned large mass difference between electrons and nuclei, this coupling of electronic and nuclear motion is negligible under many circumstances, and therefore in the sum on the right-hand side of Eq. (1.5) all terms with $j \neq i$ can be omitted in these cases. This is denoted the adiabatic approximation and leads eventually to separated equations of motion for each nuclear wavefunction $\chi_i(\mathbf{q}, t)$,

$$i\hbar\dot{\chi}_i(\mathbf{q}, t) = \left(-\frac{\hbar^2}{2}\nabla_{\mathbf{q}} \cdot \mathbf{M}^{-1}\nabla_{\mathbf{q}} + E_i(\mathbf{q}) - \frac{\hbar^2}{2}\tilde{d}_{ii}(\mathbf{q}) \right) \chi_i(\mathbf{q}, t), \quad (1.6)$$

²More strictly, the quantum state vector $|\Psi(t)\rangle$ is expanded in the complete set of the combined eigenfunctions of \hat{H}_{el} and the position operator $\hat{\mathbf{q}}$ as $|\Psi(t)\rangle = \sum_i \int d\mathbf{q}' \chi_i(\mathbf{q}', t) |\mathbf{q}'\rangle \otimes |i; \mathbf{q}'\rangle$. From this expression, the expansion (1.4) is obtained by projecting on the position eigenstate $\langle \mathbf{q} |$.

where the relation $\mathbf{d}_{ii} = 0$ valid for real electronic wavefunctions has been used, which can be always applied if the electronic states are not degenerate. Furthermore, neglecting the diagonal correction term results in the Born-Oppenheimer approximation [35] with the following equation of motion for the nuclear wavefunction:

$$i\hbar\dot{\chi}_i(\mathbf{q}, t) = \left(-\frac{\hbar^2}{2}\nabla_{\mathbf{q}} \cdot \mathbf{M}^{-1}\nabla_{\mathbf{q}} + E_i(\mathbf{q}) \right) \chi_i(\mathbf{q}, t), \quad (1.7)$$

where the electronic energy $E_i(\mathbf{q})$ as a function of the nuclear coordinates acts as an effective potential energy for the nuclear motion. On this basis, the concept of a nuclear wavepacket moving on an electronic potential energy surface was introduced.

In the following, general strategies for the simulation of nuclear motion in the framework of the Born-Oppenheimer approximation will be discussed. The implications of nonadiabatic couplings between the nuclear and electronic degrees of freedom will be outlined in Sec. 1.2.

1.1.1 Quantum nuclear dynamics

The most straightforward approach for solving Eq. (1.7) consists in a numerical procedure. For this purpose, the Schrödinger equation (1.7) can be formally integrated and assumes, if the Hamiltonian does not depend on time, the propagator form $\chi_i(t) = \exp\left(-\frac{i}{\hbar}\hat{H}t\right)\chi_i(0)$. This exponential expression can be expanded into a Taylor series in different ways. The simplest useful approach consists in setting

$$\chi_i(t + \Delta t) - \chi_i(t - \Delta t) = \left(e^{-\frac{i}{\hbar}\hat{H}\Delta t} - e^{\frac{i}{\hbar}\hat{H}\Delta t} \right) \chi_i(t), \quad (1.8)$$

after expansion up to second order leading to

$$\chi_i(t + \Delta t) = \chi_i(t - \Delta t) - \frac{2i}{\hbar}\hat{H}\chi_i(t)\Delta t, \quad (1.9)$$

which is called the second-order difference propagator³ [71]. The second-order difference approach also allows the inclusion of explicitly time-dependent terms in the Hamiltonian, such as e.g. electric fields, and was therefore employed in the quantum dynamical model calculations presented in this thesis. As a drawback, however, this propagator suffers from inaccuracies for longer propagation times. Therefore, other propagation schemes

³The practical implementation of this propagation scheme involves the representation of the wavefunction on a discrete grid in position space. The action of the potential energy term of the Hamiltonian is then obtained by multiplying the grid representations of the potential energy and the wavefunction. For the kinetic energy operator, a direct representation in position space is not possible due to its nonlocal nature in this representation. Therefore, it is common to employ the Fourier transformation to represent the kinetic energy term in momentum space, where the kinetic energy operator becomes multiplicative. After its multiplication with the wavefunction, the result is back-transformed to the position space [70].

have been developed which allow for a longer simulation time without accumulation of numerical errors [72]. However, most of these schemes are not suited to include an arbitrary time dependence of the Hamiltonian [72].

For the treatment of multidimensional systems, the computational effort of the above numerical propagation schemes without introducing further approximations rapidly becomes prohibitive, since their scaling with system size is exponential. Therefore, only systems with less than five atoms can usually be treated. For this reason, methods have been developed which allow for a simplified and more efficient description of the studied systems. Notably, the time-dependent Hartree approach (cf. Ref. [73] and references therein) and its multiconfigurational variants (cf. Refs. [73, 74]) are worth mentioning. These are based on a separation of the many-particle nuclear wavefunction into products of one-particle functions, for which effective equations for the time evolution can be derived. In this way, the computational effort is significantly reduced, allowing for the investigation of polyatomic systems. However, as with all full quantum dynamics methods, there remains the need to know in advance the global electronic potential energy surface (at least for the spatial region relevant for the studied process), which still represents a severe limitation for the investigation of complex systems including all nuclear degrees of freedom (e.g. vibrational modes). Selection of relevant vibrational coordinates or a simplified description of the molecular potentials along selected coordinates can therefore be a means to remedy this problem, though at the cost of further decrease in accuracy. Calculations are nowadays feasible for molecular systems of up to 20 degrees of freedom, although also model systems of larger dimensionality have been investigated (see e.g. Ref. [75] and references therein). For a more detailed discussion of these issues as well as for the presentation of further techniques for full quantum dynamical simulations, see Ref. [72, 73].

Whereas in the foregoing approaches, approximations were only introduced to the form of the wavefunction, whilst retaining a fully quantum mechanical time propagation, it is also possible to treat the latter in an approximate way. The most popular technique in this context is the Gaussian wavepacket method proposed by Heller [76], which assumes that the nuclear wavefunction always maintains the form of a moving Gaussian function, for the parameters of which (i.e. mean position, momentum, width, and phase) equations of motion can be derived. Notably, for the position and momentum these equations are identical to the classical Hamiltonian equations. This semiclassical approach, especially its more approximate variant with fixed widths of the Gaussian functions (frozen Gaussian) [77] have been successfully used to simulate vibrationally resolved absorption spectra and to find the system's eigenvalues based on time-dependent calculations.

1.1.2 Classical nuclear dynamics

Finally, the nuclear degrees of freedom can be treated entirely classically by propagating trajectories governed by the Newtonian (or Hamiltonian) equations of motion. For purely adiabatic dynamics on a single electronic energy surface, this assumption can be rigorously based in several ways by considering limiting cases of a full quantum mechanical description, as will be outlined in the following.

Limit of the hydrodynamic representation. By separating the quantum mechanical wavepacket into an amplitude and a phase factor as

$$\chi_i(\mathbf{q}, t) = A(\mathbf{q}, t)e^{\frac{i}{\hbar}S(\mathbf{q}, t)}, \quad (1.10)$$

the hydrodynamic form of the time-dependent Schrödinger equation (1.7) is obtained [78, 79]. Insertion of this ansatz into Eq. (1.7) and separation of real and imaginary parts leads to the two equations

$$\dot{A} + \nabla_{\mathbf{q}}A \cdot \mathbf{M}^{-1}\nabla_{\mathbf{q}}S + \frac{1}{2}A (\nabla_{\mathbf{q}} \cdot \mathbf{M}^{-1}\nabla_{\mathbf{q}}) S = 0 \quad (1.11)$$

$$\dot{S} + \frac{1}{2} (\nabla_{\mathbf{q}}S \cdot \mathbf{M}^{-1}\nabla_{\mathbf{q}}S) + E_i = \frac{\hbar^2 (\nabla_{\mathbf{q}} \cdot \mathbf{M}^{-1}\nabla_{\mathbf{q}}) A}{2A}. \quad (1.12)$$

Whereas the first equation describes the time evolution of the purely quantum mechanical amplitude A , the second one can be related to a classical analog by noting that, when identifying S with Hamilton's principal function and taking the limit $\hbar \rightarrow 0$, the classical Hamilton-Jacobi equation is obtained. Thus, for $\hbar \rightarrow 0$ the quantum mechanical equation of motion of the nuclear wavepacket turns into the classical equation of motion of a point particle. However, it is evident that the replacement of a wavepacket of finite width by a point particle is a quite crude approximation, even already for the initial conditions of a dynamical quantum system. Therefore, also a more sophisticated starting point for a classical description of wavepacket motion can be obtained by considering the density operator formulation of quantum mechanics.

Limit of the quantum mechanical phase-space density. Introducing the concept of a density operator $\hat{\rho} = |\Psi\rangle\langle\Psi|$ replaces Eq. (1.1) for time time evolution by the Liouville-von Neumann equation [80, 81],

$$i\hbar\dot{\hat{\rho}} = [\hat{H}, \hat{\rho}]. \quad (1.13)$$

The brackets in this expression indicate the commutator of the Hamiltonian and the density operator. In order to proceed towards a classical description, a classical limit of this equation has to be introduced. This can be conveniently achieved by employing a phase space picture of quantum mechanics such as the Wigner representation [82, 83]. All quantum mechanical operators are thereby transformed to functions of the coordinates \mathbf{q}

and momenta \mathbf{p} by means of the following transformation:

$$A(\mathbf{q}, \mathbf{p}) = \frac{1}{(2\pi\hbar)^N} \int dy_1 \dots dy_N \left\langle \mathbf{q} - \frac{\mathbf{y}}{2} \left| \hat{A} \right| \mathbf{q} + \frac{\mathbf{y}}{2} \right\rangle e^{i\mathbf{p}\cdot\mathbf{y}} \quad (1.14)$$

with N representing the number of nuclear coordinates. For a product of operators \hat{A} and \hat{B} the following correspondence applies:

$$\hat{A}\hat{B} \rightarrow A(\mathbf{q}, \mathbf{p}) \exp\left(\frac{\hbar}{2i}\Lambda\right) B(\mathbf{q}, \mathbf{p}) \quad (1.15)$$

with the Poisson operator $\Lambda = \overleftarrow{\frac{\partial}{\partial \mathbf{p}}} \overrightarrow{\frac{\partial}{\partial \mathbf{q}}} - \overleftarrow{\frac{\partial}{\partial \mathbf{q}}} \overrightarrow{\frac{\partial}{\partial \mathbf{p}}}$, where the arrows indicate to which side the derivatives are acting. Up to first order in \hbar , the exponential operator can be approximated as

$$\exp\left(\frac{\hbar}{2i}\Lambda\right) \approx 1 + \frac{\hbar}{2i}\Lambda. \quad (1.16)$$

In this way the commutator in Eq. (1.13) reduces to the classical Poisson bracket [83] and the Liouville equation for a phase space distribution of classical particles is obtained:

$$\begin{aligned} i\hbar\dot{\rho}(\mathbf{q}, \mathbf{p}) &= H(\mathbf{q}, \mathbf{p}) \left(1 + \frac{\hbar}{2i}\Lambda\right) \rho(\mathbf{q}, \mathbf{p}) - \rho(\mathbf{q}, \mathbf{p}) \left(1 + \frac{\hbar}{2i}\Lambda\right) H(\mathbf{q}, \mathbf{p}) \\ &= -i\hbar H(\mathbf{q}, \mathbf{p}) \Lambda \rho(\mathbf{q}, \mathbf{p}) \\ \dot{\rho}(\mathbf{q}, \mathbf{p}) &= \{H(\mathbf{q}, \mathbf{p}), \rho(\mathbf{q}, \mathbf{p})\}. \end{aligned} \quad (1.17)$$

In this spirit, the motion of a quantum mechanical wavepacket is approximated by that of a collection of classical point particles, with the classical Hamiltonian function replacing the quantum mechanical operator \hat{H} . Therefore, in the trajectory-based approaches to the dynamics of quantum systems, usually ensembles of trajectories are employed, with the initial conditions chosen such as to best represent a quantum mechanical wavepacket.

Classical motion of individual trajectories. In order to propagate the individual nuclear trajectories in time, the Newtonian equations of motion,

$$\mathbf{M}\ddot{\mathbf{q}} = \mathbf{F} = -\nabla_{\mathbf{q}} E_i(\mathbf{q}), \quad (1.18)$$

can be solved, where \mathbf{F} denotes the forces acting on the nuclei, which are obtained from the gradients $\nabla_{\mathbf{q}} E_i(\mathbf{q})$ of the electronic potential energy surface on which the nuclei move. For the solution of Eq. (1.18) usually specific numerical algorithms are employed as presented in detail in Sec. 2.1. The potential energy surface can in principle be precalculated similar to the case of full quantum dynamics. It is, however, much more convenient (and only possible in the classical framework), to calculate the forces solely for the nuclear configuration of the system present at a given time step (molecular dynamics (MD) “on

the fly”), as was first performed in combination with electronic structure calculations based on semiempirical quantum chemistry methods [41,42] and subsequently also with ab initio quantum chemistry [43]. The “on the fly” approach prevents multidimensional energy surface calculations and thus remedies the exponential scaling of computational effort with system size, thereby opening the way for employing MD methods for complex systems, strongly exceeding the limitations of quantum nuclear dynamics approaches. The electronic structure can be determined either independent of the integration of the nuclear equations of motion in each dynamics step by computing a converged solution of the electronic Schrödinger equation, or the electronic wavefunction can be propagated in time parallel to the propagation of the nuclei (Car-Parrinello molecular dynamics [44]). The latter method, however, is best suited in combination with electronic structure calculations using plane wave basis sets, and is therefore mainly applied to extended periodic systems, while the former is usually employed for molecular systems. Compared to quantum nuclear dynamics, the bottleneck in MD “on the fly” is no more the propagation of the nuclear degrees of freedom, but rather the calculation of the forces, for which in principle any electronic structure method can be used. The progress in the development of efficient electronic structure methods such as density functional theory, improved semiempirical methods as well as ab initio methods including more electron correlation (cf. Sec. 2.2) has in the last decades paved the way for extensive use of these methods for a large variety of applications. In view of the vast literature in this field, for an overview the reader is referred to the review articles [45,46] and the references cited therein.

1.2 Nonadiabatic dynamics

When the nuclear motion is accompanied by fast changes in the character of the electronic state, as e.g. at crossings or near-degeneracies of the electronic potential energy surfaces, the separation between nuclear and electronic motion underlying the Born-Oppenheimer approximation is not valid anymore. Instead, the nonadiabatic coupling terms appearing in Eq. (1.5) cannot be neglected, and the electronic state of the system can change during the nuclear dynamics. In the framework of purely quantum dynamical methods, the coupling between different energy surfaces could be in principle straightforwardly accounted for by the numerical integration of Eq. (1.5). However, in order to avoid the presence of large localized nonadiabatic couplings, frequently a transformation is employed from the adiabatic potential energy surfaces to the so-called diabatic ones, in which the nonadiabatic coupling terms are minimized [84]. Instead, new coupling terms then arise in the transformed potential energy operator. Based on this diabatic representation, a variety of wavepacket calculations including nonadiabatic effects has been performed, particularly in the context of vibronically resolved spectroscopy [84] and reactive scattering [85].

In the context of mixed quantum-classical approaches, an early contribution was made by Mott, who calculated the probability of electronic excitation of a hydrogen-like atom during collision with an α particle, where the latter was supposed to move classically [86]. Further pioneering work concerned the transition probability between two diabatic states near their intersection, for which case under certain simplifying assumptions an analytic expression was derived by Landau [47], Zener [48] and Stückelberg [49].

In the following, the focus lies on the theoretical approaches to nonadiabatic dynamics based on the classical propagation of the nuclei, considering both such methods that solely use classical trajectories, as well as such that implement several quantum corrections to the nuclear motion. With regard to the first class, two different approaches have found widespread attention: The mean-field or Ehrenfest dynamics, as well as the trajectory surface hopping (TSH) approach. These will be presented below, followed by a brief survey on methods employing quantum mechanical corrections to the classical propagation (semiclassical nuclear dynamics).

1.2.1 Ehrenfest dynamics

The basic idea of Ehrenfest or mean-field dynamics is to combine the solution of the Newtonian equations for the nuclei with the time-dependent Schrödinger equation for the electrons in a self-consistent way. For this purpose, a Lagrangian is formulated as

$$\mathcal{L} = \frac{1}{2} \dot{\mathbf{q}} \cdot \mathbf{M} \dot{\mathbf{q}} - \langle \Psi_{el} | \hat{H}_{el} - i\hbar \frac{\partial}{\partial t} | \Psi_{el} \rangle, \quad (1.19)$$

where \mathbf{M} is the nuclear mass matrix and Ψ_{el} the electronic wavefunction (cf. e.g. Ref. [87]). Upon minimization of \mathcal{L} the classical nuclear equations of motion

$$\mathbf{M} \ddot{\mathbf{q}} = -\nabla_{\mathbf{q}} E_{el} \quad (1.20)$$

are obtained. The electronic energy $E_{el} = \langle \Psi_{el} | \hat{H}_{el} | \Psi_{el} \rangle$ corresponds to the wavefunction satisfying the time-dependent Schrödinger equation

$$\hat{H}_{el} | \Psi_{el} \rangle = i\hbar \frac{\partial}{\partial t} | \Psi_{el} \rangle \quad (1.21)$$

and represents the mean value of the potential energy in the spirit of the Ehrenfest theorem [38]. The electronic wavefunction in Eq. (1.21) is propagated in time along the nuclear trajectories. This can be performed either in a direct way (numerically or using a basis set expansion), or alternatively by projecting the wavefunction on the adiabatic eigenfunctions $|i; \mathbf{q}(t)\rangle$ of \hat{H}_{el} , which then have to be determined in every time step of the propagation. In the latter case, if the wavefunction is expanded as $|\Psi_{el}[t; \mathbf{q}(t)]\rangle = \sum_i c_i(t) |i; \mathbf{q}(t)\rangle$, the time evolution of the electronic degrees of freedom is described by a

time-dependent Schrödinger equation for the expansion coefficients $c_i(t)$ as

$$i\hbar\dot{c}_i(t) = E_i[\mathbf{q}(t)]c_i(t) - \sum_j i\hbar(\mathbf{M}^{-1}\mathbf{p}) \cdot \mathbf{d}_{ij}[\mathbf{q}(t)]c_j(t), \quad (1.22)$$

where the current nuclear coordinates $\mathbf{q}(t)$ at each time step enter as parameters. In this way, quantum populations $|c_i|^2$ of the electronic states can be specified, which are used to construct the effective electronic mean-field potential for the nuclear motion as $E_{mean} = \sum_i |c_i|^2 E_i$. This approach has been successfully applied to a number of reactive scattering problems [88–90], frequently using the time-dependent Hartree-Fock approach [91–95]. Furthermore, also a number of studies concerned with the nonadiabatic dynamics in molecules after photoexcitation has been performed using e.g. the valence bond method [96] or time-dependent density functional theory in the framework of the real-time propagation approach [87, 97–101], in which the electronic equations of motion are evolved in time without an expansion into adiabatic eigenstates of the electronic Hamiltonian. Given the fact that, in the adiabatic picture, within Ehrenfest dynamics the energy gradients of several electronic states have to be calculated to obtain the mean-field force, the use of real-time methods with only a single time-dependent wavefunction being propagated in the mean-field potential is particularly advantageous, since then only a single gradient needs to be computed. The main methodological drawback of Ehrenfest dynamics, however, is a wrong asymptotic behaviour of the mean-field potential: After passing through a region of strong coupling between two electronic states, the effective potential consists of non-negligible portions from both states, and if even the coupling vanishes at later times, this composition will not change anymore. However, physically one would expect that after leaving the coupling region, the trajectory would continue its path on a single energy surface and not on a mixture [102].

1.2.2 Trajectory surface hopping

The shortcomings of Ehrenfest dynamics have motivated the idea of performing the propagation of the nuclei on pure electronic states instead of averaged ones, with the nonadiabatic effects being incorporated by allowing the nuclear trajectories to switch between electronic states in regions where the coupling is large. For the first time, this idea was discussed in the context of atomic and molecular collisions, where the scattering event can be accompanied by electron transfer or electronic excitation/relaxation. In their pioneering work, Bjerre and Nikitin described the electronic relaxation of excited Na atoms induced by collisions with molecular nitrogen using classical trajectories that move in a given electronic state and branch between the states at the intersection of the energy surfaces according to Landau-Zener transition probabilities [50]. On this methodological basis, Preston and Tully devised an extended algorithm [51] involving the numerical inte-

gration of the time-dependent Schrödinger equation (1.22) parallel to the nuclear motion. Furthermore, they introduced, besides the original trajectory-branching procedure, a simplified surface hopping technique which preserves the number of propagated trajectories by forcing them to follow only the path on that particular surface to which the switching probability is highest. This paved the way to utilize the surface hopping approach not only for collisions [103–105] but also for the nonradiative electronic relaxation in molecules after interaction with light. Two main advances have supported this development: Firstly, methodological improvement of efficient electronic structure methods which provide the necessary energies, forces and couplings is constantly taking place, accompanied by rapid technological progress in computation facilities. Secondly, the surface hopping scheme was put on a new and more solid footing by Tully who introduced the fewest-switches algorithm for calculating the hopping probabilities [52, 106], which aims at reproducing correct electronic state population dynamics whilst performing the smallest possible number of hopping events. For this purpose, the hopping from an initial state i to a final state j is allowed only if the quantum mechanical population of i decreases and that of j increases. The magnitude of the probability is determined by the change in the electronic state populations, which reads, in the density matrix version of Eq. (1.22) with $\rho_{ij} = c_i c_j^*$,

$$\dot{\rho}_{ii} = -2 \sum_k \text{Re} [(\mathbf{M}^{-1}\mathbf{p}) \cdot \mathbf{d}_{ik}\rho_{ki}] \quad (1.23)$$

$$\dot{\rho}_{ij} = -\frac{i}{\hbar} (E_i - E_j) \rho_{ij} - \sum_k (\mathbf{M}^{-1}\mathbf{p}) \cdot (\mathbf{d}_{ik}\rho_{kj} - \mathbf{d}_{kj}\rho_{ik}). \quad (1.24)$$

The probability for changing from state i to state j is then determined by the decrease of ρ_{ii} due to the coupling with j , i.e. the respective term of the sum in Eq. (1.23) times the time increment Δt , normalized by the total initial state population ρ_{ii} :

$$P_{i \rightarrow j}(t) = \frac{2\text{Re} [(\mathbf{M}^{-1}\mathbf{p}) \cdot \mathbf{d}_{ij}\rho_{ji}] \Delta t}{\rho_{ii}(t)}. \quad (1.25)$$

Since nonadiabatic relaxation is an intrinsic molecular process in which no energy exchange with the environment takes place, the hopping process, which abruptly changes the electronic energy, needs to be complemented by a procedure ensuring conservation of the total energy. This can be achieved by adjusting the nuclear kinetic energies. Due to the independent propagation of trajectories in surface hopping, this is only possible by demanding the energy conservation for each trajectory individually, although physically, this would merely be required for the ensemble as a whole. Usually, the energy conservation is achieved by rescaling the nuclear momenta in the direction of the nonadiabatic

coupling vector \mathbf{d}_{ij} [51, 107–109], such that for the momentum \mathbf{p}^β at the nucleus β

$$\mathbf{p}_{new}^\beta = \mathbf{p}_{old}^\beta - \gamma_{ij} \mathbf{d}_{ij}, \quad (1.26)$$

where, following Refs. [110, 111], the expression for the scaling coefficient γ_{ij} reads

$$\gamma_{ij} = \frac{(\mathbf{M}^{-1}\mathbf{p}) \cdot \mathbf{d}_{ij} \pm \sqrt{[(\mathbf{M}^{-1}\mathbf{p}) \cdot \mathbf{d}_{ij}]^2 + 2(\mathbf{M}^{-1}\mathbf{d}_{ij}) \cdot \mathbf{d}_{ij}(E_i - E_j)}}{(\mathbf{M}^{-1}\mathbf{d}_{ij}) \cdot \mathbf{d}_{ij}} \quad (1.27)$$

with $\mathbf{M}^{-1}\mathbf{p} = \dot{\mathbf{q}}$ as the velocity vector. In case that only the scalar coupling $D_{ij} = (\mathbf{M}^{-1}\mathbf{p}) \cdot \mathbf{d}_{ij}$ is available, the rescaling can instead be performed uniformly, such that

$$\mathbf{p}_{new} = \mathbf{p}_{old} \sqrt{\frac{E_{kin} + (E_i - E_j)}{E_{kin}}}, \quad (1.28)$$

where E_{kin} is the nuclear kinetic energy and E_i/E_j are the electronic energies of states i and j . However, if a hop to an electronic state of higher energy than the actual state is required, the nuclear kinetic energy may occasionally be insufficient to compensate for the needed increase in electronic energy. Then, usually the surface hop is prohibited (“forbidden hop”), and the direction of the nuclear velocities might be either reversed [110] or retained [112].

Drawbacks of surface hopping. The above described hopping prescription is designed in order to achieve consistency between the trajectory-averaged quantum probabilities $\bar{\rho}_{ii} = \frac{1}{N_{traj}} \sum_n \rho_{ii}^{(n)}$ and the fraction of trajectories in a given state $\Pi_i = \frac{1}{N_{traj}} \sum_n p_i^{(n)}$, where $\rho_{ii}^{(n)}$ is the quantum population of trajectory n and $p_i^{(n)}$ represents the current electronic state in which it is propagated. However, this internal consistency condition is not always fulfilled, mainly due to two reasons. Firstly, the occurrence of forbidden hops can lead to a different time evolution of the two population quantities $\bar{\rho}_{ii}$ and Π_i , since e.g. the $\bar{\rho}_{ii}$ may grow for a particular state which may be energetically inaccessible, and thus Π_i would not change. In most cases, this inconsistency is ignored, and only the fraction of trajectories Π_i is considered as the proper population from which the needed physical observables are calculated, while the $\bar{\rho}_{ii}$ are disregarded. This is mainly motivated by the idea to obtain the quantities corresponding to wavefunction expectation values by averaging over the ensemble of trajectories. Nevertheless, some modified surface hopping schemes exist which avoid the presence of forbidden transitions, such as the approach by Hammes-Schiffer et al. in which, when a surface hop would be forbidden, the nuclear velocities are modified such that the coupling between the two involved states becomes zero [113]. The second cause of internal inconsistency is due to the phenomenon of overcoherence in the electronic wavefunctions associated with each trajectory. Quantum

mechanically, if in a region of strong coupling a wavepacket is split into parts, and these parts then move away from each other, their coherence gradually decays and ultimately vanishes at large distance. However, for the case of a single classical trajectory, the associated quantum populations for the electronic states cease to change when a coupling region is left, and the electronic wavefunction retains a mixed character although the trajectory moves in a single electronic state. If then again a coupling region is reached, wrong hopping probabilities may result. To tackle this problem, several approaches introducing an empirical decoherence correction have been introduced and validated on model systems. The simplest approach consists in resetting the electronic coefficients when a region of large coupling is left. More sophisticated is the method originally introduced by Truhlar in the context of mean-field dynamics [114,115] and applied to surface hopping by Persico [116]. It is based on determining a specific coherence decay time, which depends on the gap of electronic energies and the nuclear kinetic energies of the given trajectory, such that decoherence is faster for large gap and large nuclear kinetic energy. Another method recently proposed by Persico relies on a simplified propagation of Gaussian wavepackets in both involved states after a hopping event and performing coherence decay according to the decrease of the wavepacket overlap along the trajectory [117]. A similar route has been followed by Shenvi et al. [118] who complement each trajectory by the propagation of at most a single Gaussian wavepacket per electronic state and model the decoherence as a stochastic process depending on the overlap decay between the Gaussian wavepackets between pairs of electronic states. On a different footing is another recent development of Subotnik et al. [119,120], in which parallel to the positions and momenta of each trajectory also the first moments (i.e. first-order deviations from the trajectory values of position and momentum) of these quantities are propagated. These are employed to calculate a rate constant for the decoherence between each pair of electronic states, which is subsequently used in a stochastic process to determine if the electronic wavefunction is to collapse to the current state or not. Besides the mere decay of coherences, also the issue of dephasing has been recently addressed, and a phase-corrected surface hopping scheme based on a modified propagation of the time-dependent Schrödinger equation has been presented [121,122]. It must be emphasized that most of the above-mentioned approaches to introducing decoherence into the surface hopping technique have until now only been employed in studies of low-dimensional model systems, and thorough studies of their usefulness for real molecules are not available until now.

Applications of surface hopping. In spite of the above mentioned issues, trajectory surface hopping represents one of the few approaches to nonadiabatic dynamics which have found widespread application. This is due to its complete foundation on classical nuclear dynamics, which allows for the combination with MD “on the fly” and thus to treat complex systems, which is not possible with approaches accounting for quantum correc-

tions on the nuclear dynamics. Moreover, the accuracy of surface hopping simulations can be validated by comparison with experimental results, which has been successfully performed for a variety of systems for which the nonradiative relaxation had been studied experimentally [123–128].

The applicational scope of surface hopping has been greatly advanced due to numerous developments enabling its combination with various quantum chemical methods, which has allowed for the investigation of photodynamical processes in increasingly complex molecules. This involves a nonadiabatic Car-Parrinello technique based on DFT using plane wave basis sets [129] as well as converged Born-Oppenheimer dynamics in the framework of time-dependent Kohn-Sham [130] and linear response density functional theory [127, 131, 132], semiempirical methods [111, 133] and of the *ab initio* CAS-MRCI method [134]. Moreover, recently surface hopping has been implemented in the framework of mixed quantum mechanical-molecular mechanical (QM/MM) approaches, based on semiempirical [135–137] and *ab initio* quantum chemical methods [138–140] as well as time-dependent density functional theory [141, 142]. This enables the study of systems interacting with their environment such as solution or protein. For a further overview of recent achievements, cf. also Ref. [54].

Interestingly, the surface hopping approach as explained above is not restricted to the assignment of the electronic degrees of freedom as quantum mechanical and the nuclear degrees of freedom as classical. Instead, in the context of proton transfer reactions also a separation of the proton motion from that of all the other (heavier) nuclei is possible, and surface hopping is then performed between proton vibrational quantum states [110]. Eventually, the vibrational and the electronic surface hopping can be unified to provide a technique for the simulation of proton transfer accompanied by electron excitation [143].

1.2.3 Nonadiabatic dynamics with semiclassical propagation of the nuclei

Beyond the purely trajectory-based methods, several approaches have been developed trying to retain some degree of quantum mechanical behaviour in the nuclear motion. The most relevant of them will be briefly presented below.

Liouville dynamics. Starting from the Liouville-von Neumann equation in the density operator representation of quantum mechanics, semiclassical equations of motion for the density matrix elements have been derived by performing a partial Wigner transformation [82, 83] for the nuclear degrees of freedom, followed by taking the classical limit and subsequently projecting onto diabatic [144] or adiabatic [145] electronic states. These approaches have been implemented in various ways using ensembles of classical trajectories for each propagated density matrix element. For instance, the number of trajectories representing a particular element of the density matrix can be held constant, their interaction being described via time-dependent weights assigned to each trajectory according

to the quantum mechanical electronic state populations [146,147]. This approach is computationally quite demanding since only with sufficient covering of the relevant phase space regions by trajectories an adequate representation of the density matrix elements for the entire propagation time can be achieved. Moreover, due to the interaction of the trajectories, the ensembles pertaining to each of the density matrix elements all have to be propagated simultaneously. Therefore, simplified variants have been also proposed, such as the use of only a single ensemble driven mainly by the Hamiltonian of the most relevant electronic state [148]. Further simplification involves the use of completely uncoupled trajectories [149]. Interestingly, in the latter case the description of electronic state populations turns out to be identical to that employed in standard surface hopping, whereas the applicability of the nuclear dynamics driven only by a single reference Hamiltonian is much more limited due to the higher degree of approximation. Based on the theoretical derivation given in Ref. [145], also several surface-hopping-like implementations have been proposed, in which the dynamics is partitioned into (i) the classical propagation of trajectories representing the specific density matrix elements (both diagonal elements and coherences), and (ii) the surface hopping procedure leading either to changing the state of a given trajectory or to a branching into several new ones. In these methods, hopping caused by nonadiabatic effects can be accompanied by momentum adjustment (“momentum jump”) which results from the presence of off-diagonal forces in the equations of motion [150,151]. Since this can cause numerical instabilities [151], attempts to avoid the momentum jump have been made. To this end, the off-diagonal force components can be transformed away [152], or a different derivation of the equations of motion can be employed, based on first projecting the Liouville-von Neumann equation onto basis states and only afterwards performing the Wigner transformation. In this case, off-diagonal forces do not appear [153]. The latter derivation also serves as the basis for an implementation using parameterized Gaussian-type phase space functions instead of trajectories [154]. All these methods have been shown to yield more accurate results than standard surface hopping for some selected one-dimensional model problems. However, their application to complex systems involving real molecules is severely limited by the need to propagate all trajectories at the same time and to solve complicated integral expressions to describe the electronic population dynamics.

A related approach also describes the nuclear motion in the Wigner representation, but takes one (nonclassical) term more in the \hbar expansion of the general phase space equation of motion (cf. Eq. (1.16)) [155,156]. In this way, a quantum mechanical correction to the force acting on each trajectory is introduced, which depends on the total phase space density represented by the ensemble of trajectories. Therefore, the trajectories are not propagated independently but interact with each other (entangled trajectory dynamics). The largest drawback preventing application of this approach to multidimensional

systems is, however, that the quantum correction to the force involves the third derivative of the potential energy, which could for real molecules only be determined with high computational effort.

Semiclassical dynamics based on path integrals. Besides the above discussed methods based on a semiclassical limit of the Liouville-von Neumann equation, approaches to semiclassical nuclear dynamics have been also formulated based on the path integral formalism [157,158]. Specifically, semiclassical approximations to the time evolution operator have been devised, such as the initial value representation, which involves the propagation of classical trajectories, but still accounts for effects such as nuclear interference or tunneling (cf. Refs. [159,160] and references therein). The extension of this approach to nonadiabatic coupled electron-nuclear dynamics has been performed along different lines. The method devised by Pechukas relies on a stationary phase evaluation of path integrals and leads to a classical-like time evolution containing a nonlocal force originating from the electrons [161]. Although formally appealing, this approach has proved to be computationally even more demanding than exact quantum calculations [162]. Another route has been followed more recently, based on the idea to construct a harmonic-oscillator-like continuous representation of the discrete electronic degrees of freedom, followed by turning to the classical description by analogy [163,164]. This method has been applied to the simulation of absorption spectra of molecules exhibiting strong vibronic coupling between electronic and nuclear degrees of freedom [160,165]. However, due to the computational effort its use for molecular systems accounting for all degrees of freedom is also limited.

Multiple-spawning method. This technique represents the only approach to coupled multistate dynamics beyond the classical trajectory approximation which has been up to now applied to realistic molecules [166–169]. It is based on representing the nuclear wavepackets by linear combinations of Gaussian basis functions with fixed widths (similar to Heller’s frozen Gaussian approach mentioned in Sec. 1.1), and propagating the mean positions, momenta, phase factors and weight coefficients in time. The equations of motion for positions and momenta turn out to be entirely classical, hence the Gaussian functions follow the paths of classical trajectories. However, their motion is coupled due to the presence of cross terms in the evolution equations for the weight coefficients, which allows for partial incorporation of nuclear coherence effects. Nonadiabaticity is accounted for by creating new Gaussian basis functions on the concerned electronic states in regions of strong coupling, thereby achieving population transfer. In this way, the surface-hop in the trajectory-based methods is replaced by a more gradual flow of population between the states. The multiple spawning method has been successfully combined with different quantum chemical methods for the calculation of electronic energies, gradients and couplings, and has been applied to problems such as collision-induced ionization [170], tunneling [171], vibronic spectra [172], photodynamics in solution in the framework of the

QM/MM technique [173,174], excited state dynamics involving isomerization and internal conversion [175–177]. Recently, also an extension of the method including the interaction with external laser fields has been presented [178]. Compared to the trajectory-based methods such as surface hopping, the description of the quantum mechanical character of the nuclear motion has been partially retained. However, this is achieved at the cost of calculating overlap integrals between different basis functions, and also of propagating the whole ensemble of trajectories simultaneously, which both represent severe obstacles for achieving an efficiency comparable to the surface hopping techniques.

Despite the wide variety of scientific efforts in developing more broadly applicable methods for the simulation of nonadiabatic processes in the framework of semiclassical nuclear dynamics, up to now still no method exists which would outperform the efficiency of the surface hopping approach based on performing classical MD supplemented by quantum electronic transitions. Therefore, the main methodological basis of the investigations presented in this thesis, the field-induced surface hopping method (FISH) to be presented in Chapter 3, has utilized the trajectory surface hopping approach as its fundament and represents a major advancement and generalization of this methodology. For this reason, in the following Chapter 2 first the basic procedures necessary for performing classical multistate MD simulations will be presented. Specifically, in Section 2.1 the simulation procedures for solving the classical equations of motion will be outlined, and subsequently in Section 2.2 a brief survey will be given of the methods used for the calculation of the molecular electronic structure, which represent the main computational tool to determine the needed ingredients of multistate molecular dynamics simulations, such as energies, forces and couplings.

2 Multistate Molecular Dynamics Simulations

2.1 Algorithms for solving the classical equations of motion

In the framework of the Born-Oppenheimer approximation, the nuclei of a molecule move on an electronic potential energy surface. The classical Newtonian dynamics on this surface is governed by the forces \mathbf{F} on the nuclei \mathbf{q} , which are obtained as the negative gradients of the electronic energy in the electronic state i :

$$\mathbf{M}\ddot{\mathbf{q}} = \mathbf{F} = -\nabla_{\mathbf{q}}E_i(\mathbf{q}). \quad (2.1)$$

Alternatively, using $\mathbf{p} = \mathbf{M}\dot{\mathbf{q}}$, the Hamiltonian equations can be formulated:

$$\begin{pmatrix} \dot{\mathbf{q}} \\ \dot{\mathbf{p}} \end{pmatrix} = \begin{pmatrix} \mathbf{M}^{-1}\mathbf{p} \\ -\nabla_{\mathbf{q}}E_i(\mathbf{q}) \end{pmatrix} = f(\mathbf{q}, \mathbf{p}). \quad (2.2)$$

These equations can be solved numerically by discretizing the time variable into finite steps. Usually, special algorithms are employed for this purpose which provide both numerical efficiency and satisfy formal demands such as time invariance [179]. The most common of these procedures is the Verlet algorithm [180]. It is based on a Taylor expansion of the nuclear position at the time step t_{i+1} with respect to the previous time step $t_i = t_{i+1} - \Delta t$. Using $\dot{\mathbf{q}} = \mathbf{v}$, $\ddot{\mathbf{q}} = \mathbf{a}$ and $d^3\mathbf{q}/dt^3 = \mathbf{b}$, this leads to:

$$\mathbf{q}_{i+1} = \mathbf{q}_i + \mathbf{v}_i\Delta t + \frac{1}{2}\mathbf{a}_i(\Delta t)^2 + \frac{1}{6}\mathbf{b}_i(\Delta t)^3 + \dots \quad (2.3)$$

Analogously, for t_{i-1} one obtains:

$$\mathbf{q}_{i-1} = \mathbf{q}_i - \mathbf{v}_i\Delta t + \frac{1}{2}\mathbf{a}_i(\Delta t)^2 - \frac{1}{6}\mathbf{b}_i(\Delta t)^3 + \dots \quad (2.4)$$

The sum of these two expressions provides a relation between three subsequent positions at time steps t_{i+1} , t_i and t_{i-1} , which define the original Verlet algorithm [180]:

$$\mathbf{q}_{i+1} = 2\mathbf{q}_i - \mathbf{q}_{i-1} + \mathbf{a}_i(\Delta t)^2 + \dots \quad (2.5)$$

Since both the velocities and the terms cubic in Δt cancel in Eq. (2.5), this expression is exact up to third order. The accelerations are obtained from the electronic gradients using Newton's equations (2.1). For the first step, the initial conditions are utilized:

$$\mathbf{q}_1 = \mathbf{q}_0 - \mathbf{v}_0\Delta t. \quad (2.6)$$

A shortcoming of this original Verlet procedure is the absence of the velocities in the algorithm, which are explicitly needed e.g. for constant temperature simulations. Moreover, numerical instabilities can arise due to the smallness of $(\Delta t)^2$ in Eq. (2.5) compared to the coordinate values \mathbf{q}_i . Therefore, modified approaches have been developed, such as the velocity Verlet algorithm, in which the positions, velocities and accelerations are obtained simultaneously [181]:

$$\mathbf{q}_{i+1} = \mathbf{q}_i + \mathbf{v}_i \Delta t + \frac{1}{2} \mathbf{a}_i (\Delta t)^2 \quad (2.7)$$

$$\mathbf{v}_{i+1} = \mathbf{v}_i + \frac{1}{2} (\mathbf{a}_i + \mathbf{a}_{i+1}) \Delta t. \quad (2.8)$$

The precision of all numerical integration algorithms crucially depends on the step size. For MD simulations, it is common to use a time step typically about at least ten times smaller than the fastest nuclear oscillation period, i.e. mostly between 0.1 and 2.0 fs.

Besides the above algorithms, also common general methods for the numerical solution of first-order differential equations can be employed, such as the Runge-Kutta procedure. Introducing a shorthand notation for Hamilton's equations (2.2) using $\mathbf{\Gamma} = (\mathbf{q}, \mathbf{p})^T$,

$$\dot{\mathbf{\Gamma}}(t) = f[\mathbf{\Gamma}(t)], \quad (2.9)$$

allows for a compact presentation of the most frequently used fourth order Runge-Kutta scheme [182]. It is based on the calculation of intermediate steps as follows:

$$\begin{aligned} \mathbf{\Gamma}_1 &= \mathbf{\Gamma}(t) & k_1 &= f(\mathbf{\Gamma}_1) \Delta t \\ \mathbf{\Gamma}_2 &= \mathbf{\Gamma}_1 + \frac{1}{2} k_1 & k_2 &= f(\mathbf{\Gamma}_2) \Delta t \\ \mathbf{\Gamma}_3 &= \mathbf{\Gamma}_1 + \frac{1}{2} k_2 & k_3 &= f(\mathbf{\Gamma}_3) \Delta t \\ \mathbf{\Gamma}_4 &= \mathbf{\Gamma}_1 + k_3 & k_4 &= f(\mathbf{\Gamma}_4) \Delta t. \end{aligned} \quad (2.10)$$

Finally, the coordinates and momenta at the next time step are obtained as:

$$\mathbf{\Gamma}(t + \Delta t) = \mathbf{\Gamma}(t) + \frac{\Delta t}{6} (k_1 + 2(k_2 + k_3) + k_4). \quad (2.11)$$

This methodological structure of the Runge-Kutta method immediately makes evident a major drawback compared to the Verlet algorithm: Four force evaluations per time step are necessary instead of only one in the Verlet algorithm. Moreover, the Runge Kutta method is not time invariant, which may lead to worsened energy conservation [179]. Therefore, the practical use of this method for dynamics simulations is limited.

The MD simulation of a molecule in a fixed electronic state immediately implies the conservation of the total molecular energy. However, when considering an ensemble, also the temperature can be held constant. Therefore, it is convenient to define a tem-

perature of a single trajectory, such that temperature conservation can be imposed on each trajectory separately. This temperature can be obtained from the kinetic energy $E_{kin} = \frac{1}{2} \sum_N^f M_N v_N^2$ and the number of degrees of freedom f as

$$T = \frac{2E_{kin}}{fk_B} \quad (2.12)$$

and ensures the fixed value of the true thermodynamic temperature of the ensemble, which is proportional to the ensemble average of the kinetic energy. In a simulation, the temperature can thus be controlled by modifying the nuclear velocities. This can be performed either by direct scaling of the velocities, such that the actual temperature rapidly approaches the desired value, or the system can be coupled to a heat bath, and the velocity rescaling mimicks a more gradual energy exchange with the bath, eventually also letting the system assume the desired temperature [183].

Such coupling of the system dynamics with a surrounding bath also represents the simplest approximation of dynamics including an environment, which in the molecular case could e.g. be a solvent, surface, or a protein. Another common approach for implicit inclusion of environmental influence consists in considering an additional frictional force in the classical equations of motion. This leads to the Langevin dynamics, which is based on the equation

$$\mathbf{M}\ddot{\mathbf{q}} = -\nabla_{\mathbf{q}}E_i(\mathbf{q}) - \gamma\mathbf{M}\dot{\mathbf{q}}(t) + \mathbf{F}_{rand}(t), \quad (2.13)$$

where γ is an empirical friction coefficient depending on the surrounding, and $\mathbf{F}_{rand}(t)$ represents a fluctuating random force [184]. Numerical integration of Eq. (2.13) can e.g. be performed using a modified velocity Verlet algorithm as described in Ref. [185].

More involved treatments of the influence of environment are possible on the atomistic level by considering explicitly the structure of the surrounding. This can be implemented by partitioning the complete system under study into different parts which are described at different levels of accuracy, as it is performed in the framework of mixed quantum mechanical/molecular mechanical methods (cf. Sec. 2.2.3).

2.2 Electronic structure calculations¹

At the heart of multistate molecular dynamics (MD) simulations lies the availability of electronic energies, gradients, as well as of interstate coupling elements such as nonadiabatic couplings or transition moments. Therefore, in order to go beyond simple model systems and treat real molecules, electronic structure calculations have to be performed, i.e. the stationary Schrödinger equation for the many-electron problem has to be solved. For this purpose, a large variety of methods based on different levels of approximation is available. Since in the present thesis, the focus lies on the investigation of dynamical properties under the influence of light, and the calculation of the molecular electronic structure rather serves as a tool to obtain the necessary ingredients for the dynamics simulations, in the following only those electronic structure methods which are employed for the calculations presented here will be briefly sketched. The particular choice of these methods was strongly motivated by the requirements posed by many-electronic state dynamics simulations for relatively long propagation times (up to several picoseconds), i.e. a major condition was computational efficiency and at the same time a sufficiently accurate description of both ground and excited states. Therefore, highly correlated wavefunction methods were only used for very small systems, while for the larger ones in the gas phase and in environment, instead more approximate approaches such as density functional theory or semiempirical methods were employed.

In following subsections, these methods and their relation to each other will be presented. For this purpose, first the treatment of the electronic ground and excited state energies will be outlined, and subsequently the calculation of molecular properties such as forces and couplings will be described, finally followed by a short presentation of quantum mechanical/molecular mechanical (QM/MM) methods suited for the description of quantum systems interacting with their environment.

2.2.1 Electronic energies

One-electron approximation. Since for the many-electron Schrödinger equation analytic solutions are not available, approximate forms of the wavefunction need to be employed. For almost the entire quantum chemistry, the basic assumption consists in adopting a product form for the many-electron wavefunction, such as

$$\Phi(\mathbf{x}_1 \dots \mathbf{x}_N) = \sum_k (-1)^k \phi_{p_k(1)}(\mathbf{x}_1) \dots \phi_{p_k(N)}(\mathbf{x}_N) = \frac{1}{\sqrt{N!}} \begin{vmatrix} \phi_1(\mathbf{x}_1) & \dots & \phi_N(\mathbf{x}_1) \\ \dots & \dots & \dots \\ \phi_1(\mathbf{x}_N) & \dots & \phi_N(\mathbf{x}_N) \end{vmatrix}, \quad (2.14)$$

¹Throughout this section, atomic units are employed, i.e. Planck's constant \hbar , electron mass m_e , elementary charge e , are set to unity, and so, too, is the prefactor $1/4\pi\epsilon_0$ of the Coulomb interaction.

where the required antisymmetry of the electronic wavefunction upon permutations p_k of any two electrons has been taken into account by using the structure of a determinant [186]. The variables $\mathbf{x}_i = \{\mathbf{r}_i, \mathbf{s}_i\}$ denote the combined spatial coordinates \mathbf{r}_i and spin coordinates \mathbf{s}_i of the i 'th electron. The one-electron functions $\phi_i(\mathbf{x}_j)$ are termed molecular orbitals (MOs). This representation of the wavefunction is called a Slater determinant and would be an exact solution to the many electron problem if no interaction between the electrons existed. However, since a variational principle can be formulated, stating that any approximate wavefunction will give rise to an energy expectation value higher than the exact electronic ground state energy, the Slater determinant can be taken as the starting point for formulating the search for the best approximate solution as an optimization problem [186]. For this purpose, the variation of the energy expectation value $E = \langle \Phi | \hat{H} | \Phi \rangle$ with respect to the MOs is formulated under the constraint that the MOs be orthonormal. In this way, the N electron problem represented by the full N electron Schrödinger equation is formally decoupled, giving rise to N one-electron equations (Hartree-Fock equations) determining the optimal orbitals,

$$\left(-\frac{1}{2}\nabla^2 + \hat{v}_{\text{eff}}(\mathbf{r}) \right) \phi_i = \epsilon_i \phi_i, \quad (2.15)$$

where ϵ_i is the orbital energy, and \hat{v}_{eff} denotes the effective one-particle or mean-field potential which determines the state of an individual electron [186] and is given by

$$\hat{v}_{\text{eff}}(\mathbf{r}) = \sum_j \left(\langle \phi_j | \frac{1}{|\mathbf{r} - \mathbf{r}'|} | \phi_j \rangle_{\mathbf{r}'} - | \phi_j \rangle \langle \phi_j | \frac{1}{|\mathbf{r} - \mathbf{r}'|} \right) - \sum_a \frac{Z_a}{|\mathbf{r} - \mathbf{R}_a|}, \quad (2.16)$$

with electron coordinates \mathbf{r} , \mathbf{r}' and nuclear coordinates \mathbf{R} . The first term on the right-hand side denotes the Coulomb operator, which is equivalent to the Coulomb potential in classical electrostatics, while the second term represents the nonlocal exchange operator, which is a consequence of the antisymmetry of the electronic wavefunction and hence a quantum mechanical contribution. Since the orbitals are at the same time solutions of the Hartree-Fock equations and determine the effective potential needed for their computation, the solution procedure needs to be iterative until self-consistency is achieved.

The practical route to solve the Hartree-Fock equations consists in making further assumptions on the form of the MOs. Typically, these are expanded in linear combinations of fixed basis functions, which are most frequently chosen as atom-centered Gaussian functions, such that $\phi_i(\mathbf{r}) = \sum_n c_{in} b_n(\mathbf{r})$, where $b_n(\mathbf{r}) = N x^{l_x} y^{l_y} z^{l_z} \exp[-\zeta(\mathbf{r} - \mathbf{r}_0)^2]$ with the Cartesian coordinates x , y , and z , the parameters l_x , l_y , l_z , ζ , and the center \mathbf{r}_0 . In this way, the integro-differential Hartree-Fock equations (2.15) are transformed into matrix equations [186],

$$\mathbf{FC} = \mathbf{SC}\epsilon, \quad (2.17)$$

which can be solved employing linear algebra techniques. In the above expression, \mathbf{F} is the Fock matrix, which is the matrix representation of the Fock operator $\hat{f} = -\frac{1}{2}\nabla^2 + \hat{v}_{\text{eff}}(\mathbf{r})$ (cf. Eq. (2.15)) and has, for a closed-shell system with all electrons spin-paired, the elements

$$F_{ij} = \left\langle b_i \left| -\frac{1}{2}\nabla_{\mathbf{r}_1}^2 - \sum_a^{\text{nuclei}} \frac{Z_a}{|\mathbf{r}_1 - \mathbf{R}_a|} \right| b_j \right\rangle_{\mathbf{r}_1} + \sum_{km} c_k c_m \left(\left\langle \frac{b_i(\mathbf{r}_1)b_k(\mathbf{r}_2)}{|\mathbf{r}_1 - \mathbf{r}_2|} \left| \left[2 \left| b_j(\mathbf{r}_1)b_m(\mathbf{r}_2) \right\rangle - \left| b_m(\mathbf{r}_1)b_j(\mathbf{r}_2) \right\rangle \right] \right\rangle \right) \quad (2.18)$$

$$= h_{ij} + \sum_{km} c_k c_m (2J_{ikjm} - K_{ikmj}), \quad (2.19)$$

where J_{ikjm} is a Coulomb and K_{ikmj} an exchange integral, while \mathbf{S} is the overlap matrix with elements $S_{ij} = \langle b_i | b_j \rangle$, and \mathbf{C} is the vector of orbital coefficients.

The description of the electronic structure obtained within the Hartree-Fock approach represents an effective one-electron formulation. This means that each individual electron is restricted to its orbital and experiences the presence of the other electrons only in an averaged way via the effective potential (cf. Eq. (2.15)). This results in incorrect probability amplitudes for finding an electron at a particular spatial position, which in the one-electron approximation do not explicitly depend on the other electrons' positions, while they do so in an exact treatment. This effect is termed electron correlation and its neglect contributes, besides the use of a finite basis set, the main part to the deviation of Hartree-Fock energies from the exact values.

As is well known, accounting for this deviation is decisive for the predictive value of any chemically or physically relevant property [187]. Therefore, the Hartree-Fock method as such is not commonly used to determine the electronic structure of molecular systems. Rather, it serves as a starting point for more accurate approaches in which the determination of a Hartree-Fock wavefunction is the initial step, as will be outlined below.

Correlated methods. The basic idea of correlated electronic structure methods consists in introducing more variational flexibility in the electronic wavefunction, which can e.g. be achieved by going beyond the single Slater determinant formulation. For this purpose, the simplest possibility, termed the configuration interaction (CI) method [186], is to set up the wavefunction Ψ as a linear combination of several Slater determinants Φ_i , each corresponding to a different electronic configuration, i.e. a different distribution of the electrons in the molecular orbitals (MOs):

$$\Psi = \sum_i c_i \Phi_i. \quad (2.20)$$

These Slater determinants are obtained from the optimized Hartree-Fock determinant

serving as the reference function by putting one or more electrons into higher-lying MOs. The electric energy is then obtained by finding the optimal values of the c_i which minimize the energy expectation value of the CI wavefunction, $E_{CI} = \langle \Psi | \hat{H} | \Psi \rangle$, subject to the constraint that the wavefunction remains normalized ($\langle \Psi | \Psi \rangle = 1$). This variation problem can be recast in the form of a matrix eigenvalue equation in the basis of all Slater determinants as

$$\mathbf{H}\mathbf{c} = E\mathbf{c}, \quad (2.21)$$

where $H_{ij} = \langle \Phi_i | \hat{H} | \Phi_j \rangle$, \mathbf{c} is the vector of all c_i and E is the CI energy. The solution of this equation involves diagonalization of the matrix \mathbf{H} , giving rise to the set of eigenvectors \mathbf{c} and eigenenergies E , of which the lowest corresponds to the CI ground state energy of the system. Formally, if all possible Slater determinants within a given basis set were taken into account, the CI approach would deliver the best possible solution of the many electron problem for this particular basis set (full CI). However, since the number of determinants increases factorially with the number of electrons of the system, for all but very small systems it is mandatory to truncate the CI expansion appropriately, e.g. by restricting to several classes of excitations with respect to the Hartree-Fock wavefunction, such as singly and doubly excited determinants.

As mentioned above, the determinants employed in a CI calculation are based on MOs obtained within the Hartree-Fock approach, which are not optimized for the CI wavefunction. Therefore, from a given number of electronic configurations, a much more accurate wavefunction can be constructed if the CI coefficients and the MOs are optimized simultaneously (multiconfiguration self-consistent field method, MCSCF) [187]. For several systems containing unpaired electrons such as biradicals, which even qualitatively cannot be correctly described by a single determinant wavefunction, this is mandatory to obtain meaningful results when using a limited number of electronic configurations². However, this approach is computationally very demanding, which limits its use to very small systems. Nevertheless, it forms the basis of a more applicable method, which relies on the idea to strongly restrict the number of possible determinants included in the MCSCF procedure only to those necessary to obtain a qualitatively correct wavefunction. This is achieved by considering only orbital excitations within a small “active space” of MOs, usually several of the highest occupied and lowest unoccupied ones. Within this space, a full CI expansion is performed, and the CI and MO coefficients of the resulting wavefunction are simultaneously optimized (complete active space SCF, CASSCF). The so obtained CASSCF wavefunction can subsequently be taken as the (multiconfigurational) reference function for an additional truncated CI calculation, in which the MO coefficients are held fixed, but a great many more Slater determinants are taken into account

²If a full CI calculation can be performed in the employed basis set, highly accurate results can be also obtained without performing an MCSCF procedure.

(multireference CI, MR-CI) [187]. In this way, a major part of the electron correlation energy can be accounted for. However, this approach is still very demanding, and only applicable for systems in which a reasonably small number of “active electrons” can be identified to primarily determine the electronic properties. Regardless of these restrictions in *ab initio* methods, there is another application field of CI in the framework of semiempirical approaches (*cf.* below). Formally identical to *ab initio* CI, the drastically reduced computational effort allows for much increased CI spaces, particularly for the inclusion of higher excited determinants and larger orbital active spaces also for quite large systems.

Although useful for obtaining accurate ground state energies and wavefunctions, MR-CI-based calculations are much more common as a valuable means to determine excited electronic states, as it will be discussed below.

The most straightforward general approach to the calculation of excited states starts by taking a set of many-electron wavefunctions, such as Slater determinants, as basis functions for the many-electron problem. Provided the basis set were complete, the eigenstates of the electronic Hamiltonian could be expanded in linear combinations of the basis functions. Although the completeness condition is not fulfilled for finite basis sets, this approach can be employed to obtain approximate electronic energies and wavefunctions. Technically, this is equivalent to the diagonalization of the Hamiltonian matrix in terms of the basis functions, and energies and wavefunctions are obtained as eigenvalues and eigenvectors of the Hamiltonian matrix. Thus, this procedure is in fact identical to the CI method discussed above in the context of the ground state energy, and the higher-energetic eigenvalues and eigenvectors of the CI Hamiltonian matrix can be identified with electronic energies and wavefunctions for excited states. Improvement by taking multiconfigurational CASSCF wavefunctions as reference instead of the Hartree-Fock determinant can be achieved similarly to the ground state case, and is of even more fundamental importance since the MOs optimized for a ground state Hartree-Fock wavefunction are in general unlikely to be appropriate for an excited state wavefunction as well. If several electronic states have to be determined at the same time (*e.g.* for an absorption spectrum or for performing multistate dynamics), it is useful to perform the CASSCF optimization procedure for all states simultaneously (*i.e.* to take an appropriate average of all excited state energies as the quantity to be minimized) in order to achieve a balanced description of all relevant excited states (state-averaged CASSCF) [187]. In the present thesis, the MR-CI method based on CASSCF calculations has been used to calculate several potential energy curves of the diatomic K_2 molecule (*cf.* Chapter 9).

Although the framework of the Hartree-Fock approximation supplemented by the treatment of electron correlation using the MR-CI method represents a systematic way to obtain more and more accurate results, the rapidly increasing computational effort restricts the applicability of this approach to systems with only a small number of active

electrons. In particular, in cases where a large number of energy evaluations is necessary, such as in dynamics simulations, the use of ab initio correlated methods comes to its limits. Therefore, in the following a class of methods will be discussed, which retain the principal structure of the Hartree-Fock and consecutive correlation methods, but allow for higher computational efficiency by introducing approximations to the integrals over basis functions present in Hartree-Fock.

Semiempirical methods. Historically, the computational effort in evaluating the molecular integrals occurring in the solution of the Hartree-Fock equations (cf. Eq. (2.19)) provided a strong motivation for developing the more approximate semiempirical methods capable to treat larger systems. Although nowadays the computational capabilities usually allow for Hartree-Fock calculations and even for the application of more advanced correlated methods to common molecules of several tens of atoms, semiempirical methods are by no means obsolete. Quite the contrary, they find their application fields in areas where a large number of energy calculations is necessary, such as MD simulations. Particularly in combination with correlation treatments such as CI, semiempirical methods can offer both an accurate and efficient description of ground and excited electronic states, which has motivated their use for several studies presented in this thesis.

In the following, the fundamental assumptions of semiempirical methods as well the specific approximations made in the PM3 and OM2 methods employed in this thesis will be briefly reviewed. The most important approximations in semiempirical theories are: (i) consideration of valence electrons only, (ii) use of a minimal basis set, i.e. the minimal number of basis functions necessary to accommodate the given number of electrons. Furthermore, depending on the method, several classes of integrals over basis functions are neglected, simplified or parameterized. The methods used in this thesis all rely on the modified neglect of diatomic differential overlap (NDDO) approach, which includes the following approximations: Firstly, in the matrix equation (2.17) the overlap matrix \mathbf{S} is replaced by the unit matrix. Furthermore, all integrals needed for the construction of the Fock matrix (cf. 2.19) are either parameterized or neglected. For the one-electron part of the Fock matrix, if two basis functions i, j are situated on the same atomic center a , the matrix element is given by

$$\begin{aligned} h_{ij} &= \left\langle i \left| -\frac{1}{2}\nabla^2 - \frac{Z_a}{|\mathbf{r} - \mathbf{R}_a|} \right| j \right\rangle \delta_{ij} - \sum_{b \neq a} \left\langle i \left| \frac{Z_b}{|\mathbf{r} - \mathbf{R}_b|} \right| j \right\rangle \\ &= U_{ii}\delta_{ij} - \sum_{b \neq a} Z_b \langle i s_b | j s_b \rangle, \end{aligned} \quad (2.22)$$

where Z_a, Z_b are the nuclear charges, U_{ii} is the ionization potential for the atomic orbital i , and s_b is a spherical charge distribution replacing the nuclear point charge. The elements involving basis functions at different atomic centers are given as $h_{ij} = \frac{1}{2}S_{ij}(\beta_i + \beta_j)$, with

the overlap integral $S_{ij} = \langle i|j \rangle$ and the numerical resonance parameters β_i . For the two-electron integrals, all terms involving basis functions on more than two atomic centers are set to zero. The one-center Coulomb and exchange integrals replaced by parameters. For the two-center two-electron integrals also the exchange terms are neglected. The evaluation of the remaining two-center two-electron integrals is performed by replacing the electric charge cloud by a multipole expansion, i.e. a point charge for the interaction of two s orbitals, a dipole for an s-p interaction and a quadrupole for a p-p interaction. These dipoles and quadrupoles are also represented by two or four point charges fixed at some parameterized distance from the atomic center. The determination of semiempirical parameters is nowadays usually performed by considering a test set of molecules and then optimizing simultaneously all parameters with the aim to minimize the averaged error of several molecular quantities. The difference between the various semiempirical methods based on the NDDO approximation mainly arises from the treatment of the interaction of the atomic cores. While in an ab initio theory like Hartree-Fock, the internuclear interaction energy should cancel its interelectronic counterpart large distances, this is not anymore the case within the approximate NDDO framework. Therefore, in the PM3 method [188] the following modified expression is used:

$$V_{nn} = \sum_{a < b}^{nuc} Z_a Z_b \langle s_a s_b | s_a s_b \rangle (1 + e^{-\alpha_a R_{ab}} + e^{-\alpha_b R_{ab}}) + \frac{Z_a Z_b}{R_{ab}} \sum_{k=1}^2 \sum_{m=a,b} a_{km} e^{-b_{km} (R_{ab} - c_{km})^2}. \quad (2.23)$$

In this expression, Z_i are nuclear charges, s_i are spherical charge distributions, R_{ab} denotes the internuclear distance, and α_i , a_{km} , b_{km} , c_{km} are parameters. A slightly different expression is used in the older AM1 method [189], which is besides that essentially identical to PM3, though employing different numerical values of the parameters due to a different optimization procedure.

The assumption of the NDDO approximation that two-electron integrals involving more than two atomic centers can be neglected is based on the basis functions being orthogonal. However, this is in general not the case for the minimal basis sets used in semiempirical methods, rendering the above assumption somewhat questionable. Therefore, attempts have been made to devise semiempirical methods that employ orthogonalized basis sets. The OM2 method developed by Weber and Thiel [190, 191] provides an orthogonalization correction to all integrals occurring in an NDDO calculation, supplemented by several three-center terms. This method has been evidenced to provide an improved description of the structural and energetic ground state properties of several organic and bioorganic molecules as compared to the PM3 or AM1 methods [192].

Semiempirical methods, due to their underlying approximations, are computationally far more efficient than Hartree-Fock calculations, which in principle allows much larger

molecules to be treated. This is even more pronounced in the context of semiempirical calculations including electron correlation, such as MR-CI, which in this framework can be employed very efficiently to molecules for which a full ab initio correlation calculation would be too demanding. The possibility to employ large active spaces and to include highly excited determinants allows for very large numbers of determinants to be included in the CI calculation, which is especially valuable for excited state calculations. Important computational savings can be additionally achieved by ensuring the correct spin state of the employed basis functions in the CI calculation. Physically, it is required that the total electronic wavefunction represents an eigenstate of the total spin operator of the system. While Slater determinants constructed from spin orbitals (spatial orbitals associated with α or β spin, respectively) are not in general spin eigenfunctions, linear combinations of them fulfilling this demand can be constructed. These “spin-adapted configuration state functions” (CSFs) are then used as new many-electron basis functions in the CI problem. The procedure for their construction can be based on group theoretical considerations. Particularly attractive in this context is the graphical unitary group approach (GUGA), which provides the connection between Slater determinants and spin-adapted CSFs by utilizing the properties of the unitary group of order N for a system of N electrons. This technique constitutes the basis of the semiempirical CI formalism [193] used in this thesis.

Thanks to the optimization of the semiempirical parameter sets with respect to experimental data, results obtained in this way can for particular molecules be even of better quality than the ones obtained from parameter-free methods, such as ab initio MR-CI using a small active space. Although this strongly depends on the molecule under study, necessitating careful comparison with experimental or high-quality theoretical results, it has e.g. provided a reasonably accurate description of the ground and excited electronic states of biomolecules such as adenine or flavins, which are in the focus of the investigations presented in Chapters 10 and 11 of this thesis.

Notwithstanding the accuracy achievable in the semiempirical framework, there are several classes of systems which cannot be properly accounted for. Most prominently among them are transition metals and heavy elements exhibiting relativistic effects, for which no adequate semiempirical parameterizations are available. For this reason, in order to study systems such as small noble metal clusters, as an alternative the density functional theory (DFT) was used instead in this thesis and will be sketched in the following paragraph.

Density functional theory (DFT). This approach ranks in general terms of accuracy between semiempirical and correlated ab initio wavefunction methods. Usually, the computational effort is comparable to that of Hartree-Fock, but unlike the latter, electron correlation is accounted for in an approximate fashion. Therefore, DFT methods have found widespread use in contemporary computational chemistry applications.

The methodological basis of DFT is provided by the finding of Hohenberg and Kohn that for the unambiguous determination of expectation values, such as energies, of an N -electron system, not the complete N -electron wavefunction needs to be known, but already the one-electron density,

$$\rho(\mathbf{r}_1) = \int d\mathbf{r}_2 \dots d\mathbf{r}_N d\mathbf{s}_1 \dots d\mathbf{s}_N \Psi^*(\mathbf{x}_1, \mathbf{x}_2, \dots, \mathbf{x}_N) \Psi(\mathbf{x}_1, \mathbf{x}_2, \dots, \mathbf{x}_N), \quad (2.24)$$

is sufficient [194], which is obtained by integrating the squared wavefunction over all spin coordinates \mathbf{s}_i and all but one spatial coordinates \mathbf{r}_i , and thus only depends on a single spatial electron coordinate. However, the exact expression from which the energy can be calculated as a functional of $\rho(\mathbf{r}_1)$ is not known. Nevertheless, Hohenberg and Kohn proved the existence of a variational principle stating that the energy expectation value of any trial density derived from an antisymmetric N -electron wavefunction is always larger than the true ground state energy [194]. Since the energy functional is unknown, however, approximate expressions have been introduced and applied for several model systems such as the noninteracting homogeneous electron gas [195–197]. The applicability of these approaches to molecular systems was very limited, though. A practically useful approach could be formulated by Kohn and Sham [198] who expressed the density by an auxiliary wavefunction constructed from orbitals in a single determinant form. Applying the variational principle to these orbitals leads to the Kohn-Sham equations, which are entirely analogous to the Hartree-Fock equations given in Eq. (2.15), with the exception that in the effective potential the nonlocal exchange operator is replaced by an approximate local exchange-correlation potential $v_{xc}(\mathbf{r})$:

$$v_{\text{eff}}^{KS}(\mathbf{r}) = \left[\sum_j \left(\langle \phi_j | \frac{1}{|\mathbf{r} - \mathbf{r}'|} | \phi_j \rangle_{\mathbf{r}'} + v_{xc}(\mathbf{r}) \right) - \sum_a \frac{Z_a}{|\mathbf{r} - \mathbf{R}_a|} \right]. \quad (2.25)$$

The exchange-correlation potential can be approximated in many ways, often using empirical parameters from experiments or high-accuracy calculations. In this form, Kohn-Sham density functional theory can be viewed as a sort of semiempirical correction to Hartree-Fock, which retains the simple one-determinant structure of the wavefunction, but includes approximate electron correlation in terms of v_{xc} . Formally, the exchange-correlation potential is defined as the functional derivative of an exchange-correlation energy, $v_{xc}(\mathbf{r}) = \frac{\delta E_{xc}[\rho(\mathbf{r})]}{\delta \rho(\mathbf{r})}$. The functional form of E_{xc} usually involves complex analytical expressions of the density, as well as of its gradient. The basic relation goes back to Dirac, who derived an analytic expression for the exchange energy of the homogeneous electron gas [197]. Later improvements involve the introduction of terms that depend on the density gradient [199], leading to the general form of gradient-corrected functionals

(generalized gradient approximation, GGA),

$$E_x^{GGA} = \text{const} \cdot \int \rho^{4/3}(\mathbf{r}) d\mathbf{r} - \int F_X(\chi) \rho^{4/3}(\mathbf{r}) d\mathbf{r}, \quad (2.26)$$

where the first term is the Dirac exchange expression, and the density gradient is accounted for in the second term by the dimensionless variable

$$\chi(\mathbf{r}) = \frac{|\nabla\rho(\mathbf{r})|}{\rho^{4/3}(\mathbf{r})}. \quad (2.27)$$

In the present thesis, the GGA functional of Perdew, Burke and Ernzerhof (PBE) was employed, which is based on an analytical fit to the numerically calculated exchange and correlation energies of a system with slowly varying electron density [200]. Further approaches to the construction of exchange-correlation functionals also rely adding partially Hartree-Fock exchange (hybrid functionals) [201,202], or taking into account higher derivatives of the density (cf. Ref. [192], section 8.4.2). Moreover, also new empirical corrections have been developed, introducing e.g. dispersion interaction, which is only poorly described in standard functionals [203].

Technically, the usual implementation of Kohn-Sham DFT is also to a great extent analogous to the Hartree-Fock method, such that the orbitals are expanded in linear combinations of atomic orbitals, which then leads to matrix representations of the Kohn-Sham equations that are solved using linear algebra techniques. The only difference to Hartree-Fock consists in the computation of the exchange-correlation part of the involved matrix elements, which cannot be performed analytically due to the complicated functional form of these terms. Therefore, the density is represented on a spatial grid and the integration is performed numerically [204,205].

While in the frame of wavefunction-based approaches, excited states can be obtained formally easily by diagonalization of the Hamiltonian matrix in an appropriate many-electron basis, their determination is less straightforward in DFT, where no systematically approximated ground state wavefunction is available. Therefore, in order to arrive at a practical approach to excited state properties based on DFT, a different methodology is employed, which will be outlined in the following.

Time-dependent density functional theory (TDDFT). The DFT formalism as sketched above provides a means to approximately calculate the electronic ground state of a molecular system. Although there is no direct variational approach to calculating excited state densities, an approximate treatment of excited states becomes possible in the framework of the time-dependent density functional theory. Based on the finding of Runge and Groß that in analogy to the stationary Hohenberg-Kohn theorem also the time-dependent electron density is (up to a phase factor) in a one-to-one correspondence

with the time-dependent wavefunction [206], determination of this density should suffice to determine time-dependent properties. One can formulate a time-dependent variational principle for the action

$$A = \int_{t_0}^{t_1} \left\langle \Psi(t) \left| i \frac{\partial}{\partial t} - \hat{H}(t) \right| \Psi(t) \right\rangle dt, \quad (2.28)$$

from which, considering that the wavefunction is a functional of the time-dependent density and representing this density using molecular orbitals, the time-dependent Kohn-Sham equations follow as

$$\hat{H}_{KS} \phi_i(\mathbf{r}, t) = i \frac{\partial}{\partial t} \phi_i(\mathbf{r}, t) \quad (2.29)$$

with the Kohn-Sham Hamiltonian

$$\hat{H}_{KS} = \left(-\frac{1}{2} \nabla^2 + v_{\text{eff}}^{KS}(\mathbf{r}, t) \right). \quad (2.30)$$

The effective potential is the time-dependent generalization of its stationary counterpart given in Eq. (2.25). The basic difference is the presence of a time-dependent exchange-correlation potential $v_{xc}(\mathbf{r}, t)$, which, however, in the limit of a slowly varying external potential, can be well approximated by the stationary $v_{xc}(\mathbf{r})$ (adiabatic approximation of TDDFT) [207, 208]. This allows one to employ the exchange-correlation functionals of ground state DFT also in the framework of TDDFT.

In principle, the equations (2.29) can be solved in two ways. One possible approach consists in a numerical procedure. For this purpose, in order to obtain excited state energies, the system can be perturbed by an external impulsive potential (e.g. an electric field), and the subsequent electronic evolution can be simulated in real time. From the time-dependent expectation values obtained in this way, frequency- or energy-dependent properties such as excitation energies can be determined by Fourier transformation [209, 210]. It should be noted, that the real-time propagation also opens a possibility to simulate the electron dynamics under perturbations such as laser pulses of finite time duration. In this way, as was briefly discussed in Sec. 1.2, coupled electron-nuclear self-consistent mean-field dynamics can be performed without diagonalizing the electronic Hamiltonian in terms of adiabatic basis states.

Most recent applications of TDDFT, though, rely on the linear response formalism for determining excited state properties [207, 208, 211] in terms of adiabatic electronic states. In order to derive the working equation for this approach, the system is formally exposed to a small perturbation, which leads to a change in the orbitals as well as in the Kohn-Sham Hamiltonian. To first order, the variation of the orbitals is $\phi_i(t) = e^{-i\epsilon_i t} (\phi_i^0 + \delta\phi_i(t))$, while the Kohn-Sham Hamiltonian becomes $\hat{H}_{KS} = \hat{H}_{KS}^0 + \delta\hat{H}_{KS}$. Introducing these quantities in Eq. (2.29) and retaining only the terms linear in the perturbation leads to

$$\hat{H}_{KS}^0 \delta\phi_i(t) + \delta\hat{H}_{KS} \phi_i^0 = \epsilon_i \delta\phi_i(t) + i \frac{\partial}{\partial t} \delta\phi_i(t). \quad (2.31)$$

The orbital variation can be expressed using an expansion in terms of the virtual Kohn-Sham orbitals as

$$\delta\phi_i(t) = e^{-i\omega t} \sum_k^{virt} X_{ki} \phi_k^0(\mathbf{r}) + e^{i\omega t} \sum_k^{virt} Y_{ki} \phi_k^0(\mathbf{r}). \quad (2.32)$$

Inserting this expansion into Eq. (2.31), multiplying from left by ϕ_n and integrating leads to

$$\begin{aligned} (\epsilon_n - \epsilon_i) \begin{pmatrix} X_{ni} \\ Y_{ni} \end{pmatrix} + \sum_k^{virt} \sum_j^{occ} \left[\begin{pmatrix} Y_{kj} \\ X_{kj} \end{pmatrix} \left\langle \phi_n \phi_k \left| \frac{\delta\hat{H}_{KS}[\rho]}{\delta\rho} \right| \phi_j \phi_i \right\rangle \right. \\ \left. + \begin{pmatrix} X_{kj} \\ Y_{kj} \end{pmatrix} \left\langle \phi_n \phi_j \left| \frac{\delta\hat{H}_{KS}[\rho]}{\delta\rho} \right| \phi_k \phi_i \right\rangle \right] = \omega \begin{pmatrix} X_{ni} \\ -Y_{ni} \end{pmatrix}. \end{aligned} \quad (2.33)$$

Employing the definitions

$$A_{abij} = \delta_{ab} \delta_{ij} (\epsilon_a - \epsilon_i) + \left\langle \phi_a \phi_j \left| \frac{\delta\hat{H}_{KS}[\rho]}{\delta\rho} \right| \phi_b \phi_i \right\rangle \quad (2.34)$$

$$B_{abij} = \left\langle \phi_a \phi_j \left| \frac{\delta\hat{H}_{KS}[\rho]}{\delta\rho} \right| \phi_b \phi_i \right\rangle \quad (2.35)$$

allows for the formulation of Eq. (2.33) as the TDDFT matrix eigenvalue equation

$$\begin{pmatrix} \mathbf{A} & \mathbf{B} \\ -\mathbf{B} & -\mathbf{A} \end{pmatrix} \begin{pmatrix} \mathbf{X} \\ \mathbf{Y} \end{pmatrix} = \omega \begin{pmatrix} \mathbf{X} \\ \mathbf{Y} \end{pmatrix}, \quad (2.36)$$

the eigenvalues ω of which can be identified with the electronic transition energies of the system, while the eigenvectors (\mathbf{X}, \mathbf{Y}) contain the expansion coefficients for the orbital variation.

In this form, TDDFT represents a valuable tool for the calculation of excited state energies and electronic absorption spectra in a wide variety of systems, usually working best for valence-excited states [207, 212]. Besides that, however, there are several limitations of TDDFT pertaining to other types of excited states. Most fundamentally, it has to be noted that linear response TDDFT represents a single-excitation formalism. This becomes evident from the dependence of the electron density on the Kohn-Sham orbitals,

$$\rho(\mathbf{r}) = \sum_{i=1}^N \phi_i^*(\mathbf{r}) \phi_i(\mathbf{r}), \quad (2.37)$$

from which the first-order density variation can be shown to consist only of products of

occupied and virtual orbitals,

$$\delta\rho = \sum_i^{occ} (\delta\phi_i^* \phi_i + \phi_i^* \delta\phi_i) = \sum_k^{virt} \sum_i^{occ} [(X_{ki} \phi_k^* \phi_i + Y_{ki} \phi_i^* \phi_k) e^{i\omega t} + (X_{ki} \phi_i^* \phi_k + Y_{ki} \phi_k^* \phi_i) e^{-i\omega t}], \quad (2.38)$$

corresponding to single excitations out of the Kohn-Sham reference determinant. Therefore, the description of states exhibiting double excitation or multireference character is not possible. Other well-known problems of TDDFT involve the incorrect description of Rydberg states due to an artificially lowered onset of the ionization continuum, as well as the underestimation of charge transfer excitation energies due to a wrong asymptotic behavior of the interaction energy between two charge densities. However, advances have been made in designing improved functionals providing better treatment of these problems [207, 212].

2.2.2 Molecular Properties

Electronic gradients. As outlined in Sec. 1.1, the mandatory prerequisite for classical MD simulations is the availability of the forces acting on the nuclei. In the framework of the “on the fly” class of procedures these are obtained as the negative gradients of the electronic energy with respect to the nuclear coordinates. In principle, two approaches can be employed for this purpose. The numerical method consists in calculating the electronic energy at a number of slightly distorted structures around the reference geometry and then approximating the gradient by finite differences along all coordinates. Although easy to implement, this method suffers from significant accuracy problems inherent to the finite difference approach. Attempting to tackle this drawback by increasing the number of points used in the numerical calculation scheme strongly increases the computational effort (for f nuclear degrees of freedom the minimum number of energy evaluations is $2f$, which would need to be much increased to significantly improve the results), thus making it impractical for large molecules. A more accurate and efficient alternative relies on the analytic calculation of the gradients [213], which requires much more theoretical development and programming effort in advance, but, with commercial codes readily available for this purpose, largely outperforms the numerical methods. For the derivation of analytical formulae for the energy gradient it has to be taken into account that both the Hamiltonian as well as the wavefunction depend on the nuclear coordinates. The wavefunction dependence is twofold: There is an explicit dependence introduced by the use of atom-centered (mostly Gaussian) basis sets, and an implicit dependence of the variation parameters (CI and MO coefficients), which also change with the nuclear geometry. Given a fully variational wavefunction, i.e. one whose energy expectation value has been optimized with respect to all variation parameters, the energy can be expressed as a function of nuclear

coordinates \mathbf{R} and variation parameters $\mathbf{C}(\mathbf{R})$. The derivative is then formally

$$\frac{dE}{dR_a} = \frac{\partial E}{\partial R_a} + \sum_i \frac{\partial E}{\partial C_i} \frac{\partial C_i}{\partial R_a}. \quad (2.39)$$

If the wavefunction is fully optimized, however, the sum on the right-hand side of Eq. (2.39) is zero since $\frac{\partial E}{\partial C_i} = 0$. The partial derivative of the energy can be decomposed by inserting the expectation value expression $E = \langle \Psi | \hat{H} | \Psi \rangle$, leading to

$$\frac{\partial E}{\partial R_a} = \left\langle \Psi \left| \frac{\partial \hat{H}}{\partial R_a} \right| \Psi \right\rangle + 2\text{Re} \left\langle \frac{\partial \Psi}{\partial R_a} \left| \hat{H} \right| \Psi \right\rangle. \quad (2.40)$$

The first part of this expression is the real physical contribution, coming from the nuclear-coordinate dependence of the Hamiltonian, and is termed the Hellmann-Feynman force [214, 215]. The second contribution, called the Pulay force [216], stems from the dependence of the basis set on the nuclear coordinates and is only present if atom-centered basis sets are employed. In the limit of a complete basis set, this contribution vanishes, but for common calculations using finite basis sets, in most cases it cannot be neglected.

For wavefunctions which are not fully variationally optimized, such as in truncated CI methods, the gradients have to be calculated by taking into account the wavefunction response on the nuclear displacements, $\frac{\partial C_i}{\partial R_a}$, for the subset of variation parameters for which $\frac{\partial E}{\partial C_i} \neq 0$. In the CI case, for instance, these are the MO coefficients. Such parameters may have been fully optimized in a simplified energy calculation, such as Hartree-Fock in the example considered here. In this way, an energy \tilde{E} is obtained, and the condition $\frac{\partial \tilde{E}}{\partial C_i} = 0$ holds. Taking the total derivative of this condition with respect to R_a leads to

$$\sum_j \frac{\partial^2 \tilde{E}}{\partial C_i \partial C_j} \frac{\partial C_j}{\partial R_a} = -\frac{\partial^2 \tilde{E}}{\partial C_i \partial R_a}, \quad (2.41)$$

or, in matrix notation,

$$\mathbf{w}\mathbf{C}^a = -\mathbf{v}^a, \quad (2.42)$$

where $(\mathbf{w})_{ij} = \partial^2 \tilde{E} / (\partial C_i \partial C_j)$, $(\mathbf{C}^a)_i = \partial C_i / \partial R_a$, and $(\mathbf{v}^a)_i = \partial^2 \tilde{E} / (\partial C_i \partial R_a)$. The expression (2.42) corresponds to as many equations as there are nuclear coordinates. Formally solving for \mathbf{C}^a and inserting in Eq. (2.39) leads to

$$\begin{aligned} \frac{dE}{dR_a} &= \frac{\partial E}{\partial R_a} - \sum_i \frac{\partial E}{\partial C_i} \left[\sum_j (\mathbf{w}^{-1})_{ij} \mathbf{v}_j^a \right] \\ &= \frac{\partial E}{\partial R_a} - \sum_j \left[\sum_i (\mathbf{w}^{-1})_{ij} \frac{\partial E}{\partial C_i} \right] \mathbf{v}_j^a. \end{aligned} \quad (2.43)$$

The expression in brackets in the last line now corresponds to solving only a single set of response equations [217],

$$\mathbf{w}^T \mathbf{z} = \mathbf{x} \quad (2.44)$$

with $x_i = \partial E / \partial C_i$. Having determined the \mathbf{z} vector, all components of the gradient can be obtained as

$$\frac{dE}{dR_a} = \frac{\partial E}{\partial R_a} - \mathbf{z}^T \cdot \mathbf{v}^a, \quad (2.45)$$

thus the effort of the calculation is essentially independent of the number of nuclear coordinates.

The calculation method outlined above is in principle applicable to all types of wavefunction-based energy expressions. As mentioned before, the partial derivative of the energy contains the derivative of the Hamiltonian, which is a one electron operator. The additional terms of the wavefunction force are essentially the derivatives of Gaussian basis functions with respect to the coordinates of their center, which are also Gaussian atomic orbitals with higher angular momentum. Finally, the wavefunction response calculated in Eq. (2.44) involves changes of the MO coefficients with the nuclear displacement. These techniques have been implemented in the last decades for a multitude of ab initio and semiempirical quantum chemical methods, in particular for those employed in this thesis, semiempirical CI [193, 218], and ground state DFT [219–221]. Also for the excited state energies from linear response approaches such as TDDFT, analytical gradients based on the above explained \mathbf{z} vector approach have been formulated and implemented in commercial programs [222–224].

Nonadiabatic couplings. The intrinsic coupling between adiabatic electronic states due to the breakdown of the Born-Oppenheimer approximation is determined by the nonadiabatic coupling gradient $\mathbf{d}_{IJ} = \langle \Psi_I | \nabla_{\mathbf{R}} | \Psi_J \rangle$. In this subsection, for clarity the electronic states are marked with a capitalized index, whereas individual MOs are referred to with a lower case index. For a general CI wavefunction (cf. Eq. (2.20)), the coupling gradient may be expanded as

$$\mathbf{d}_{IJ} = \langle \mathbf{c}^I | \nabla_{\mathbf{R}} | \mathbf{c}^J \rangle + \sum_{kk'} c_k^{*I} c_{k'}^J \langle \phi_k | \nabla_{\mathbf{R}} | \phi_{k'} \rangle, \quad (2.46)$$

where the $\mathbf{c}^I, \mathbf{c}^J$ are vectors of CI coefficients [225]. The first term of Eq. (2.46) can be related to the CI gradient by

$$\langle \mathbf{c}^I | \nabla_{\mathbf{R}} | \mathbf{c}^J \rangle = \frac{\langle \mathbf{c}^I | \nabla_{\mathbf{R}} \mathbf{H} | \mathbf{c}^J \rangle}{E_I - E_J}, \quad (2.47)$$

which allows for the use of gradient routines in order to calculate this part of the nonadiabatic coupling [226]. The second term of Eq. (2.46) can be reduced to gradients of MO

coefficients and atomic basis functions [225]. In the framework of the semiempirical implementation [111] used in this thesis, however, it is neglected due to its relative smallness in regions of substantial coupling [227, 228]. In nonadiabatic dynamics simulations, the nonadiabatic coupling vector enters the time-dependent Schrödinger equation exclusively in terms of a dot product with the nuclear velocities. This product, termed the scalar coupling D_{IJ} , can be related to the total time derivative of the wavefunction,

$$\begin{aligned}\dot{\mathbf{R}} \cdot \mathbf{d}_{IJ} &= D_{IJ} \\ &= \dot{\mathbf{R}} \cdot \langle \Psi_I | \nabla_{\mathbf{R}} | \Psi_J \rangle \\ &= \left\langle \Psi_I \left| \frac{d}{dt} \right| \Psi_J \right\rangle,\end{aligned}\tag{2.48}$$

which can be numerically determined, e.g. employing finite differences. In this way, evaluation of the complete gradient expression (2.46) can be avoided.

Nonadiabatic coupling in TDDFT. The calculation of nonadiabatic couplings in the framework of the TDDFT method requires a representation of the wavefunction based on Kohn-Sham (KS) orbitals. Since, as shown in Eq. (2.38), within the linear response method the electron density variation only contains contributions from single excitations of occupied to virtual KS orbitals, it is straightforward to assume a configuration interaction singles (CIS)-like expansion for the excited state electronic wavefunction. For a closed-shell system, the construction of this wavefunction has been explained in Refs. [127, 132]. For open shell systems, such as the Ag₃ cluster presented in Chapter 7, the wavefunction can be constructed as

$$|\Psi_K(\mathbf{r}; \mathbf{R}(t))\rangle = \sum_{i,a} c_{\alpha,i,a}^K |\Phi_{\alpha,i,a}(\mathbf{r}; \mathbf{R}(t))\rangle + \sum_{i,a} c_{\beta,i,a}^K |\Phi_{\beta,i,a}(\mathbf{r}; \mathbf{R}(t))\rangle,\tag{2.49}$$

where $|\Phi_{\alpha,i,a}(\mathbf{r}; \mathbf{R}(t))\rangle$ and $|\Phi_{\beta,i,a}(\mathbf{r}; \mathbf{R}(t))\rangle$ represent singly excited Slater determinants in the α and β spin subspaces in which one electron has been promoted from the occupied orbital ϕ_i to the virtual orbital ϕ_a with spin α or β , respectively [59]. The expansion coefficients $c_{\alpha,i,a}^K$ and $c_{\beta,i,a}^K$ in Eq. (2.49) are determined such that the wavefunction in Eq. (2.49) corresponds to the same density response as the one obtained by the linear response TDDFT procedure. Then, as shown in Ref. [132], the expansion coefficients are connected to the solutions \mathbf{X} and \mathbf{Y} of the TDDFT eigenvalue problem according to

$$c_{\alpha,i,a}^K = (\epsilon_{\alpha,a} - \epsilon_{\alpha,i})^{-1/2} (X_{\alpha,ia} + Y_{\alpha,ia})\tag{2.50}$$

$$c_{\beta,i,a}^K = (\epsilon_{\beta,a} - \epsilon_{\beta,i})^{-1/2} (X_{\beta,ia} + Y_{\beta,ia}).\tag{2.51}$$

In this way, an excited state wavefunction $|\Psi_K(\mathbf{r}; \mathbf{R}(t))\rangle$ is constructed, which can be employed to calculate the scalar nonadiabatic couplings, e.g. in an approximate way by using the finite difference for the time derivative,

$$D_{KI} \left(\mathbf{R} \left(t + \frac{\Delta t}{2} \right) \right) \approx \frac{1}{2\Delta t} [\langle \Psi_K(\mathbf{r}; \mathbf{R}(t)) | \Psi_I(\mathbf{r}; \mathbf{R}(t + \Delta t)) \rangle - \langle \Psi_K(\mathbf{r}; \mathbf{R}(t + \Delta t)) | \Psi_I(\mathbf{r}; \mathbf{R}(t)) \rangle]. \quad (2.52)$$

From Eq. (2.52) it can be seen that the nonadiabatic coupling is obtained as the overlap of two electronic wavefunctions for the states K and I at subsequent timesteps t and $t + \Delta t$, which can be further reduced to the overlap of spatial Kohn-Sham orbitals and eventually of basis functions as described in Refs. [127, 132].

Electric transition dipole moments. These quantities determine the coupling strength between electronic states due to an external electric field via the dipole coupling term $-\boldsymbol{\mu}_{KI} \cdot \mathbf{E}(t)$ and are defined as

$$\boldsymbol{\mu}_{KI}(\mathbf{R}(t)) = \langle \Psi_K(\mathbf{r}; \mathbf{R}(t)) | \hat{\boldsymbol{\mu}}_{el}(\mathbf{r}) | \Psi_I(\mathbf{r}; \mathbf{R}(t)) \rangle, \quad (2.53)$$

where $\hat{\boldsymbol{\mu}}_{el}(\mathbf{r}) = -e \sum_n^N \mathbf{r}_n$ is the electronic dipole operator for a system with N electrons. Therefore, if the wavefunction for two electronic states is available, each component of the respective transition dipole moment can simply be calculated using the above integral. For methods relying on Cartesian Gaussian atomic orbitals as basis functions, multiplication of a component of $\mathbf{r} = (x, y, z)$ by the wavefunction means the conversion of any basis function corresponding to angular momentum l to one of $l + 1$, thus the calculation of $\boldsymbol{\mu}_{KI}$ involves entirely the same types of integrals as those employed in an overlap calculation, i.e. over products of different basis functions.

For the case of TDDFT, where formally no excited state wavefunction is available, the approximate wavefunction ansatz of Eq. (2.49) can be employed to compute the transition dipole moments according to

$$\boldsymbol{\mu}_{KI} = \langle \Psi_K(\mathbf{r}; \mathbf{R}(t)) | \hat{\boldsymbol{\mu}}_{el}(\mathbf{r}) | \Psi_I(\mathbf{r}; \mathbf{R}(t)) \rangle \quad (2.54)$$

$$= \sum_{i,a} \sum_{j,b} c_{\alpha,i,a}^{*K} c_{\alpha,j,b}^I \langle \Phi_{\alpha,i,a}(\mathbf{r}; \mathbf{R}(t)) | \hat{\boldsymbol{\mu}}_{el}(\mathbf{r}) | \Phi_{\alpha,j,b}(\mathbf{r}; \mathbf{R}(t)) \rangle + \sum_{i,a} \sum_{j,b} c_{\beta,i,a}^{*K} c_{\beta,j,b}^I \langle \Phi_{\beta,i,a}(\mathbf{r}; \mathbf{R}(t)) | \hat{\boldsymbol{\mu}}_{el}(\mathbf{r}) | \Phi_{\beta,j,b}(\mathbf{r}; \mathbf{R}(t)) \rangle, \quad (2.55)$$

where a and b indicate virtual and i and j occupied orbitals, respectively [59, 229]. The dipole matrix elements on the right hand side of Eq. (2.55) can be reduced to the time-dependent transition dipole moments between Kohn-Sham orbitals [229].

2.2.3 Quantum mechanical/molecular mechanical (QM/MM) approach for inclusion of the environment

Notwithstanding the availability of very efficient electronic structure methods applicable to quite complex molecules, the complete quantum chemical description of systems such as molecules in solution, on surfaces, or biological macromolecules such as proteins or DNA still cannot be performed without further approximations. A possible strategy to devise a treatable approach consists in partitioning the system in one part which is described fully quantum mechanically (QM part), and another one (the environment), for which a molecular mechanics treatment is sufficient (MM part)³ [230–233]. The interaction of the QM and MM subsystems can be accounted for by different approximations. In the case of a molecule in solvent environment, where no chemical bonds between the two parts are present, as considered in this thesis, two approaches are available. In the mechanical embedding scheme, only the nonbonding interaction between the QM and MM parts is considered, while the electronic structure of the QM system is not influenced by the MM part. In this case the nonbonding interaction between both subsystems can be accounted for by the difference of the MM energies of the combined system (X+Y) and the QM system (X) alone. The total energy of the combined system can then be written as

$$E_{QM/MM} = E_{QM}(X) + E_{MM}(X + Y) - E_{MM}(X). \quad (2.56)$$

In contrast, the electrostatic embedding scheme takes into account the polarization of the QM wavefunction due to the environment by including the point charges from the MM part in the QM Hamiltonian. This allows for a more accurate description of the interaction between QM and MM parts, yet at the cost of higher computational effort. If the electrostatic effects of the solvent on the solute molecule are small, as in the case of solvated adenine investigated in this thesis, the more efficient mechanical embedding scheme thus represents a valuable approach to the combination of QM/MM with multistate dynamics simulations in the framework of FISH.

2.2.4 Choice of electronic structure methods employed in this thesis

The light-driven electron-nuclear dynamics simulations in the framework of the FISH method which will be presented in the subsequent chapters of this thesis have been performed using different electronic structure methods, selected according to their appro-

³Molecular mechanics represents an empirical approach to molecular energies as a function of their geometry. The electronic structure is completely neglected, and the energy is represented as a function of bond lengths and angles which are modelled by analytic functions. Moreover, nonbonding interactions such as electrostatic and van der Waals interactions are also accounted for. The necessary parameters such as force constants, equilibrium values of bond lengths and angles, as well as the partial atomic charges and van der Waals parameters are preset and define the specific force field model. Parameter values are usually determined from the experiment or from quantum chemical calculations.

priateness for the studied problems. For the dynamics and TRPES simulations of small noble metal clusters presented in Chapter 7, DFT and TDDFT have been used for the electronic structure. This was motivated by the ability these methods to provide an accurate ab initio description of such metallic systems, while at the same time being efficient enough to allow for dynamics calculations in a large manifold of excited states.

The control of electronic state populations in the potassium dimer presented in Chapter 9, which was studied in order to validate the applicability of FISH to optimal control, was performed using potential energy curves obtained from state-averaged CAS-MRCI calculations. The use of such a high-level correlated method was possible due to both the smallness of the system as such, as well as by the fact that for the electronic states under study, it was sufficient only to consider the two 4s electrons present in K_2 as the active ones, thus the active space could be kept relatively small.

The two examples of control in biomolecules interacting with their environment, i.e. adenine (Chapter 10) and flavins (Chapter 11), posed much higher demands on the efficiency of the employed methods. For both simulations, extended propagation times due to the use of long laser pulses (up to 5 ps) were necessary, and in addition a large number of simulations employing different laser fields had to be performed. Therefore, semiempirical methods were chosen for the electronic structure. In the framework of MR-CI for the excited states, these provide an accurate description of the spectroscopic properties of the studied systems. Specifically, in the case of adenine the OM2 method has been previously validated as an accurate approach [125]. For the case of flavin molecules, the most reliable description was achieved in the framework of the PM3 parameterization.

3 Field-Induced Surface Hopping Method (FISH)

In this section, our FISH method [55], which represents the basis of all theoretical results presented in this thesis, will be explicated. The aim of this approach is the simulation of laser-driven coupled electron-nuclear dynamics in complex molecular systems accounting for all nuclear degrees of freedom. This is achieved by combining quantum mechanical electronic state population dynamics, directly including the laser field, with classical nuclear dynamics. To this end, independent trajectories are propagated in the manifold of adiabatic electronic states, and the transfer of electronic population induced by the laser field is accounted for by allowing the trajectories to change their current state. For this purpose, a stochastic process is employed, in which hopping probabilities are determined by the changes of the quantum mechanical populations of each state along the trajectories. In this way, a readily applicable method has been designed which can be combined with classical MD “on the fly” in the framework of any quantum chemical method for which the needed energies, gradients and couplings are available. From a methodological point of view, the FISH method has been inspired by the previously established surface hopping schemes of Tully and others (cf. Section 1.2). However, the FISH method provides a more general applicability than these since it allows for explicit inclusion of field-induced couplings between electronic states in addition to the nonadiabatic effects. Only the latter are already accounted for in the field-free surface hopping method according to Tully.

This chapter is structured as follows: First, in Sec. 3.1 the basic equations of motion of a molecular system driven by an external field are set up, and a partial classical limit for the nuclear degrees of freedom is taken, leading to equations of motion for a phase space density. Subsequently, in Sec. 3.2, classical trajectories are introduced to represent the semiclassical phase space density, and in Sec. 3.3 the surface hopping procedure for determining the electronic state of the trajectories is explained. In Sec. 3.4, this is followed by a description of the overall algorithm for performing FISH simulations. Finally, the general scope of the FISH method is elucidated in Sec. 3.5.

3.1 Semiclassical time evolution of a molecular system

In the framework of the density operator formalism introduced in Sec. 1.1, the equation of motion for a system described by a Hamiltonian \hat{H}_0 is the Liouville-von Neumann equation

$$i\hbar\dot{\hat{\rho}} = [\hat{H}_0, \hat{\rho}]. \quad (3.1)$$

As discussed in Sec. 1.1, for a molecular system the Hamiltonian can be split into the nuclear kinetic energy and an electronic part as $\hat{H}_0 = \frac{1}{2}\hat{\mathbf{p}} \cdot \mathbf{M}^{-1}\hat{\mathbf{p}} + \hat{H}_{el}$. Within the Born-Oppenheimer approximation, a complete set of eigenfunctions of the electronic Hamilto-

nian for fixed nuclear coordinate \mathbf{q} can be introduced according to Eq. (1.3), from which eigenenergies $E_i(\mathbf{q})$ and eigenstates $|i; \mathbf{q}\rangle$ are determined that are parametrically dependent on the nuclear coordinates. Subsequently utilizing the complete basis set formed by combining the eigenstates of \hat{H}_{el} with those of the nuclear position operator $\hat{\mathbf{q}}$, $|\mathbf{q}\rangle \otimes |i; \mathbf{q}\rangle$, the total Hamiltonian can be spectrally decomposed as

$$\hat{H}_0 = \sum_j \int d\mathbf{q}' |\mathbf{q}'\rangle \otimes |j; \mathbf{q}'\rangle \left(-\frac{\hbar^2}{2} \nabla_{\mathbf{q}'} \cdot \mathbf{M}^{-1} \nabla_{\mathbf{q}'} + E_j(\mathbf{q}') \right) \langle j; \mathbf{q}'| \otimes \langle \mathbf{q}'|. \quad (3.2)$$

This enables the introduction of the Born-Oppenheimer nuclear Hamiltonians

$$\hat{H}_i(\mathbf{q}) = \langle i; \mathbf{q}| \otimes \langle \mathbf{q}| \hat{H}_0 | \mathbf{q}\rangle \otimes |i; \mathbf{q}\rangle \quad (3.3)$$

associated to the electronic states $|i; \mathbf{q}\rangle$. In the presence of external perturbations such as e.g. electric or magnetic fields, a coupling operator can be defined in a similar way as

$$\hat{V} = \sum_{ij} \int d\mathbf{q}' |\mathbf{q}'\rangle \otimes |i; \mathbf{q}'\rangle \hat{V}_{ij}(\mathbf{q}', t) \langle j; \mathbf{q}'| \otimes \langle \mathbf{q}'|, \quad (3.4)$$

from which the electronic matrix element can be obtained as

$$\hat{V}_{ij}(\mathbf{q}, t) = \langle i; \mathbf{q}| \otimes \langle \mathbf{q}| \hat{V} | \mathbf{q}\rangle \otimes |j; \mathbf{q}\rangle. \quad (3.5)$$

This leads to a generalized form of the Liouville-von Neumann equation,

$$i\hbar \dot{\hat{\rho}} = [\hat{H}_0 + \hat{V}, \hat{\rho}], \quad (3.6)$$

or, in terms of electronic matrix elements $\hat{\rho}_{ij} = \langle i | \hat{\rho} | j \rangle$,

$$i\hbar \dot{\hat{\rho}}_{ij} = \hat{H}_i \hat{\rho}_{ij} - \hat{\rho}_{ij} \hat{H}_j + \sum_k \left(\hat{V}_{ik} \hat{\rho}_{kj} - \hat{\rho}_{ik} \hat{V}_{kj} \right). \quad (3.7)$$

For the ease of reading, the coordinate dependency has been omitted in the above equations, as it will be also done in the following. In order to proceed towards a mixed quantum-classical formulation, the Wigner transformation is introduced, and the classical limit is taken similar to the derivation given in Sec. 1.1 (cf. Eqs. (1.15)-(1.17)), but this time only for the nuclear degrees of freedom. This leads to a set of coupled equations for the phase space representations of the diagonal ($\rho_{ii}(\mathbf{q}, \mathbf{p}, t)$) and off-diagonal ($\rho_{ij}(\mathbf{q}, \mathbf{p}, t)$) density matrix elements:

$$\dot{\rho}_{ii} = \{H_i, \rho_{ii}\} + \sum_k \left(\frac{2}{\hbar} \text{Im} [V_{ik} \rho_{ki}] - 2 \text{Re} [(\mathbf{M}^{-1} \mathbf{p}) \cdot \mathbf{d}_{ik} \rho_{ki}] \right) \quad (3.8)$$

$$\begin{aligned} \dot{\rho}_{ij} = & -i\omega_{ij} \rho_{ij} + \frac{1}{2} (\{H_i, \rho_{ij}\} + \{H_j, \rho_{ij}\}) + \left[\frac{i}{\hbar} V_{ij} + (\mathbf{M}^{-1} \mathbf{p}) \cdot \mathbf{d}_{ij} \right] (\rho_{ii} - \rho_{jj}) \\ & + \sum_{k \neq i, j} \left[\frac{i}{\hbar} (V_{kj} \rho_{ik} - V_{ik} \rho_{kj}) - (\mathbf{M}^{-1} \mathbf{p}) \cdot (\mathbf{d}_{ik} \rho_{kj} - \mathbf{d}_{kj} \rho_{ik}) \right], \end{aligned} \quad (3.9)$$

where the diagonal density matrix elements determine the quantum mechanical state populations and the off-diagonal elements describe the coherence. The curly braces denote the Poisson brackets (cf. Eq. (1.17)) and H_i are the Hamiltonian functions for the electronic state i . The quantity ω_{ij} is the energy gap between the electronic states i and j , $\mathbf{d}_{ji} = \langle j | \nabla_{\mathbf{q}} | i \rangle$ denotes the nonadiabatic coupling elements describing the intrinsic coupling between nuclear and electronic degrees of freedom, with $\nabla_{\mathbf{q}}$ indicating the derivative with respect to the nuclear coordinates.

The time evolution of the phase space functions can now be separated into different physical contributions. For the diagonal terms $\rho_{ii}(\mathbf{q}, \mathbf{p}, t)$, the Poisson bracket $\{H_i, \rho_{ii}\}$ corresponds to the phase space density flow within the electronic state i , while the second term in Eq. (3.8) describes the population transfer between the state i and all other states k induced by the coupling terms. Similarly, for the coherences $\rho_{ij}(\mathbf{q}, \mathbf{p}, t)$, these two contributions are also present. However, in this case the Poisson brackets correspond to the evolution of the phase space function on an averaged surface of the states i and j . Furthermore, the additional first term $-i\omega_{ij} \rho_{ij}$ corresponds to the temporal phase change of the coherence.

The above equations can be used as a starting point for numerical solution procedures, in which the individual density matrix elements in phase space can be represented on a discrete grid or as ensembles of classical trajectories, as it has been discussed in Sec. 1.2 (cf. also Refs. [144, 146, 147]). However, since the FISH method aims at providing an approach of general applicability for complex molecular systems, the conceptual pathway followed here is based on using a single ensemble of trajectories to represent the dynamics of the entire phase space density.

3.2 Introduction of classical trajectories

Within the FISH approach, the nuclear phase space functions $\rho_{ii}(\mathbf{q}, \mathbf{p}, t)$ are represented by an ensemble of independent trajectories propagated in the respective electronic states, while the phase space coherences are disregarded. It should be noted, however, that on the level of individual trajectories, the electronic part of the coherences is nevertheless

accounted for, as it will be explained in Sec. 3.3 below. Given a number of N trajectories, $\rho_{ii}(\mathbf{q}, \mathbf{p}, t)$ can be expressed by a swarm of time-dependent δ functions

$$\rho_{ii}(\mathbf{q}, \mathbf{p}, t) = \frac{1}{N} \sum_k \theta_i^k(t) \delta[\mathbf{q} - \mathbf{q}_k^i(t; \mathbf{q}_0, \mathbf{p}_0)] \delta[\mathbf{p} - \mathbf{p}_k^i(t; \mathbf{q}_0, \mathbf{p}_0)] \quad (3.10)$$

where the set of coordinates $\mathbf{q}_k^i(t; \mathbf{q}_0, \mathbf{p}_0)$ and momenta $\mathbf{p}_k^i(t; \mathbf{q}_0, \mathbf{p}_0)$ denotes a trajectory k propagated in the electronic state i with initial conditions \mathbf{q}_0 and \mathbf{p}_0 . The parameter $\theta_i^k(t)$ has a value of unity if the trajectory k resides in the state i , and of zero otherwise.

The initial phase space distribution can e.g. be obtained by discrete sampling of a quantum mechanical Wigner distribution for the harmonic normal modes ω_n of the molecular system [83]:

$$\rho_{00}(\mathbf{q}_0, \mathbf{p}_0) = \prod_{n=1}^{N_{modes}} \frac{\alpha_n}{\pi \hbar} \exp \left[-\frac{\alpha_n}{\hbar \omega_n} (p_{0n}^2 + \omega_n^2 q_{0n}^2) \right], \quad (3.11)$$

where q_{0n} and p_{0n} are the ground state normal coordinates and conjugate momenta, while $\alpha_n = \tanh(\hbar \omega_n / 2k_b T)$ is a factor including effects of a finite temperature.

The nuclear trajectories obey the classical Newtonian equations of motion,

$$\dot{\mathbf{p}}(t) = - \sum_i \theta_i(t) \nabla_{\mathbf{q}} E_i[\mathbf{q}(t)], \quad (3.12)$$

which can be solved numerically using the Verlet algorithm as described in Sec. 2.1 [180]. In Eq. (3.12) the parameter $\theta_i(t)$ has a value of unity for the electronic state in which the trajectory is propagated at time t and of zero for all other states. $E_i[\mathbf{q}(t)]$ is the adiabatic potential energy of the electronic state i . The forces acting on the nuclei ($-\nabla_{\mathbf{q}} E_i[\mathbf{q}(t)]$) need to be calculated only for the given nuclear configuration in each time step ("on the fly").

If an interaction with the environment such as solution is present, dissipative effects on the nuclear motion can be approximately accounted for by employing the Langevin equation of motion

$$\dot{\mathbf{p}}(t) = - \sum_i \theta_i(t) \nabla_{\mathbf{q}} E_i[\mathbf{q}(t)] - \gamma \mathbf{p}(t) + \mathbf{F}_{rand}(t). \quad (3.13)$$

instead of Eq. (3.12) for calculating the forces acting on the nuclei (cf. Sec. 2.1). Here, γ is an empirical friction coefficient and F_{rand} represents a random force. This equation can be numerically solved using e.g. a modified version of the Verlet algorithm [185]. The solution of Eqs. (3.12) or (3.13) provides continuous nuclear trajectories which reside in pure electronic states and may switch between these according to the quantum mechanical occupation probabilities given by ρ_{ii} , as worked out below.

3.3 Surface hopping procedure in FISH

In order to describe the electronic degrees of freedom on the level of classical nuclear trajectories, the set of equations (3.8)-(3.9) for the whole ensemble has to be transformed to its counterpart for each individual trajectory. For this purpose, the density matrix elements $\rho_{ij}(\mathbf{q}, \mathbf{p}, t)$ are rewritten as

$$\rho_{ij}(\mathbf{q}, \mathbf{p}, t) = \tilde{\rho}_{ij}(\mathbf{q}, \mathbf{p}, t) e^{-\eta_{\mathbf{q}}(\mathbf{q}-\mathbf{q}_t)^2} e^{-\eta_{\mathbf{p}}(\mathbf{p}-\mathbf{p}_t)^2} = \tilde{\rho}_{ij}(\mathbf{q}, \mathbf{p}, t) \mathcal{P}(\mathbf{q}, \mathbf{q}_t, \mathbf{p}, \mathbf{p}_t), \quad (3.14)$$

where \mathcal{P} represents a Gaussian function in phase space with time-dependent centers \mathbf{q}_t and \mathbf{p}_t . This expression can be inserted into Eqs. (3.8)-(3.9). For clarity, in the following this will be elaborated only for the general matrix element ρ_{ij} , since the corresponding Eq. (3.9) contains Eq. (3.8) for the diagonal elements as a special case. Thus, it follows:

$$\begin{aligned} & \dot{\tilde{\rho}}_{ij} \mathcal{P} + 2[\eta_{\mathbf{q}} \dot{\mathbf{q}}_t (\mathbf{q} - \mathbf{q}_t) + \eta_{\mathbf{p}} \dot{\mathbf{p}}_t (\mathbf{p} - \mathbf{p}_t)] \tilde{\rho}_{ij} \mathcal{P} \\ &= -i\omega_{ij} \tilde{\rho}_{ij} \mathcal{P} + \frac{1}{2} (\{H_i, \tilde{\rho}_{ij} \mathcal{P}\} + \{H_j, \tilde{\rho}_{ij} \mathcal{P}\}) \\ &+ \left[\frac{i}{\hbar} V_{ij} + (\mathbf{M}^{-1} \mathbf{p}) \cdot \mathbf{d}_{ij} \right] (\tilde{\rho}_{ii} \mathcal{P} - \tilde{\rho}_{jj} \mathcal{P}) \\ &+ \sum_{k \neq i, j} \left[\frac{i}{\hbar} (V_{kj} \tilde{\rho}_{ik} \mathcal{P} - V_{ik} \tilde{\rho}_{kj} \mathcal{P}) - (\mathbf{M}^{-1} \mathbf{p}) \cdot (\mathbf{d}_{ik} \tilde{\rho}_{kj} \mathcal{P} - \mathbf{d}_{kj} \tilde{\rho}_{ik} \mathcal{P}) \right]. \end{aligned} \quad (3.15)$$

The Poisson brackets can be expanded as

$$\{H_i, \tilde{\rho}_{ij} \mathcal{P}\} = \{H_i, \tilde{\rho}_{ij}\} \mathcal{P} + \{H_i, \mathcal{P}\} \tilde{\rho}_{ij} \quad (3.16)$$

$$= \{H_i, \tilde{\rho}_{ij}\} \mathcal{P} - 2\eta_{\mathbf{p}} \frac{\partial H_i}{\partial \mathbf{q}} (\mathbf{p} - \mathbf{p}_t) \tilde{\rho}_{ij} \mathcal{P} + 2\eta_{\mathbf{q}} \frac{\partial H_i}{\partial \mathbf{p}} (\mathbf{q} - \mathbf{q}_t) \tilde{\rho}_{ij} \mathcal{P}. \quad (3.17)$$

In this way, Eq. (3.15) is composed of terms that are either proportional to $(\mathbf{q} - \mathbf{q}_t) \mathcal{P}$, to $(\mathbf{p} - \mathbf{p}_t) \mathcal{P}$, or to \mathcal{P} only. Therefore, the equation is satisfied if the expressions pertaining to each of these factors vanish identically. This gives rise to separated equations of motion for $\tilde{\rho}_{ij}$, \mathbf{q}_t , and \mathbf{p}_t :

$$\begin{aligned} \dot{\tilde{\rho}}_{ij} \mathcal{P} &= -i\omega_{ij} \tilde{\rho}_{ij} \mathcal{P} + \frac{1}{2} (\{H_i, \tilde{\rho}_{ij}\} + \{H_j, \tilde{\rho}_{ij}\}) \mathcal{P} \\ &+ \left[\frac{i}{\hbar} V_{ij} + (\mathbf{M}^{-1} \mathbf{p}) \cdot \mathbf{d}_{ij} \right] (\tilde{\rho}_{ii} \mathcal{P} - \tilde{\rho}_{jj} \mathcal{P}) \\ &+ \sum_{k \neq i, j} \left[\frac{i}{\hbar} (V_{kj} \tilde{\rho}_{ik} \mathcal{P} - V_{ik} \tilde{\rho}_{kj} \mathcal{P}) - (\mathbf{M}^{-1} \mathbf{p}) \cdot (\mathbf{d}_{ik} \tilde{\rho}_{kj} \mathcal{P} - \mathbf{d}_{kj} \tilde{\rho}_{ik} \mathcal{P}) \right] \end{aligned} \quad (3.18)$$

$$\dot{\mathbf{q}}_t \mathcal{P} = \frac{1}{2} \left(\frac{\partial H_i}{\partial \mathbf{p}} + \frac{\partial H_j}{\partial \mathbf{p}} \right) \mathcal{P} \quad (3.19)$$

$$\dot{\mathbf{p}}_t \mathcal{P} = -\frac{1}{2} \left(\frac{\partial H_i}{\partial \mathbf{q}} + \frac{\partial H_j}{\partial \mathbf{q}} \right) \mathcal{P}, \quad (3.20)$$

in which for later convenience the Gaussian functions \mathcal{P} have been retained. Subsequently, for all three equations, the phase space integral over \mathbf{q} and \mathbf{p} is taken. Assuming that the density matrix element $\tilde{\rho}_{ij}$ vanishes for $\mathbf{q} \rightarrow \pm\infty$, $\mathbf{p} \rightarrow \pm\infty$, the integral over the Poisson brackets in Eq. (3.18) vanishes, too. To solve the remaining integrals, the limit of an infinitely narrow Gaussian function \mathcal{P} is considered. This corresponds to $\eta_{\mathbf{q}}$ and $\eta_{\mathbf{p}}$ going towards infinity, in which case the Gaussian turns into a delta function:

$$\lim_{\substack{\eta_{\mathbf{q}} \rightarrow \infty \\ \eta_{\mathbf{p}} \rightarrow \infty}} \mathcal{P}(\mathbf{q}, \mathbf{q}_t, \mathbf{p}, \mathbf{p}_t) \rightarrow \delta(\mathbf{q} - \mathbf{q}_t) \delta(\mathbf{p} - \mathbf{p}_t). \quad (3.21)$$

Performing the phase space integration now leads to the replacement of the coordinates \mathbf{q} and momenta \mathbf{p} by the time-dependent quantities $\mathbf{q}_t = \mathbf{q}(t)$ and $\mathbf{p}_t = \mathbf{p}(t)$. Therefore, the density matrix elements $\tilde{\rho}_{ij}$ finally depend only parametrically on the actual time-dependent values of coordinates and momenta for a given trajectory,

$$\dot{\tilde{\rho}}_{ii} = \sum_k \left(\frac{2}{\hbar} \text{Im} [V_{ik}[\mathbf{q}(t)] \tilde{\rho}_{ki}] - 2 \text{Re} [(\mathbf{M}^{-1} \mathbf{p}(t)) \cdot \mathbf{d}_{ik}[\mathbf{q}(t)] \tilde{\rho}_{ki}] \right) \quad (3.22)$$

$$\begin{aligned} \dot{\tilde{\rho}}_{ij} = & -\frac{i}{\hbar} (E_i[\mathbf{q}(t)] - E_j[\mathbf{q}(t)]) \tilde{\rho}_{ij} + \sum_k \left[\frac{i}{\hbar} (V_{kj}[\mathbf{q}(t)] \tilde{\rho}_{ik} - V_{ik}[\mathbf{q}(t)] \tilde{\rho}_{kj}) \right. \\ & \left. - (\mathbf{M}^{-1} \mathbf{p}(t)) \cdot (\mathbf{d}_{ik}[\mathbf{q}(t)] \tilde{\rho}_{kj} - \mathbf{d}_{kj}[\mathbf{q}(t)] \tilde{\rho}_{ik}) \right]. \end{aligned} \quad (3.23)$$

The motion of the trajectories is governed by Eqs. (3.19)-(3.20). In the spirit of the surface-hopping methodology relying on the propagation of trajectories on pure electronic energy surfaces, it suffices to consider the case $i = j$, giving rise to equations of motion for the nuclear trajectories according to

$$\dot{\mathbf{q}}(t) = \frac{\partial H_i}{\partial \mathbf{p}(t)} \quad (3.24)$$

$$\dot{\mathbf{p}}(t) = -\frac{\partial H_i}{\partial \mathbf{q}(t)}. \quad (3.25)$$

These are the classical Hamiltonian equations, thus corroborating the assumption made in Sec. 3.2 that the complete phase space density can be represented by an ensemble of nuclear trajectories evolving according to the classical equations of motion.

The above derived Eqs. (3.22)-(3.23) allow for the description of electronic population dynamics along classical nuclear trajectories. Notably, this formulation is fully equivalent to that introduced by Tully [52], who assigned in an ad-hoc fashion an electronic Schrödinger equation to each nuclear trajectory:

$$i\hbar\dot{c}_i(t) = E_i[\mathbf{q}(t)]c_i(t) + \sum_j (V_{ij}[\mathbf{q}(t), t] - i\hbar(\mathbf{M}^{-1}\mathbf{p}(t)) \cdot \mathbf{d}_{ij}[\mathbf{q}(t)])c_j(t), \quad (3.26)$$

where $c_i(t)$ are the expansion coefficients of the electronic wavefunction in the basis of adiabatic electronic states. From this equation, density matrix elements can be calculated as $\tilde{\rho}_{ij} = c_i c_j^*$. This in turn allows for transforming the Schrödinger equation (3.26) into equations of motion for the density matrix elements, which emerge as identical to the set of Eqs. (3.22)-(3.23). Therefore, the presented derivation provides a formal justification for the use of Eq. (3.26) for the electronic population dynamics.

The FISH method extends the common surface hopping approaches by augmenting the description of field-free electronic relaxation dynamics by the interaction with external couplings V_{ij} . Typically, these are given as the electric dipole coupling, i.e.

$$V_{ij} = -\boldsymbol{\mu}_{ij}[\mathbf{q}(t)] \cdot \mathbf{E}(t) \quad (3.27)$$

with the transition dipole moment $\boldsymbol{\mu}_{ij}$ and the electric field strength \mathbf{E} . However, recently, also a quadratic field coupling has been implemented in order to approximate the two-photon excitation in strong nonresonant laser fields, which is mediated by a manifold of high-energy states [234]. In this case, it can be shown that the coupling arises due to a dynamic transition polarizability as

$$V_{ij} = -\frac{1}{4\hbar} \boldsymbol{\mathcal{E}}^T(t) \cdot \boldsymbol{\alpha}_{ij}[\mathbf{q}(t), t] \boldsymbol{\mathcal{E}}(t), \quad (3.28)$$

where $\boldsymbol{\mathcal{E}}(t)$ is the field envelope. Moreover, also magnetic dipole couplings, which play an important role in the dynamics of enantiomers of chiral molecules interacting with polarized light, can be employed [235]. In addition, it was recently demonstrated that the spin-orbit coupling between electronic state manifolds of different spin symmetry can be a posteriori introduced on the same footing [236].

The Schrödinger equation (3.26) is solved parallel to the propagation of the nuclear equations of motion in order to obtain the time-dependent electronic state coefficients c_i . For this purpose, numerical solution methods such as the Runge-Kutta algorithm are used. Typically, the integration time step $\Delta\tau$ is chosen to be much smaller than the time

step Δt used for the nuclear integration since the oscillations of the c_i occur on a much shorter time scale than the nuclear motion.

Based on the solution of Eq. (3.26) for each individual trajectory, the electronic population transfer is modelled by allowing the trajectories to switch between the electronic states according to a probability derived from the coefficients c_i . This procedure is related to Tully's surface hopping method [52] which has been developed in order to describe field-free nonadiabatic transitions in molecular systems. However, as already outlined in the beginning of this chapter, the FISH method provides a more general framework since also couplings induced by external fields are considered. It should be noted that in the absence of electric fields, e.g. in cases in which the dynamics is continued after the end of a laser pulse, the FISH method becomes equivalent to the field-free nonadiabatic surface hopping procedure.

In principle, the hopping process of switching from electronic state i to state j can be performed either after each nuclear integration time step Δt , or, alternatively, after each electronic integration time step $\Delta\tau$, which is much smaller than Δt . The actual choice depends on how the hopping probabilities $P_{i\rightarrow j}$ are computed. According to the original procedure of Tully, these can be obtained as

$$P_{i\rightarrow j}(t) = (-1) \frac{\left(\frac{2}{\hbar} \text{Im}[V_{ij}\rho_{ji}] - 2\text{Re}[(\mathbf{M}^{-1}\mathbf{p}) \cdot \mathbf{d}_{ij}\rho_{ji}]\right) \Delta t}{\rho_{ii}(t)} \quad (3.29)$$

after each nuclear time step [52]. The expression in brackets in the numerator of Eq. (3.29) corresponds to a single term of the sum in Eq. (3.22), indicating the rate of change of probability amplitude between the states i and j . Multiplying by the time step Δt yields the total amount of probability exchange between these states, and division by the current population of the initial state leads to a normalized probability. Finally, this expression is only evaluated if the numerator is negative, i.e. if there is a population loss in the initial and a gain in the final state. In this case, the minus sign ensures a positively definite value of the probability. If the numerator is positive, corresponding to population transfer in the opposite direction, the probability is set to zero. The hopping probability derived in this way has been commonly used in many applications of Tully's surface hopping method. However, due its explicit dependence on fast changing quantities such as the electronic coherences ρ_{ij} and the couplings V_{ij} which can include a rapidly oscillating electric field, it suffers from the drawback that for not sufficiently small time steps, numerical discrepancies can arise and cause erroneous results. Therefore, it was proposed already in the context of field-free surface hopping to calculate the hopping probabilities and perform the hopping procedure after each small electronic time step instead, thus replacing the nuclear time step Δt by its electronic counterpart $\Delta\tau$ in Eq. (3.29) [132].

However, an alternative procedure for calculating the hopping probabilities can be also formulated, which is based only on the more slowly varying electronic state populations, thus avoiding a direct dependence on rapidly oscillating coherences or external fields [237]. For this purpose, the probabilities to depopulate the initial state i and to populate the final state j are first calculated separately. The depopulation probability of state i is obtained from the population change during a time step Δt , normalized to the actual population of this state:

$$P_{\text{depopulate } i} = \Theta(-\dot{\rho}_{ii}) \frac{-\dot{\rho}_{ii}}{\rho_{ii}} \Delta t. \quad (3.30)$$

By definition, this probability can be nonzero only if the population of state i decreases, which is ensured by the Θ function in Eq. (3.30). The expression $\dot{\rho}_{ii}\Delta t$ can be calculated from the populations in successive nuclear time steps t and $t + \Delta t$ as $\dot{\rho}_{ii}\Delta t = \rho_{ii}(t + \Delta t) - \rho_{ii}(t)$, such that no explicit calculation of time derivatives is necessary. If the depopulation probability of state i is nonzero, the probability to populate state j depends on the change of the population $\dot{\rho}_{jj}$, which must be positive. Since, however, this condition can be simultaneously fulfilled for several electronic states at the same time, the probability to populate the particular state j is obtained by normalizing to the total rate of change of all states k with growing population (cf. the denominator of Eq. (3.31) below):

$$P_{\text{populate } j} = \frac{\Theta(\dot{\rho}_{jj})\dot{\rho}_{jj}}{\sum_k \Theta(\dot{\rho}_{kk})\dot{\rho}_{kk}}. \quad (3.31)$$

Given these probabilities for the depopulation of state i and the population of state j , the total probability for hopping from i to j is obtained as [237]:

$$P_{i \rightarrow j} = P_{\text{depopulate } i} P_{\text{populate } j} = \Theta(-\dot{\rho}_{ii}) \Theta(\dot{\rho}_{jj}) \frac{-\dot{\rho}_{ii}}{\rho_{ii}} \frac{\dot{\rho}_{jj}}{\sum_k \Theta(\dot{\rho}_{kk})\dot{\rho}_{kk}} \Delta t. \quad (3.32)$$

This final expression for the hopping probability allows for performing the state switching procedure in each nuclear time step, since, as mentioned above, the populations typically vary much more slowly than the couplings and coherences employed in Eq. (3.29) which usually contain rapidly oscillating terms. Therefore, the use of Eq. (3.32) is of particular advantage in the context of field-driven dynamics, and consequently this procedure has been employed in all FISH simulations presented in this thesis.

3.4 Simulation procedure

The simulation of the laser-induced dynamics in the framework of the FISH method, using the above derived approach, can now be cast in the following steps:

- (i) Initial conditions for an ensemble of trajectories are generated by sampling e.g. the canonical Wigner distribution function (cf. Eq. (3.11)) or a long classical trajectory

in the electronic ground state, and the initial electronic states for the trajectories are assigned. For a simulation including optical fields, usually the electronic ground state is initially populated.

- (ii) Each trajectory is classically propagated in the given electronic state by solving the Newton (Eq. (3.12)) or if necessary the Langevin (Eq. (2.13)) equations of motion. Simultaneously, all density matrix elements ρ_{ij} are calculated by numerical integration either directly from Eq. (3.22) or from the electronic state coefficients obtained by integration of Eq. (3.26).
- (iii) In order to determine in which electronic state the trajectory is propagated, the hopping probabilities are calculated according to Eq. (3.29) or (3.32). In a stochastic process, a uniform random number between zero and unity is employed to decide if a state switch should occur. After a successful hop, the trajectory is continued on the new electronic state. If the hopping event is caused by the intrinsic nonadiabatic coupling, a velocity rescaling procedure according to Eq. (1.26) or (1.28) is applied in order to ensure conservation of the total system energy. In the case of hopping due to external fields, the energy conservation condition is not imposed and therefore no rescaling is applied.
- (iv) After the trajectories are completed, electronic state populations and other properties such as spectroscopic observables or the phase space distribution of the nuclear degrees of freedom can be obtained by averaging over the entire ensemble. Moreover, in order to get an insight into mechanistic details of the studied processes, also the motion along individual trajectories can be analysed.

3.5 Scope of FISH

The mixed quantum-classical FISH method presented in the foregoing sections provides a unique framework for the simulation of laser-induced photodynamics in complex molecular systems. This has been achieved by the combination of classical nuclear dynamics with a quantum mechanical treatment of electronic state population dynamics in the presence of electric fields. In particular, population transfer processes in moderately strong fields such as coherent Rabi oscillations are very well described, as it has been evidenced on comparative studies of several model systems and small clusters [55, 63, 238]. Due to the classical description of the nuclear degrees of freedom, allowing for the efficient “on the fly” calculation of the electronic structure, for the first time a methodological framework has been established which allows both the treatment of large molecules and the explicit consideration of laser excitation beyond the perturbative limit.

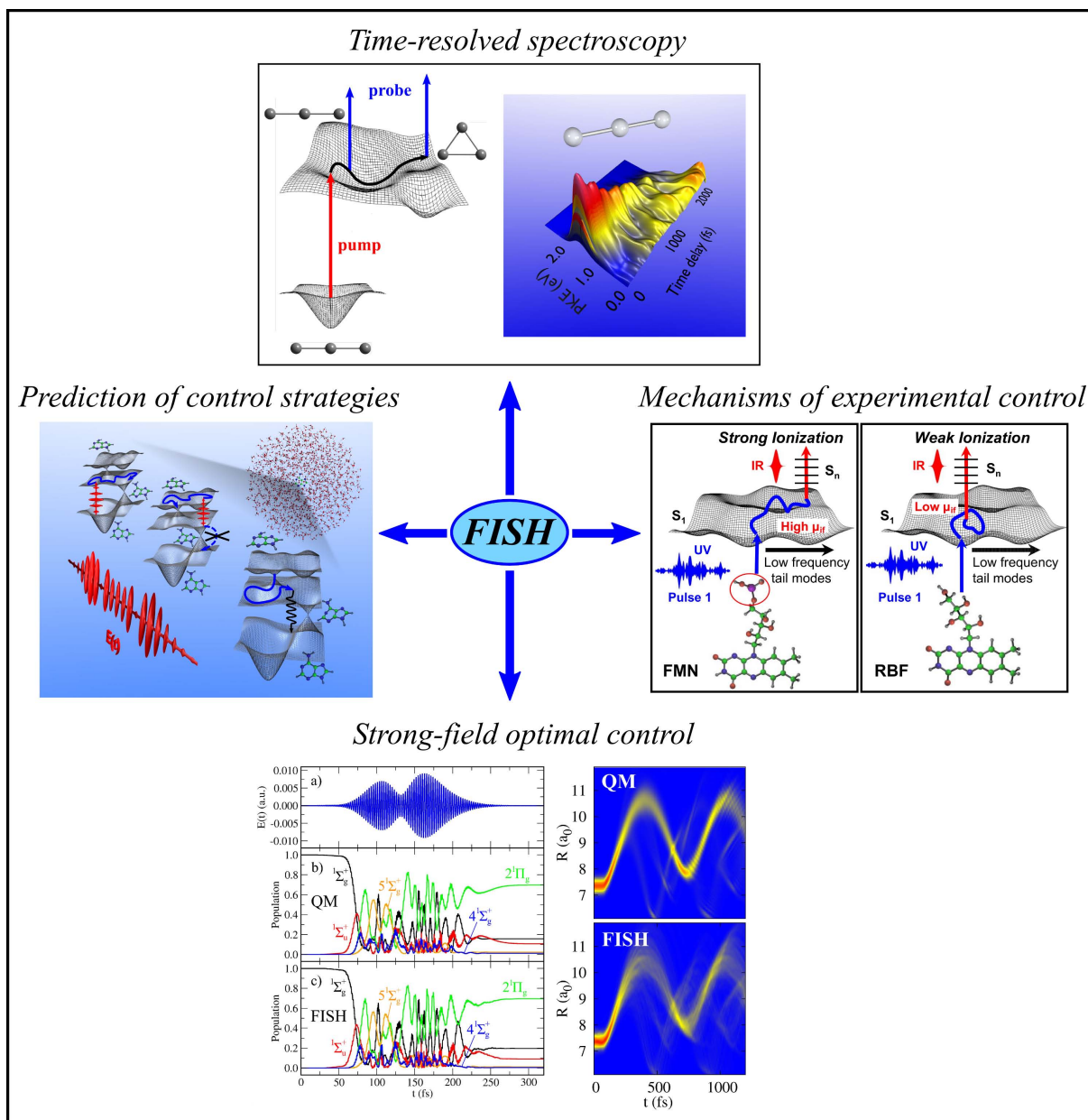


Figure 3.1: Scope of possible applications for the FISH method in the areas of ultrafast time-resolved spectroscopy and coherent quantum control.

The ability of FISH to accurately describe coupled electronic-nuclear dynamics driven by laser fields of moderate intensity opens a multitude of application possibilities in photochemistry and photophysics. Notably, the dynamics induced by laser pulse sequences can be simulated and used to calculate time-resolved spectroscopic observables. This allows for establishing a direct connection with experimental time-resolved spectra and provides a versatile means for their interpretation at the molecular level. Moreover, possible experiments may be also anticipated by theoretical predictions, which can serve to stimulate new experimental techniques and establish the conditions needed to observe specific molecular processes. In this context, the FISH method has been advanced for the simulation of time-resolved photoelectron spectra by an approximate description of the photoionization continuum [59], which will be presented in Chapter 6 of this thesis. Moreover, in the framework of FISH recently also a method for the simulation of time-resolved harmonic spectra, which provide a sensitive probe for coupled electron-nuclear dynamics, has been devised [238].

Beyond the mere analysis of processes, the interaction of molecules with light can also be utilized to achieve control by employing shaped laser pulses. In this context, the FISH method offers a particularly convenient way to simulate coherent control experiments. This is due to the explicit inclusion of the laser field in the FISH equations (3.26), which allows for employing laser pulses of arbitrary shapes in the simulations. Therefore, similar to the common experimental procedure, the electric fields can be iteratively optimized by using genetic algorithms [239], as it has been shown in Refs. [55, 63]. Alternatively, simple parameterized pulse forms may be proposed without the need for optimization, and the effect of parameter changes on the studied systems can be predicted [64]. In this way, decisive knowledge about suitable control fields can be gained, providing valuable information for experimental realizations. In addition, FISH provides also the opportunity to employ experimentally optimized laser fields in the simulation [67]. This allows for a molecular-level investigation of the dynamical processes underlying the experimental control and provides a route both for revealing the mechanism of control as well as of how this mechanism is reflected in the specific form of the optimized laser field. Within this thesis, control-related applications are the main subject of the Chapters 9, 10, and 11. Conclusively, the main application areas of FISH are summarized in Fig. 3.1.

The necessary ingredients needed to perform a FISH simulation are electronic state energies, their negative gradients with respect to the nuclear coordinates (forces), as well as the transition dipole matrix elements and nonadiabatic couplings between the electronic states, which all may be calculated “on the fly” along the nuclear trajectories. To obtain the above quantities, in principle the whole spectrum of quantum chemistry methods can be used. However, since ensembles of trajectories have to be propagated, which in the case of optimal control simulations has to be performed several times repeat-

edly, the computational demands for such simulations can become quite high. Therefore, the use of computationally efficient methods is advisable, provided they prove sufficiently accurate for the given problem. In particular, application of time-dependent density functional theory (TDDFT) has become possible due to the development of nonadiabatic couplings [127,131,132,240] and transition dipole moments between excited states [229]. Furthermore, also semiempirical quantum chemical models, which have been recently adapted to calculate arbitrary transition dipole moments and nonadiabatic couplings [111], offer a convenient and efficient possibility. However, the applicability of FISH simulations is not restricted to isolated molecules. Rather, also the molecular surrounding of the systems can be included at different levels of accuracy, such as by performing dissipative Langevin dynamics or by explicit inclusion of the environment in the framework of QM/MM methods. In this way, the influence of solvent, surfaces or protein environment on the photodynamical processes may be studied. In conclusion, the FISH method opens new routes to interesting applications in ultrafast spectroscopy and coherent control, a selection of which will be discussed in the following chapters 7, 9, 10, and 11.

4 Formal Aspects and Validation of FISH

The approximate description of coupled electron-nuclear dynamics underlying all surface-hopping approaches, including also FISH, requires the accuracy and applicability of these methods to be thoroughly validated by comparison with exact quantum dynamics. Although the FISH method formally features no additional approximations compared to field-free surface hopping, the field-induced excitation process makes relevant certain additional aspects which would otherwise play only a minor role. In the present chapter, three issues concerning the accuracy of FISH will be investigated. In the first place, the question of internal consistency will be addressed, which represents a well-examined subject in the context of field-free surface hopping. The specific aspects of this problem related to FISH will be discussed in Sec. 4.1. Subsequently, in Sec. 4.2 the issue of missing coherence decay (overcoherence), also a common problem in surface hopping methods, will be studied with the particular focus on its implications on time-resolved pump-probe spectroscopies involving sequential laser excitation and deexcitation steps. The chapter concludes with Sec. 4.3, presenting an issue specific to FISH, namely the mixed quantum-classical description of the field-induced excitation process itself and the implications of neglecting the quantum mechanical nature of the nuclei on the correct distribution of vibrational energy during the excitation. The sections of this chapter focus on the presentation of the comparative results that allow for the validation of FISH against quantum dynamics. Methodological details such as the parameters employed for the model systems and laser fields are provided in Appendix A.

4.1 Forbidden hops and internal consistency

As discussed in Sec. 1.2, a major requirement for the accuracy of surface hopping procedures is the internal consistency, i.e. the agreement of the fraction Π_i of trajectories residing in a particular electronic state with the averaged values $\bar{\rho}_{ii}$ of the quantum electronic state populations $|c_i|^2$ obtained from the Schrödinger equation (3.26). The main reason for the occurrence of poor internal consistency in surface-hopping approaches in general has been identified as the presence of forbidden hops due to energy conservation requirements (cf. Sec. 1.2). In FISH, contrary to field-free surface-hopping dynamics, this internal inconsistency problem is less pronounced, since, in the presence of a sufficiently intense and resonant field, most of the hopping events are caused by the matter-field interaction, which does not imply energy conservation for the molecular system. Therefore, no forbidden hops can arise in the time period of strong field coupling. The internal consistency of FISH in such cases is illustrated in Fig. 4.1, in which the sequential excitation in a three-state model system has been simulated employing the hopping procedure according to Eq. (3.32). Comparison of the fractional surface hopping state populations

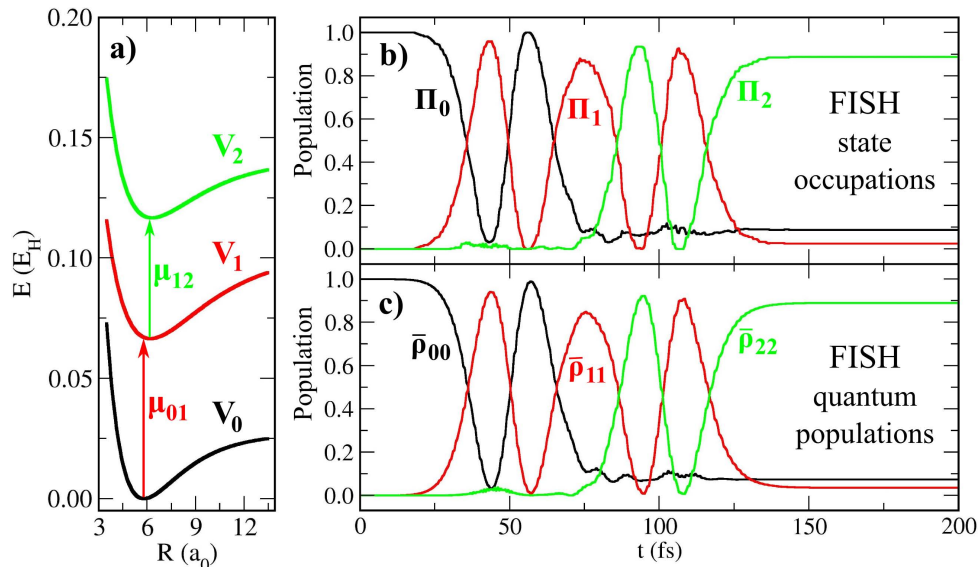


Figure 4.1: Illustration of the internal consistency of FISH for sequential excitation in a 3-state model system using two 35 fs laser pulses centered at 50 fs and 100 fs, respectively. The first pulse is resonant to the $0 \rightarrow 1$ and the second one to the $1 \rightarrow 2$ transition. Excellent agreement between the fractional state occupations Π_i and the averaged quantum populations $\bar{\rho}_{ii}$ is observed.

Π_i presented in Fig. 4.1b) with the averaged quantum populations $\bar{\rho}_{ii}$ shown in Fig. 4.1c) reveals perfect agreement. However, if nonadiabatic effects play a role during time periods of negligible field coupling, energy conservation is required and forbidden hops can occur similar to the case of Tully’s field-free surface hopping procedure, with the implications on the internal consistency of the simulation as discussed in Sec. 1.2.

A second source of internal inconsistency present in all surface-hopping based approaches also occurs in the absence of forbidden hops and is related to the description of quantum mechanical coherence in surface hopping. This issue will be discussed in the following paragraph.

4.2 Quantum coherence in FISH

Field-induced electronic excitation represents a typical coherent process in which the wavefunctions of the coupled states are characterized by a precisely defined phase relation. As it has been previously demonstrated on a number of examples, coherent electronic excitation is fully accounted for in the framework of the FISH method, which allows for the accurate simulation of population dynamics occurring in moderately intense fields, such as Rabi oscillations [55]. Furthermore, coherent excitation constitutes the basis for coherent control of molecular processes in strong fields, which can also be accurately simulated in the frame of FISH as will be shown in Chapter 9 and has been recently published in Ref. [63]. However, as a surface hopping method, FISH also has inherited a

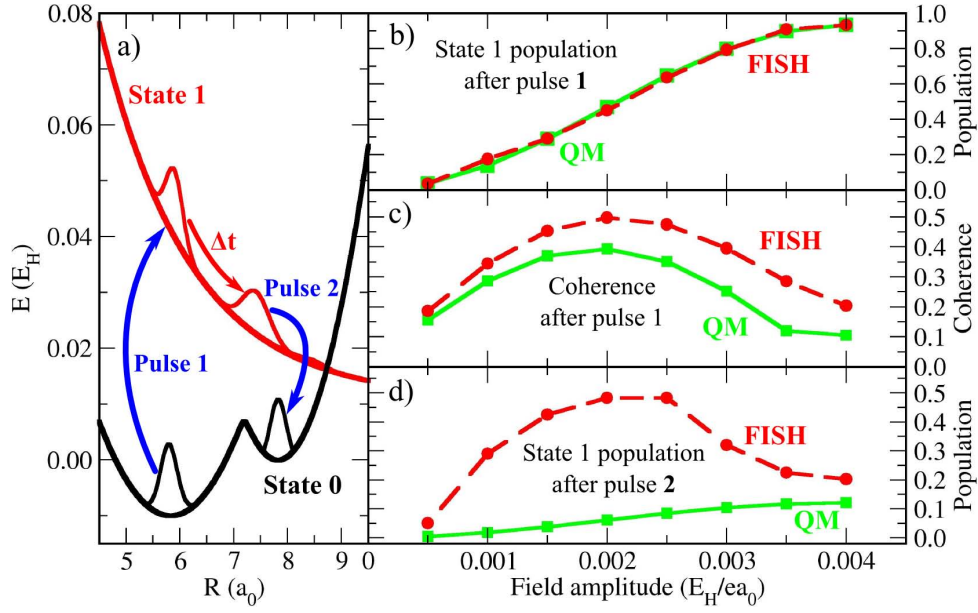


Figure 4.2: Overcoherence in FISH for pump-dump excitation using 5 fs pulses at $t_1 = 20$ fs/ $t_2 = 80$ fs. a) Potentials of the 2-state system and schematic illustration of the wavepacket dynamics. Right panel: Comparison of quantities from full quantum dynamics (green) and FISH simulations (red) as a function of the field amplitude: b) Population of state 1 after pulse 1 (at 25 fs), c) Modulus of the coherence between states 0 and 1 after pulse 1 (at 25 fs), d) Population of state 1 after pulse 2 (at 90 fs). The coherences in the FISH simulation are obtained by averaging $\rho_{ij} = c_i^* c_j$ over the entire ensemble.

drawback related to coherence, namely the phenomenon of overcoherence [116]. In order to make this clear, first the quantum mechanical nature of coherence will be considered. For two nuclear wavepackets $\chi_i(\mathbf{R})$ and $\chi_j(\mathbf{R})$, e.g. generated during electronic excitation, the coherence is defined as an overlap integral, $\rho_{ij} = \int d\mathbf{R} \chi_i^*(\mathbf{R}) \chi_j(\mathbf{R})$. Therefore, if the two wavepackets move spatially away from each other, their coherence must vanish. By contrast, in surface hopping the individual trajectories are propagated independently of each other, and thus no information about the spatial separation of different trajectories is available. Therefore, the coherence cannot, as in quantum dynamics, be defined by the spatial overlap of two wavepackets, but is just represented by the product of two electronic state coefficients as $\rho_{ij} = c_i^* c_j$, which remains constant after leaving a coupling region. For this reason, also the ensemble-averaged coherence remains constant if no coupling is present, and therefore no decay of coherence due to nuclear motion occurs in surface hopping, which may cause internal inconsistency [116]. Although not desirable from a methodological standpoint, this type of inconsistency can be neglected in several cases if the fractional state occupations for the given problem are sufficiently correct, as then the averaged quantum probabilities can be simply disregarded [112, 113, 116]. Nevertheless, beyond the more technical question of internal inconsistency, the lack of decoherence can, in certain cases, also lead to qualitative errors in the population dynamics, particularly

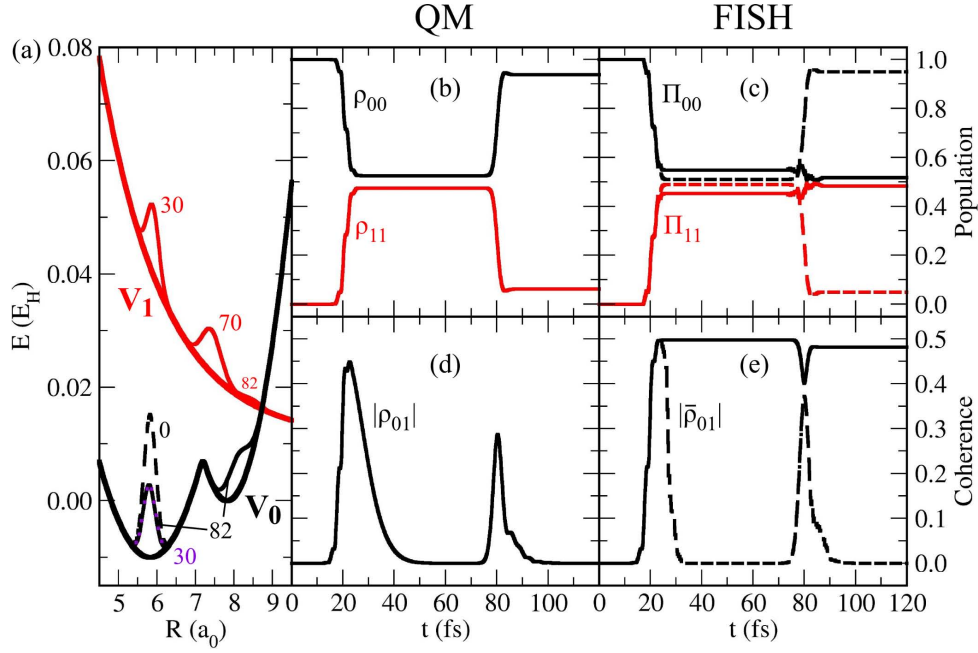


Figure 4.3: Overcoherence within FISH in a simulation of pump-dump excitation using 5 fs pump and dump pulses at $t_1 = 20$ fs/ $t_2 = 80$ fs. a) Potential functions of the 2-state system and quantum wavepackets at selected times (values in fs). b)/c) Time-dependent populations obtained by full quantum dynamics simulations and FISH. d)/e) Modulus of the coherence as function of time. The coherences in the FISH simulation are obtained by averaging $\rho_{ij} = c_i^* c_j$ over the entire ensemble. Full lines in c)/e): uncorrected FISH simulation. Dashed lines: FISH simulation employing an overlap-based decoherence correction. The uncorrected FISH method wrongly describes the effect of the dump pulse due to the lack of coherence decay. Introducing a correction accounting for this effect leads to much better agreement between FISH and quantum coherences and thus also of the populations.

if the trajectories experience the presence of strong coupling during several separate time periods of the studied dynamics. A typical case might consist in the sequential excitation of a system with time-delayed laser pulses, as is common in various pump-probe or pump-dump experiments. Therefore, in the following the issue of overcoherence will be studied on three prototypical cases for field-induced excitation, and the ability of FISH to properly treat them will be discussed.

Implications of a non-decaying coherence magnitude. Most basically, it is evident that problems concerning overcoherence are dependent on the magnitude of the coherence terms during the studied process, and it can be surmised that the smaller the coherence created in an excitation process is, the smaller also the implications of overcoherence will be. In order to quantify this, dynamics in the model system shown in Fig. 4.2a) has been studied both using numerically exact quantum dynamics and employing FISH dynamics. The model system is characterized by a double well potential representing the lower electronic state 0, and a dissociative upper state 1. Short-pulse excitation of the

wavepacket initially situated in the left well of state 0 to the higher state 1 leads to a fast passage of the excited state wavepacket towards a position directly above the right well of the state 0, to which it is dumped by a second laser pulse. By varying the field strength of the first laser pulse, the excitation efficiency can be controlled almost completely in the range between 0 and 100 %, as shown in Fig. 4.2b). The agreement between quantum mechanical and FISH excitation is very good for this process. In Fig. 4.2c), the magnitude of the coherence ρ_{01} between the states immediately after the end of the first laser pulse is shown, illustrating that the largest coherence is created if about half of the electronic state population is transferred from state 0 to state 1. If almost no, or almost complete population transfer takes place, the coherence is significantly smaller. Also for the coherences, good agreement between quantum and FISH simulations is present. However, these coherences strongly influence the accuracy of FISH in reproducing the effect of the second laser pulse, as can be inferred from Fig. 4.2d). It is clearly visible that, while for the lowest as well as for the highest field intensities, good agreement of the quantum mechanical and the FISH results is observed, significant deviations are present for intermediate field strengths, which cause only partial population transfer and therefore large coherences. Therefore, in such situations the effect of overcoherence is most pronounced.

Aiming at a more detailed analysis of this issue, in the following the population dynamics induced by an intensity of the first laser pulse of $0.002 E_H/ea_0$, leading to 50 % population transfer from state 0 to state 1, will be investigated. The model system as well as the nuclear wavepackets at selected time steps are shown in Fig. 4.3a). As already stated above, the used pump pulse induces about 50 % population transfer, as depicted for the full quantum dynamics simulation in Fig. 4.3b). In this way, a large coherence ρ_{01} is created, which due to the nuclear motion decreases to zero before the dump pulse sets in (cf. Fig. 4.3d)). The latter then leads to a complete transfer of the state 1 population to the right well of the state 0 potential. In the FISH simulation, the decay of coherence is not reproduced and the averaged coherence stays constant, as can be seen from Fig. 4.3e) (full line). As a consequence, the action of the dump pulse is not properly reproduced, since only very small net population transfer takes place as shown in Fig. 4.3c). Identifying the constant magnitude of the coherence as the main source for this deviation, a possible remedy can be sought in introducing a coherence decay correction in the FISH algorithm. As outlined in Sec. 1.2, in the context of field-free surface hopping, several techniques have been suggested for this purpose [116–120]. For the case presented here, a modification of the decay-of-Gaussian-overlap method of Ref. [117] has been employed, as discussed in detail in Appendix B. In this way, as shown as a dashed line in Fig. 4.3e), the coherence ρ_{01} could be completely removed in the modified FISH simulation, which subsequently lead to a correct description of the population dynamics induced by the dump pulse.

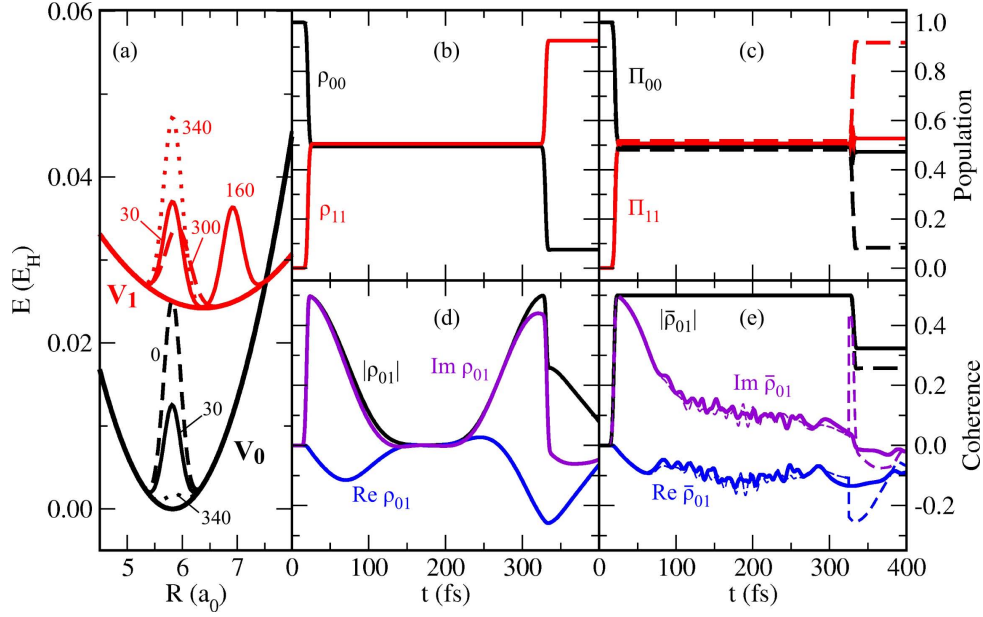


Figure 4.4: Quantum dynamics simulation of pump-repump excitation at wavepacket recurrence using 5 fs pump and repump pulses at $t_1 = 20$ fs/ $t_2 = 331$ fs. a) Potential functions of the 2-state system and quantum wavepackets at selected times (values in fs). b) Time-dependent populations obtained by full quantum dynamics simulations. c) Full lines: Populations obtained from FISH simulations. Dashed lines: FISH simulation with the coherences reset at $t = 325$ fs to the quantum dynamics values (cf. e)). d) Modulus (full line), real (blue) and imaginary (violet) parts of the quantum coherence ρ_{01} as a function of time. e) Modulus (full line), real (blue) and imaginary (violet) parts of the quantum coherence ρ_{01} obtained from the FISH simulation by averaging $\rho_{ij} = c_i^* c_j$ over the entire ensemble. Dashed lines: coherence terms reset to the quantum values at $t = 325$ fs.

Influence of coherence phase. Besides the direct implications of a non-decaying coherence magnitude on the population dynamics, there is another, more subtle source of error caused by overcoherence. To illustrate this, a different model system was investigated, now consisting of two displaced harmonic potentials. The excitation scheme is of a pump-repump type, such that the first pulse creates a wavepacket in the upper state and the second pulse sets in exactly after a full oscillation period of the upper state wavepacket has been completed, i.e. when two wavepackets again overlap in space (cf. Fig. 4.4a)). The quantum dynamical simulation shows that this should lead to a sequential population transfer from the lower to the upper state, such that each pulse transfers about 50 % and finally the population almost completely resides in the upper state, as shown in Fig. 4.4b). Inspection of the FISH populations depicted in Fig. 4.4 shows that, while the effect of the first pulse is in perfect agreement with the quantum simulation, the action of the second pulse is not reproduced. In this case, however, this cannot be attributed to a wrong magnitude of the coherence, since Fig. 4.4d) makes clear that, although after the first pulse the quantum coherence drops to zero, subsequently it rises

again and reaches almost its previous maximal value before the second pulse sets in. In the FISH simulation, as expected, the coherence decay is not present, but since it simply stays constant, it again matches the magnitude of its quantum dynamics counterpart just before the second pulse occurs (cf. Fig. 4.4e)). Therefore, introducing a correction for coherence decay, similar to the previous example, would not be beneficial here. The real cause of error can be revealed by looking not only at the magnitude of the coherence, but also on its real and imaginary parts. These are entirely different in the quantum and FISH simulations, which is particularly true before the onset of the second laser pulse. (cf. Figs. 4.4d) and 4.4e)). This means that in this case the phase of the coherence, which depends on the real and imaginary parts as $\phi = \tan(\text{Im}(\rho_{01})/\text{Re}(\rho_{01}))$, makes the difference. Resetting this phase to the quantum mechanical value at $t=325$ fs accordingly leads to a correct dynamics for the action of the second pulse, as can be seen from the dashed lines in Fig. 4.4b) and c). This example shows that also the evolution of the phase difference between two wavepackets can be decisive for the dynamics. The inclusion of such effects into surface hopping simulations is a more involved task than the decay of the coherence modulus, and by now only very few attempts to develop appropriate corrections have been made [121, 122], however without taking into account the specific requirements of field-induced dynamics.

Processes not influenced by overcoherence. Although the issue of overcoherence is frequently present in a variety of situations, there are also cases in which it has no implications on the accuracy of the dynamics simulation. This aspect will be illustrated on the example of a typical pump-probe setup as depicted in Fig. 4.5a): Pump excitation brings part of the population from state 0 to state 1, where subsequent dynamics occurs. Then, after a certain time delay, the state 1 wavepacket is projected to the final detection state 2 by a probe pulse. The electronic state populations and coherences obtained by a full quantum dynamics simulation of this process are depicted in Fig. 4.5b) and d). The pump pulse employed in this simulation transfers about half of the population from state 0 to state 1, inducing a large coherence between the two states. However, as the two wavepackets subsequently move to different spatial regions, the coherence between the states 0 and 1 starts to decay, eventually reaching zero just before the probe pulse sets in. The latter transfers the state 1 population completely to the detection state 2. In Fig. 4.5c) and e), these results are confronted with a FISH simulation for the same system. Clearly, here the coherence ρ_{01} does not decay and remains constant after the pump pulse. However, inspection of Fig. 4.5c) shows that this does not affect the population dynamics between the states 1 and 2 induced by the probe pulse. The reason is that the population transfer between states 1 and 2 is entirely determined by the coherence ρ_{12} , which is correctly reproduced by the FISH dynamics. The erroneous coherence ρ_{01} plays no role in the coupling between the states 1 and 2 and therefore does not influence the population

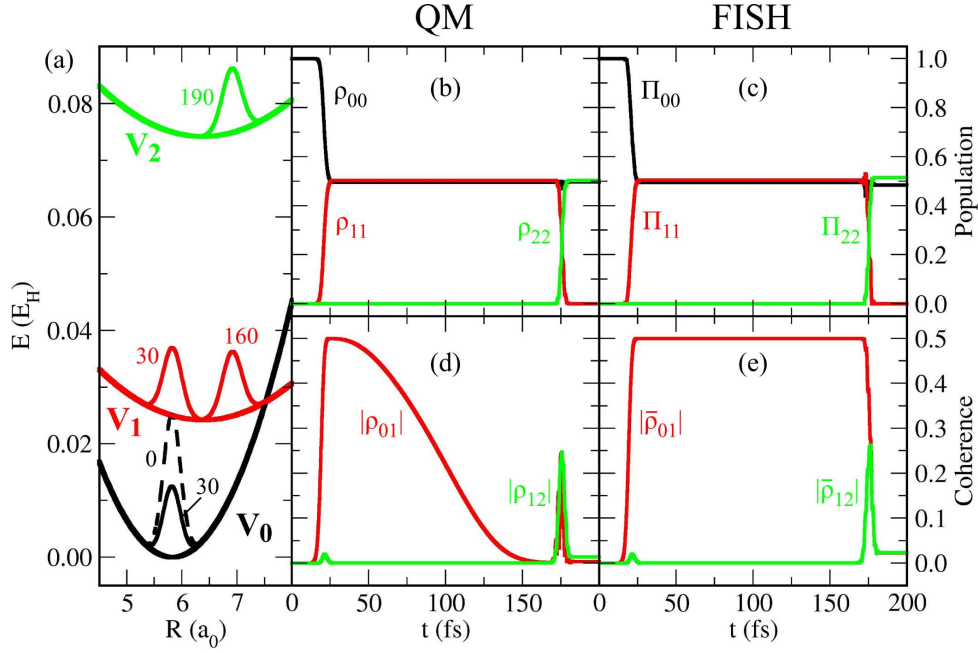


Figure 4.5: Overcoherence within FISH in a simulation of pump-probe excitation using 5 fs pump and dump pulses at $t_1 = 20$ fs/ $t_2 = 175.5$ fs. a) Potential functions of the 3-state system and quantum wavepackets at selected times (values in fs). b)/c) Time-dependent populations obtained by full quantum dynamics simulations and FISH. d)/e) Modulus of relevant coherence terms as a function of time. The coherences in the FISH simulation are obtained by averaging $\rho_{ij} = c_i^* c_j$ over the entire ensemble. The FISH populations agree well with those obtained from full quantum dynamics since the wrong coherence term ρ_{01} does not influence the $1 \rightarrow 2$ excitation.

transfer between these two states. This evidences that for cases in which, in a sequential excitation scheme, the second pulse invokes the coupling between a pair of states which did not contribute to the dynamics before, the results of FISH dynamics agree well with full quantum dynamics regardless of the presence of an incorrect coherence term associated with another pair of states.

In summary, the following conclusions can be drawn: Overcoherence represents an issue that occurs in all variants of surface hopping techniques, and therefore has also been inherited by the FISH method. It is present if parts of the ensemble assigned to different electronic states move apart in space after the coupling has ceased. This effect is most pronounced if the magnitude of the coherence is large, which occurs when about half of the electronic state population is transferred in the excitation process. By contrast, if the population transfer is either very small or almost complete, the effect of overcoherence is much less significant. For cases in which the wavepackets move apart without again overlapping in space, the overcoherence problem may be removed by applying a decoherence correction which mimicks the quantum mechanical coherence decay. Only if besides the magnitude also the phase of the coherence matters, corrections are less straightforward,

and methodological progress suitable for field-driven simulations is necessary in order to correctly describe the dynamics. Apart from that, in several other cases the overcoherence may be present, but does not lead to errors in the coupled electron nuclear dynamics. This arises in situations in which, after the creation of a large coherence, couplings at later times do not affect the initial pair of states between which the coherence is wrong, but other states to which no coupling has occurred before. Most notably, this applies for the population transfer invoked during pump-probe spectroscopic techniques, which can therefore be accurately simulated in the framework of FISH dynamics.

4.3 Field-induced excitation and distribution of vibronic energy

Besides the issue of decoherence, another aspect crucial for the validation of FISH is the nature of the light-induced excitation process. Quantum mechanically, the excitation between a pair of electronic states takes place between the two manifolds of vibrational quantum states associated with each of the involved electronic potential energy surfaces. The excitation efficiency between pairs of such states is determined (i) by the matrix elements $\langle 1, v' | \boldsymbol{\mu}_{01} | 0, v \rangle$ involving both the electronic transition dipole matrix element $\boldsymbol{\mu}_{01}$ and the overlap of the vibronic states $|0, v\rangle$ and $|1, v'\rangle$, and (ii) by the resonance of the field frequency with respect to the energy difference between the two vibronic states. However, within the mixed quantum-classical framework of FISH, there are no vibrational quantum states present, and for each trajectory the excitation efficiency depends (i) on the specific value of $\boldsymbol{\mu}_{01}$ at the given nuclear geometry, as well as (ii) on the resonance of the field frequency with respect to the vertical electronic excitation energy for this geometry. Since these two sets of conditions are significantly different, the question can be raised to which extent the electronic excitation as simulated in the framework of the FISH method is comparable to the exact quantum mechanical excitation process. The present subsection therefore serves to provide a comparison between quantum dynamical and FISH excitations in terms of the distribution of vibrational energy, thereby allowing for a validation of the accuracy of the electronic excitation within the FISH method.

For this purpose, model calculations have been performed employing one-dimensional potentials of different curvature, as well as laser fields of different time duration. The composition of the quantum mechanical wavepackets has then been analysed in terms of vibrational eigenfunctions and was compared to an approximate assignment of vibrational “states” in the FISH simulations. To this end, the total energies E_{traj} of each trajectory have been used to calculate an approximate integer vibrational quantum number according to $v = \frac{E_{traj}}{\hbar\omega_i} - \frac{1}{2}$, where ω_i is the vibrational frequency associated with the electronic potential V_i . The corresponding vibrational state populations have been obtained by averaging over the ensemble.

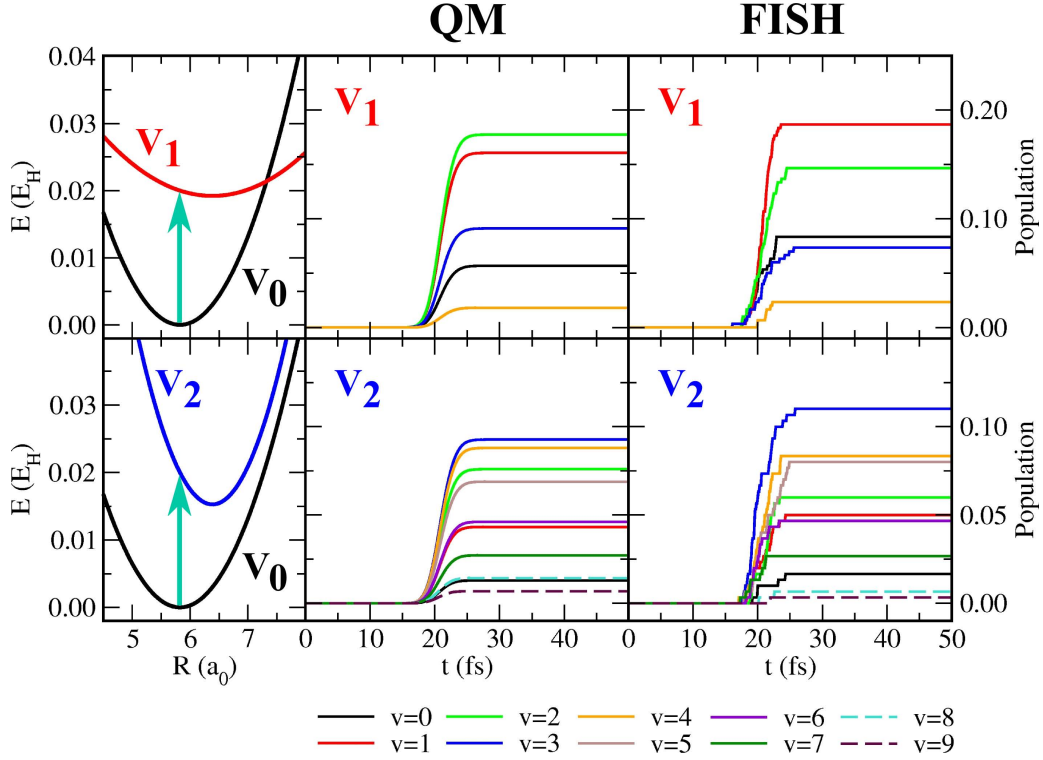


Figure 4.6: Vibrational state population in the upper state after excitation by a resonant 5 fs laser pulse (indicated as turquoise arrow) which leads to 50 % population transfer. Upper panel: Excitation to the shallow potential V_1 . Lower panel: Excitation to the steep potential V_2 . The quantum populations have been obtained by projecting the current upper state wavepacket on the vibrational eigenstates. The FISH populations correspond to the definition of approximate vibrational quantum numbers as $v = \frac{E_{traj}}{\hbar\omega_i} - \frac{1}{2}$, rounded to the nearest integer, with E_{traj} as the total energy of the trajectory and ω_i as the vibrational frequency associated with the potential V_i .

The chosen model systems consist of a pair of harmonic potentials where the excited state either has a more shallow curvature than the ground state (potentials V_0 versus V_1) or a steeper one (potentials V_0 versus V_2). The particle moving in these potentials has a mass corresponding to the reduced mass of the sodium dimer, exhibiting a vibrational period of 159 fs in the potential V_0 .

First, the excitation using a short laser pulse of 5 fs duration was investigated. In this way, the excitation process could be studied without significant influence of the nuclear dynamics since on the time scale of excitation the nuclei are almost stationary. Using a field intensity which overall transfers about 50 % of the population from the ground to the excited electronic state leads to the time-dependent vibrational state populations shown in Fig. 4.6. Clearly, for excitation to the shallow potential V_1 , there are relatively few vibrational states (up to $v = 4$) populated in the excitation process. The approximate vibrational state populations defined for the FISH simulations are to a major extent similar to those obtained quantum mechanically. Excitation to the steeper potential V_2

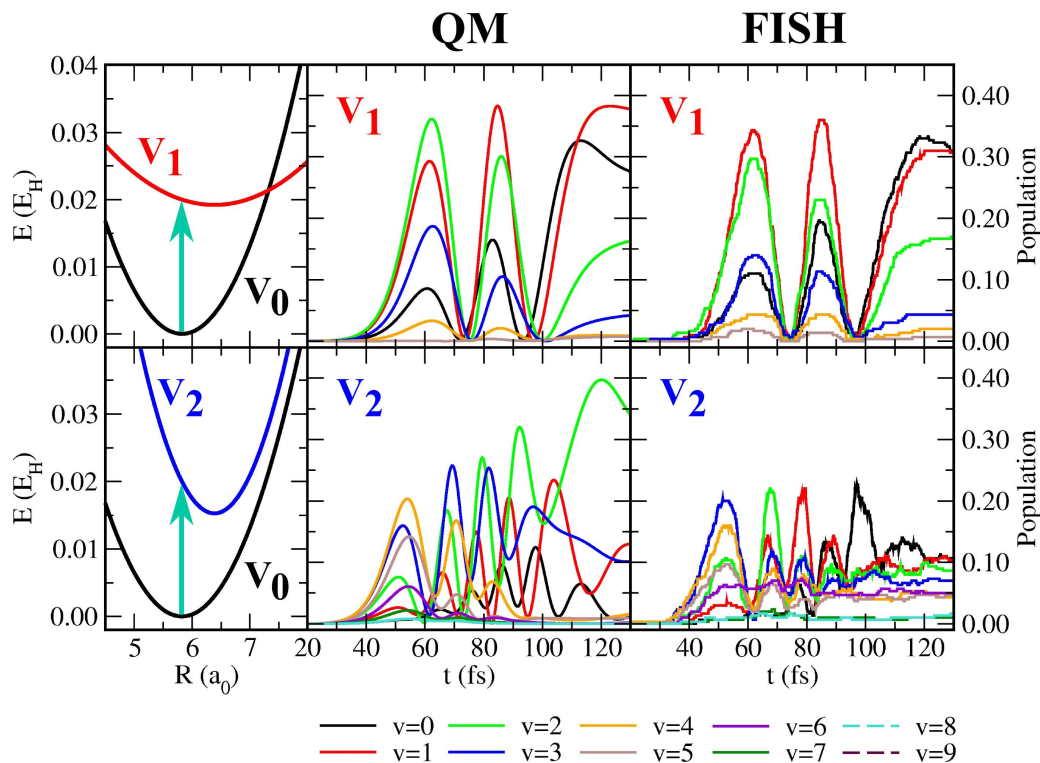


Figure 4.7: Vibrational state population in the upper state after excitation by a resonant 50 fs laser pulse (indicated as turquoise arrow). Upper panel: Excitation to the shallow potential V_1 . Lower panel: Excitation to the steep potential V_2 .

causes the population of a larger number of vibrational states up to $v = 9$. Nevertheless, the agreement between quantum and FISH simulations is still reasonably good. In both cases, accordingly also the total electronic state populations agree well, as shown in Appendix A.3. Therefore, it can be concluded that despite the different nature of the excitation process in the full quantum mechanical and in the mixed quantum-classical FISH cases, the FISH method allows for a qualitatively correct simulation of the excitation, and the distribution of vibrational energy in the classical ensemble of trajectories largely resembles that of the quantum mechanical wavepacket.

Taking into account that the use of 5 fs pulses implies that during the excitation process the nuclei are almost stationary, in order to study the interplay of electronic excitation and nuclear motion also longer laser pulses of 50 fs duration have been employed for both pairs of potentials V_0/V_1 and V_0/V_2 . The vibrational state populations obtained due to these pulses are depicted in Fig. 4.7. The population dynamics is now characterized by coherent Rabi oscillations, which occur on a similar time scale as the nuclear motion. Whereas for the shallow potential V_1 again a good agreement between the quantum and FISH results is observed, for the case of V_2 the FISH simulation is accurate only for the initial part of the dynamics up to 60 fs, while for later times large deviations occur. Subsequently, these also effect the total electronic state populations, which start to diverge for times after 80

fs, as shown in Appendix A.3. In contrast, no such deviations are found for the dynamics involving the shallow potential V_1 (cf. also Appendix A.3). Thus, an initially incorrect distribution of vibrational energies upon electronic excitation can lead eventually also to wrong electronic population dynamics in the FISH simulation.

From these model studies, it can be concluded that the FISH method qualitatively correctly describes the excitation process both for very short laser pulses in general, as well as for longer pulses provided that the excited state potential is not very steep and only a small number of vibrational states is involved in the excitation. However, for very steep excited state potentials and longer laser pulses, such as the case shown in Fig. 4.7 for V_2 , the concurrence of excitation to a large number of vibrational states and of the duration of the excitation process on a time scale of substantial nuclear motion poses a challenge for the correct distribution of vibrational energies upon electronic excitation in the framework of FISH. Nevertheless, this represents an extreme case, since in multidimensional systems, the gradient differences between pairs of potential energy surfaces are often not so pronounced. Moreover, in the presence of a large number of vibrational modes which are coupled due to anharmonic effects, which is a typical situation for polyatomic molecules, the coherent population oscillations observed for the one-dimensional case in Fig. 4.7 are usually washed out to a major extent. This leads to much more incoherent dynamics which is expected to be less sensitive to the detailed agreement of quantum mechanical and classical vibrational energy distributions. Therefore, in such cases the electronic excitation in the frame of FISH can be still considered reasonably accurate to allow for a realistic picture of the photoexcitation in complex molecular systems.

4.4 Conclusions

Several formal aspects and possible drawbacks inherent to surface hopping approaches have been studied in the context of FISH simulations and have been validated against numerically exact quantum dynamics simulations. For this purpose, selected model cases have been investigated with a specific focus on the accuracy of the laser-induced population dynamics. Specifically, the internal consistency problem was revisited, and excellent agreement between the fractional electronic state occupations and the averaged quantum populations was found in the absence of forbidden surface hops. It has been pointed out that the effect of forbidden hops, which are the main reason for poor internal consistency in surface hopping, is of minor significance during time periods in which the coupling of electronic states is mainly caused by the laser field, since then no conservation of the molecular energy is required and hence no additional forbidden hops occur.

Besides the internal consistency, another major issue in surface hopping is the lack of quantum decoherence due to the independent-trajectory description of the nuclear dy-

namics. It has been shown on the example of pump-dump and pump-probe excitations that this may lead to incorrect population dynamics in FISH if initially a large coherence between electronic states is generated. This occurs in a most pronounced way if about half of the electronic population is transferred from one state to another. For cases in which the exact quantum mechanical coherence completely vanishes, but the FISH counterpart stays constant, it could be shown that introducing an empirical coherence decay correction can provide a remedy to the overcoherence problem. However, the presently available approaches are best suited to low-dimensional model systems, and it is still an open question how to devise an efficient and accurate correction procedure applicable to complex systems. Even more methodological progress is desirable for such cases in which not the magnitude but the phase of the coherence is decisive, since only few approaches for fixing this problem in the context of field-free dynamics are available at present. However, in the present work an important class of excitation schemes could be identified in which the incorrect description of decoherence does not lead to wrong population dynamics. This occurs in pump-probe excitations, in which the probe step affects a pair of electronic states which beforehand has not yet been coupled by the pump step and for which therefore no incorrect coherence term can be present.

Finally, the electronic excitation process itself was studied, aiming to investigate the implications of the classical treatment of the nuclei in FISH on the correct distribution of vibrational energies in those portions of the trajectory ensemble that change their electronic state due to photoexcitation. To this end, electronic potentials with different steepness and laser pulses of different durations compared to the time scale of the nuclear motion were considered. For most cases, very good agreement between FISH and quantum dynamics was found, except for situations in which the difference in steepness is very large and the pulse duration is long enough to be accompanied by significant nuclear motion. However, it can be assumed that these effects found in one-dimensional systems will be less pronounced in polyatomic molecules, in which many nuclear degrees of freedom are coupled and the quantum mechanical vibrational dynamics is much less coherent.

Overall, the FISH method reveals its capability to well reproduce the quantum dynamics also for cases which are assumed to be problematic from a theoretical standpoint. A number of situations in which lower accuracy has to be envisaged can be identified, and for several of them correctives can be proposed.

Part II

FISH simulation of ultrafast observables

5 Ultrafast spectroscopy

The idea to follow the course of dynamical processes in molecules in real time has been a long-standing goal scientists strove for. In the last decades, the progress of laser technology to enable the creation of extremely short light pulses with durations on the femtosecond and even attosecond time scales, has made this goal to a great extent become reality, thereby opening fascinating insights into fundamental molecular phenomena. Although the specific experimental setups for realizing such investigations may differ in details, almost all of them as a common basis share the pump-probe technique, which relies on the action of two time-delayed ultrashort laser pulses. The first of these (pump pulse) serves to excite the system to a nonequilibrium configuration, which may be an excited electronic state, or an ionized state obtained by photodetachment. In the so prepared nonequilibrium state, dynamical processes are initiated, which may involve changes both in the nuclear and electronic degrees of freedom of the system. The course of these processes is then interrupted after a precisely adjusted time delay by the second laser pulse (probe) transferring the system to a final state used for detection. For this purpose, both absorption or emission of radiation, as well as the formation of ions and photoelectrons can be utilized. Most frequently, either fluorescence emission or photoelectrons are detected.

The first experimental realizations of femtosecond pump-probe measurements were achieved by Zewail et al. who investigated excited state dissociation dynamics in small di- and triatomic molecules [16, 241–244]. Using the laser-induced fluorescence intensity as the detection signal, they were able to monitor the wavepacket motion initiated by the pump pulse photoexcitation. This enabled the determination of time scales for molecular processes and revealed information on transition state geometries as well as on the specific form of the molecular potential energy surfaces. In particular, on the example of the NaI molecule, nonadiabatic predissociation dynamics at the avoided crossing of a bound and a dissociative electronic state could be observed [242, 243]. Furthermore, it could be also demonstrated that for simple diatomic systems such as iodine (I_2) even the complete reconstruction of the potential energy curve based on time-resolved spectroscopic data was possible [245]. Since then, numerous applications of time-resolved femtosecond spectroscopy have been presented, investigating a multitude of processes such as dissociation, isomerization, electron or proton transfer, as well as vibrational and electronic relaxation processes (for a comprehensive overview, cf. the review articles [19, 246]). Besides fluorescence or transient absorption detection, photoionization represents a particularly attractive choice as a probe step. This is due to a number of advantages, such as the absence of forbidden transitions, and to the much richer information content inherent to both the spectral and angular distribution of photoelectrons as well as to the molecular ions produced after photoionization. In particular, the energy- and angle-resolved photoelectron

distribution provides valuable information on the nature of the ionizing electronic state. Therefore, nonadiabatic relaxation processes, which are reflected in temporal changes of the electronic state character, can be directly observed. This makes time-resolved photoelectron spectroscopy (TRPES) and its angle-resolved variant a highly valuable tool for the investigation of coupled electron-nuclear dynamics in molecular systems. Consequently, the central focus of this part of the thesis lies on the simulation of TRPES signals, which will be discussed at full length in the following Chapter 6.

Before, some general remarks on the connection of time-resolved spectroscopic data with the underlying molecular processes are appropriate. Basic kinetic information about the studied systems can be already gained by phenomenological modeling using rate equation approaches, e.g. based on the optical Bloch equations for quantum multilevel systems. Assuming the presence of several distinct processes and their respective branching ratios, the temporal behaviour of measured femtosecond spectroscopic signals can be decomposed into individual components characterized by rate constants [19]. In this way, first estimations on the time scales inherent to the investigated system can be obtained. Moreover, as mentioned above, for diatomic systems the information contained in the spectroscopic data even allows for the reconstruction of the molecular potential energy curves. However, this is no longer possible for more complex systems, as in these cases the interplay of a large number of degrees of freedom makes the spectroscopic signals much more intricate. Therefore, in order to get a molecular-level picture of the various entangled dynamical processes occurring, quantum simulations accounting for the detailed electronic and geometrical structure of the system are mandatory. Most straightforwardly, full quantum dynamics simulations of the coupled electron-nuclear dynamics under the influence of the pump and probe laser fields can be performed in order to obtain a real-time picture of the wavepacket motion induced by the pump and probe lasers. Yet, as discussed in Chapter 1.1, this approach is only applicable for small systems or dimensionally reduced models for which global potential energy surfaces can be precalculated. Therefore, in order to simulate the dynamics of larger molecules, accounting for all degrees of freedom and avoiding the precalculation of high-dimensional potential energy surfaces, the use of efficient mixed quantum-classical simulation methods based on molecular dynamics “on the fly” is of great advantage. In this context, the FISH method [55] presented in Chapter 3 represents a particularly attractive approach, since it explicitly accounts for the laser excitation and can be directly connected with quantum chemical methods for the description of the electronic structure. For this reason, in the following the prospects of the FISH method for simulating various types of pump-probe signals will be briefly outlined. The extension of FISH to the simulation of time-resolved photoelectron (TRPE) spectra will be elaborated in detail in Chapter 6.

The idea of FISH to include the laser excitation process directly into nonadiabatic dynamics simulations straightforwardly enables its use for simulating such types of pump-probe (or pump-dump) spectroscopies which only involve dynamics in bound electronic states of the studied system. In this way, e.g. transient absorption (TA) spectra, where the probe step leads to the population of higher excited states, or time-resolved stimulated emission (SE) spectra, where the radiative return back to the ground state is induced, can in principle be simulated, as it will be sketched in the following. In a crude approach, the pump excitation might be explicitly described in the framework of FISH employing Eq. (3.26), whereas the probe step could be approximated by considering time-dependent oscillator strengths from the current state to higher-lying ones or to the ground state, respectively. Such oscillator strengths can be readily obtained from electronic transition dipole moments calculated along the classical trajectories propagated in the framework of FISH. More elaborately, also the probe pulse might be explicitly included in the FISH dynamics, and the spectroscopic signal might be computed from the quantum populations of the detection states induced by the probe pulse. In this way, the following expressions for the TA and time-resolved SE spectra can be proposed:

$$S_{TA}(t, E) \sim \frac{1}{N_{traj}} \sum_k^{N_{traj}} \sum_f |c_{k,f}(t)|^2 \delta(E - [E_f - E_i]) \quad (5.1)$$

$$S_{SE}(t, E) \sim \frac{1}{N_{traj}} \sum_k^{N_{traj}} |c_{k,0}(t)|^2 \delta(E - [E_0 - E_i]). \quad (5.2)$$

Here, the indices i and f represent the initial and final states before and after the action of the probe pulse. In this way, transient spectra along ensembles of trajectories propagated in the framework of FISH can be simulated. However, in order to go beyond the bound state excitations and to include the photoionization continuum, aiming at the simulation of time-resolved photoelectron spectra, an extension of the FISH method is necessary. Therefore, after a short general introduction to the methodology of TRPES, the main part of Chapter 6 will be devoted to the extension of FISH for the simulation of TRPES.

6 Time-resolved photoelectron spectroscopy (TRPES)

6.1 Introduction

The use of photoionization as a probe step has proved to be a powerful approach for the interrogation of ultrafast processes. This has led to the development of the TRPES technique [56–58], which features a number of advantages compared to other pump-probe procedures. Most importantly, photoionization, in contrast to e.g. excited state absorption, is always an allowed process, such that there are no dark quantum states in TRPES. Therefore, the observation of dynamical processes is not restricted to a temporal window in which some bright states are involved, but instead the complete course of the dynamics can be followed, only provided that the probe pulse is able to ionize the system. Moreover, the detection of photoelectrons, being charged particles, can be performed very sensitively. Not only can the spectrum of photoelectron kinetic energies be obtained, but also the angle-resolved distribution of the photoelectrons can be measured [58, 247], from which important conclusions on the nature of the ionizing molecular states can be drawn. Simultaneous detection of the produced molecular ions or their possible fragmentation products can reveal further information. In general, in the framework of TRPES both vibrational and electronic dynamics can be observed, and in some cases also a distinction between these two processes may be possible. A schematic presentation of the principle of TRPES is provided in Fig. 6.1.

In recent years, TRPES has been used to probe excited state dynamics in a variety of systems. In the following, some illustrative references will be provided, without claiming to give a comprehensive survey. In small metal clusters, nonradiative electronic relaxation [61, 62, 248–250] and photodesorption of ligands [251] have been investigated, while in the case of organic molecules, both electronic relaxation and molecular vibrations have been observed, leading to the possibility to distinguish the fingerprints of both processes in the spectrum [252]. Fundamental studies, which are also valuable for comparison with theoretical approaches, have been performed on the internal conversion in pyrazine, involving both energy-resolved TRPES [253] as well as time-resolved photoelectron anisotropy maps [254, 255]. Much experimental effort has also been devoted to the nonradiative deactivation of biomolecules, with particular attention to nucleobases such as adenine [256–258] (cf. also Chapter 10). Moreover, isomerization reactions in photo-switchable molecules that are important for the design of functional materials have been monitored using TRPES [259]. Recent developments involve the improvement of angular detection and even of adopting the molecule’s own perspective (molecular frame) in order to circumvent the effect of rotational averaging present in a statistical sample [260, 261]. Furthermore, also the first steps towards TRPES experiments in the liquid phase are

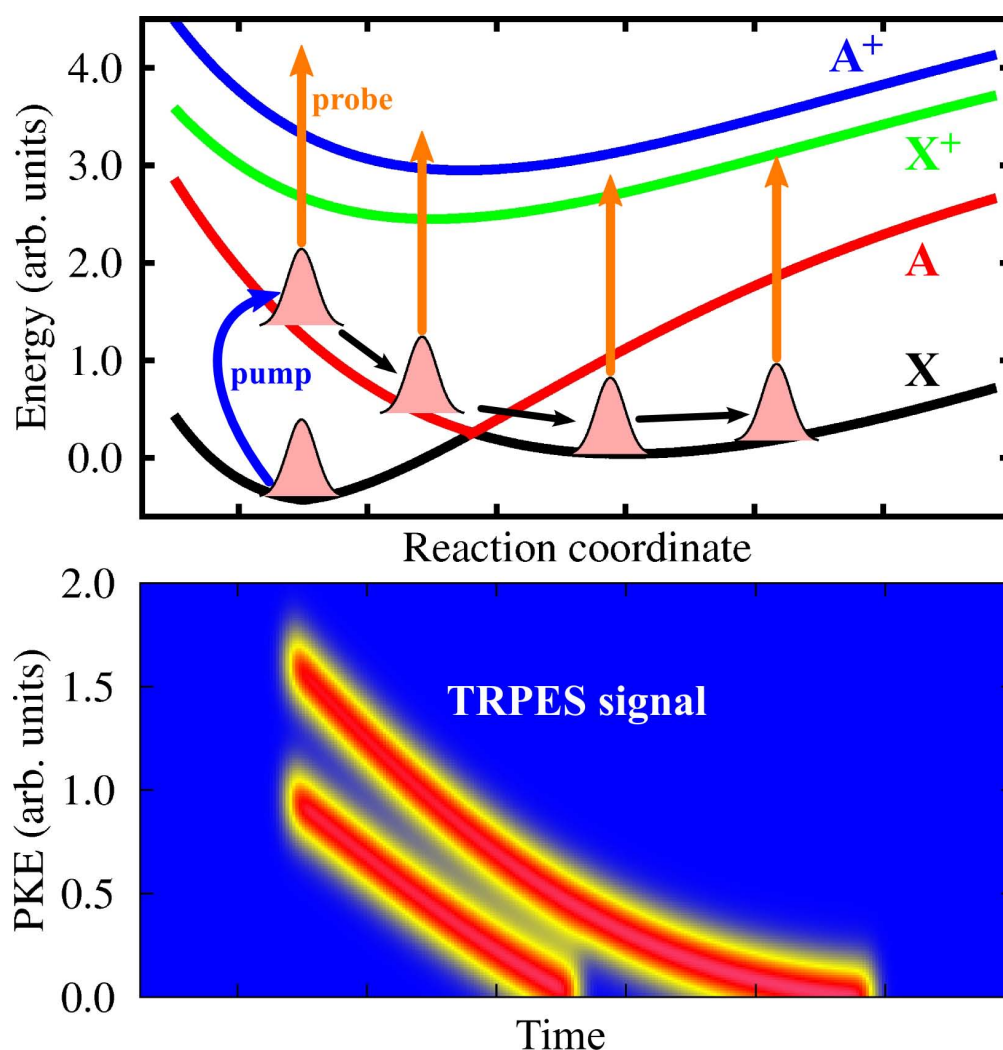


Figure 6.1: Schematic illustration of the TRPES method. Upper panel: A wavepacket (light red) is transferred by the pump pulse (blue) from the ground state X to the excited state A, in which dynamical processes set in, leading the wavepacket to a conical intersection between the X and A states and then back to the X state. During the wavepacket evolution (indicated by black arrows), the dynamics is mapped by the probe pulse (orange) onto the cation states X⁺ and A⁺. However, depending on the current energy gap between neutral and ionic states, not all ionic states can be reached by the probe pulse (cf. last orange arrow on the right). Lower panel: TRPES signal corresponding to the dynamics shown above. The upper feature in the PKE distribution (starting at 1.6 energy units) corresponds to ionization to the X⁺, the lower one to the A⁺ state. Depending on the actual course of the dynamics, the photoelectron signal not only indicates the energetic evolution of the system state but may also contain signatures of underlying nuclear vibrations (not shown in the scheme). Moreover, influenced by the transition dipole moments for ionization, transitions to a particular ionic state may be preferred or suppressed.

presently taken [262].

Parallel to these experimental achievements, theoretical approaches for simulation of TRPE spectra have been devised, based on coupled electron-nuclear dynamics simulations using different approximations. Initial theoretical studies have been performed by Seel and Domcke more than 20 years ago, based on an expansion of the nuclear wavepackets in terms of eigenstates and a discretization of the electronic continuum, with the transition dipole moments for ionization treated as constant [263]. Subsequently, a number of studies have been reported in which numerical nonadiabatic wavepacket propagation was performed, but the issue of describing the ionization continuum was circumvented by employing perturbation theory expressions for the field-matter interaction [264–268]. Clearly, employing such approaches only allowed for the calculation of energy-resolved signals, neglecting completely the angular dependency. However, this latter issue has been addressed by several studies based on wavepacket dynamics in which the photoelectron has been described employing different approximations for scattering states, and both one- [269–271] as well as multidimensional systems have been investigated [272–275].

Notwithstanding these efforts, the foundation of the above mentioned methods on quantum nuclear dynamics restricts their use to small systems or reduced-dimensional models. Approaches to calculate TRPES for complex molecules under inclusion of all nuclear degrees of freedom necessarily have to employ more efficient classical or semiclassical methods for the nuclear motion. In the framework of the so-called *ab initio* multiple spawning method (cf. Sec. 1.2), the semiclassical simulation of nonadiabatic dynamics has been utilized to calculate TRPE spectra of several DNA bases [276, 277]. A more intuitive and far more efficient approach to nonadiabatic dynamics is represented by multistate surface-hopping molecular dynamics based on classical trajectories, as it has been discussed in Chapter 1.2. Employing the Wigner distribution approach for representing the initial ensemble, TRPE spectra have been simulated using nonadiabatic molecular dynamics combined with a perturbation theory treatment of the probe process, both using the Condon approximation [62, 127, 132, 278] as well as approximating the transition dipoles to the continuum in the framework of the Stieltjes imaging approach [229].

While in the above mentioned semiclassical studies only field-free nonadiabatic dynamics simulations have been performed, and thus the details of the pump step have been neglected, the field-induced surface hopping method (FISH) [55] discussed in Chapter 3 offers the unique possibility to include the laser fields directly into the excited state nonadiabatic dynamics simulations. In this way, the effect of the pump pulse on the dynamics is explicitly accounted for. In this chapter the augmentation of the FISH method by an approximate description of the ionization continuum is presented, which allows for the simulation of laser-driven photoionization processes using laser pulses with arbitrary shapes and therefore can be employed both to simulate the spectroscopic observables as

well as to control the photoionization process. This approach enables for the first time the simulation of time-resolved spectroscopic signals in complex molecular systems without the need to restrict the number of degrees of freedom and simultaneously explicitly accounting for the shape of the driving laser fields.

In the remainder of this chapter, the theoretical formulation of the FISH method extended by the discretized continuum approximation for the description of the photoionization and the simulation of TRPES signals will be presented. In addition, the influence of the quantum mechanical nature of the vibrational motion on the appearance of the spectra will be discussed. The results presented here have been published in Ref. [59]. In the subsequent Chapter 7, the method will be illustrated on the simulation of TRPES for the small noble metal clusters Ag_3 and Au_7^- .

6.2 Time-resolved photoelectron spectra within the FISH method

6.2.1 Discretized continuum approximation for photoionization

In the framework of the FISH method, the temporal evolution of the electronic quantum state is described by individual electronic state occupations of each trajectory, which are averaged over the classical ensemble. During the propagation of the trajectories, the state occupations may change stochastically according to hopping probabilities, which are calculated quantum mechanically using Eq. (3.29) or (3.32). For this purpose, an electronic Schrödinger equation,

$$i\hbar\dot{c}_i(t) = E_i[\mathbf{R}(t)]c_i(t) - \sum_j \left(\boldsymbol{\mu}_{ij}[\mathbf{R}(t)] \cdot \mathbf{E}(t) + i\hbar\dot{\mathbf{R}} \cdot \mathbf{d}_{ij}[\mathbf{R}(t)] \right) c_j(t), \quad (6.1)$$

is assigned to each trajectory $\mathbf{R}(t)$ and is solved for the electronic state coefficients c_i , taking into account the coupling of states by the laser field $\mathbf{E}(t)$ and by the nonadiabatic couplings \mathbf{d}_{ij} .

An extension of this method to the simulation of time-dependent ionization processes requires, in addition to the bound electronic state dynamics, the inclusion of transitions to the ionization continuum. Therefore, a description of the electronic continuum states has to be introduced. Within the FISH method, this can be achieved by augmenting the time-dependent Schrödinger equation (6.1) for the bound states by a set of equations describing the ionization continuum, and allowing the system to switch from the bound to the ionized states.

In order to derive these equations, as a starting point the electron-nuclear wavefunction of a combined system with both bound and continuum states is considered, which can be written as

$$\Psi(\mathbf{r}, \mathbf{R}, t) = \sum_i^{neutr} \chi_i^{(N)}(\mathbf{R}, t) \Psi_i^{(N)}(\mathbf{r}; \mathbf{R}) + \sum_j^{ion} \int dE \chi_j^{(N-1)}(\mathbf{R}, E, t) \mathcal{A} \left[\Psi_j^{(N-1)}(\mathbf{r}; \mathbf{R}) \phi_j(E) \right], \quad (6.2)$$

where $\chi_i^{(N)}(\mathbf{R}, t)$ and $\chi_j^{(N-1)}(\mathbf{R}, E, t)$ represent the nuclear wavepacket in the bound and continuum states, respectively, $\Psi_i^{(N)}(\mathbf{r}; \mathbf{R})$ and $\Psi_j^{(N-1)}(\mathbf{r}; \mathbf{R})$ are the electronic eigenfunctions of the N -electron or $(N-1)$ -electron Hamiltonians, while $\phi_j(E)$ is a free electron scattering state. The antisymmetrized product $\mathcal{A} \left[\Psi_j^{(N-1)}(\mathbf{r}; \mathbf{R}) \phi_j(E) \right]$ represents the continuum eigenfunctions of the Hamiltonian for the combined system of ion and free electron, in which the electron-core interaction has been neglected. The summations extend over the complete sets of N -electron (“neutr”) and $(N-1)$ -electron (“ion”) states. For the ease of reading, the N -electron system will be referred to as “neutral” in the following, while the $(N-1)$ -electron system will be denoted as “ionized”. However, the derivation is generally applicable for any pair of species which differ in their electron number by one, such as e.g. also an anionic and a neutral species. The wavefunction ansatz in Eq. (6.2) can be inserted into the full electron-nuclear time-dependent Schrödinger equation including the coupling to the electric field, and a set of equations for the time evolution of the continuum portion of the nuclear wavepacket of the ionized system $\chi_j^{(N-1)}(\mathbf{R}, E, t)$ can be derived following Ref. [279], giving rise to

$$i\hbar \dot{\chi}_j^{(N-1)}(\mathbf{R}, E, t) = \left(-\frac{\hbar^2}{2} \nabla_{\mathbf{R}} \cdot \mathbf{M}^{-1} \nabla_{\mathbf{R}} + E_j^{(N-1)}(\mathbf{R}) + E \right) \chi_j^{(N-1)}(\mathbf{R}, E, t) - \sum_i^{neutr} \boldsymbol{\mu}_{ij}(\mathbf{R}, E) \cdot \mathbf{E}(t) \chi_i^{(N)}(\mathbf{R}, t), \quad (6.3)$$

where $E_j^{(N-1)}(\mathbf{R})$ corresponds to the energy of the j 'th excited state of the cation and E is the kinetic energy of the released photoelectron. In order to connect Eq. (6.3) with trajectory-based FISH simulations, a mixed quantum-classical approximation related to Tully's original procedure will be employed. First, the nuclear wavepackets are separated into amplitude and phase terms in the spirit of the Bohm-Madelung representation of quantum mechanics (cf. Eq. (1.10), Refs. [78, 79])

$$\chi_j^{(N-1)}(\mathbf{R}, E, t) = A_j^{(N-1)}(\mathbf{R}, E, t) \exp \left[\frac{i}{\hbar} S_j^{(N-1)}(\mathbf{R}, E, t) \right] \quad (6.4)$$

$$\chi_i^{(N)}(\mathbf{R}, t) = A_i^{(N)}(\mathbf{R}, t) \exp \left[\frac{i}{\hbar} S_i^{(N)}(\mathbf{R}, t) \right]. \quad (6.5)$$

Inserting these expressions into Eq. (6.3) and appropriately separating terms into two equations yields [106]

$$\begin{aligned} \dot{S}_j^{(N-1)} &= -\frac{1}{2} \left(\nabla_{\mathbf{R}} S_j^{(N-1)} \cdot \mathbf{M}^{-1} \nabla_{\mathbf{R}} S_j^{(N-1)} \right) - E_j^{(N-1)} \\ &\quad + \frac{\hbar^2 (\nabla_{\mathbf{R}} \cdot \mathbf{M}^{-1} \nabla_{\mathbf{R}}) A_j^{(N-1)}}{A_j^{(N-1)}} \end{aligned} \quad (6.6)$$

$$\begin{aligned} i\hbar \dot{A}_j^{(N-1)} &= -i\hbar \left(\nabla_{\mathbf{R}} A_j^{(N-1)} \cdot \mathbf{M}^{-1} \nabla_{\mathbf{R}} S_j^{(N-1)} + \frac{1}{2} A_j^{(N-1)} (\nabla_{\mathbf{R}} \cdot \mathbf{M}^{-1} \nabla_{\mathbf{R}}) S_j^{(N-1)} \right) \\ &\quad - \sum_i^{neutr} \boldsymbol{\mu}_{ij} \cdot \mathbf{E} A_i^{(N)} \exp \left[\frac{i}{\hbar} \left(S_i^{(N)} - S_j^{(N-1)} \right) \right]. \end{aligned} \quad (6.7)$$

While the first of the above equations can be interpreted as a quantum mechanical analog to the Hamilton-Jacobi equation for the nuclear motion in the electronic state j , the second one describes the time evolution of the amplitude functions $A_j^{(N-1)}(\mathbf{R}, E, t)$. The latter change in time both due to the spatial variation of amplitude and phase in the same electronic state, represented by the terms

$$\nabla_{\mathbf{R}} A_j^{(N-1)} \cdot \mathbf{M}^{-1} \nabla_{\mathbf{R}} S_j^{(N-1)} + \frac{1}{2} A_j^{(N-1)} (\nabla_{\mathbf{R}} \cdot \mathbf{M}^{-1} \nabla_{\mathbf{R}}) S_j^{(N-1)}, \quad (6.8)$$

as well as due to the couplings with the bound electronic state amplitudes, given by

$$- \sum_i^{neutr} \boldsymbol{\mu}_{ij} \cdot \mathbf{E} A_i^{(N)} \exp \left[\frac{i}{\hbar} \left(S_i^{(N)} - S_j^{(N-1)} \right) \right] \quad (6.9)$$

Hence, the terms (6.9) are responsible for population transfer between different electronic states. Interpreting $S_i^{(N)}$ and $S_j^{(N-1)}$ as classical actions allows for the substitution¹

$$S_i^{(N)} - S_j^{(N-1)} = \int_0^t \left(E_j^{(N-1)} + E - E_i^{(N)} \right) dt, \quad (6.10)$$

with $E_i^{(N)}$ as the electronic energy of the neutral state i . Thus, Eq. (6.7) becomes

$$\begin{aligned} i\hbar \dot{A}_j^{(N-1)} &= -i\hbar \left(\nabla_{\mathbf{R}} A_j^{(N-1)} \cdot \mathbf{M}^{-1} \nabla_{\mathbf{R}} S_j^{(N-1)} + \frac{1}{2} A_j^{(N-1)} (\nabla_{\mathbf{R}} \cdot \mathbf{M}^{-1} \nabla_{\mathbf{R}}) S_j^{(N-1)} \right) \\ &\quad - \sum_i^{neutr} \boldsymbol{\mu}_{ij} \cdot \mathbf{E} A_i^{(N)} \exp \left[\frac{i}{\hbar} \int_0^t \left(E_j^{(N-1)} + E - E_i^{(N)} \right) dt \right]. \end{aligned} \quad (6.11)$$

¹This substitution uses the definition of the action integral as $S = \int (T - V) dt$ with T as the kinetic and V as the potential energy. In the present case, the latter is replaced by the electronic energies $E_i^{(N)}$ or $E_j^{(N-1)} + E$, respectively.

Comparison of Eq. (6.11) with the time evolution equation for the electronic state coefficients $a_j^{(N-1)}(E, t)$ of a multilevel system in the interaction picture,

$$i\hbar\dot{a}_j^{(N-1)} = - \sum_i^{neutr} \boldsymbol{\mu}_{ij} \cdot \mathbf{E} a_i^{(N)} \exp \left[\frac{i}{\hbar} \int_0^t \left(E_j^{(N-1)} + E - E_i^{(N)} \right) dt \right], \quad (6.12)$$

reveals that in both equations the terms describing the population transfer between different electronic states are completely analogous. Thus, it is possible to relate the amplitude functions $A_j^{(N-1)}(\mathbf{R}, E, t)$ of the wavepacket to the coefficients $a_j^{(N-1)}(E, t)$ and to use Eq. (6.12) for describing the change in the electronic state populations. In order to be consistent with the formulation of the FISH method worked out in Sec. 3, Eq. (6.12) is transformed to the Schrödinger picture by employing the definition $a_j = c_j \exp \left(\int_0^t \frac{i}{\hbar} (E_j + E) dt \right)$, which leads to

$$i\hbar\dot{c}_j^{(N-1)}(E, t) = (E_j^{(N-1)}[\mathbf{R}(t)] + E)c_j^{(N-1)}(E, t) - \sum_i^{neutr} \boldsymbol{\mu}_{ij}[\mathbf{R}(t), E] \cdot \mathbf{E}(t) c_i^{(N)}(t). \quad (6.13)$$

This equations describes the time evolution of the quantum amplitudes $c_j^{(N-1)}(E, t)$ of a continuum state $\mathcal{A} \left[\Psi_j^{(N-1)}(\mathbf{r}; \mathbf{R}) \phi_j(E) \right]$ with the energy $E_j^{(N-1)} + E$. To obtain a finite set of working equations, the photoelectron kinetic energy can be discretized in the relevant range, thus replacing the ionization continuum by a set of densely spaced discrete states.

From this result, an approximate description of photoionization in the framework of the FISH method can be devised by augmenting Eq. (6.1) for the bound electronic state dynamics with Eq. (6.13). The system of these two sets of equations provides a basis for the simulation of laser-driven photoionization processes and can be used to calculate the TRPE spectra. The intensity of the TRPES signal at a particular value of the photoelectron kinetic energy E is then obtained from the continuum state populations after the end of the ionization pulse by averaging over the whole ensemble of individually propagated trajectories according to:

$$S(t_d, E) = \frac{1}{N_{traj}} \sum_k^{N_{traj}} \sum_j^{ion} |c_{k,j}^{(N-1)}(E, t \rightarrow \infty)|^2. \quad (6.14)$$

Altogether, the simulation of TRPES signals in the framework of the FISH method proceeds in the following steps:

- (i) Initial conditions for the nuclear trajectories are determined
- (ii) FISH dynamics simulations are performed in a manifold of bound electronic states under the explicit influence of the pump laser pulse according to Eq. (6.1) and e.g. (3.12)

- (iii) Along the obtained FISH trajectories, the probe step is simulated for each chosen pump-probe time delay by performing numerical integration of the Schrödinger equation (6.13) in the manifold of the current bound state and the set of discretized continuum states over the duration of the probe pulse
- (iv) The spectroscopic signal at a given time delay is obtained according to Eq. (6.14) from the asymptotic populations of the continuum states after the action of the probe pulse, averaged over the ensemble of trajectories.

In this way, time-resolved photoelectron spectra generated by moderately intense pump and probe pulses with arbitrary shapes can be simulated. For the first time, this allows for the simulation of spectroscopic observables in complex molecular systems accounting for all nuclear degrees of freedom and simultaneously going beyond the weak-field limit by explicitly accounting for the pulse shapes. Therefore, in addition to the mere simulation of spectroscopic signals, also the combination with optimal control in order to steer the photoionization process or to shape the outgoing electronic wavepackets is straightforward. The approach developed here represents thus a general framework for simulating time-dependent photoionization dynamics based on classical trajectories. Depending on the degree of sophistication used for the description of the ionization continuum, different levels of approximation can be considered. In particular, if the transition dipole moments between the bound and continuum states, the calculation of which is computationally challenging, are not available, simplified treatments such as the Condon approximation of constant transition dipole moments can be employed. It should be noted that such a procedure for calculating TRPES becomes, for laser pulses of Gaussian form and in the weak-field perturbation theory limit, also equivalent to the analytical formulation used e.g. in Ref. [62, 132].

However, due to the classical description of the nuclear motion, the influence of vibrational quantum states on the ionization transition and thus on the form of the TRPES signal is not accounted for in this approach. This implies the assumption that the vibrational energy of the wavepacket does not change upon ionization. Although being a reasonable approximation for many systems in which the electronic excitation is dominated by the transitions between the vibrational ground states of both involved electronic states, this condition may not be fulfilled in certain cases, and therefore it is of significance to investigate how the inclusion of vibrational quantum states may change the appearance of a TRPES signal. Therefore, this aspect will be qualitatively discussed in the following subsection.

6.2.2 Role of vibrational quantum states

In a mixed quantum-classical approach such as FISH, in which the quantum mechanical description only pertains to the electronic degrees of freedom, while the nuclei are treated classically, the efficiency of an electronic transition depends on (i) the resonance between the frequencies of the excitation field and the vertical electronic transition and (ii) the coupling strength determined by the value of the electronic transition dipole moment at the current nuclear geometry. By contrast, if the nuclear motion is treated quantum mechanically, the excitation process proceeds between two manifolds of vibrational quantum states associated to the lower and upper electronic states, respectively. The excitation efficiency is then determined by the resonance between the field and each pair of vibronic (combined electronic-vibrational) states in the lower and upper electronic potential energy surfaces, and by the vibronic transition dipole moment between these states.

In the following, the aim is to obtain a semiclassical formulation accounting approximately for the quantum mechanical nature of the nuclear motion. For this purpose, the full quantum mechanical Eq. (6.3) is projected onto the vibrational eigenstates $|v_j\rangle$ of the j' th cationic electronic state, leading to

$$i\hbar\dot{c}_{v_j}^{(N-1)}(E, t) = \left(E_{j,0}^{(N-1)} + E_{v_j}^{(N-1)} + E \right) c_{v_j}^{(N-1)}(E, t) - \sum_i^{neutr} \langle v_j | \boldsymbol{\mu}_{ij}(\mathbf{R}, E) | \chi^{(N)}(\mathbf{R}, t) \rangle_{\mathbf{R}} \cdot \mathbf{E}(t), \quad (6.15)$$

with the vibrational expansion coefficients $c_{v_j}^{(N-1)}$, the minimum value $E_{j,0}^{(N-1)}$ of the electronic energy surface of the cationic state j and the energy $E_{v_j}^{(N-1)}$ of the corresponding vibrational state. Expanding the neutral state wavepacket $\chi_i^{(N)}(\mathbf{R}, t)$ as

$$\chi_i^{(N)}(\mathbf{R}, t) = c_i^{(N)}(t) e^{-\eta_{\mathbf{R}}(\mathbf{R} - \mathbf{R}(t))^2} \quad (6.16)$$

and considering the limit $\eta_{\mathbf{R}} \rightarrow \infty$ leads to a δ -function representation of the wavepacket,

$$\chi_i^{(N)}(\mathbf{R}, t) \approx c_i^{(N)}(t) \delta(\mathbf{R} - \mathbf{R}(t)). \quad (6.17)$$

This gives rise to a semiclassical approximation of the dipole integral in Eq. (6.15) as

$$\langle v_j | \boldsymbol{\mu}_{ij}(\mathbf{R}, E) | \chi^{(N)}(\mathbf{R}, t) \rangle_{\mathbf{R}} \approx \varphi_{v_j}^*[\mathbf{R}(t)] \boldsymbol{\mu}_{ij}[\mathbf{R}(t), E] \chi_i^{(N)}[\mathbf{R}(t)] = F_{i,v_j}[\mathbf{R}(t)] \boldsymbol{\mu}_{ij}[\mathbf{R}(t), E], \quad (6.18)$$

where φ_{v_j} is the vibrational wavefunction of the state v_j , F_{i,v_j} represents a classical approximation for the time-dependent Franck-Condon (FC) factor and $\boldsymbol{\mu}_{ij}$ is the transition dipole

moment, all evaluated at the position of the nuclear trajectory $\mathbf{R}(t)$. Thus, Eq. (6.15) becomes

$$i\hbar\dot{c}_{v_j}^{(N-1)}(E, t) = \left(E_{j,0}^{(N-1)} + E_{v_j}^{(N-1)} + E \right) c_{v_j}^{(N-1)}(E, t) - \sum_i^{neutr} c_i^{(N)}(t) F_{i,v_j}[\mathbf{R}(t)] \boldsymbol{\mu}_{ij}[\mathbf{R}(t), E] \cdot \mathbf{E}(t). \quad (6.19)$$

This provides a semiclassical framework for studying the dependence of the TRPES signal on vibrational FC factors.

In order to investigate qualitatively the influence of this approximate quantum treatment of the vibrational degrees of freedom on the TRPES, in the following, low field intensities are assumed, and first order perturbation theory is applied in a similar way as devised in Refs. [280, 281]. For laser pulses of Gaussian form,

$$\mathbf{E}(t) = \mathbf{E}_0 \exp \left[-\frac{(t-t_d)^2}{2\sigma_{pr}^2} \right] \cos \left[\frac{E_{pr}}{\hbar} (t-t_d) \right], \quad (6.20)$$

this allows one to derive an analytic expression for the continuum state population. After integrating over the duration of the probe pulse, the population of a specific cationic vibrational state $|v_j\rangle$ corresponding to the photoelectron kinetic energy E is given by

$$\begin{aligned} \left| c_{v_j}^{(N-1)}(E, t \rightarrow \infty) \right|^2 &\sim \sum_i^{neutr} \int_{-\infty}^{\infty} d\tau |F_{i,v_j}|^2 |\boldsymbol{\mu}_{ij}|^2 e^{-\frac{(\tau-t_d)^2}{\sigma_{pr}^2}} \\ &\times \exp \left(-\frac{\sigma_{pr}^2}{\hbar^2} \left[E_{pr} - \left(E_{j,0}^{(N-1)} + E_{v_j}^{(N-1)} - E_i^{(N)} - E_{i,vib}^{(N)} \right) - E \right]^2 \right), \end{aligned} \quad (6.21)$$

where σ_{pr} is the temporal width of the probe pulse and E_{pr} its energy, while $E_i^{(N)}$ is the electronic and $E_{i,vib}^{(N)}$ the vibrational energy of the neutral wavepacket. Within a classical description based on localized trajectories, the quantum energies $E_i^{(N)} + E_{i,vib}^{(N)}$ and $E_{j,0}^{(N-1)} + E_{v_j}^{(N-1)}$ of the wavepackets, consisting of an electronic and a vibrational part, can be approximated by the total energies of the classical system, $E_i^{(N)}[\mathbf{R}(t)] + E_{i,vib}^{(N)}[\mathbf{R}(t)]$ and $E_j^{(N-1)}[\mathbf{R}(t)] + E_{j,vib}^{(N-1)}[\mathbf{R}(t)]$, respectively. The FC factor then becomes a function of the continuous vibrational energies of the neutral and the cation as $F_{ij} \left(E_{i,vib}^{(N)}, E_{j,vib}^{(N-1)} \right)$. Upon ionization, the vibrational energy can be partly transformed into the photoelectron kinetic energy. The total population for a state of given photoelectron kinetic energy E can thus be obtained by integration over the range of vibrational energies $E_{j,vib}^{(N-1)}$.

Therefore, in the classical approximation the photoelectron signal can be calculated according to

$$\begin{aligned}
 S(t_d, E) &\sim \frac{1}{N_{tr}} \sum_{j}^{N_{tr}} \sum_{i}^{ion} \sum_{i}^{neutr} \int_0^\infty dE_{j,vib}^{(N-1)} \int_{-\infty}^\infty d\tau \left| F_{ij}(E_{j,vib}^{(N-1)}) \right|^2 \left| \boldsymbol{\mu}_{ij}(\mathbf{R}(\tau), E) \right|^2 e^{-\frac{(\tau-t_d)^2}{\sigma_{pr}^2}} \\
 &\times \exp \left(-\frac{\sigma_{pr}^2}{\hbar^2} \left[E_{pr} - \left(E_j^{(N-1)}(\mathbf{R}(\tau)) + E_{j,vib}^{(N-1)} - E_i^{(N)}(\mathbf{R}(\tau)) - E_{i,vib}^{(N)} \right) - E \right]^2 \right).
 \end{aligned} \tag{6.22}$$

Altogether, in this chapter, the extension of the FISH method for the simulation of time-resolved photoelectron spectra has been presented. Based on the discretization of the ionization continuum combined with a mixed quantum-classical approximation for the coupled electron-nuclear dynamics for the ionization process, a set of equations has been derived which serves to augment the original FISH equations in order to account for the photoionization. This approach is applicable to complex molecular systems including all degrees of freedom and using moderately intense laser fields with arbitrary shapes. Therefore, it represents a valuable and general framework for the simulation of time-resolved photoelectron spectra as well as for the control of the photoionization process.

In addition, the effects of the quantum mechanical nature of the vibrational degrees of freedom have been investigated using a semiclassical approximation. This allows for an examination of how the appearance of TRPE spectra is influenced by the FC factors between vibrational quantum states. In the following chapter, this methodological framework will be applied for the simulation of TRPES in small metal nanoclusters.

7 TRPES study of the nonadiabatic relaxation in small clusters

7.1 Introduction

The scope of the above presented method for the simulation of TRPES will be illustrated by studies of the laser-induced nonadiabatic dynamics in small metal clusters. Such systems, while having only a limited number of nuclear degrees of freedom, already exhibit a complex electronic structure which is reflected in a high density of states as well as in the presence of strong nonadiabatic relaxation effects connected with electronic state degeneracies at particular highly symmetric geometries. In general, the investigation of ultrafast processes in metal clusters is of fundamental importance for establishing the relation between structure, size, optical properties, and the time scales of nonradiative processes determining their photoemission. This is of particular significance due to the strongly nonscalable properties of small clusters, which make them promising building blocks for novel optical and catalytic materials. Notably, the emissive properties of clusters are important in the context of their potential use as emitters in new photonic and biosensing materials. Formally, small clusters result from a continued size reduction of bulk metals to small molecular-like units. This leads to a change in their electronic structure from band-like properties typical for the solid state to a discrete level structure found in molecular systems, which also results in drastically different optical properties. A prototype for this type of nanocluster systems is the silver trimer, Ag_3 , which is characterized by a number of energetically well-isolated excited electronic states in the energy region below 3.5 eV [282, 283]. The dynamics of neutral Ag_3 has been so far studied experimentally in the framework of the negative ion-to neutral-to positive ion (NeNePo) spectroscopy [284, 285]. This technique involves the preparation of the system in its anionic state Ag_3^- , which assumes a linear equilibrium geometry. Photodetachment by a pump laser pulse creates the neutral cluster in its electronic ground state, for which the linear structure represents a non-equilibrium state, thus inducing geometrical relaxation towards the triangular structure. This is monitored by photoionization with a time-delayed probe pulse, yielding an ion (or photoelectron) signal as a function of the delay time between pump and probe pulses, which contains information about the nature and time scales of the involved processes. In contrast to TRPES, which will be considered here, the NeNePo signal is not energy-resolved and therefore equivalent to a TRPES signal integrated over all photoelectron energies, thus containing a lower amount of information. However, a detailed analysis of the dynamical processes investigated by either time-resolved spectroscopic technique requires to be complemented by theoretical simulations which allow for a direct connection between the spectroscopic signals and the underlying molecular dynamics. This was

accomplished for the case of NeNePo spectroscopy by semiclassical simulations of the dynamics of Ag_3 in the ground electronic state, monitoring the structural evolution from the linear to the triangular geometry [281]. In this way, the time scales of the geometrical relaxation could be identified, as well as the fundamental features of internal vibrational energy redistribution and its nature such as resonant and dissipative. In contrast to the ground state dynamics of Ag_3 , which involves only adiabatic geometric relaxation, the excited state dynamics is expected to exhibit also strong nonadiabatic effects which can open new photochemical reaction channels not available in the ground state. Therefore, in the first part of the following results section 7.3, the FISH simulation of TRPES of Ag_3 is presented with the aim to establish the connection between the spectroscopic signal and the underlying dynamical processes.

In contrast to neutral clusters, for negatively charged species a number of experimental TRPES studies has been performed. Similar to Ag_3 , for anionic silver clusters containing up to 20 atoms, relatively short relaxation times ranging from less than 100 fs for Ag_3^- to about 4 ps for Ag_7^- have been observed [286], which are also attributed to structural deformations leading to energy level crossings and thus to more rapid internal conversion. Such behaviour has been also found for certain anionic gold clusters (Au_7^- and Au_8^-) in which molecular-like internal conversion to the ground state caused by strong changes of the geometrical structure occurs within 1-2 ps after excitation of the lowest-lying electronic transition, followed by strong structural fluctuations in the hot ground state [62]. Other gold clusters, however, are characterized by long-lived excited states (Au_3^- , Au_5^- and Au_6^-) [62,287]. This illustrates impressively the strongly size-dependent properties of small metal clusters, resulting in order-of-magnitude changes of the electronic lifetimes just upon adding or removing a single atom. Relatively long excited state lifetimes are also found for other clusters composed of closed d-shell atoms, such as mercury [249,250]. This is usually attributed to the presence of discrete excited electronic states which are well-separated from neighbouring ones. In stark contrast to that, for open d-shell transition metal (e.g. Ni, Pd, Pt) clusters exhibiting a high electronic state density, ultrafast electronic relaxation accompanied by changes in the character of the electronic state occurs on time scales below 100 fs following the excitation, closely resembling the behaviour of bulk metals [248,288,289].

Interestingly, such fundamentally different relaxation regimes can also occur within the very same system depending on the excitation conditions. In particular, in the second part of Sec. 7.3 it will be shown that Au_7^- , when excited into a higher-energy region characterized by a high density of states, exhibits a relatively fast internal conversion to lower-lying excited states without large-amplitude nuclear motion, similar to the bulk behaviour. As discussed above, for lower energy excitation, the relaxation is molecular-like in contrast.

In this chapter, simulated TRPES for the small noble-metal clusters Ag_3 and Au_7^- will be presented. This choice of systems serves to emphasize the conceptual scope of TRPES simulations within the FISH method: On the one hand, it allows for the prediction of TRPES prior to experimental realization, thus providing stimulation for new experiments. This aspect will be illustrated on the example of Ag_3 . On the other hand, it provides a versatile means for analysing experimentally obtained spectra and for establishing the connection between measured signals and dynamical processes at the molecular level, which will be outlined on the example of Au_7^- .

The remainder of this chapter is structured as follows: First, the computational procedures will be presented in Sec. 7.2. Subsequently, in Sec. 7.3 first the results obtained for neutral Ag_3 will be discussed and the approximations made as well as their influence on the appearance of the TRPES signal will be critically examined. These results have been published in Refs. [59,60]. Thereafter, the TRPES of Au_7^- obtained by an excitation energy of 3.12 eV will be presented and compared to experimental measurements. The results of this subsection have been published in Ref. [61]. Finally, conclusions are given in Sec. 7.4.

7.2 Computational Procedures

The field-induced nonadiabatic dynamics of Ag_3 in the framework of the FISH method has been performed using the spin-unrestricted linear response TDDFT. For this purpose, the PBE exchange-correlation functional [200] combined with the triple zeta valence plus polarization atomic basis set (TZVP) [290] and the relativistic 19 electron effective core potential (RECP) of the Stuttgart group [291] have been employed. The initial coordinates and momenta \mathbf{R}_0 and \mathbf{P}_0 have been sampled i) from a long ground state trajectory of the neutral species at 300 K for the triangular start geometry and ii) from a ground state trajectory of the anionic species at 300 K for the linear start geometry. A total number of 48 trajectories has been used for the further simulations. The FISH dynamics with direct inclusion of the pump laser pulse has been carried out in the ground state and i) six excited states for the triangular geometry and ii) 8 excited states for the linear geometry. For the nuclear motion, the Newtonian equations have been integrated using the velocity-Verlet algorithm (cf. Eq. (2.7)) with a timestep of 1.0 fs, while the electronic equations of motion (Eq. (6.1) and (6.13)) have been integrated with a time step of 10^{-4} fs. The nonadiabatic couplings and transition dipole moments along the trajectories, needed for the FISH simulations, have been calculated in the frame of TDDFT using the approach presented in Refs. [59,127,132]. In each dynamics step, the hopping probabilities were calculated and the decision if a switch between states occurs was made in a stochastic process. For times after 90 fs, when the duration of the pump pulse was

over, the nuclear velocities were uniformly rescaled after hopping events in order to ensure energy conservation.

The photoionization due to the probe pulse has been simulated using the FISH procedure augmented by the discretized continuum approximation presented in Sec. 6.2. For this purpose, the electronic continuum corresponding to the cationic ground state was approximated by 110 discrete energy levels above the ionization limit with an equal spacing of 0.027 eV. The transition dipole moments for the ionization from the bound neutral electronic state in which the trajectory is propagated to the ionized states ($\mu_{ij}[\mathbf{R}(t), E]$ in Eq. (6.13)) have been all set to a constant value. The ionized population has been calculated along each trajectory for each given time delay t_d of the probe pulse by numerically propagating the time-dependent Schrödinger equation (6.13) in the manifold of the current neutral excited electronic state and the states above the ionization limit under the influence of the probe pulse. The propagation of Eq. (6.13) was performed over the finite width of a Gaussian probe pulse in the time interval $-3\sigma \dots +3\sigma$, where σ is connected to the full width at half maximum Δt of the pulse by $\sigma = \Delta t (2\ln 2)^{-1/2}$. The final populations of the ionized states were obtained for the time after the probe pulse was over and were subsequently employed to calculate the TRPES signal using Eq. (6.14). For studying the influence of vibrational FC factors, the TRPES was also calculated according to Eq. (6.22). For this purpose, a model FC factor distribution of Gaussian form around the initial vibrational energy $E_{i,vib}^{(N)}$ of the neutral wavepacket was assumed as

$$F_{ij} \left(E_{i,vib}^{(N)}, E_{j,vib}^{(N-1)} \right) = \exp \left[-\frac{1}{2\sigma^2} \left(E_{i,vib}^{(N)} - E_{j,vib}^{(N-1)} \right)^2 \right]. \quad (7.1)$$

This allows for explicit integration of Eq. (6.22) over $E_{j,vib}^{(N-1)}$, thus the influence of the FC factors can be studied based on analytic expressions. In the present case, width parameters of $\sigma = 0.5$ eV and $\sigma = 1.5$ eV have been employed.

For the simulation of field-induced dynamics and TRPES in Au_7^- , the approach employed was essentially the same as for Ag_3 . However, the initial conditions were obtained from a harmonic Wigner distribution at 50 K, and in total 70 trajectories were propagated for the isomer 1, and 18 for isomer 2 (cf. Sec. 7.3.2). Due to the higher pump energy of 3.12 eV as compared to Ag_3 , a number of 50 bound electronic states had to be included. The ionization continuum was discretized using 120 energy levels spaced by 0.027 eV.

7.3 Results and discussion

In the following the simulated TRPES of Ag_3 and Au_7^- , based on the combination of FISH dynamics with TDDFT as devised in Sec. 6.2, are presented. These investigations serve to demonstrate the capability of FISH to simulate ultrafast spectroscopic observables of small metallic particles, which are characterized by a complex manifold of excited states and strong nonadiabatic couplings for particular geometries of the systems. The simulations include the pump laser pulse explicitly in the bound-state coupled electron-nuclear dynamics, while the probe pulse only serves to ionize the system without propagation of trajectories in the ionized state. The specific choice of systems emphasizes the two applicational aspects of TRPES simulations using FISH: Either the time-resolved observables can be predicted, and conditions for later experimental realization can be determined, as shown on the example of Ag_3 , or existing experimental findings can be analysed and interpreted with the aid of theoretical simulations, as outlined for the case of Au_7^- .

7.3.1 Excited state dynamics and TRPES of Ag_3

The investigation of the photodynamics and TRPES in Ag_3 serves the purpose to obtain for the first time an insight into the ultrafast photophysical processes in the excited states of this system, thus extending the available results concerning only ground state dynamics. As a starting point for the dynamics simulations presented in the following, two different sets of initial conditions have been employed: (i) The triangular equilibrium geometry of the Ag_3 cluster in the ground 2B_2 state; (ii) The linear geometry of Ag_3 in the ground electronic state, which has ${}^2\Sigma_u^+$ symmetry. The latter corresponds to the equilibrium configuration of the anionic species Ag_3^- and constitutes a transition state for the neutral Ag_3 cluster. Accordingly, whereas the first simulation represents the excitation of triangular Ag_3 clusters prepared in the ground state of the neutral species, the second simulation refers to a situation where the neutral, linear Ag_3 clusters are produced by ultrafast photodetachment from the anionic species, as conducted, e.g., in the framework of NeNePo spectroscopy [281, 284].

The electronic absorption spectra for both the triangular and linear geometries are shown in Fig. 7.1a) and b), respectively. The excited states which are populated by the pump pulse and hence are the starting points for the nonadiabatic relaxation (3^2B_2 for the triangular structure, $3^2\Sigma_g^+$ for the linear one) are marked by arrows and the character of the corresponding transitions is indicated by the dominant molecular orbital excitations. In addition, the symmetry labels, transition energies and oscillator strengths for the eight lowest-lying transitions are summarized in Table 7.1.

Triangular Ag ₃				Linear Ag ₃			
State	Symmetry	T _e (eV)	f _e	State	Symmetry	T _e (eV)	f _e
0⟩	² B ₂	0.00	-	0⟩	² Σ _u ⁺	0.00	-
1⟩	² ² B ₂	0.40	0.003	1⟩	² Σ _g ⁺	1.24	0.027
2⟩	² A ₂	2.22	0.000	2⟩	² ² Σ _g ⁺	2.14	0.015
3⟩	⁴ A ₁	2.40	0.001	3⟩	² Π _g	2.24	0.001
4⟩	³ ² B ₂	2.59	0.039	4⟩	² Π _g	2.25	0.001
5⟩	² A ₁	2.85	0.003	5⟩	² Δ _g	2.52	0.000
6⟩	⁴ ² B ₂	2.98	0.150	6⟩	² Δ _g	2.53	0.000
7⟩	⁴ B ₂	3.20	0.000	7⟩	⁴ Σ _u ⁺	2.66	0.000
8⟩	² ² A ₁	3.35	0.099	8⟩	³ ² Σ _g ⁺	2.72	0.641

Table 7.1: Symmetry labels and oscillator strengths of the low-lying excited states of triangular and linear Ag₃ calculated using TDDFT (cf. Sec. 7.2).

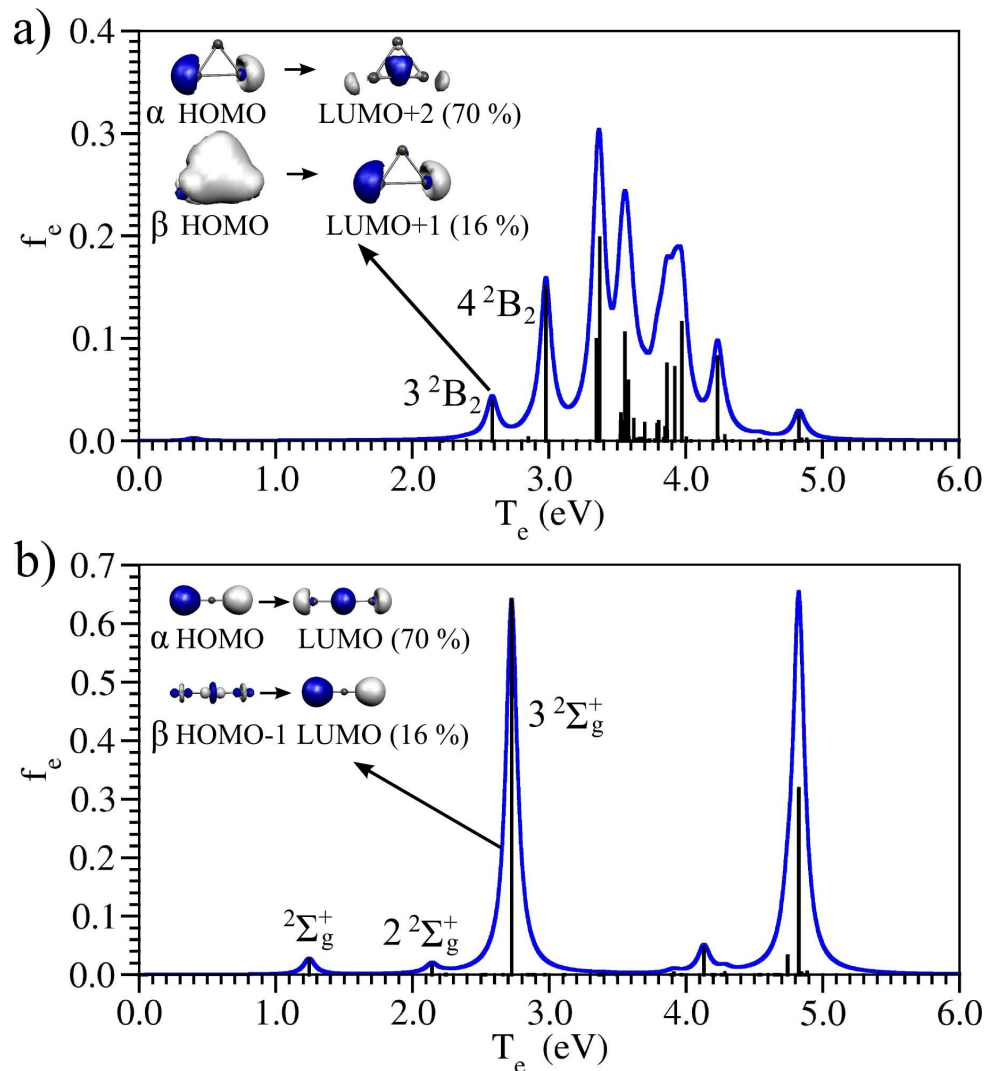


Figure 7.1: Electronic absorption spectra of triangular (a) and linear Ag₃ (b). Vertical bars represent the electronic transitions, each being broadened by a Lorentzian distribution. The dominant excitations corresponding to the transition to (a) the state |4⟩ (³²B₂) and to (b) the state |8⟩ (³²Σ_g⁺) are shown.

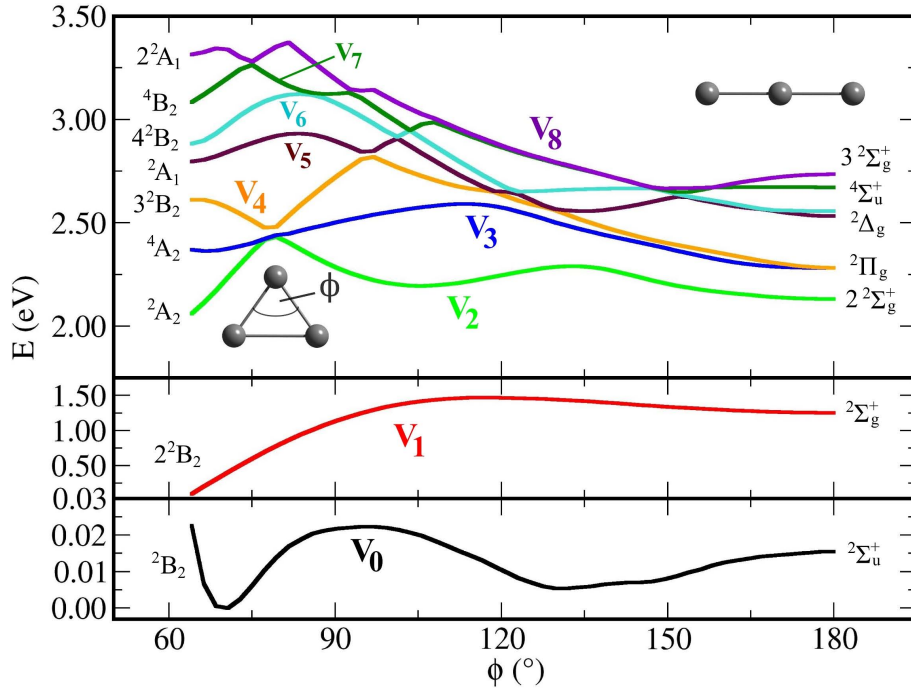


Figure 7.2: Section of the potential energy surfaces for the ground and 8 excited states of Ag_3 along the bending coordinate connecting the triangular with the linear geometry.

In the low energy regime, the spectrum of the triangular cluster is characterized by a transition of moderate intensity at 2.59 eV, corresponding to the 3^2B_2 state, as well as by a stronger transition at 2.98 eV which corresponds to the 4^2B_2 state. Up to 3.2 eV, several states of other symmetries are present, which however do not bear significant intensity in the spectrum. For the linear structure, as shown in Fig. 7.1b, an intense transition at 2.72 eV occurs, corresponding to the $3^2\Sigma_g^+$ state which is dominated by HOMO-LUMO excitation as also shown in Fig. 7.1. Furthermore, two states of $2^2\Sigma_g^+$ symmetry with only weak intensity are present at 1.24 and 2.14 eV. The other excited states present up to 3 eV exhibit essentially no intensity in the spectrum. Since in the adiabatic picture the character of the excited states can change during the dynamics, and the symmetry of the system is not preserved either, in the following the symmetry labelling of the states will be replaced by the general numeric notation $|0\rangle$ - $|8\rangle$ for the electronic states included in the simulation. Thus, the initially populated states are $|4\rangle$ (3^2B_2) for the triangular and $|8\rangle$ ($3^2\Sigma_g^+$) for the linear geometry.

For illustrative purposes, sections of the potential energy surfaces of the electronic states $|0\rangle$ - $|8\rangle$ along the bending coordinate connecting the triangular with the linear structure are shown in Fig. 7.2. It can be seen that the energetic locations of the excited states are strongly structure dependent. The ground state, as already mentioned, has a minimum for an obtuse triangular structure. For the state $|4\rangle$, which is mainly populated in the simulation starting in the triangular geometry, there is a minimum at a bending

angle of about 80° corresponding to an opening of the triangle. Since at this geometry the energies of the states $|2\rangle$, $|3\rangle$ and $|4\rangle$ are nearly degenerate, nonadiabatic transitions from $|4\rangle$ to the lower states are expected to occur. The state $|8\rangle$, which is mainly populated in the simulation starting at the linear geometry, has a shallow minimum at 150° , where also near-degeneracy with lower-lying states occurs.

In the following both the excited state population dynamics and the simulated TRPES for the two sets of initial conditions corresponding to i) the triangular structure (the equilibrium ground state electronic configuration) and ii) the linear structure (the transition state in the ground electronic configuration) will be presented.

i) Initial conditions for triangular geometry: Pump excitation is achieved by a Gaussian pulse with a width of $\Delta t = 50$ fs and an energy which is resonant to the lowest-lying intense transition at 2.59 eV, corresponding to the state $|4\rangle$. The pulse intensity was $4.2 \cdot 10^{11} \text{ W/cm}^2$, which is sufficient to induce considerable population in the state $|4\rangle$. A higher intensity would cause Rabi oscillations, in this way making the excitation efficiency very sensitive to the pulse duration. The population dynamics induced by the pump pulse is shown in Fig. 7.3. In spite of the resonant pulse energy, the state $|4\rangle$ is only populated to about 50% even though the applied pulse intensity is relatively high. This is due to very low transition dipole moments to that state in a significant part of the initial ensemble. The sensitivity of the transition dipole moments to the nuclear configuration is illustrated in Fig. 7.4, which shows the absolute values of the transition dipole moments μ_{n4} along a selected trajectory. After the pump pulse has ceased, the state $|4\rangle$ population decays with a time constant of 196 fs mainly via the third to the second excited state, and the depopulation of the 4th state is essentially complete after 500 fs. Subsequently, the population of the state $|2\rangle$ decays within 2000 fs almost entirely via the first excited state to the ground state.

The dynamical processes induced by the laser excitation are characterized by large geometrical fluctuations affecting all normal modes, the symmetry labels and frequencies of which are given in Table 7.2. Ultimately, the dynamical processes result in fragmentation of the cluster, mainly to $\text{Ag} + \text{Ag}_2$, for about 25 % of the propagated trajectories. This is initially caused by the electronic excitation due to the pump pulse which leads to a strong energy transfer from the laser field to the cluster. Subsequent nonadiabatic processes accumulate a significant part of this energy almost equally in all vibrational degrees of freedom, which results in heating and finally in fragmentation.

Normal mode	Symmetry	$\nu(\text{cm}^{-1})$
bending	A_1	50.9
antisymmetric stretch	B_2	123.2
symmetric stretch	A_1	175.3

Table 7.2: Normal modes of neutral triangular Ag_3 calculated using DFT (cf. Sec. 7.2).

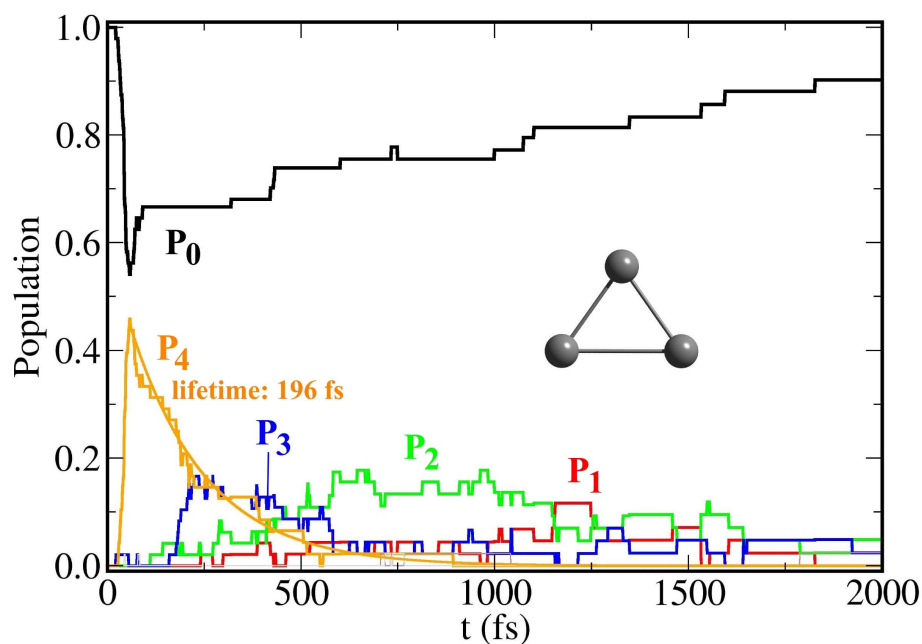


Figure 7.3: Population of the ground and 4 excited electronic states of Ag_3 during the FISH simulation starting in the triangular geometry for an ensemble of 48 trajectories. The pump excitation with an energy of 2.59 eV mainly populates the state $|4\rangle$.

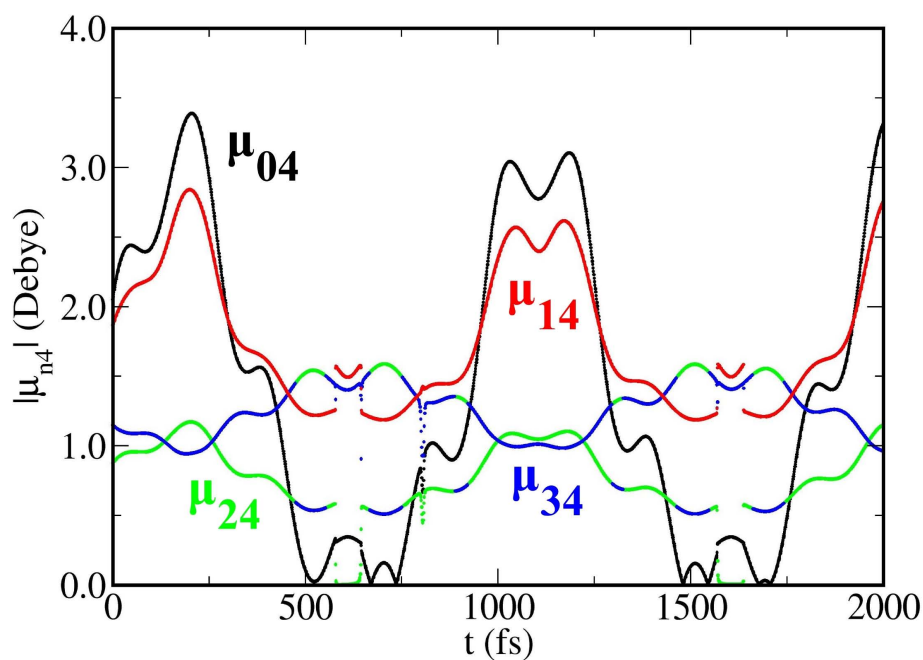


Figure 7.4: Absolute values of selected transition dipole moments along one selected nuclear trajectory of Ag_3 started in the triangular geometry.

The simulated TRPES obtained by the approach presented in Section 6.2 is shown in Fig. 7.5a). For the probe pulse, a 50 fs Gaussian with an energy of 5.71 eV and a maximum field intensity of $2.6 \cdot 10^{10} \text{ W/cm}^2$ was used in order to achieve efficient ionization. The probe pulse energy was chosen slightly below the ionization potential of the ground state (6.1 eV) in order to selectively probe the excited state population. It can be seen that the initial excitation to the state $|4\rangle$ is mirrored in the appearance of a strong photoelectron kinetic energy (PKE) signal in the range from 1.7 to 2.7 eV. This signal decays and shifts to lower PKE values mainly within 1000 fs, reflecting the depopulation of the state $|4\rangle$. For later times, only low intensity remains for PKE higher than 0.2 eV, corresponding to those trajectories which remain in excited states until the end of the simulation. The signal intensity near zero kinetic energy can be attributed to the trajectories in the ground state. In order to obtain a more quantitative picture of the PKE distribution, in Fig. 7.5b) the time-dependent photoelectron signal intensities for different kinetic energy intervals are presented. After initial excitation, a strong photoelectron signal intensity is obtained for the kinetic energies between 1.6 and 3.0 eV which then decreases to around one tenth at 1000 fs. Beginning around the same time, the highest intensity is observed for photoelectrons with kinetic energies between 0.0 and 0.5 eV. The strong decay of intensity for higher PKE values is also reflected in the photoelectron spectra for fixed probe pulse delays shown in Fig. 7.5c). While for a short time delay of 200 fs there is a strong signal for PKEs between 1.5 and 2.5 eV, for later times the relative intensities for small PKEs around zero increase (from 0.4 at 200 fs to 1.0 at 1500 fs), whereas the maximum PKE decreases from 2.5 eV at 200 fs to 1.3 eV at 1500 fs.

With the aim to investigate the influence of vibrational Franck-Condon factors on the appearance of the photoelectron spectra, also the TRPES for the triangular start geometry has been calculated according to Eq. (6.22) as outlined in the last part of Section 6.2. The TRPES for a model FC factor distribution given by

$$F_{ij} \left(E_{i,vib}^{(N)}, E_{j,vib}^{(N-1)} \right) = \exp \left(-\frac{1}{2\sigma^2} \left(E_{i,vib}^{(N)} - E_{j,vib}^{(N-1)} \right)^2 \right) \quad (7.2)$$

with energy widths σ of 0.5 eV and 1.5 eV are shown in 7.6a) and b), respectively. As can be seen, the main effect of increasing σ , which implies expanding the energy range in which the FC factors are large, consists in filling the PKE distribution, which was previously peaked at the maximum kinetic energies, into the range of lower energies. This corresponds to the transfer of part of the probe pulse energy into the vibrational degrees of freedom, giving rise to photoelectrons with lower kinetic energies.

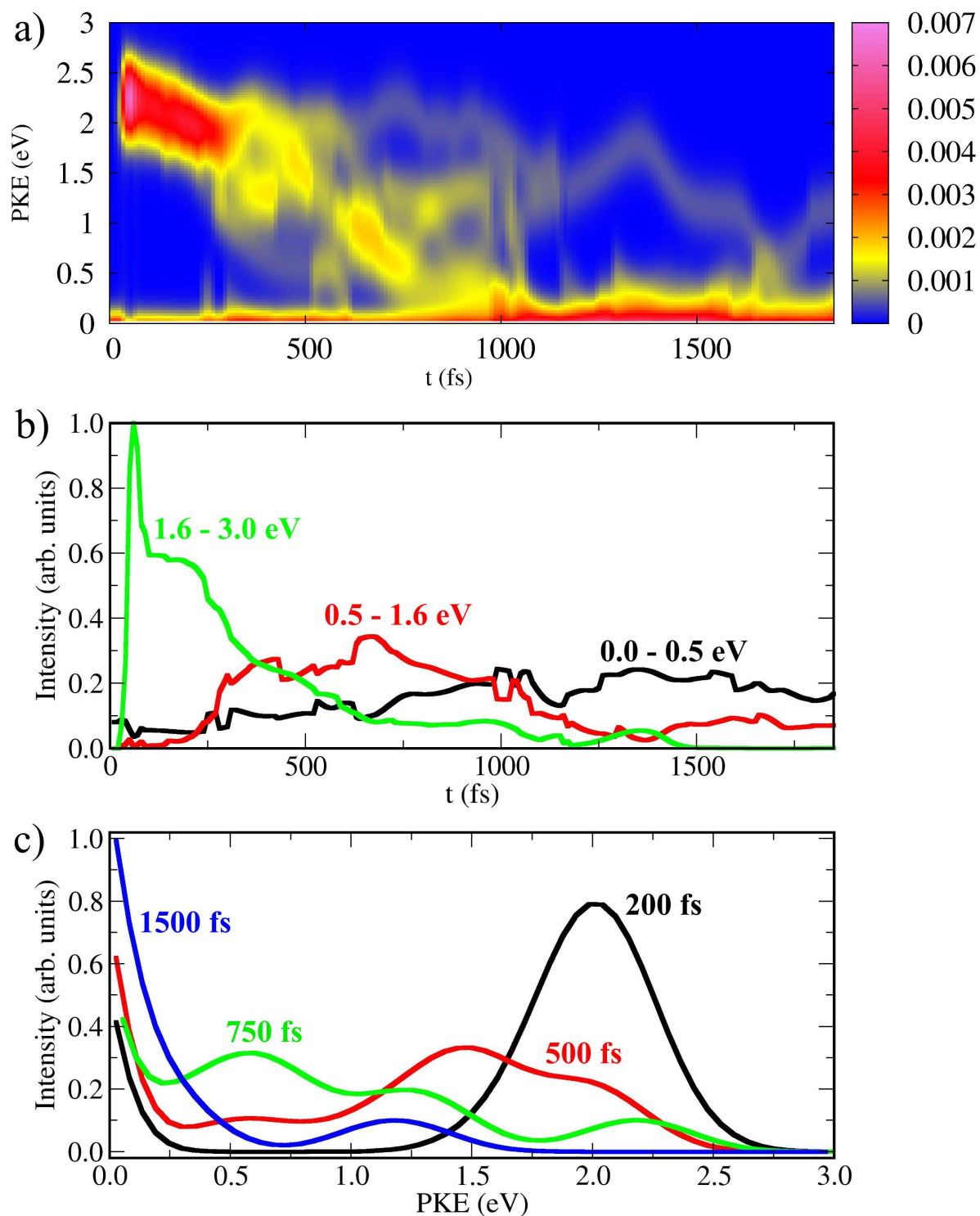


Figure 7.5: a) Time-resolved photoelectron spectrum of Ag_3 obtained from the FISH dynamics starting in the triangular geometry for a probe pulse of 5.71 eV. b) Time-dependent photoelectron signal intensities for different photoelectron kinetic energy (PKE) intervals. c) Photoelectron spectra for different time delays of the probe pulse. The signals in b) and c) have been normalized with respect to the highest peak.

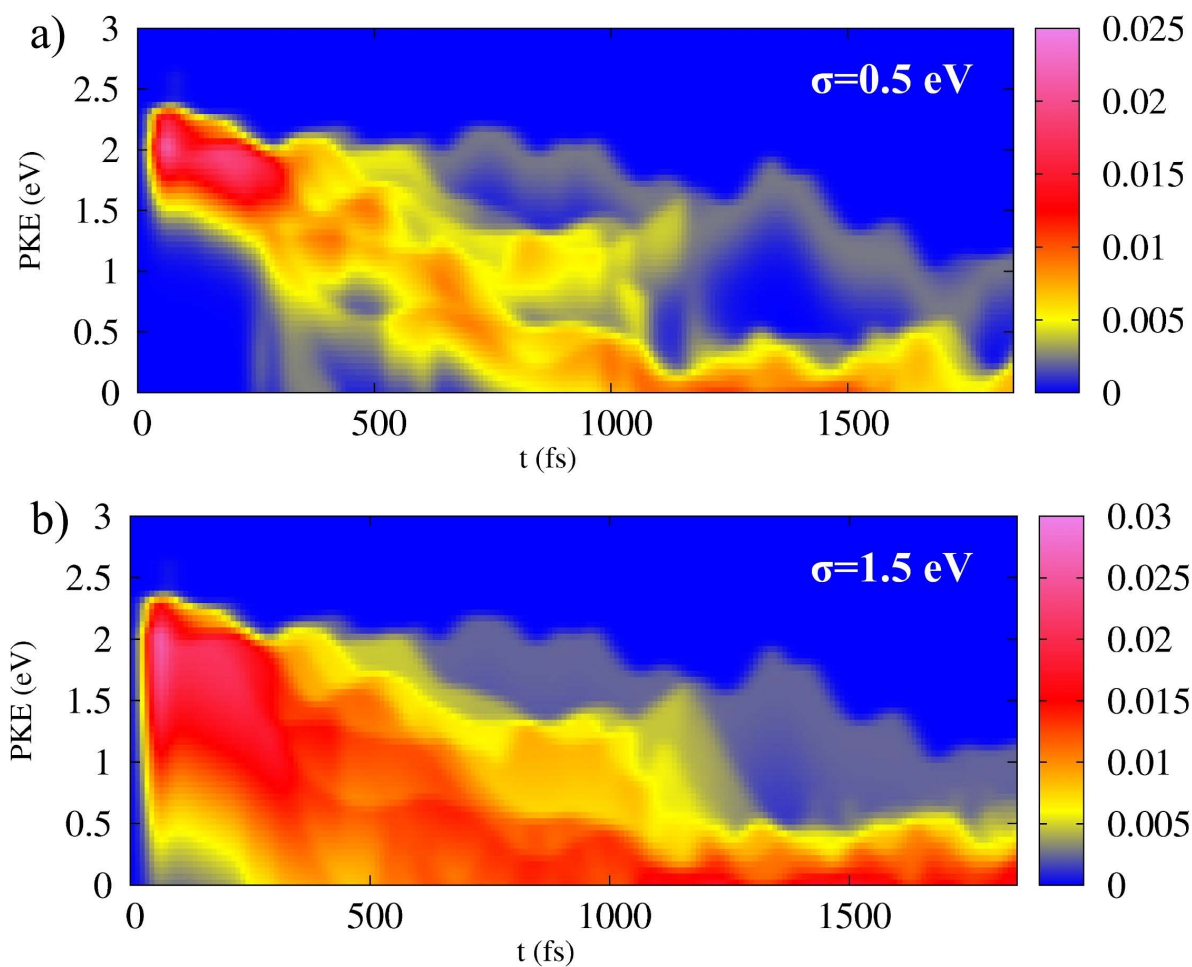


Figure 7.6: Time-resolved photoelectron spectra of Ag_3 calculated using the first order perturbation theory expression of Eq. (6.22) for the triangular initial geometry. The probe pulse energy is 5.71 eV. An approximate Franck-Condon (FC) factor distribution according to Eq. (7.2) was assumed. The signal has been calculated for two different widths of the FC factor distribution: a) $\sigma = 0.5$ eV, b) $\sigma = 1.5$ eV.

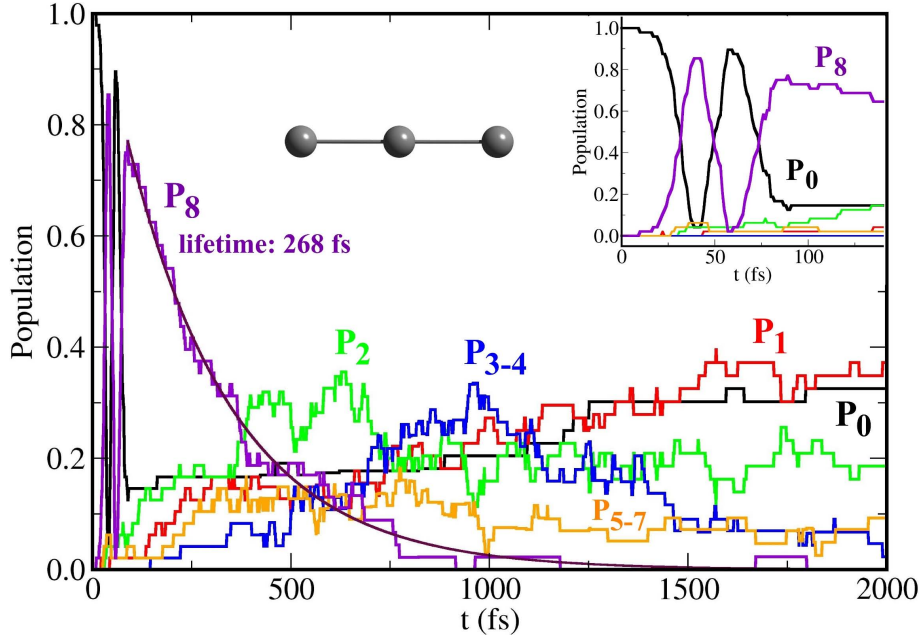


Figure 7.7: Population of the ground and 8 excited electronic states of Ag_3 during the FISH simulation starting in the linear geometry. The pump excitation with an energy of 2.72 eV mainly populates the state $|8\rangle$.

ii) Initial conditions for linear geometry: The population dynamics induced by a pump pulse resonant with the intense transition ${}^2\Sigma_u^+ \rightarrow 3^2\Sigma_g^+$ (state $|0\rangle$ to state $|8\rangle$) at 2.72 eV is shown in Fig. 7.7. In contrast to the triangular geometry, the excitation of the transient linear geometry of Ag_3 is far more efficient due to large transition dipole moments to the state $|8\rangle$ for the entire initial ensemble. Therefore, the application of a pump pulse of smaller intensity ($7.6 \cdot 10^{10} \text{W}/\text{cm}^2$) than in the case of the triangular structure significantly populates this state. After initial Rabi oscillations (cf. inset of Fig. 7.7), the state $|8\rangle$ population reaches about 80 %. Subsequently, the nonradiative relaxation of this state occurs with a time constant of 268 fs and is essentially completed after 750 fs. The population is transferred partially into the manifold of the states $|4\rangle$ - $|7\rangle$, but mainly in the second excited state whose population reaches $\approx 30\%$ after 500 fs. For later times, the population of state $|2\rangle$ decays almost equally into the $|1\rangle$ and $|3\rangle$ excited states. However, the state $|3\rangle$ is also depopulated for times after 1000 fs. At the end of the simulation time of 2000 fs, both the populations of the ground and the first excited state have reached about 30 %, whereas 20 % remain in the second and 10 % in the higher excited states. In this simulation the nuclear dynamics during the nonadiabatic relaxation is characterized by large geometric fluctuations, involving all normal modes of the cluster, the frequencies and symmetries of which are given in Table 7.3. This behaviour is similar to the previous case starting from the triangular geometry. However, the amount of cluster fragmentation of about 45 % is even higher due to the more efficient excitation which leads to a stronger energy transfer from the laser field to the cluster.

Normal mode	Symmetry	$\nu(\text{cm}^{-1})$
bending	Π_u	31.0
symmetric stretch	Σ_g^+	108.3
antisymmetric stretch	Σ_u^+	179.4

Table 7.3: Normal modes of linear anionic Ag_3^- calculated using DFT (cf. Sec. 7.2).

The simulated TRPES for the initially linear system is shown in Fig. 7.8a). In this case, a 50 fs Gaussian probe pulse with an energy of 6.0 eV, and again a maximum field intensity of $2.6 \cdot 10^{10} \text{W/cm}^2$ were employed. Due to the high excitation efficiency of the pump pulse (see also Fig. 7.7), a strong signal centered around a PKE of 1.7 eV occurs after Rabi oscillations, indicating the population of the state $|8\rangle$. During the dynamics, the intensity of this signal decreases and a new feature evolves around 0.4 eV, reflecting the population transfer from the state $|8\rangle$ to the lower-lying excited states. Furthermore, also the total signal intensity decreases as a result of population transfer to the ground state which cannot be ionized by the applied probe pulse due to the ionization potential of 7.1 eV for the linear structure. Overall, the decay of TRPES intensity is slower than in the triangular case. The time-dependent photoelectron signal intensities for selected PKE intervals shown in Fig. 7.8b) clearly confirm this observation. After excitation, the photoelectrons in the energy range between 1.2 and 2.2 eV have the highest intensity at short delay times (0.9 at ≈ 100 fs) and lower intensities at longer delay times (about 0.1 after 1800 fs). For low PKEs in the range between 0.0 and 0.8 eV the intensity increases from zero to 0.5 as a function of the delay time. However, at the end of the simulation, there is still some intensity of photoelectrons with higher energies. This behaviour is also reflected in the photoelectron spectra for fixed probe pulse delay shown in Fig. 7.8c). For the early delay times of 200 fs, the maximum PKE is centered at ≈ 1.7 eV with a relative intensity of ≈ 1.0 . Then this maximum decreases to ≈ 0.15 at a delay time of 1750 fs. In addition, a new peak is evolving at a PKE of ≈ 0.4 eV starting with an intensity of ≈ 0.3 at 500 fs to almost 0.6 at 1750 fs which reflects the transfer of population to the lower excited states $|1\rangle$ and $|2\rangle$.

The comparison of simulated TRPES for the different choices of starting geometries (triangular vs. linear) illustrates the structural influence on the excited state dynamics and the corresponding time scales. In the triangular case, there is almost complete decay of the excited state population within 1 ps. For the linear starting geometry, which is of interest in the context of transition state spectroscopy and excited state dynamics, the depopulation of the highest excited state involved is almost equally fast. However, a significant part of the population is not transferred to the ground state but to lower-lying excited states within a time scale of about 2 ps. Thus the decay of the total excited states population is much slower for the linear than in the triangular starting geometry.

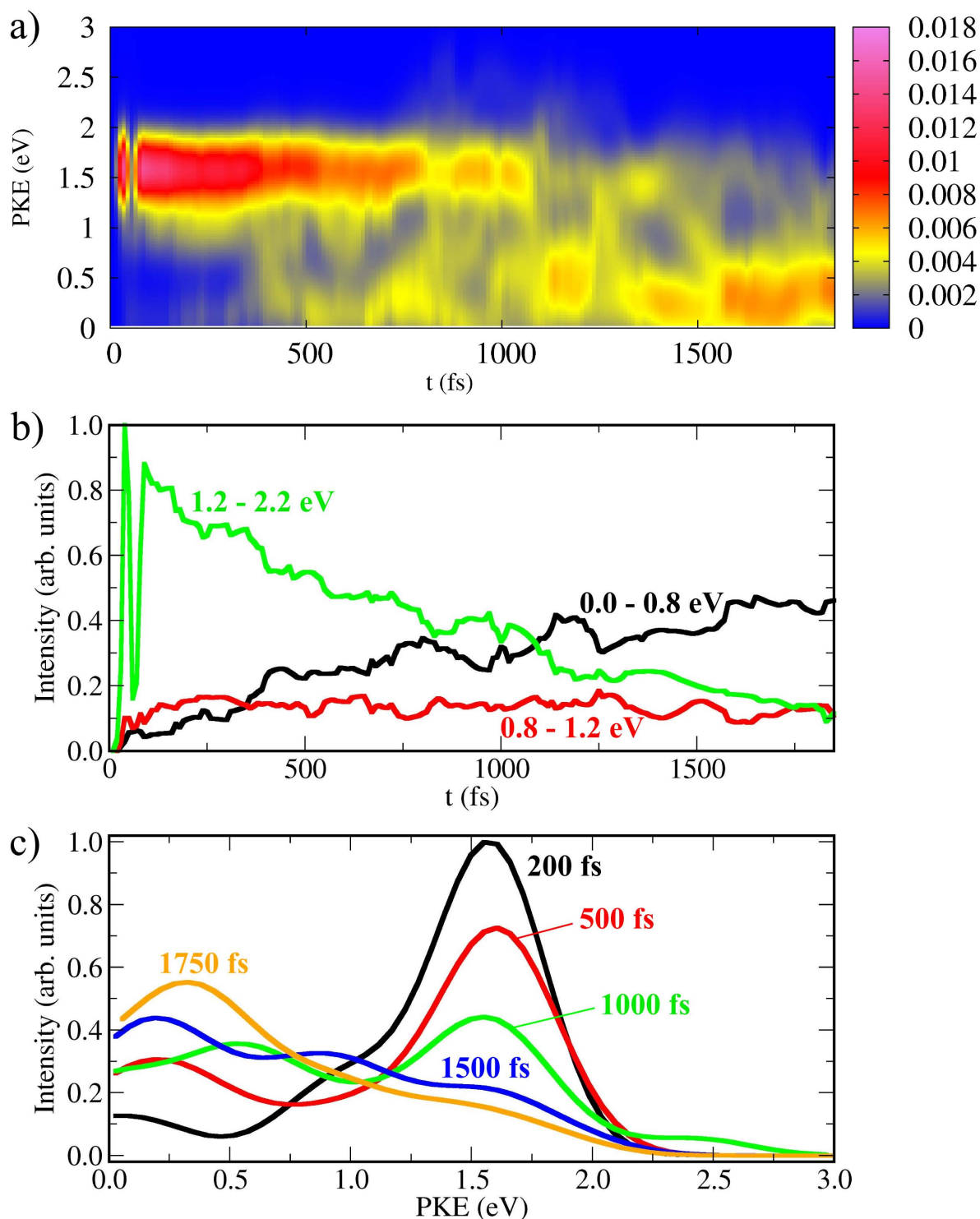


Figure 7.8: a) Time-resolved photoelectron spectrum of Ag_3 obtained from the FISH dynamics starting in the linear geometry for a probe pulse of 6.0 eV. b) Time-dependent photoelectron signal intensities for different photoelectron kinetic energy intervals. c) Photoelectron spectra for different time delays of the probe pulse. The signals in b) and c) have been normalized with respect to the highest peak.

The theoretical predictions obtained here can be confronted with the results of two types of experimental studies of TRPES. For the equilibrium starting geometry of Ag_3 two-pulse driven TRPES, which involves excitation followed by ionization, can be performed. For the linear starting geometry of the transition state of Ag_3 a three-pulse driven NeNePo TRPES, involving ionization of Ag_3^- followed by a sequence of excitation and ionization of the resulting Ag_3 , may be proposed for experimental realization.

7.3.2 Excited state dynamics and TRPES of Au_7^-

The first validation of TRPES simulated employing the novel approach presented in Sec. 6.2 with experimental results has been obtained on the example of the anionic Au_7^- cluster. The excited state dynamics of this system has been investigated experimentally and theoretically already some time ago using irradiation by a 1.56 eV laser pulse [62].¹ In this excitation regime, the first excited state is populated, in which rapidly large-amplitude nuclear motion sets in and leads to structural isomerization of the cluster. During this process, a conical intersection with the ground state is reached and the system is transferred back to the ground state within less than 1 ps. Subsequently, due to the large gain in kinetic energy during the ensuing dynamics in the ground state, a melting-like behaviour has been observed. This is clearly reminiscent of processes occurring in molecules characterized by discrete and well-separated energy levels.

In the present collaborative study [61], a higher excitation energy of 3.12 eV has been used. The dynamical processes induced by the pump excitation give rise to the experimentally measured TRPES shown in Fig. 7.9 (right part). It is characterized by two peaks, which are initially situated at photoelectron kinetic energies of 0.8 and 1.3 eV, respectively. Both peaks only slightly shift to lower energies during the time period of 800 fs shown in Fig. 7.9. However, their intensity gradually decreases, which can be attributed to less efficient ionization of the clusters in the course of the dynamics. The experimental findings are to a major extent reproduced by the theoretical TRPES also shown in Fig. 7.9 (left part). The position of the peaks is almost identical, and also a slight shift to lower energies can be observed for later times. Due to the constant transition dipole moments for ionization employed in the simulation, the decrease in peak heights is less well reproduced. The FISH simulations underlying the calculated TRPES allow for an analysis of the dynamical processes behind the spectroscopic signal. Since for Au_7^- two almost energetically degenerate lowest-lying isomers are present [292], dynamics simulations have been performed for both of them, and the TRPES has been obtained by averaging over both ensembles with equal weights.

¹The theoretical method used in this study relied on field-free dynamics in the first excited state until the conical intersection with the ground state was reached. The TRPES was approximated using a modification of the perturbation theory approach from Ref. [281].

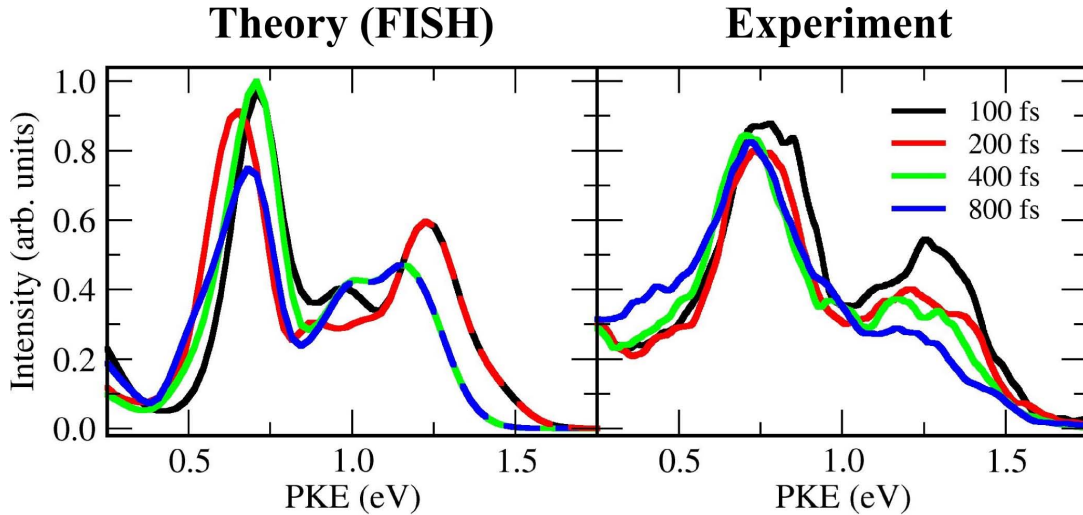


Figure 7.9: (Left) Time-resolved photoelectron spectrum of Au_7^- obtained from the FISH dynamics. (Right) Experimental TRPES of Au_7^- . The signals have been normalized with respect to the highest peak. Adapted from Ref. [61]

The electronic structure of the two isomers is illustrated in Fig. 7.10 by the densities of electronic states up to 3.3 eV. Characteristically, it can be seen that in the low-energy regime up to 2.3 eV well-separated electronic states are present, while for higher energies the states become more and more closely spaced, leading to a higher density of states. The pump pulse, whose energy width is indicated in red in Fig. 7.10, leads to the population of a manifold of energetically close-lying electronic states centered at the pulse energy of 3.12 eV. This is also evident from the electronic state population dynamics obtained within the FISH simulation and shown in Fig. 7.11. Initial excitation thus leads to the population of the electronic state manifold III. Subsequently, electronic relaxation occurs within the region of high state density, leading in average to a 0.3 eV decrease of the electronic energy within the propagation time of 1 ps. Accordingly, the population dynamics is characterized by a decay of the region III population, accompanied by an increase of the populations of regions II and I. After 600 fs, also the population of region II starts to decay, such that the main part of the excited state population becomes situated in region I, i.e. at the lower edge of the high state density region. From there, only very few trajectories decay further within 1 ps, and no return to the ground state is observed. The loss of electronic energy is compensated for by an increase of the nuclear vibrational energy, which is reflected in weak oscillations of the nuclear framework. However, in contrast to the dynamics in low-lying excited states, no large-amplitude motion or structural isomerization occurs. A more detailed analysis of the dynamical processes obtained in this collaborative work is presented in Ref. [61]. Here, it suffices to point out that the joint theoretical and experimental investigations performed in Ref. [62] and [61] have revealed the presence of two distinctly different excitation regimes in Au_7^- , in which either

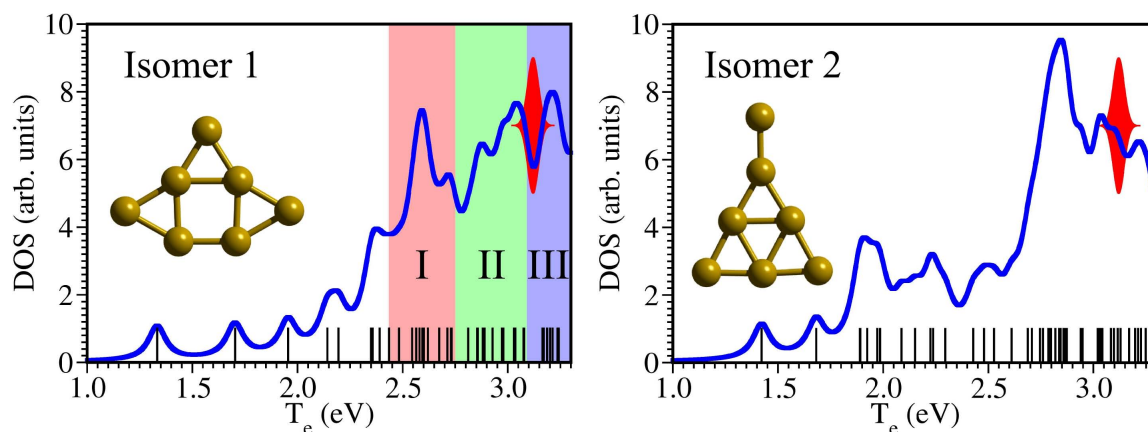


Figure 7.10: Electronic densities of state (DOS) for the two lowest-lying isomers of Au_7^- . The individual transition lines (black sticks) have been broadened by a Lorentzian width of 0.1 eV (blue curve). The spectral position and width of the pump laser pulse centered at 3.12 eV is indicated in red .

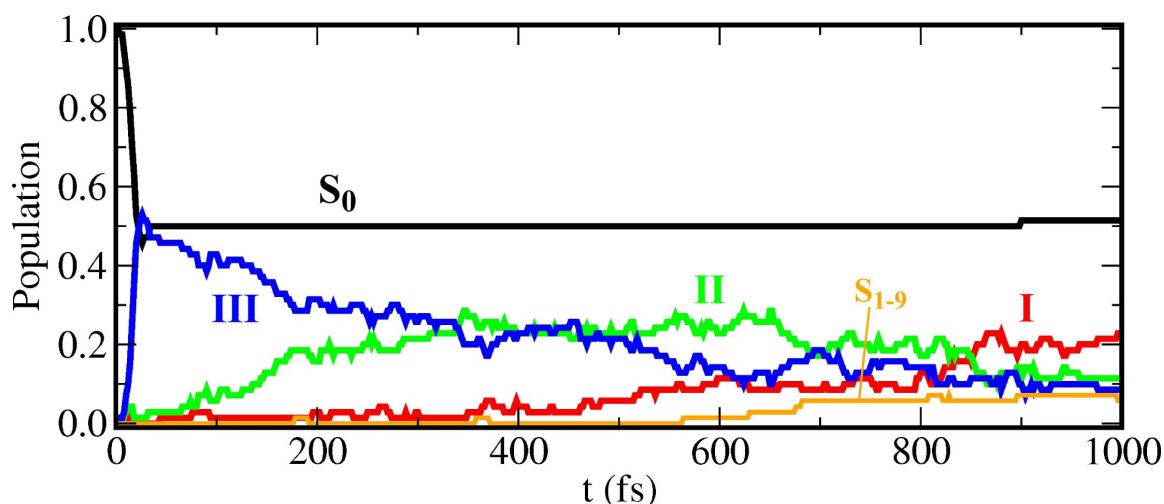


Figure 7.11: Electronic state population dynamics of the isomer 1 of Au_7^- for the ground state (S_0 , black), the low-lying excited states (orange) as well as for the high-lying excited states from energy regions I (red), II (green), and III (blue) (cf. Fig. 7.10) obtained using the FISH method with the experimental pump pulse of 3.12 eV [293].

a molecular-like internal conversion process involving isomerization, or a more bulk-like relaxation, in which electronic energy from a manifold of close-lying states is transferred to the vibrational degrees of freedom without large-amplitude nuclear motion, takes place. Consequently, the relaxation processes occurring in such small clusters can be controlled by the choice of the electronic excitation energy, opening the perspective for developing cluster-based materials with bespoke optical response properties.

7.4 Conclusions

In this chapter, the FISH method extended by the discretized continuum approximation for the photoionization as devised in Chapter 6 has been employed to simulate the TRPES of the small metal nanoclusters Ag_3 and Au_7^- . In this way, for the first time trajectory-based simulations accounting for all nuclear degrees of freedom have been performed under the explicit influence of pump and probe laser pulses in order to simulate a time-resolved spectroscopic observable. As a first illustration, the prototype example of the Ag_3 cluster was chosen, which is characterized by a high density of excited electronic states and strong nonadiabatic effects. The mechanism and the time scale of the nonradiative excited state relaxation have been determined for two sets of initial conditions: (i) starting from a ground state equilibrium ensemble around the triangular structure, (ii) starting from the linear structure which corresponds to the equilibrium geometry for the anion and represents a transition state of the neutral species. For both simulations, it has been shown how the fingerprint of the underlying dynamics is reflected in the TRPES. Moreover, the influence of a model Franck-Condon factor distribution on the appearance of TRPES signals has been examined, which is important for the interpretation of experimental results. In addition to Ag_3 , also the TRPES of Au_7^- , for which experimental data are available, has been simulated, and very good agreement with the experiment has been found. Also in this case, the analysis of the dynamics simulations has allowed for the elucidation of the molecular processes underlying the specific appearance of the spectra. These two examples illustrate the applicability of FISH for the simulation of experimental spectroscopic observables, emphasizing both the ability to theoretically predict the appearance of the signal as well as to utilize simulations to help analyse and interpret experimentally obtained data. Moreover, since the presented approach is based on the FISH method with its broad applicational scope, it provides a unique opportunity to simulate experimental spectroscopic signals and to identify the mechanism of photochemical processes in a multitude of complex systems such as metallic nanoclusters, biochromophores interacting with the environment, or molecules in solution.

Part III

Coherent control in complex systems using FISH

8 Concepts and applications of coherent control in molecular systems

A particularly attractive area in molecular physics is the coherent control using optimally shaped laser fields, which is based on the idea of using light to steer the course and outcome of a chemical or physical process in a precisely defined way. While in the common approaches to the control of chemical reaction pathways external parameters such as temperature, pressure or concentrations of reactants are adjusted, the interaction of light with reactants has the potential of being much more precisely tunable. The advent of laser technology, with the more and more improved ability to generate ultrashort light pulses with durations on the time scales of nuclear and electronic motion, has nowadays enabled the experimental realization of numerous strategies for coherent control at the molecular level. The basic concepts, however, have been devised from the theoretical side already in the early stages of ultrafast laser physics. As a starting point served the idea to selectively excite a specific vibrational mode of a molecule by infrared light in order to achieve bond breaking [294]. However, it soon became clear that the needed accumulation of vibrational energy in the respective mode usually does not happen fast enough to compete with processes of ultrafast intramolecular energy redistribution (IVR) [295–298], especially when laser pulses of longer duration than the typical vibrational time scales are used. Therefore, different strategies were proposed, which rely on utilizing ultrashort laser pulses of durations in the sub-ps time regime. Such pulses are able to induce dynamical processes and to intervene in the ultrafast dynamics in a precisely defined way, thereby also exploiting the quantum mechanical nature of molecular motion.

The earliest control strategy has been developed by Tannor, Kosloff and Rice [20, 299, 300] and consists in the sequential action of two ultrashort laser pulses [cf. Fig. 8.1a)]. The first of these pulses (pump pulse) excites the system to a non-equilibrium configuration, which subsequently leads to the onset of dynamical processes. After a specific time delay, a second pulse is acting, which either brings the system back to the ground state (dump pulse), or leads to further excitation to a detection state, e.g. by ionization (probe pulse). This approach has later been experimentally verified on the example of controlling the ratio between molecular and dissociative ionization of the sodium dimer [301]. In another early realization, the variation of the pulse delay allowed for controlling the formation yield of the XeI molecule [302].

The second major strategy for coherent control is less intuitive, as it relies on quantum interference effects in a subtle way. Devised by Brumer and Shapiro [21, 22, 303, 304], this approach is based on the interplay of different reaction pathways which can be steered by varying the phase difference between two laser fields of different frequencies. This can lead to constructive interference for one of the reaction pathways, and to destructive

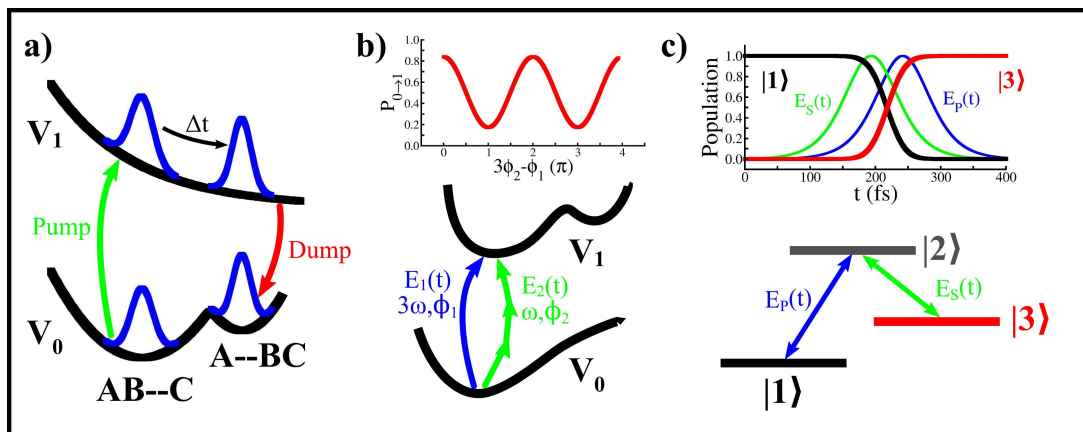


Figure 8.1: Strategies for coherent control in molecular systems. a) Tannor-Rice pump-dump control. b) Brumer-Shapiro interference control. c) Stimulated Raman adiabatic passage (STIRAP).

interference for the other, thus enhancing one of the product channels, as schematically depicted in Fig. 8.1b). The first realizations of this strategy involve the modulation of excitation and ionization efficiency in Kr [305] and Hg atoms [306], as well as in the HCl molecule [307]. Control of product distributions was first achieved on the example of molecular vs. dissociative ionization of the HI molecule [308].

While in the early pioneering experimental work control was achieved by variation of a single parameter only, later technological progress in laser pulse shaping allowed for the precise fine-tuning of several laser parameters (for an overview see Ref. [309]), leading to the first realizations of multi-parameter control. In the context of the Tannor Kosloff Rice scheme, this involves, besides the time delay, e.g. the pulse frequency [310–313], frequency chirp [314], pulse width [315], or field amplitude [316].

Besides the above mentioned control strategies, the use of strong laser fields opens additional possibilities for the manipulation of processes. In the framework of adiabatic passage techniques, the coupling of electronic states by strong fields leads to Rabi oscillations that may achieve complete population exchange. In particular, Raman processes utilizing transiently populated intermediate states are relevant in this research field, such as the stimulated Raman adiabatic passage technique (STIRAP) [317–319] illustrated in Fig. 8.1c), first experimentally realized for the selective population of vibrational states in the sodium dimer [318].

In order to determine optimal pulse parameter values for a process under study, in simple cases knowledge about several system parameters, as e.g. excitation energies or vibrational periods, can provide valuable information. However, with increasing system complexity, this approach will cease to be practical for finding the best parameters. Instead, mathematical techniques can be used, which, based on a quantum mechanical description of the studied system, may lead to predictions of optimal field parameters us-

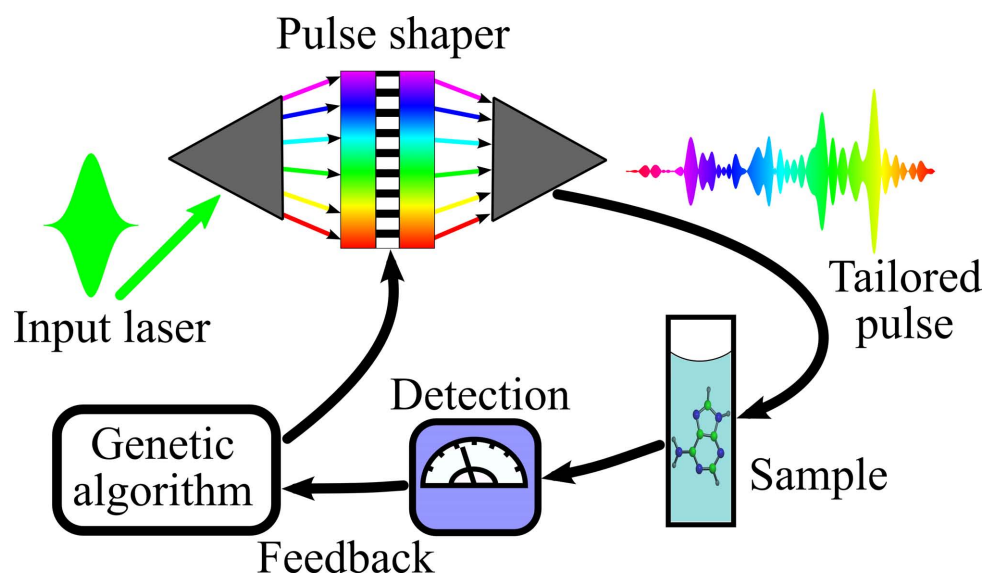


Figure 8.2: Principle of adaptive closed-loop control: The incoming laser pulse is spectrally decomposed, amplitudes and phases are tailored, and the resulting shaped pulse is irradiated on the sample. The detection signal is fed to a computer system where its ability to achieve the optimization goal is assessed. New pulse parameters based on this information are then constructed, which are passed to the pulse shaper. The whole procedure is iteratively repeated until the optimization goal is fulfilled.

ing a variational formulation of the control problem [320–325]. These techniques typically rely on field-driven quantum dynamics simulations and therefore share the limitations of the latter regarding size and complexity of the systems. Therefore, their applicability beyond few-dimensional systems is severely restricted.

An alternative, which has by now developed into the most widely used approach to the coherent control in complex systems, has been proposed two decades ago by Judson and Rabitz [27]. Their idea was to utilize the response of the molecular system provoked by the acting control field as a feedback signal for an iterative optimization procedure (“closed-loop learning”, CLL, cf. Fig. 8.2). For this purpose, adaptive optimization techniques, such as genetic algorithms [239,326], are commonly used, which are inspired by the process of biological evolution. The starting point of these techniques is the random generation of many different parameter sets (the “population”) and their encoding as “genes”. Using a properly constructed target function, the ability of each parameter set to produce a desired outcome (“fitness”) is evaluated, and based on this evaluation a selection of genes is chosen for constructing a subsequent generation of new parameters. For this purpose, the representations of the old parameters are recombined, mimicking the crossover of genes occurring in biological cell division. This leads to reproduction of favourable genes, while the unfavourable ones become extinct. In order to avoid too fast an onset of uniformity in the population, it is also common to introduce a small probability for random changes in the genes, thus mimicking also mutations.

In this way, the optimization problem is in fact solved by the studied system itself, thus avoiding complicated theoretical simulation procedures. After the first more technical implementations of the closed loop learning technique combined with optical pulse compression and shaping [23–26], the first experimental application to a molecular system has been reported by Bardeen et al., who optimized the electronic excitation efficiency in an organic dye molecule [327]. In the context of chemical reactivity, first results were obtained by Gerber et al., who investigated the photodissociation of the organic iron carbonyl $[(C_5H_5)Fe(CO)_2Cl]$ and achieved a significant degree of control for the formation ratio of different photoproducts [328]. Similar results were also obtained by Wöste et al. on the manganese carbonyl $[(C_5H_5)Mn(CO)_3]$ [329, 330]. Further applications involve selective bond breaking in other organic molecules [331, 332], isomerization in biological [333, 334] and organic chromophores [335], as well as the control of excitation energy transfer in biological light-harvesting systems [336, 337]. In addition, the CLL approach has been employed to achieve selective vibrational excitation via Raman [338] or electronic pump-dump processes [339]. Using a technique for wavefunction reconstruction, even the radial shape of a highly excited atomic Rydberg state wavefunction has been optimized to match a selected target [340]. Moreover, nonlinear optical properties as the high-harmonic generation in noble gas atoms have been controlled [341], and recently, also the control of the spatial field distribution has been achieved and utilized to induce spatially localized electron emission in a nanostructure [342]. In simple systems, the efficiency of ionization processes has been controlled [343–345], and even isotope selectivity of the ionization process could be achieved [346]. For a more comprehensive overview of the literature, compare also the review articles and books given as Ref. [28–34]. It should be emphasized that beyond the control on the time scale of nuclear motion, technological progress has in the last years also enabled the control of processes directly involving electronic motion on the attosecond time scale [347–350].

Notwithstanding this experimental success of the adaptive optimization technique for controlling even very complex molecular processes, a major drawback of this method is the usually also very complex form of the optimized laser fields. This prevents in most cases a straightforward interpretation of how the fields act at a molecular level and therefore is of limited help in finding the mechanism underlying the control. A possible remedy to this problem might consist in successively reducing the pulse complexity by imposing restrictions on the functional form or decreasing the number of optimization parameters. In this context, it has been shown that starting from a freely optimized control pulse involving several hundreds of parameters, the covariance properties of the obtained fitness data can be used to identify a small number of certain linear combinations of parameters which contribute the main part to the control. In this way, the dimension of the control space could be reduced to less than ten parameters, at the same time retaining almost

the full variational flexibility and hence ability to achieve control [351].

Another, particularly convenient strategy consists in the construction of simplified shaped laser pulses that a priori depend only on a small number of parameters to be varied [352–354]. Simple examples include variation of the time delay between different subpulses or their relative intensity. Greater flexibility of pulse forms can be achieved by employing an analytical expression for the spectral phase, such as a triangular shape or a sine function. In this way, only few parameters are present, which often have an intuitive connection to the pulse appearance. Their effect on the controlled system can be investigated by scanning an appropriate range of values [355–358]. The control space spanned by such parameters is often small enough to be completely sampled, hence a control landscape [359–361] can be obtained and extrema of the optimization target function can be found without performing a full iterative optimization procedure [362–365]¹. Moreover, in some cases the pulse parameters can be directly connected to properties of the studied system, and insights into the control mechanism can be obtained, e.g. as it has been done in studies of the wavepacket dynamics in alkali dimers using simple pump-probe techniques [301] or more complicated laser pulse trains obtained by spectral phase modulation [353].

Although the use of simplified laser pulses has led to important insights into the control mechanism in several cases, a thorough molecular-level understanding can only be gained if experimental results are complemented by theoretical simulations. For small molecules or reduced-dimensional models of larger systems, theoretical optimization of control fields can be performed based on quantum dynamics simulations, both in the framework of variational optimal control theory (for an overview cf. Ref. [361], § 3 and references cited therein) as well as employing the adaptive closed-loop learning method similar to the experimental procedure. As an illustrative example for the direct use of experimentally optimized laser fields in quantum dynamics simulations in order to gain an immediate insight into the molecular mechanisms behind the experimental findings, the study of the ionization processes in alkali dimers [345, 369] is mentioned.

However, in view of the limitations inherent to full quantum dynamics simulations, progress in theoretical methodology is necessary in order to also allow for molecular-level simulations of complex systems under the influence of realistic optimized pulses. This can be achieved in the framework of mixed quantum-classical methods based on the description of nuclear dynamics using classical trajectories. In this context, the FISH method discussed in Chapter 3 provides a powerful tool for the simulation of control experiments,

¹Although there has recently been some debate about the nature of the extrema of control landscapes, in particular concerning the existence of optimization traps (local extrema) [366–368], it could be shown for isolated quantum systems that, provided certain well-defined criteria for the systems and control fields are met, all extrema are global ones [361, 367]. Therefore, the convergence of optimization procedures to the global extrema of the optimization target can be ensured in these cases.

at the same time taking into account all nuclear degrees of freedom and explicitly including the molecule-field interaction. This allows for the use of arbitrarily shaped laser fields in the simulations, thus opening the possibility either to theoretically optimize the fields in an iterative procedure, or, alternatively, to employ experimentally optimized laser fields directly in the simulation. Moreover, also control landscapes can be theoretically explored by scanning the pulse parameters in an appropriate range of values. Owing to these opportunities, for the first time the connection between experimental pulses and intrinsic dynamical processes for real molecules can be established, thus elucidating the mechanism underlying the control.

Before turning towards application-oriented investigations using FISH, the following Chapter 9 will be devoted to a thorough comparative study on the fundamental validation of the method for the simulation of coherent quantum control. For this purpose, on the example of the potassium dimer molecule, the selective population of energetically close-lying excited states using shaped laser fields will be simulated both using the FISH method and numerically exact quantum dynamics [63]. The comparison of results obtained by the two methods will establish the accuracy of FISH for simulating coherent control processes, which will provide a basis for applying the method to much more complex molecular systems.

Subsequently, the theoretical design of simplified laser pulses shaped for control in complex systems will be illustrated in Chapter 10 on the example of manipulation of excited state dynamics in the nucleobase adenine interacting with water environment [64]. This is motivated by the aim to exploit the approach of reducing pulse complexity also in the framework of theoretical simulations. In this context, it is in fact of particular advantage, since it provides a means to avoid iterative optimization procedures, given the fact that the time scales of dynamics simulations can be considerably larger than those for running the respective experimental measurements.

Since within the FISH method the electric field is directly included in the dynamics simulations, also the most straightforward approach of combining experimental optimal control with theory is possible: Experimentally obtained laser pulses can be employed directly in theoretical simulations of the dynamical processes in the studied system. In this way, a real-time picture of the dynamics at molecular level can be obtained, and the direct connection to experimental observations can be made. This will be illustrated on the example of optimal dynamic discrimination of flavin molecules [67] in Chapter 11 of this thesis.

9 Validation of FISH:

Coherent control of selective photoexcitation in K_2

9.1 Introduction

Since the FISH method employs classical trajectories for the nuclear dynamics, the fundamental question has to be addressed to which extent it can take into account the electronic and nuclear coherence effects which are at the heart of the coherently controlled dynamics. In previous work it has been demonstrated that FISH simulations can perfectly account for the coherent Rabi oscillations between two coupled electronic states in a two-level model system [55]. Moreover, on the example of several one-dimensional systems it could be shown that FISH almost perfectly reproduces the results of full quantum dynamics simulations [55, 238]. In the present chapter, the focus lies on the strong field control and the ability of the FISH method to describe coherent processes in a system with several coupled electronic states. For this purpose, the potassium dimer has been selected as a prototype, since accurate potential energy curves and transition dipole moments for this system are available. Moreover, the strong field control using the selective population of dressed states (SPODS) scheme, which was previously experimentally applied to potassium atoms [370–372], has been already demonstrated on this molecular example using quantum dynamics simulations [373], and, recently, also experimentally [374]. Within SPODS, the excitation to a manifold of excited electronic states by a phase coherent double pulse sequence is used to steer the final state population. Almost perfect selectivity in populating different target states has been achieved by varying the time delay between the two subpulses. Due to its conceptual clarity, the SPODS control scheme is particularly suitable for a systematic investigation of coherent control in the framework of the mixed quantum-classical FISH method. Therefore, in the following it will be demonstrated that FISH accurately describes the coherent electronic processes induced within the SPODS control scheme and leads to results which are in almost perfect agreement with the exact quantum dynamics simulations. These findings, together with the applicability of FISH to complex systems with many degrees of freedom, provide a strong fundament for using the FISH method for the simulation of coherent control in systems ranging from polyatomic (bio)molecules and clusters to complex nanostructures and supramolecular assemblies or systems interacting with their environment, such as solvent or surfaces.

This chapter is organized as follows: First, the computational details are presented in Section 9.2. Subsequently, in Section 9.3 the results are presented and discussed. Finally, conclusions are given in Section 9.4. The results presented in this chapter have been published in Ref. [63].

9.2 Computational Procedures

9.2.1 Ab initio potential energy curves and transition dipole moments

Both the quantum dynamical as well as the FISH simulations have been performed using precalculated potential energy curves and distance-dependent electric transition dipole moments for the K_2 molecule. For this purpose, the multireference configuration interaction (MRCI) method [375–377] was employed as implemented in the MOLPRO program package [378]. As reference states in the MRCI calculation, state-averaged complete active space self-consistent field (CASSCF) wavefunctions [379, 380] were used. The K atoms were described using a 1-electron effective core potential [381] together with a (7s5p7d2f)/[6s5p5d2f] Gaussian basis set [382] as well as the core polarization potential from Ref. [383]. The active space for the CASSCF calculations was constructed from the occupied orbital and 15 virtual ones. Subsequently, the MRCI calculations including single and double excitations from all reference wavefunctions have been performed. This approach has previously been proven to yield precise results for K_2 [382, 384]. The potential energy curves for the $X^1\Sigma_g^+$, $A^1\Sigma_u^+$, $4^1\Sigma_g^+$, $2^1\Pi_g$ and $5^1\Sigma_g^+$ states, as well as the transition dipole moments between the $X^1\Sigma_g^+$ and $A^1\Sigma_u^+$, and between the $A^1\Sigma_u^+$ and the higher-lying $4^1\Sigma_g^+$, $2^1\Pi_g$ and $5^1\Sigma_g^+$ states have been calculated for internuclear distances between 5.25 and 25.0 a_0 , with $a_0 = 0.529$ as the Bohr radius.

9.2.2 Quantum dynamics simulations

The quantum dynamics of K_2 has been simulated employing the grid-based numerical solution of the nuclear Schrödinger equation using a second-order difference propagator [72]. The values of the potential energy as well as of the transition dipole moments at the 256 grid points for nuclear distances between 4 and 15 a_0 were obtained by B-spline interpolation. As initial condition, the lowest vibrational eigenstate of the electronic ground state $X^1\Sigma_g^+$ was chosen. The time step for the dynamics was 0.005 fs, and the propagation was performed over 60 fs. The laser coupling of the electronic states was described by the electric dipole interaction $-\boldsymbol{\mu}_{ij}(\mathbf{R}(t)) \cdot \mathbf{E}(t)$. The electric field was parameterized in the time domain according to

$$E(t) = \left(E_1 e^{-2\ln 2(t/\Delta t)^2} + E_2 e^{-2\ln 2((t-\tau)/\Delta t)^2} e^{i\omega_0 \tau} \right) e^{i\omega_0 t}. \quad (9.1)$$

with a frequency ω_0 of 1.49 eV (830 nm), a width of $\Delta t = 14.1$ fs and amplitudes for the subpulses of $E_1 = 0.0011 E_H/ea_0$ ($4.17 \cdot 10^{10} \text{W/cm}^2$) and $E_2 = 0.005 E_H/ea_0$ ($8.78 \cdot 10^{11} \text{W/cm}^2$), where E_H/ea_0 is the atomic unit of electric field strength. The polarization of the field was assumed to be 45° with respect to the internuclear axis of the molecule. This field was employed in the simulations as given in Eq. (9.1), without performing

the rotating wave approximation, in contrast to the simulations presented in Ref. [373]. For the pulse delay τ , different values in the range from 11.8 to 13.1 fs have been used. Experimentally, such ultrashort femtosecond pulse pairs with precisely adjusted time delay (up to a precision of 0.3 attoseconds) have been recently realized by Baumert et al. and have been applied to the SPODS control in potassium atoms [385].

9.2.3 FISH simulations

For the FISH dynamics, 300 initial conditions were sampled from a canonical Wigner distribution function at 10 K, and the nuclei were propagated classically in the respective electronic states by solving the Newtonian equations of motion using the velocity Verlet algorithm [180, 181] with a time step of 0.2 fs. The total propagation time was the same as for the quantum dynamics. The necessary forces have been obtained "on the fly" from the numerical gradients of the potential energy curves. According to the FISH procedure, the trajectories were allowed to switch between the electronic states in a probabilistic manner. For this purpose, the time-dependent Schrödinger equation (3.26) was integrated numerically in the basis of the electronic states along the nuclear trajectories, employing a time step of $8 \cdot 10^{-5}$ fs. Notice, that in the present contribution only the dipole coupling between the electronic states was taken into account and the nonadiabatic couplings present in Eq. (3.26) were neglected. The probabilities for hoppings between the electronic states were calculated from the quantum mechanical state populations $\rho_{ii} = c_i^* c_i$ according to Eq. (3.32). In order to improve the statistics of the hopping events, the whole ensemble of initial conditions was propagated twice.

9.2.4 Pulse optimization

The ability of longer laser pulse sequences to selectively populate a chosen excited state has been examined by optimizing a double pulse sequence in a restricted parameter space. For this purpose, the field parameterization given in Eq. (9.1) has been generalized to

$$\begin{aligned}
 E(t) = & E_1 e^{-2 \ln 2 ((t-\tau_1)/\Delta t_1)^2} e^{i\omega_1(t-\tau_1)} \\
 & + E_2 e^{-2 \ln 2 ((t-\tau_2)/\Delta t_2)^2} e^{i\omega_2(t-2\tau_1+\tau_2)}.
 \end{aligned} \tag{9.2}$$

Using a genetic algorithm [239], the field parameters E_i , ω_i , τ_i , and Δt_i have been optimized with the target to maximize the population of the $2^1\Pi_g$ state after the field has ceased. The optimization procedure was performed employing FISH simulations with a smaller ensemble of 72 trajectories.

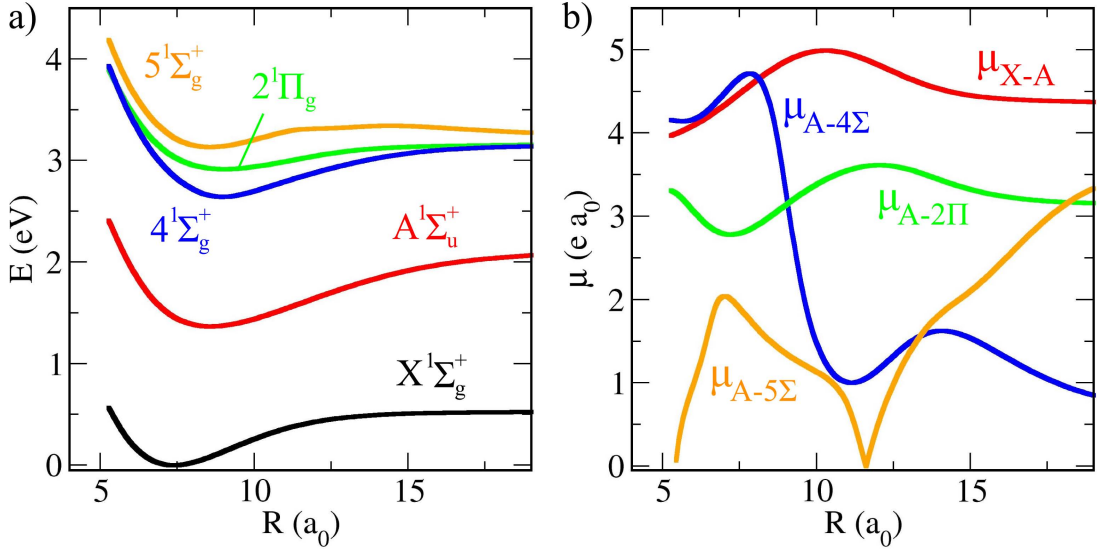


Figure 9.1: a) CAS-MRCI potential energy curves for the electronic states $X^1\Sigma_g^+$, $A^1\Sigma_u^+$, $4^1\Sigma_g^+$, $2^1\Pi_g$ and $5^1\Sigma_g^+$ of K_2 . b) Transition dipole moments between the $A^1\Sigma_u^+$ and the $X^1\Sigma_g^+$, $4^1\Sigma_g^+$, $2^1\Pi_g$ and $5^1\Sigma_g^+$ states as a function of the internuclear distance.

9.3 Results and discussion

The calculated potential energy curves for the electronic ground state $X^1\Sigma_g^+$ and four electronically excited states ($A^1\Sigma_u^+$, $4^1\Sigma_g^+$, $2^1\Pi_g$ and $5^1\Sigma_g^+$) of K_2 , which serve as the basis for the quantum dynamical and FISH simulations, are presented in Fig. 9.1a). The first optically allowed excited state ($A^1\Sigma_u^+$) can be easily reached in a single photon process with 830 nm light. The three higher excited states $4^1\Sigma_g^+$, $2^1\Pi_g$ and $5^1\Sigma_g^+$ lie closely together and are in principle also accessible from the $A^1\Sigma_u^+$ state using 830 nm excitation. This opens a possibility to control the population of these higher excited states by using phase-coherent double pulses as previously demonstrated by Wollenhaupt and Baumert [373]. The relevant transition dipole moments between the considered states strongly depend on the internuclear distance as shown in Fig. 9.1b).

With the aim to explore the ability of the FISH method to describe coherent control of the electronic state population, FISH simulations have been performed, following Ref. [373] using the excitation laser field given in Eq. (9.1) and systematically varying the parameter τ in the range from 11.8 fs to 13.1 fs. For comparison, numerically exact quantum dynamics simulations have been also performed. The resulting dependence of the final electronic state population on the time delay τ is presented in Fig. 9.2. As can be seen from the quantum dynamical simulations, the time delay has a strong influence on the final population of the $4^1\Sigma_g^+$ and $5^1\Sigma_g^+$ states such that almost complete reversal of the corresponding populations can be achieved. Specifically, maximal population of the $4^1\Sigma_g^+$ state of $\sim 75\%$ is obtained for $\tau=12.0$ fs while the population of the $5^1\Sigma_g^+$ state is

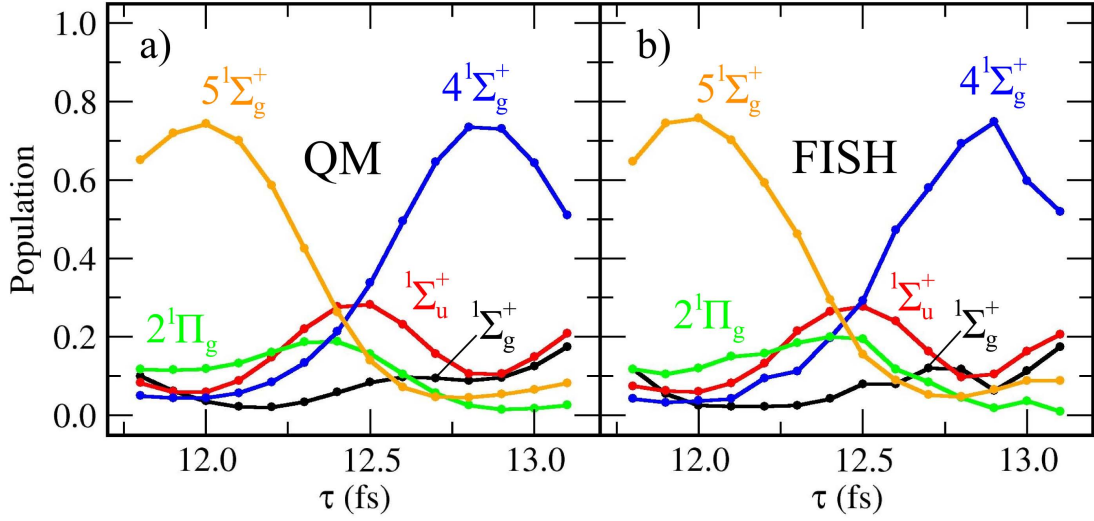


Figure 9.2: Final state populations after excitation with a short phase-coherent double pulse as a function of the time delay τ between the two subpulses [cf. Eq. (9.1)]. a) Results obtained from quantum dynamics, b) results obtained from FISH simulations.

kept below 10 % in this case. In contrast, for $\tau=12.9$ fs the population of the $5^1\Sigma_g^+$ is maximized while the population of the $4^1\Sigma_g^+$ remains lower than 10 %. As can be seen from Fig. 9.2b), the FISH simulations very well reproduce the quantum dynamics results of the final electronic state populations.

In order to examine the details of the electronic state population dynamics within the FISH method and to validate them against the full quantum mechanical results, the time-dependent populations obtained using the values of $\tau=12.0$ fs and 12.9 fs, which correspond to the maximal final populations of the $4^1\Sigma_g^+$ or $5^1\Sigma_g^+$ states, respectively, are presented in Fig. 9.3. The excitation field (blue line) together with the relative temporal phase (red line) for $\tau=12.0$ fs is shown in Fig. 9.3a). The relative temporal phase, which was obtained from the complex field as

$$\varphi = -i \ln \left[e^{-i\omega_0 t} \frac{E(t)}{|E(t)|} \right], \quad (9.3)$$

smoothly varies between zero and $\approx +2.1$. The population dynamics obtained fully quantum mechanically and in the framework of the FISH method are presented in Fig. 9.3b) and 9.3c). In both cases, the ground state population is transferred via transient occupation of the $A^1\Sigma_u^+$ and $2^1\Pi_g$ finally to the $5^1\Sigma_g^+$ state, the population of which ultimately reaches about 75 %. Overall, the time-dependent populations obtained in the frame of FISH follow closely the full quantum mechanical results. It should be noted that, in contrast to Ref. [373], in the present simulations the rotating wave approximation is not employed and therefore the electronic state populations exhibit additional small oscillations corresponding to the counter-rotating corrections to the rotating wave approximation.

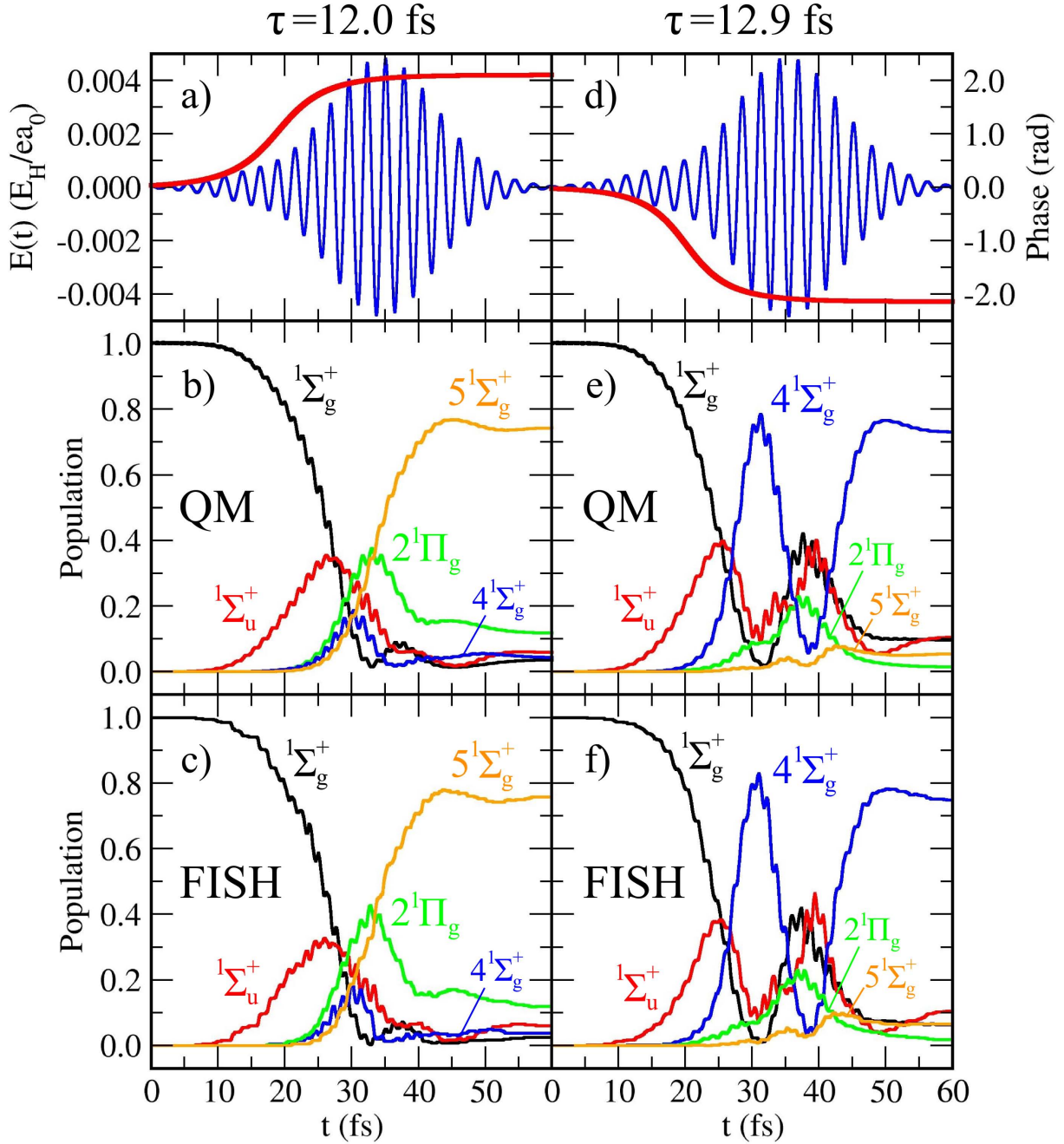


Figure 9.3: Left panel: a) Temporal field strength (blue) and relative temporal phase (red, cf. Eq. (9.3)) of the double pulse with time delay $\tau=12.0$ fs. The field strength is given in atomic units ($1E_H/ea_0 \hat{=} 5.14 \cdot 10^{11} V/m$). b)/c) Time-dependent electronic state populations obtained by quantum dynamics (b) and by employing the FISH method (c). Right panel: d)/e)/f): Same as left panel, but for a time delay of 12.9 fs.

For $\tau=12.9$ fs the overall envelope of the electric field is unchanged, but the relative temporal phase varies now from zero to ≈ -2.1 as shown in Fig. 9.3d). This phase change leads to dramatically different dynamics. The resulting state populations are presented in Fig. 9.3e) for the full quantum and in Fig. 9.3f) for the FISH simulation. In both cases, after initial population of the $A^1\Sigma_u^+$ state, the $4^1\Sigma_g^+$ state starts to be populated immediately and reaches a maximal value of 80 % after 30 fs. Subsequently, due to the larger transition dipole moment between the $A^1\Sigma_u^+$ and the $4^1\Sigma_g^+$ state as compared to the $5^1\Sigma_g^+$ state, large-amplitude Rabi oscillations occur and lead to population transfer back to the $X^1\Sigma_g^+$ and $A^1\Sigma_u^+$ states, and also partly to the $2^1\Pi_g$ state. After 38 fs the population of $4^1\Sigma_g^+$ state has diminished to a value of only 4 %. However, after 40 fs the $4^1\Sigma_g^+$ state begins again to be populated, reaching a final value of almost 75 % after the pulse has ceased. Similar to the previous case, the comparison between full quantum and FISH dynamics shows perfect agreement.

In order to address the mechanism underlying the selective population of states by only changing the phase of the driving laser field, in the following the role of the electronic coherences between the intermediate $A^1\Sigma_u^+$ state and the final states $4^1\Sigma_g^+$ and $5^1\Sigma_g^+$ are analyzed for the quantum dynamics simulation. Starting from the time-dependent Schrödinger equation for nuclear wavepackets in a manifold of electronic states (cf. Eq. (1.7)),

$$i\hbar\dot{\chi}_i(R, t) = \left(-\frac{\hbar^2}{2m} \frac{\partial^2}{\partial R^2} + E_i(R) \right) \chi_i(R, t) - \sum_k \boldsymbol{\mu}_{ik}(R) \cdot \mathbf{E}(t) \chi_k(R, t), \quad (9.4)$$

with m as the reduced mass of the diatomic, an equation for the population transfer between the states can be derived similar to Eq. (3.8) as

$$\dot{\rho}_{ii}(t) = \frac{d}{dt} \int dR \chi_i^*(R, t) \chi_i(R, t) = -\frac{2}{\hbar} \sum_k \int dR \boldsymbol{\mu}_{ik}(R) \cdot \mathbf{E}(t) \text{Im} [\chi_k(R, t) \chi_i^*(R, t)]. \quad (9.5)$$

This means that the population change of a state i caused by the coupling to a state k can be to first order approximated by one summand of the right-hand side. If the electronic transition dipole moments are only slightly dependent on the nuclear coordinate, as it is in the present case within the spatial extent of the wavepacket, Eq. (9.5) can be further simplified by taking the transition dipole moment at the center of the nuclear wavepacket R_0 out of the integral, followed by introducing the electronic coherences $\rho_{ki}(t) = \int dR \chi_k(R, t) \chi_i^*(R, t)$, which leads to

$$\dot{\rho}_{ii}(t) = -\frac{2}{\hbar} \sum_k \boldsymbol{\mu}_{ik}(R_0) \cdot \mathbf{E}(t) \text{Im} [\rho_{ki}(t)]. \quad (9.6)$$

Since the selectivity of the excitation process depends crucially on the intermediate pop-

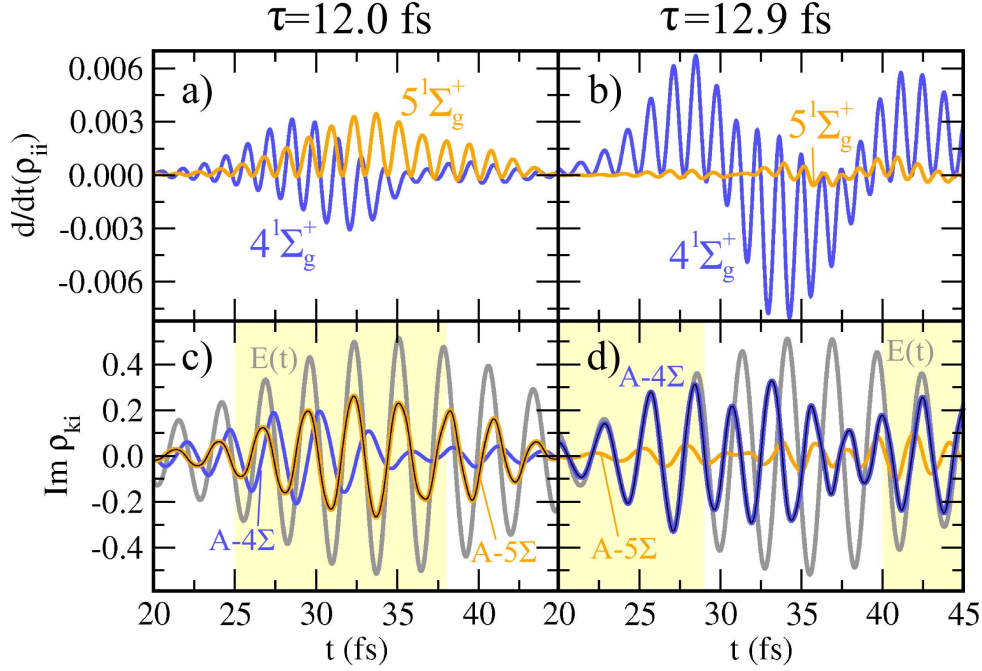


Figure 9.4: (Upper panel) Contribution from the $A^1\Sigma_u^+$ state to the rate of change of the $4^1\Sigma_g^+$ and $5^1\Sigma_g^+$ state populations for the double pulse excitation with $\tau=12.0$ fs (a) and $\tau=12.9$ fs (b). (Lower panel) Imaginary part of the electronic coherences between the $A^1\Sigma_u^+$ and $4^1\Sigma_g^+$ (blue) or $5^1\Sigma_g^+$ (orange) states, respectively, for $\tau=12.0$ fs (c) and $\tau=12.9$ fs (d). The temporal field strength is also indicated (grey curve). Yellow background indicates time periods in which the field is resonant to and in phase with the imaginary part of the coherence of the $5^1\Sigma_g^+$ state (c) or $4^1\Sigma_g^+$ state (d).

ulation transfer from the $A^1\Sigma_u^+$ state to either of the final states $4^1\Sigma_g^+$ and $5^1\Sigma_g^+$, the respective rates of change according to Eq. (9.5) are presented in the upper panel of Fig. 9.4. From part a), it becomes evident that for the pulse with $\tau=12.0$ fs, although both final states exchange almost equal amounts of population with the intermediate state, only for the $5^1\Sigma_g^+$ state this exchange is always positive, whereas for the $4^1\Sigma_g^+$ state exchange occurs in both directions, thus minimizing the net population transfer. By contrast, for the case of $\tau=12.9$ fs, the population exchange with the $5^1\Sigma_g^+$ state is much more pronounced than that with the $4^1\Sigma_g^+$ state, which in this case also reflects the higher transition dipole moment (cf. Fig. 9.1b)). The main reason for this distinctly different behaviour becomes clear by inspection of the lower panel of Fig. 9.4, in which the imaginary parts of the coherences between the intermediate and final states are shown together with the temporal field amplitude. The product of these two quantities determines to a major extent the population exchange shown in the upper panel of Fig. 9.4, as is manifest from Eq. (9.6). As both the field and the coherences oscillate in time, it is clear that their product assumes the largest possible values if these oscillations are in phase with each other. For the field with $\tau=12.0$ fs, this occurs only with the coherence to the $5^1\Sigma_g^+$ state, as shown in Fig. 9.4c). In contrast, for $\tau=12.9$ fs the oscillations are in phase between

the field and the coherence to the $4^1\Sigma_g^+$ state (cf. Fig. 9.4d)) during the time periods between 20-30 fs and 38-45 fs, in which the population transfer to that state is positive. In both cases, the field is always out of phase with the oscillations of the respective other coherence. Thus, it can be concluded that adjusting the time delay τ between the two laser pulses with a sub-fs precision tunes the field oscillations in such a way that they are exactly in phase with the coherences pertaining either to the pair $A^1\Sigma_u^+/4^1\Sigma_g^+$ or to $A^1\Sigma_u^+/5^1\Sigma_g^+$, while being out of phase to the other, respectively. In this way, population transfer takes place selectively to that state to which phase-matching occurs.

The fact that this subtle mechanism is perfectly reproduced by the FISH simulations (cf. Fig. 9.3) clearly indicates that the FISH method is adequate for simulation and control of coherent electronic state population dynamics in a manifold of several coupled electronic states. Since the FISH method can be straightforwardly coupled with either *ab initio* or semiempirical molecular dynamics, this opens a possibility to control coherent electronic processes as well as to simulate time-resolved spectroscopies in complex systems, even such as biomolecules interacting with the environment, which is far beyond the reach of full quantum dynamics simulations and represents one of the major goals of this thesis.

The ability of the FISH method to correctly describe the coupled electron-nuclear dynamics in a manifold of several electronic states is not restricted to the short pulse limit, in which no significant nuclear motion occurs, but also applies to the case in which the laser pulse duration is longer and the internuclear separation changes considerably. As an illustration, a double pulse sequence of longer time duration has been optimized with the aim to achieve a maximal final population of the $2^1\Pi_g$ state. The resulting pulse as well as the time-dependent electronic state populations for both the quantum dynamical and the FISH simulation are shown in Fig. 9.5. The first subpulse induces population transfer between the ground state and the excited $A^1\Sigma_u^+$, $5^1\Sigma_g^+$ and $2^1\Pi_g$ states until $t \approx 130$ fs. Under the influence of the second pulse at later times only Rabi cycles between the ground state and the $2^1\Pi_g$ state are induced via the $A^1\Sigma_u^+$, while the populations of all other states remain very small. Finally, when the field ceases, a $2^1\Pi_g$ population of ~ 70 % is reached. Comparison between the exact quantum dynamics [Fig. 9.5b)] and FISH [Fig. 9.5c)] clearly shows that, also in the case where the wavepacket moves substantially during the action of the pulse, the FISH electronic state populations agree very well with the full quantum dynamics results.

The time evolution of the internuclear distance R and the corresponding momentum P is illustrated in Fig. 9.6 in terms of probability distributions for both the full quantum dynamics and the FISH dynamics employing the optimized pulse from Fig. 9.5a). For the quantum dynamics, these distributions are obtained from the wavepackets in position

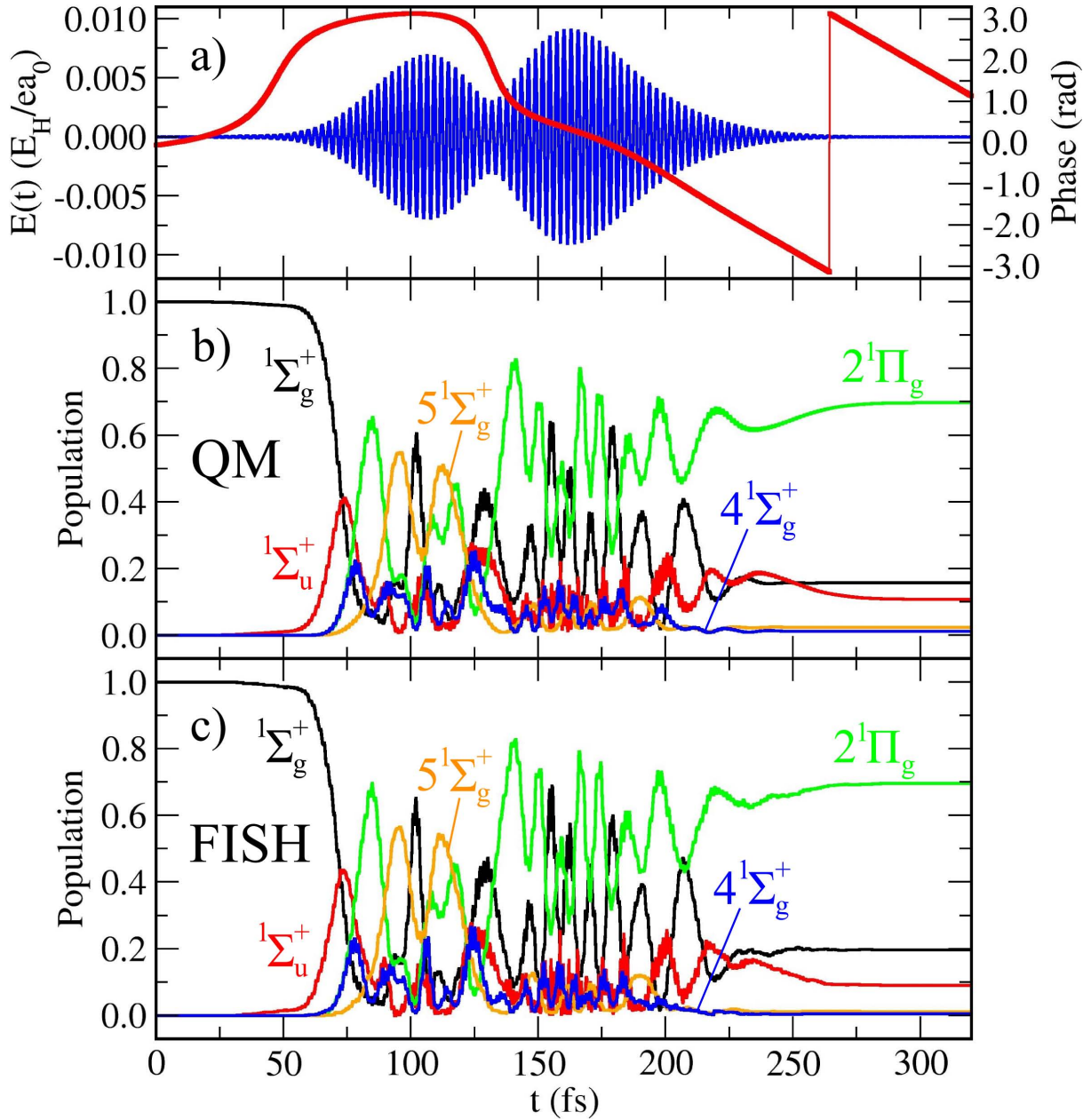


Figure 9.5: a) Temporal field strength (blue) and relative temporal phase (red) of the optimized long double pulse with a time duration of about 150 fs. The phase has been obtained using Eq. (9.3) with $\omega_0 = \frac{1}{2}(\omega_1 + \omega_2)$. b)/c) Time-dependent electronic state populations obtained by quantum dynamics (b) and by employing the FISH method using the ensemble of 300 trajectories (c).

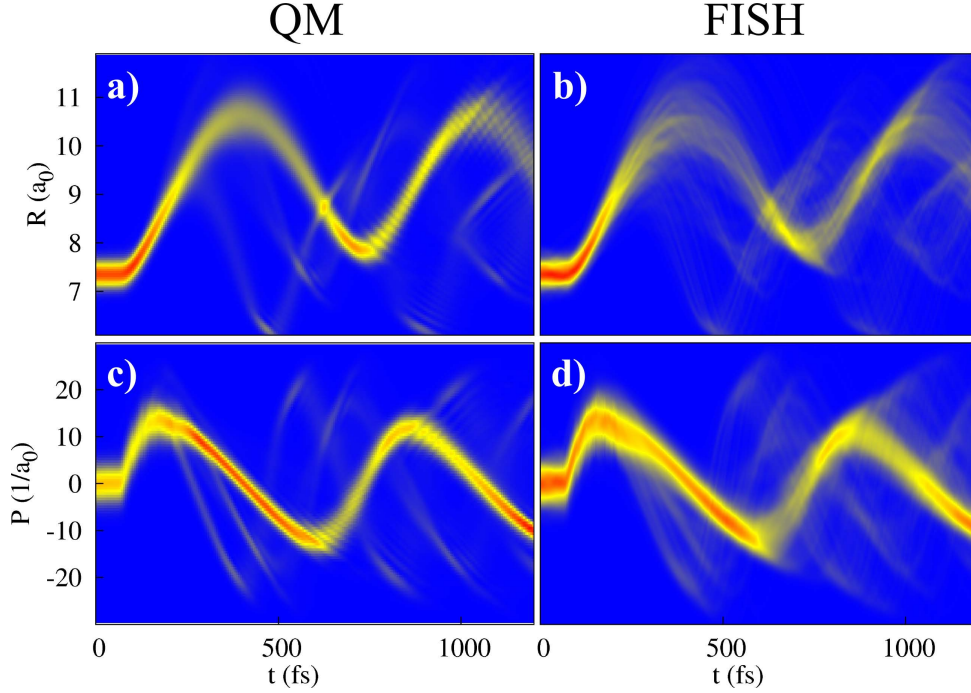


Figure 9.6: Position and momentum probability distributions according to Eqs. (9.7)-(9.10) for the dynamics induced by the optimized double pulse shown in Fig. 9.5a) employing quantum dynamics [a) and c)] as well as the FISH method [b) and d)]. The label a_0 denotes the Bohr radius, $a_0 = 0.529\text{\AA}$. Blue color represents zero probability density, yellow and red denote increasing positive values.

and momentum space as

$$\mathcal{P}_{pos}^{qm}(R) = \sum_j |\chi_j(R)|^2 \quad (9.7)$$

$$\mathcal{P}_{mom}^{qm}(P) = \sum_j |\phi_j(P)|^2 = \sum_j \left| \frac{1}{\sqrt{2\pi\hbar}} \int dR e^{iPR} \chi_j(R) \right|^2, \quad (9.8)$$

where the index j denotes the electronic state. In the case of FISH, semiclassical probability distributions are obtained by convoluting each trajectory with a Gaussian function of width $\Delta R = 0.15 a_0$ in position and $\Delta P = 2.5 a_0^{-1}$ in momentum space and averaging over the whole ensemble:

$$\mathcal{P}_{pos}^{cl}(R) = \frac{1}{N} \sum_k^N e^{-\frac{4\ln 2}{\Delta R^2}(R-R_k)^2} \quad (9.9)$$

$$\mathcal{P}_{mom}^{cl}(P) = \frac{1}{N} \sum_k^N e^{-\frac{4\ln 2}{\Delta P^2}(P-P_k)^2}. \quad (9.10)$$

As can be seen from Fig. 9.6a) the main part of the position wavepacket, starting from the ground state minimum around $7.4 a_0$, steadily moves to larger internuclear distances until

it reaches the outer turning point at $10.1 a_0$ after ~ 350 fs. Since the field has already ceased after 250 fs, the subsequent dynamics is dominated by the wavepacket oscillation in the $2^1\Pi_g$ state with a period of ~ 750 fs. Similarly, also the momentum oscillates with this period [cf. Fig. 9.6c)]. The same behaviour is seen for the FISH simulations [cf. Fig. 9.6b) and d)]. Although the overall agreement is very good, after 700 fs the quantum dynamics simulation exhibits characteristic interference features which are a consequence of nuclear coherence [cf. the fringe-like structures around 800 fs in Fig. 9.6a)]. Such phenomena as a matter of principle cannot be present in FISH simulations due to the purely classical propagation of the nuclear degrees of freedom. However, the effect of the electronic coherence is fully accounted for since the electronic degrees of freedom are propagated quantum mechanically according to Eq. (3.26).

A complementary viewpoint may be obtained by analysing the dynamical processes in terms of the phase space distribution. For this purpose, the quantum mechanical nuclear wavepackets $\chi_j(R)$ have been Wigner transformed [82] as

$$\begin{aligned} W_{qm}(R, P) &= \sum_j W_j(R, P) \\ &= \frac{1}{2\pi\hbar} \sum_j \int dY \chi_j^* \left(R - \frac{Y}{2} \right) \chi_j \left(R + \frac{Y}{2} \right) e^{\frac{i}{\hbar}PY}. \end{aligned} \quad (9.11)$$

As can be seen from Fig. 9.7 the main part of the quantum mechanical Wigner distribution exhibits an elliptical-like motion in the phase space as it is expected for a bound potential. Interestingly, after 300 fs negative contributions appear in the distribution, which can be attributed partly to portions of the wavepacket moving in other states than the mainly populated $2^1\Pi_g$, and partly to quantum mechanical nuclear interferences. The semiclassical FISH phase space density also shown in Fig. 9.7 is obtained by folding the individual trajectories with Gaussian phase space functions of width $\Delta R = 0.15 a_0$ for the position and $\Delta P = 2.5 a_0^{-1}$ for the momentum variable as

$$W_{cl}(R, P) = \frac{1}{4N\pi^2\sqrt{\sigma_R\sigma_P}} \sum_k^N e^{-\frac{4\ln 2}{\Delta R^2}(R-R_k)^2} e^{-\frac{4\ln 2}{\Delta P^2}(P-P_k)^2} \quad (9.12)$$

and evolves in time very similarly to the full quantum mechanical Wigner distribution. In particular, the maxima of the phase space density evolve essentially identically in the quantum and FISH simulations, whereas the width of the classical distribution becomes slightly larger for later times of the dynamics. Regarding the negative features of the quantum mechanical Wigner function, those belonging to wavepacket motion in less populated electronic states appear also in the semiclassical distribution, but with a positive sign (see e.g. Fig. 9.7 in the snapshot at 1050 fs the narrow feature at $R \approx 8.5 a_0$ and P

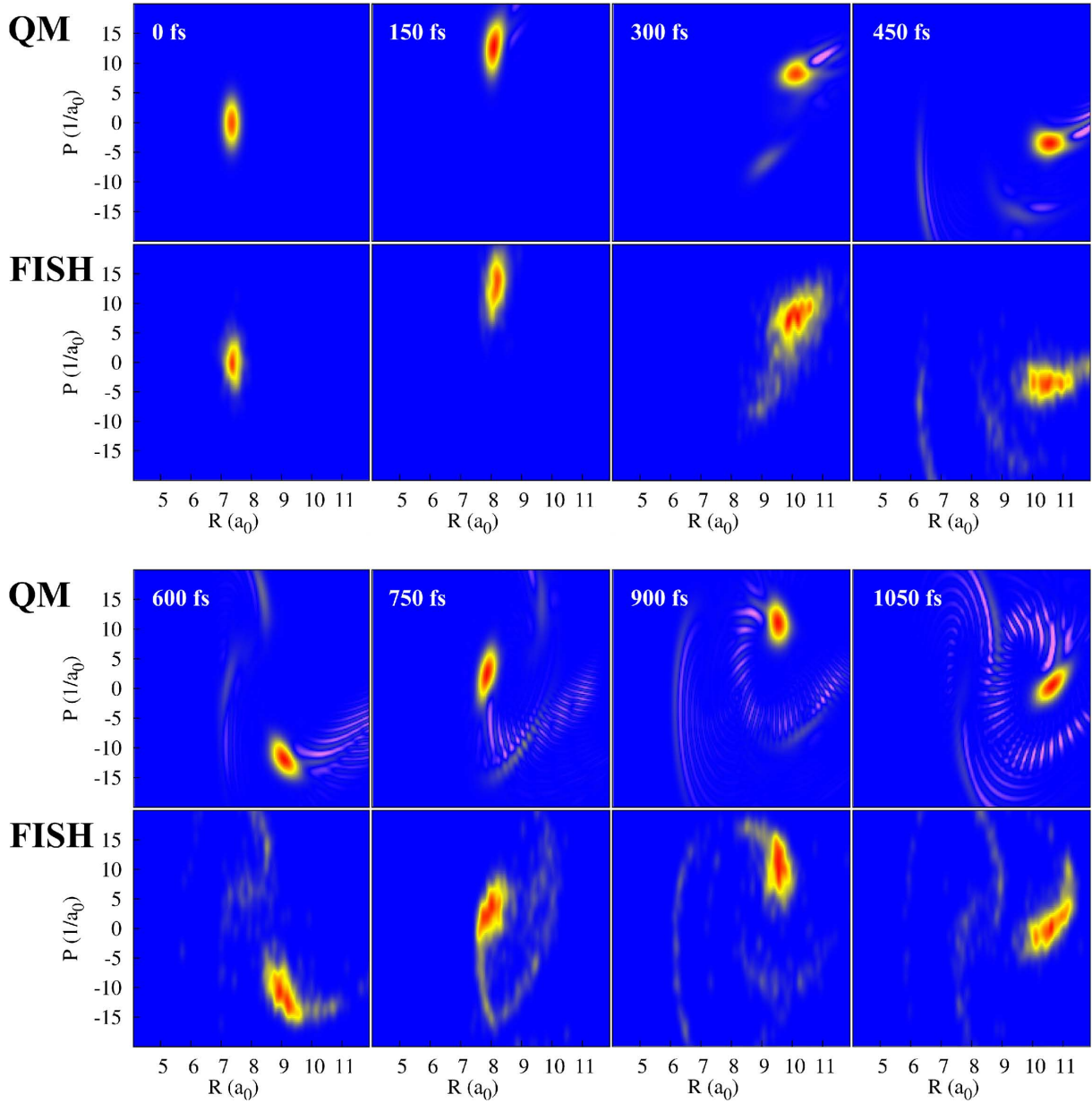


Figure 9.7: Quantum mechanical Wigner distribution function W_{qm} and classical phase space distribution W_{cl} obtained from FISH simulations for selected timesteps of the dynamics driven by the optimized double pulse from Fig. 9.5a). Violet areas correspond to negative values of the distribution, blue to zero, yellow and red to increasing positive values.

between 5 and 15 a_0^{-1}), whereas those parts corresponding to interferences are not present (e.g. for 1050 fs the periodic feature above the main part of the wavepacket, for R between 9 and 11 a_0 and P between 4 and 13 a_0^{-1}), since they are not described within the mixed quantum-classical FISH simulations as discussed above.

From the above discussed results, it becomes evident that the FISH method very accurately reproduces both the electronic and the nuclear quantum dynamics. For the present example, this is also true for the coherences between the electronic states, which are essentially identical in the FISH and quantum simulations, as shown in Appendix C, Fig. C.1. Consequently, in the following the electronic coherences obtained in the frame of FISH will be applied to gain further insight into the mechanism underlying the control. Similar to the case of short pulses discussed before, the resonant in-phase oscillations of the field amplitude and the imaginary parts of the coherences between the coupled states are of crucial importance for the selective excitation process. Therefore, in Fig. 9.8 these quantities are depicted for all pairs of electronic states coupled by the optimized field for the time period up to 150 fs. For comparison, also the populations of the respective target states are shown, and the parameters of the optimized laser pulse are given in Table 9.1.

Parameter	Value
E_1	$4.713 \cdot 10^{-3} E_H / ea_0$
ω_1	1.521 eV
Δt_1	73.54 fs
τ_1	120.8 fs
E_2	$8.390 \cdot 10^{-3} E_H / ea_0$
ω_2	1.473 eV
Δt_2	86.48 fs
τ_2	151.6 fs

Table 9.1: Optimized pulse parameters for maximizing the population of the $2^1\Pi_g$ state [cf. Eq. (9.2)].

From part a) of Fig. 9.8, it is visible that at the very beginning of the pulse phase-matching occurs between the field oscillation and the imaginary part of the coherence between the ground state and the intermediate $A^1\Sigma_u^+$ state, initiating population transfer from the ground state. Later on, the pulse is, during different time periods, resonantly in phase to the imaginary part of the coherence between the intermediate state $A^1\Sigma_u^+$ and either of the three possible final states $4^1\Sigma_g^+$, $5^1\Sigma_g^+$ or $2^1\Pi_g$. However, most frequently this phase-matching occurs to the $2^1\Pi_g$ state, which consequently already after 140 fs assumes the highest population (cf. Fig. 9.8b)). During the remaining part of the pulse (not shown completely), both the resonance and phase-matching conditions are less well fulfilled for all states. This is mainly due to the gradual changes of the energy gaps between the states resulting from the nuclear motion. Specifically, this involves a decrease in the

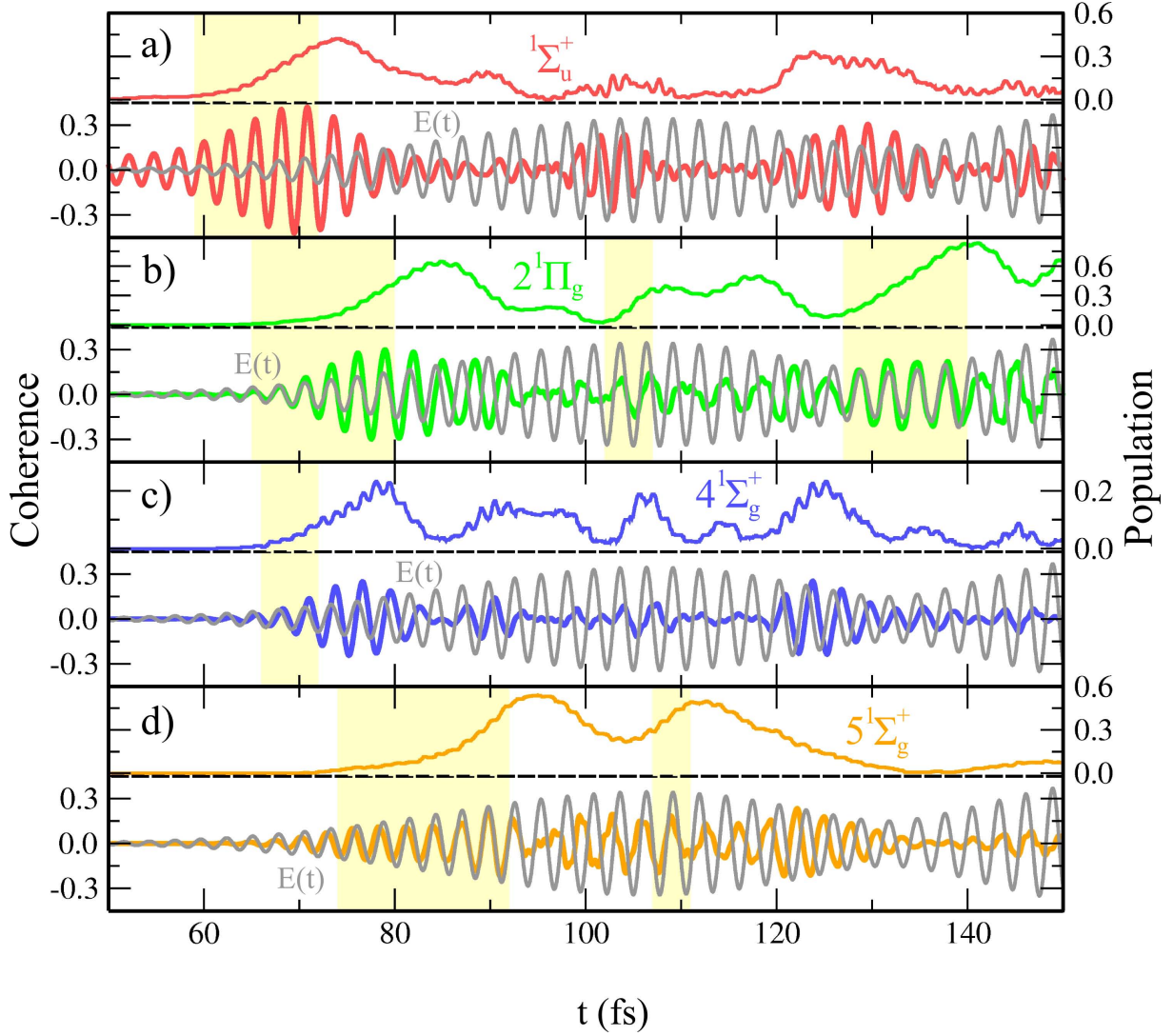


Figure 9.8: Time evolution of FISH electronic state populations and imaginary parts of coherences compared to the laser field oscillation. Coloured lines in the upper panels of a), b), c), d) represent the FISH populations, while in the respective lower panels the imaginary parts of the ensemble-averaged coherences, $\text{Im} \bar{\rho}_{ij}$, are shown. The grey lines indicate the field strength $E(t)$. The following cases are shown: (a) Population of $A^1\Sigma_u^+$, coherence between $A^1\Sigma_u^+$ and $X^1\Sigma_g^+$, (b) population of $2^1\Pi_g$, coherence between $2^1\Pi_g$ and $A^1\Sigma_u^+$, (c) population of $4^1\Sigma_g^+$, coherence between $4^1\Sigma_g^+$ and $A^1\Sigma_u^+$, (d) population of $5^1\Sigma_g^+$, coherence between $5^1\Sigma_g^+$ and $A^1\Sigma_u^+$. Yellow background indicates time periods in which the field is in phase with the imaginary part of the shown coherences.

gap between the $2^1\Pi_g$ and the $A^1\Sigma_u^+$ states, which is partially compensated for by the optimal laser field exhibiting a likewise lowered frequency of the second subpulse (cf. Table 9.1). Consequently, the detuning of the field from the resonance to this gap never exceeds 0.1 eV, and eventually approaches zero towards the end of the optimal pulse. Conversely, for the $4^1\Sigma_g^+$ and $5^1\Sigma_g^+$ states, the field is increasingly detuned by up to 0.2 and 0.3 eV from the resonance for $t > 150$ fs. In addition, the second subpulse accounts for the systematically smaller transition dipole moments for the $2^1\Pi_g - A^1\Sigma_u^+$ transition as compared to the transition from the ground to the $A^1\Sigma_u^+$ state by exhibiting a higher intensity than the first one (cf. Table 9.1). Altogether, these findings show that due to (i) the interplay of resonant in-phase oscillation of the optimized laser field and the imaginary parts of the coherences between selected pairs of electronic states and (ii) the adaptation of the pulse parameters to time-dependent changes of coupling strengths and resonance conditions, the optimal field is tailored such as to most effectively drive the electronic state population to the $2^1\Pi_g$ state. This detailed picture of the selective excitation processes illustrates impressively the use of simulations to obtain profound insights into the mechanisms underlying optimal control.

9.4 Conclusions

It has been demonstrated by comparison with exact quantum dynamics simulations that the FISH method can accurately describe coherently driven electron-nuclear dynamics in a system with several coupled electronic states. This can be utilized to coherently control a sequential two-photon electronic excitation and to achieve a selective population of the desired electronic state. Moreover, using an optimized laser pulse with a duration on the time scale of the nuclear motion, it could be demonstrated that the FISH method is also able to reproduce the coupled electron-nuclear dynamics in this case, even in spite of the absence of minor nuclear coherence effects. For both types of laser fields, the mechanism of selective state population could be explained by subtle resonance and phase-matching conditions between the driving field and electronic coherences between the coupled states. These findings provide a basis for using the FISH method for the control of photochemistry and photophysics in more complex molecular systems, which is possible in connection with molecular dynamics "on the fly". In the following Chapters 10 and 11, this will be illustrated on two selected examples for control in biomolecular systems interacting with their environment.

10 Coherent control in the condensed phase: Laser pulse trains for manipulating the photodynamics of solvated adenine

10.1 Introduction

Optimal control based on iterative pulse optimization represents, as discussed in Chapter 8, an efficient means to experimentally generate laser fields capable to steer various processes in molecular systems. It is commonly based on the optimization of a large number of individual parameters, obtained e.g. by decomposing the electric field into discrete spectral components and varying the associated amplitude or phase values. The resulting pulse forms are usually quite complex and mostly not interpretable in a simple way. Therefore, such experimental data are often insufficient to provide the mechanism underlying the control, and strategies to gain a deeper insight have to be developed. Besides the direct application of experimental laser fields in theoretical simulations, which will be illustrated in the subsequent Chapter 11, another possible strategy consists in the reduction of complexity, e.g. by utilizing simple analytically parameterized pulse shapes, as discussed in Chapter 8. In particular, parameterization of the spectral phase by a sine function leads to laser pulse trains with specific temporal and spectral patterns. Such pulse trains have been employed in the present chapter for the manipulation of excited state dynamics and nonradiative decay in solvated adenine.

The presence of nonradiative internal conversion processes that compete with the light-induced dynamics poses a great challenge for the application of optimal control since these processes rapidly bring the system back to the lowest excited or even to the ground electronic state. In this context, the question can be raised if also this type of processes can be manipulated by adequately shaped laser pulses. In this way, nonradiative lifetimes could be enhanced in order to enable selective spectroscopic studies of excited states or even to invoke fluorescence of otherwise non-fluorescent molecules. This issue has been addressed in several contributions based on a fully quantum mechanical description of the studied molecular systems. On the example of the pyrazine molecule, in which without control the internal conversion between the two lowest excited states S_2 and S_1 takes place on the timescale of 20 fs [127,253], it has been shown that selective population of specific vibronic states in the S_2 - S_1 manifold can result in a significant slowdown of the internal conversion [386]. Moreover, based on the interference properties of different vibronic states, an elongation of the S_2 lifetime can even be achieved if no isolated long-living states exist in the chosen energy range, provided that these states fulfill certain overlap criteria with the exact eigenstates of the system [387,388]. However, such simulations rely on a quan-

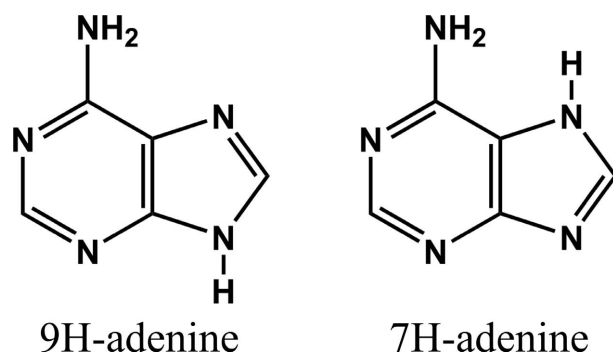


Figure 10.1: Chemical formulae of the 9H and 7H tautomers of adenine, differing by the position of the H atom on nitrogen in the five-membered ring.

tum mechanical treatment of the nuclear motion, and therefore simplifying assumptions such as selecting a limited number of normal modes or an approximate treatment of the vibronic quantum states have been adopted in order to keep the computational effort reasonable. Consequently, this type of control is not applicable in the framework of a mixed quantum-classical simulation which is mandatory to treat complex molecular systems accounting for all nuclear degrees of freedom. Yet it is exactly complex systems such as e.g. DNA and RNA nucleobases that are prominent examples for very fast internal conversion and that already in isolated form are too large for full quantum dynamics simulations, let alone in combination with an environment such as a nucleic acid strand or a solvent. Therefore, in the present chapter the possibilities of manipulating the excited state lifetimes will be investigated employing the combination of mixed quantum-classical FISH dynamics with the quantum mechanical-molecular mechanical (QM/MM) approach. The prototype system chosen for this purpose is the nucleobase adenine in water environment. Nucleic acids and their constituent nucleobases are indeed characterized by very short excited state lifetimes upon ultraviolet irradiation both in aqueous environment [389–392] and in the gas phase [393]. From the standpoint of biological evolution, this can be traced back to the need for stability of the genetic information encoded within the nucleic acids, which would be destroyed if the nucleobases underwent photochemical reactions after being exposed to sunlight. Therefore, in the early stages of molecular evolution only those chemical species might have survived which could sufficiently fast dissipate the gained energy before any harmful reactions could take place.

The mechanism of the ultrafast excited state decay of adenine has been the subject of numerous experimental and theoretical studies. In solution, the two tautomeric forms 7H- and 9H-adenine, differing in the position of an H atom, are present (cf. Fig. 10.1), of which the 9H-form is the dominant one [394]. Time-resolved photoelectron spectroscopy studies have shown that, in the gas phase, the 9H-tautomer exhibits an excited state lifetime of about 750 fs after resonant excitation to the lowest-lying bright $\pi\pi^*$ states at 267 nm [256,257]. However, the lifetimes are found to be strongly wavelength-dependent [258],

reaching up to 9 ps for excitation at 277 nm [395]. Theoretical studies based on nonadiabatic molecular dynamics using both semiempirical [125] and ab initio quantum chemical methods [126] have revealed a two-step relaxation mechanism involving several conical intersections between the electronic states. The initially excited bright state relaxes very rapidly to the lowest excited state with a time constant of ~ 20 fs, followed by the relaxation to the ground state with a time constant of ~ 550 fs.

In aqueous solution, the time scales for nonradiative relaxation are considerably shorter. Experimental investigations have obtained lifetimes for the dominant 9H-tautomer of 180 fs by transient absorption [394], about 550 fs by time-resolved fluorescence [396] and <300 fs by photon echo experiments [397]. Theoretical nonadiabatic dynamics simulations employing the semiempirical OM2-multireference configuration interaction method combined with the QM/MM approach have yielded a lifetime of 410 fs [136], whereas in the framework of the time-dependent density functional tight-binding method (TDDFTB),¹ explicitly including the water molecules in the first solvation shell, the nonadiabatic relaxation proceeds within less than 200 fs [403].

In the context of such ultrafast nonadiabatic relaxation, the aim of the present chapter is to explore to which extent the excited state lifetimes of adenine can be affected using simple parameterized pulse trains, thus avoiding the need for full closed-loop field optimization. This represents the first step towards the manipulation of the excited state lifetimes of complex systems with the ultimate goal to selectively induce the fluorescence of DNA nucleobases.

The chapter is structured as follows: In Section 10.2, the theoretical approach is outlined by presenting the combination of field-induced surface hopping (FISH) with the QM/MM approach and the procedure for the design of laser pulse trains. Subsequently, the computational details are given in Section 10.3. The results of the nonadiabatic dynamics of solvated adenine driven by laser pulse trains are presented in Section 10.4. Finally, conclusions and outlook are given in Section 10.5. Most of the results presented in this chapter have been published in Ref. [64].

10.2 Theoretical Approach

In order to simulate the laser-driven dynamics of adenine in aqueous solution, the FISH method [55] presented in Chapter 3 has been combined with the QM/MM approach. This allows for a general treatment of laser driven dynamics in complex systems interacting with various types of environments such as solvents, surfaces or proteins. Furthermore,

¹TDDFTB is the tight-binding analog to the TDDFT method. It is based on the density functional tight-binding method, which represents an approximate DFT approach relying on a second-order expansion of the total energy obtained within the Kohn-Sham formulation with respect to charge density fluctuations around a fixed reference density. For a detailed description of this approach cf. Refs. [398–402].

analytically parameterized laser pulse trains are constructed and applied for the manipulation of excited state dynamics of adenine in water.

10.2.1 Combination of FISH with the QM/MM approach

Combining the FISH method with QM/MM represents a general approach to nonadiabatic dynamics simulations under direct influence of laser fields for molecular systems interacting with their environment. This extends previous work on field-free QM/MM nonadiabatic dynamics in the framework of time-dependent density functional theory [141]. In the present approach, the laser field is now explicitly included, thus allowing for the use of arbitrarily complex pulse forms suitable for manipulation and control of excited state dynamics. The basic idea of the QM/MM of separating the system into a quantum mechanically described (QM) part and an environment which is treated by molecular mechanics (MM part), has been outlined in Sec. 2.2.3. In principle, the FISH method can be combined with both the mechanical and electrostatic embedding schemes presented this Section. In the present study, the more efficient mechanical embedding scheme was employed for solvated adenine. This choice was motivated by the fact that the electrostatic embedding is significantly more time consuming in the context of FISH simulations in which a large number of control pulses is used to drive the dynamics of an ensemble of trajectories. Furthermore, the comparison between the mechanical and electrostatic embedding schemes on selected trajectories lead to very similar results, thus revealing only a very small influence of the electrostatic interaction between water and adenine on the excited state dynamics and by that justifying the use of mechanical embedding (cf. also the population dynamics shown in Fig. 10.3 for mechanical and in Appendix D for electrostatic embedding).

The total energy of the combined system in the frame of mechanical embedding was obtained according to Eq. (2.56). The forces needed to perform molecular dynamics "on the fly" are determined from the gradient of Eq. (2.56), and both the nonadiabatic couplings as well as the transition dipole moments were calculated only for the QM part.

10.2.2 Design of laser pulse trains

In order to perform the control of the excited state dynamics, phase shaping by an analytical mask function in the spectral domain has been used. Specifically, the laser field parameterized in the frequency domain as

$$E(\omega) = E_0 \exp \left[-\frac{4 \ln 2}{w_{1/2}^2} (\omega - \omega_0)^2 \right] \exp [i\phi(\omega)], \quad (10.1)$$

with amplitude E_0 , central frequency ω_0 , spectral width $w_{1/2}$ and phase ϕ , has been modulated employing a sinusoidal phase modulation

$$\phi(\omega) = a \sin [\tau(\omega - \omega_0) + c]. \quad (10.2)$$

This procedure provides complex pulse forms in the time domain, the features of which only depend on the choice of the three parameters a , τ , and c . Consequently, the control landscape can be fully sampled without the need for iterative optimization. In the time domain, the laser fields defined by Eq. (10.1) consist of a train of temporally separated subpulses. The phase modulation parameters a , τ , and c determine the intensity variation within the pulse train, the time separation of the subpulses and the sine or cosine character of the modulation function, respectively.

10.3 Computational Procedures

The equilibrated structure of the solvated 9H-adenine, which is the dominant species present in water, has been obtained by the following steps: First, adenine was placed into a cubic water box of 49.2 Å side length, and classical force field molecular dynamics with periodic boundary conditions using the TINKER package [404] was performed over 20 ps at a temperature of 300 K until the system was equilibrated. For adenine, the OPLS-AA force field parameters [405–409] were used, while water was described by the TIP-3P parameters [410]. Subsequently, a water sphere with a radius of 35 Å was cut around the adenine molecule, and the system was further equilibrated by performing a ground state QM/MM dynamics simulation using the mechanical embedding scheme. The QM part consisted of the adenine molecule, for which the semiempirical OM2 method [190,191] was employed. From the QM/MM trajectory obtained in this way, a number of 100 initial conditions was finally generated by sampling at regular time intervals. In order to obtain an almost ideal water sphere, the water droplets of each structure were further truncated to a radius of 20 Å. In this way, adenine was solvated by about 1400 water molecules.

The FISH-QM/MM simulations have then been performed in the manifold of the ground and the three lowest excited states. For this purpose, the OM2 method combined with the GUGA multireference configuration interaction [193,411] was employed in the framework of the MNDO program [412], and all single and double excitations out of the ground-state determinant and of the leading configurations of the three excited states (cf. Fig. 10.2b)) were taken into account within an active space of the six highest occupied and four lowest virtual orbitals. The nuclear trajectories were propagated by numerical solution of Newton's equations of motion using the velocity Verlet algorithm [180] with a time step of 0.25 fs. The total propagation time depended on the applied laser field and was chosen to be ~ 1000 fs longer than the duration of the field. Along each trajectory

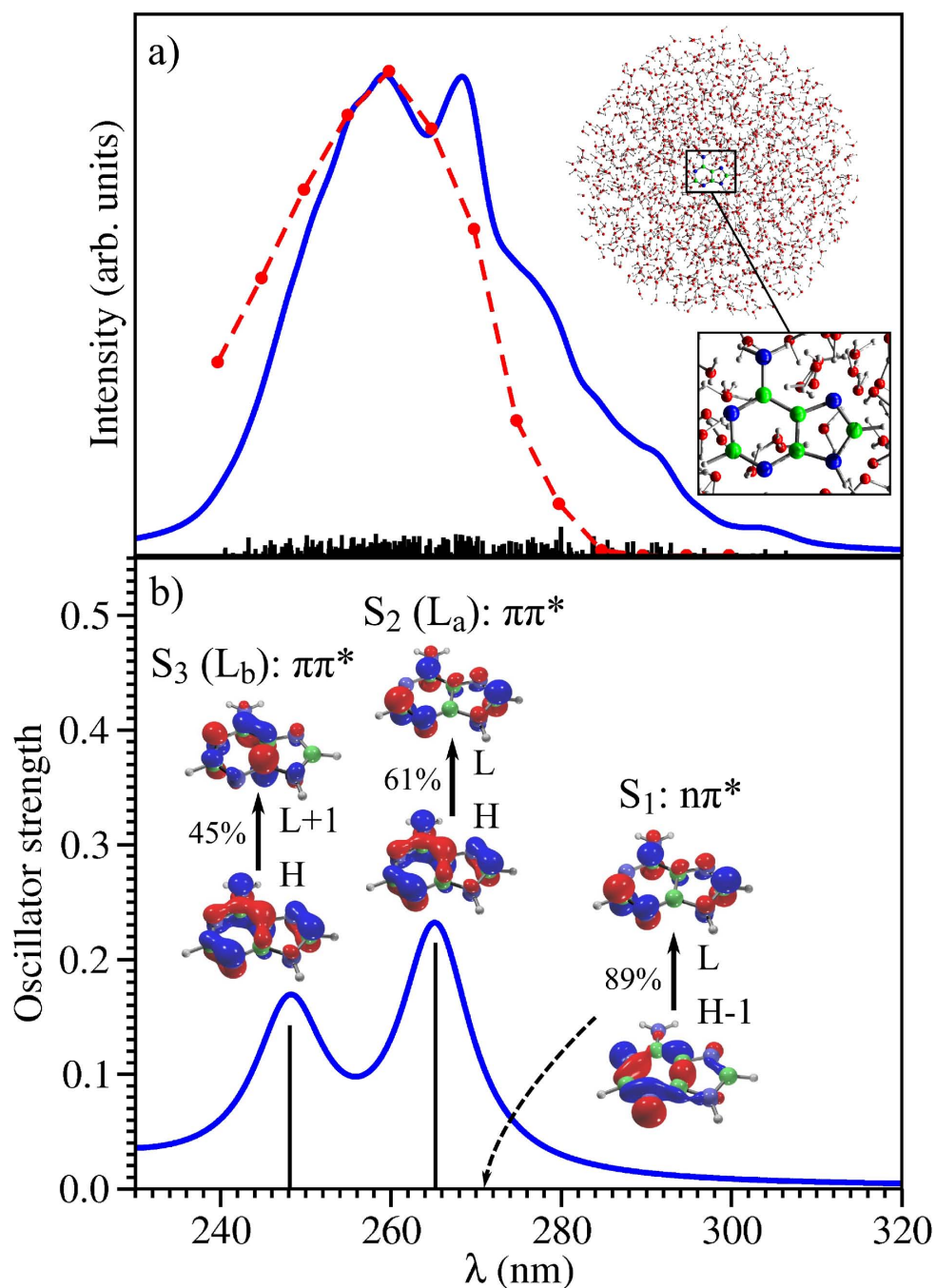


Figure 10.2: a) Theoretical electronic absorption spectrum of adenine in a water sphere for the ensemble of 100 initial conditions. The individual transitions (black sticks) have been broadened by a Lorentzian width of 5 nm (blue curve). For comparison, the experimental absorption spectrum of Kohler et al. [394] is also shown (red points). b) Theoretical electronic absorption spectrum for the equilibrium structure of isolated adenine. The dominant orbital excitations contributing to the three lowest-lying transitions are illustrated, with H indicating the highest occupied and L the lowest unoccupied molecular orbital.

$\mathbf{R}(t)$, the time-dependent Schrödinger equation (3.26) including the nonadiabatic coupling and the coupling to the laser field was integrated using the Runge-Kutta procedure with a time step of $2.5 \cdot 10^{-5}$ fs. The electronic state coefficients obtained in this way were used to calculate the hopping probabilities according to Eq. (3.32). If the average absolute value of the field within a nuclear time step was lower than 10^{-6} a.u., the nuclear velocities were rescaled in the direction of the nonadiabatic coupling vector in order to assure energy conservation. For higher field strengths, energy exchange with the field was assumed and thus no velocity rescaling was applied.

The laser fields employed in the simulations were parameterized in the frequency domain using a sinusoidal phase modulation as described in Section 10.2.2. Specifically, 1024 discrete frequency values in the range between 4.33 eV (287 nm) and 4.98 eV (249 nm) around a central frequency of 4.66 eV (266 nm) have been employed. The Gaussian width $w_{1/2}$ of the spectral amplitude was 0.19 eV. For the phase modulation parameters the values $a = \frac{\pi}{2}, \pi, \frac{3}{2}\pi, 2\pi$, $\tau = 20$ fs, 40 fs, 60 fs, 80 fs, 100 fs and $c = 0, \frac{\pi}{2}, \pi, \frac{3}{2}\pi$ have been used, giving rise to 80 different pulse trains in total. The pulses in the time domain are obtained by discrete Fourier transformation as $E(t) = \sum_n E(\omega_n) \exp(i\omega_n t)$. The unshaped pulse has a duration of ≈ 50 fs (full width at half maximum of 20 fs), whereas the durations of the pulse trains vary between 150 and 2000 fs depending on the pulse parameters. The maximum field amplitudes of the pulses correspond to intensities of $\approx 7 \cdot 10^{12} \frac{\text{W}}{\text{cm}^2}$.

10.4 Results and Discussion

In this section the excited state dynamics simulations of solvated adenine under the influence of laser pulse trains, obtained by the combined FISH-QM/MM approach outlined in Section 10.3, will be presented. It will be demonstrated that pulse trains can be designed which modify the course of the excited state dynamics and lead to a significantly extended residence time of adenine in the electronically excited states.

The calculated electronic absorption spectrum of adenine embedded in a water sphere of 20 Å radius is shown in Fig. 10.2a) together with the experimental spectrum of Kohler et al. [394]. The maximal absorption is located between 250 and 280 nm for both the theoretical and the experimental spectrum, with a slight red shift of the theoretical spectrum. For a more detailed insight into the electronic structure, in addition the calculated absorption spectrum of isolated adenine for the optimized ground state structure is shown in Fig. 10.2b). As discussed in the literature, the electronic structure of adenine in the low wavelength range is characterized by two bright states of $\pi\pi^*$ character (L_a and L_b) as well as by a low-lying dark $n\pi^*$ state [413–415], which are also indicated in Fig. 10.2b). The exact ordering of these states has been found to strongly depend on the used quantum

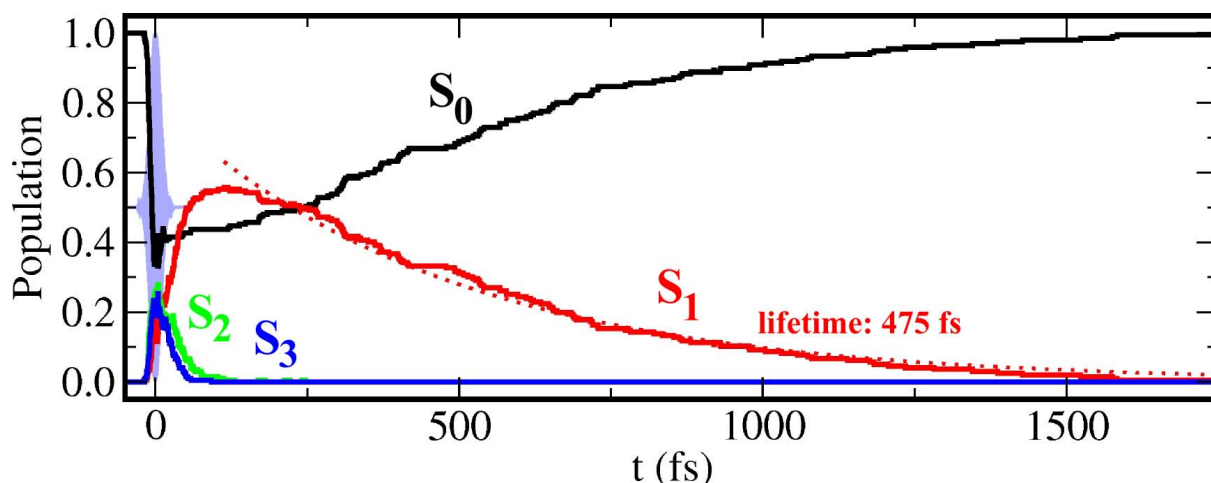


Figure 10.3: Population dynamics of solvated adenine induced by the fourier-limited laser pulse at 266 nm (indicated in light blue), showing almost complete return to the ground state after 1000 fs.

chemical method as well as on the actual molecular structure for which the calculation is performed [125, 416–418]. This means that, within an ensemble of initial conditions necessary to simulate a temperature-broadened spectrum, an unambiguous state ordering cannot be given and is of minor importance for the properties of the system.

Irradiation of solvated adenine by an ultrashort resonant laser pulse of 266 nm wavelength therefore leads to simultaneous excitation of the three lowest excited states, as shown in Fig. 10.3. This is followed by ultrafast population transfer to the S_1 state within ~ 50 fs, leading to almost 60 % population of this state. Subsequently, the decay to the ground state takes place with a time constant of 475 fs, which is comparable to the theoretical and experimental results from the literature discussed in the introductory chapter 10.1.

In order to investigate the influence of the laser pulse shape on the dynamical processes in the excited states, a set of pulse trains has been constructed based on the Fourier-limited Gaussian pulse in the frequency domain. For this purpose, the phase modulation by a sine function (cf. Eq. (10.2)) was applied and, in total, 80 pulse trains have been generated by employing three parameters (a , τ , and c) with the values given in Section 10.3. These pulse trains differ mainly in the time delay as well as in the intensity pattern of their subpulses. For illustration, the time profiles of the pulse trains with parameter $c = 0$ are shown in Fig. 10.4. The whole set of 80 pulses has been subsequently employed in QM/MM FISH dynamics with an ensemble of 50 trajectories, and the ability of the pulses to efficiently excite the adenine and to keep population in excited states has been assessed. This allows for the construction of a three-dimensional control landscape as a function of the parameters a , τ , and c . A two-dimensional section for the fixed value $c = 0$ is presented in Fig. 10.5 for two different control targets. First, the maximal S_1 population

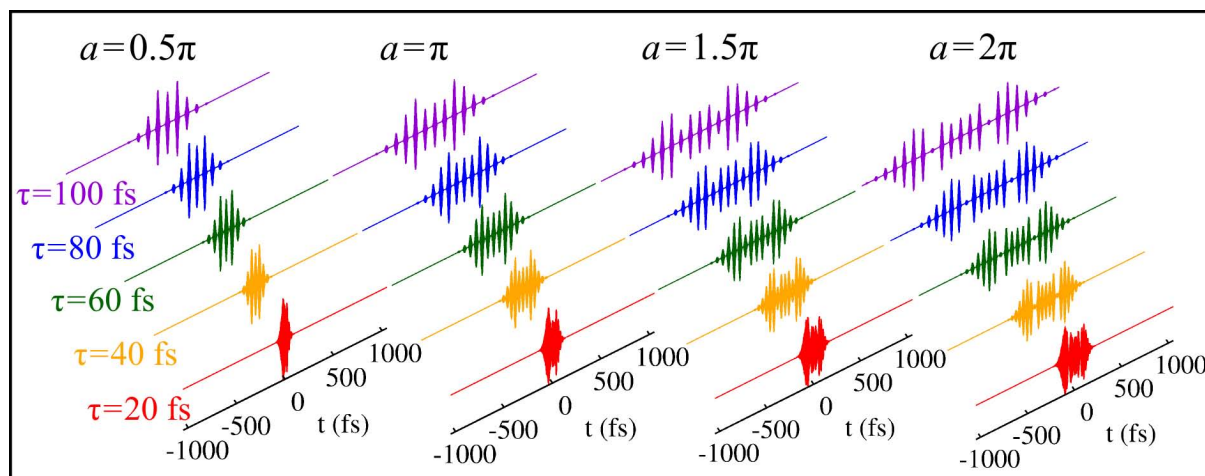


Figure 10.4: Time profile of the pulse trains constructed by sinusoidal phase modulation $\phi(\omega) = a \sin(\tau(\omega - \omega_0))$, employing values for a between 0.5π and 2π and values for τ between 20 and 100 fs.

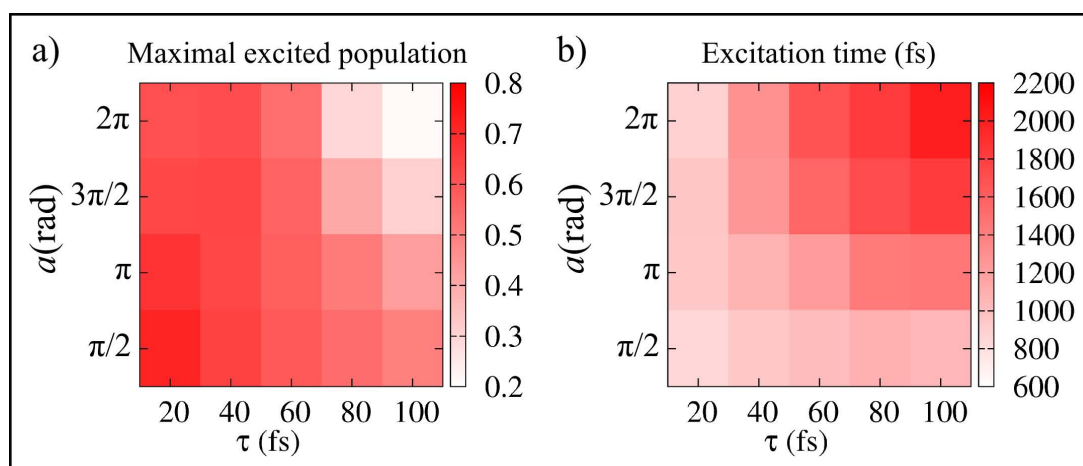


Figure 10.5: Effect of the laser pulses shown in Fig. 10.4 on the excited state dynamics in adenine as function of a and τ . a) Maximal population of the S_1 state after the end of the pulse train. b) Time duration in fs until the S_1 population drops below 30 % after the end of the pulse train. High values are indicated by dark, low values by light grey levels.

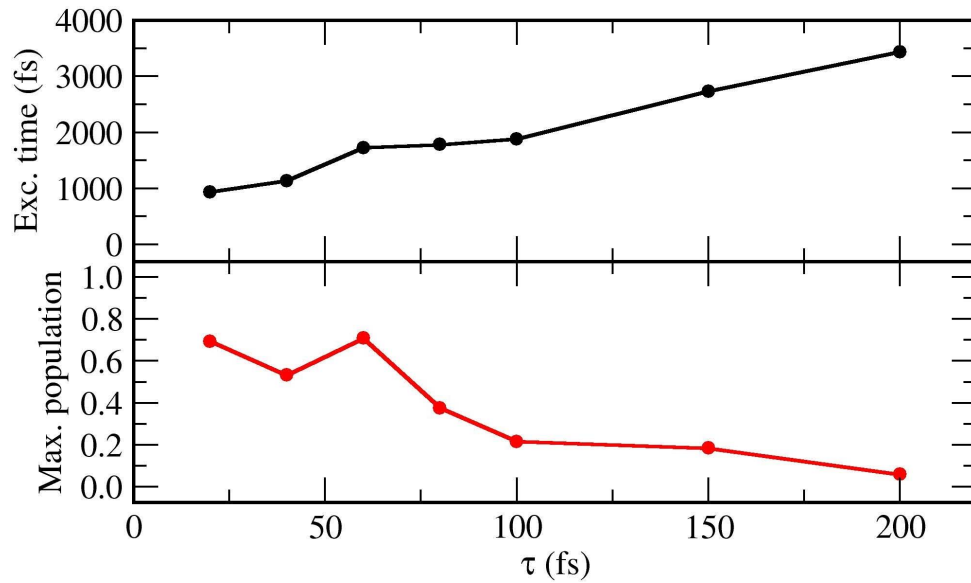


Figure 10.6: Effect of the laser pulses shown in Fig. 10.4 on the excited state dynamics in adenine as function τ for fixed values of $a = 2\pi$ and $c = 0$. Upper panel: Time duration in fs until the S_1 population drops below 30 % after the end of the pulse train. Lower panel: Maximal population of the S_1 state after the end of the pulse train.

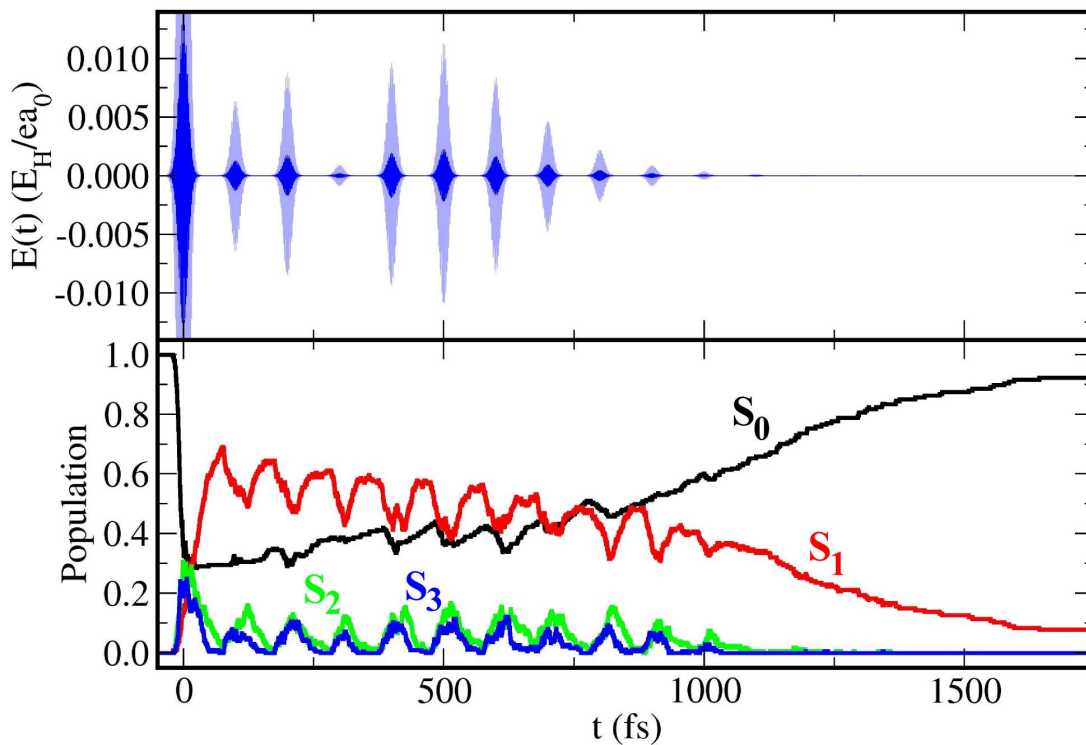


Figure 10.7: Upper panel: Efficient pulse train (blue) obtained by superposition of the unshaped pulse and a pulse train with $a = 2\pi$ and $\tau = 80$ fs. For visual clarity, in the background the same pulse is shown in light blue in fivefold magnification. Lower panel: Population dynamics induced by the laser pulse train which keeps the excited state population above 40 % for 1000 fs.

is shown in Fig. 10.5a), which demonstrates that the largest population transfer to the S_1 state is obtained for small values of a and τ . The associated temporal pulse form is characterized by a short pulse duration of ~ 150 fs and overlapping subpulses (cf. Fig. 10.4), thus only small differences to an unshaped pulse are present. Secondly, in order to reveal the influence of the pulse parameters on the time interval during which a significant population remains in the excited states, in Fig. 10.5b) the time range in which the S_1 population is kept above a threshold of 30 % is presented. The longest time intervals are obtained for high values both of a and τ . In the corresponding pulse trains, the total pulse duration amounts up to 2 ps and the subpulses are well separated. Moreover, the total pulse intensity is distributed over a larger time interval, thus leading to lower field amplitudes for the individual subpulses (cf. Fig. 10.4). Interestingly, these pulses are just the least efficient ones for achieving the first control target of inducing a high population of the S_1 state. In addition, for the value $a = 2\pi$, the excitation times and maximal populations in the extended range of τ values up to 200 fs are shown in Fig. 10.6, indicating that for the largest values of τ the nonradiative relaxation starts to outweigh the field excitation due to the large time intervals between the subpulses. Besides these findings for pulses with $c = 0$, very similar results are obtained for the other values of c .

Based on these insights, a laser pulse has been constructed with the aim to simultaneously achieve a high initial excitation efficiency and to keep the population in excited states for a sufficient time. For this purpose the original unshaped pulse was superposed by the pulse train obtained with the parameter values $a = 2\pi$, $\tau = 80$ fs and $c = 0$. The temporal structure of the resulting pulse beginning at $t=0$ fs is shown in Fig. 10.7 (upper panel). The population dynamics induced by this pulse, shown in the lower panel of Fig. 10.7, is distinctly different to that due to the unshaped pulse (cf. Fig. 10.3). Initial excitation to all three excited states by the first intense subpulse is followed by ultrafast decay of the S_2 and S_3 population to S_1 within 50 fs.

However, before further relaxation to the ground state can occur, the next subpulse leads to re-excitation from S_1 to S_2 and S_3 . In this way, the population is cycled between the S_1 and higher S_2 and S_3 states by a series of pump excitations followed by nonadiabatic decay to the S_1 state. These pump excitations induced by the substructures of the pulse train serve to prevent the nonadiabatic relaxation from the S_1 state to the ground state, which would otherwise take place without the control pulse. In this way the population is kept in the excited states for about 1000 fs, which is about twice as long as the intrinsic lifetime of 475 fs. The dynamical processes under the influence of the pulse train are further illustrated by the analysis of a selected trajectory as shown in Fig. 10.8. As indicated by the background colours in the upper panel of this Figure, the dynamics takes place mostly in the excited state manifold, between the states of which several hops occur.

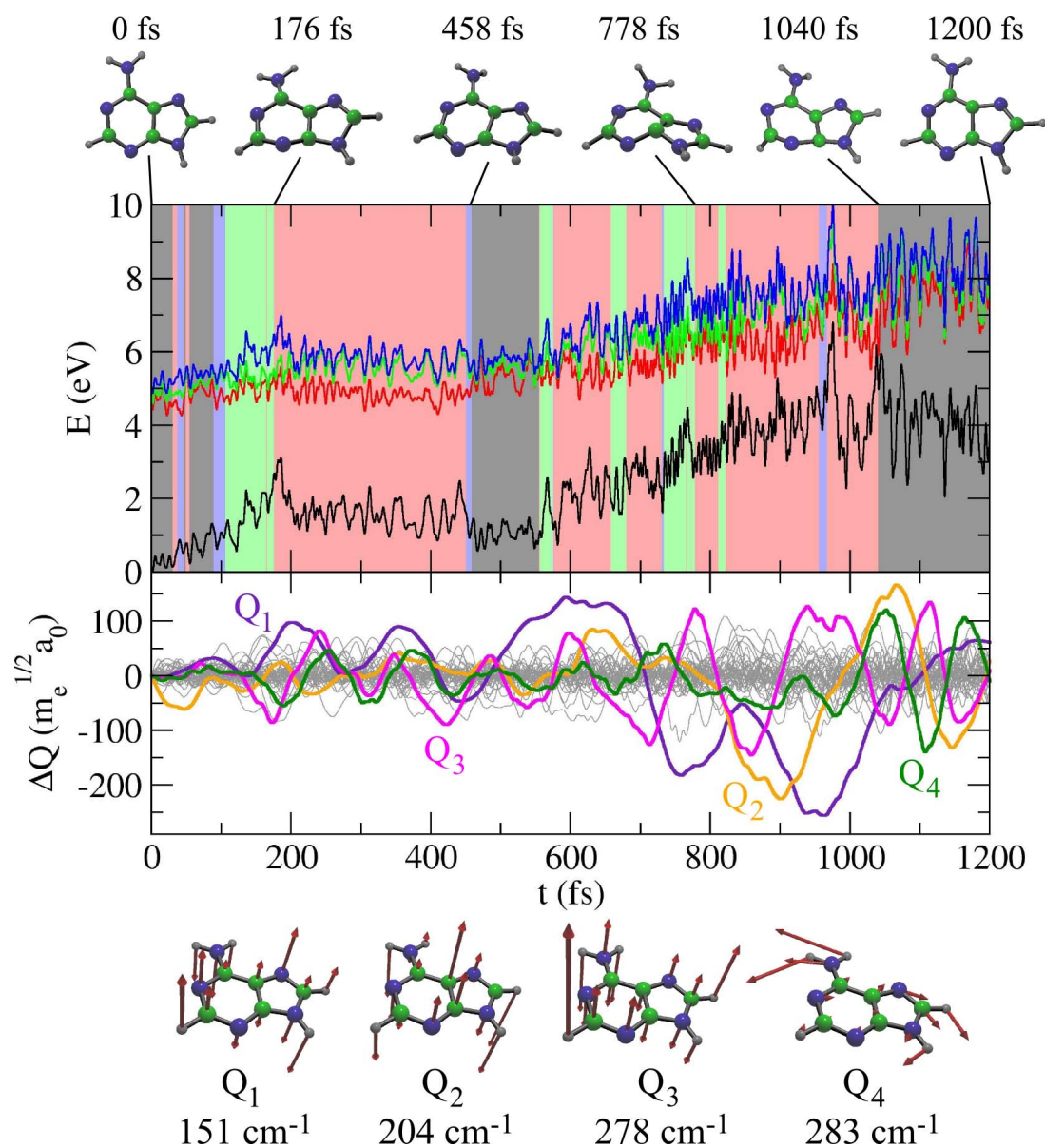


Figure 10.8: Analysis of a selected trajectory of adenine in water driven by the pulse train shown in Fig. 10.7a). Upper panel: Energies of the electronic states S_0 (black), S_1 (red), S_2 (green), and S_3 (blue) along the trajectory. The current state as a function of time is indicated by the background colour. Snapshots of the structures of adenine at given time steps are shown above. Lower panel: Normal mode displacements along the trajectory. The displacement vectors of the selected modes showing the largest change during the dynamics are visualized below.

The structural snapshots at selected time steps make clear that the electronic excitation mainly results in motion lifting the planarity of the ring system, and also partly in out-of-plane motion of the amino group as well as of the hydrogen at a carbon atom of the six-membered ring, whereby structures in the vicinity of two conical intersections are reached (see below). The final return to the ground state occurs at 1040 fs, at a configuration in which the energy gap to the ground state only amounts to 0.89 eV. Subsequently, the planarity is restored, as can be seen from the snapshot at 1200 fs. Analysing the motion in terms of normal mode displacements shown in the lower panel of Fig. 10.8 evidences the dominant contribution of low-energy vibrations of the ring system to the nuclear dynamics. This finding is characteristic for all trajectories of the ensemble. Moreover, the nuclear dynamics induced by the unshaped pulse (cf. Fig. 10.3) is also comparable, although, as discussed above, the electronic dynamics is entirely different.

From the population dynamics shown in Fig. 10.7 it becomes clear that after the pulse train has ceased, nonadiabatic relaxation to the ground state occurs within about 500 fs, which is similar to the relaxation induced by an unshaped pulse (cf. Fig. 10.3). In most cases the ground state is reached at a very small S_1 - S_0 energy gap, indicating that the transition happens in the vicinity of a conical intersection (CI). The characterization of CIs in ring systems can be accomplished by classifying their structure according to the Cremer Pople parameters [419], which quantify the ring puckering for a given CI. In the case of adenine, there are two doubly degenerate CIs relevant for the nonadiabatic dynamics [125,126], which are classified as ${}^1S_6/{}^6S_1$ and ${}^2E/E_2$ in the notation introduced by Boeyens [420] and are depicted in the right part of Fig. 10.9. The ${}^1S_6/{}^6S_1$ CI has the lowest energy (3.9 eV above the ground state minimum), whereas the ${}^2E/E_2$ CI lies about 0.2 eV higher.

As recently found by Thiel et al., within the OM2 approach the nonadiabatic relaxation of adenine to the ground state proceeds mostly in the vicinity of the ${}^1S_6/{}^6S_1$ CI [136] both in the gas phase and in water. In order to investigate how formed pulse trains influence the dynamical pathways taken in the excited electronic states, the Cremer Pople parameters for the final hops from S_1 to S_0 have been determined for the trajectories driven by the pulse train of Fig. 10.7 and are shown in Fig. 10.9. Evidently, most of the trajectories hop in the vicinity of the ${}^1S_6/{}^6S_1$ CIs, similar to the case of field-free nonadiabatic dynamics, while the contribution of the ${}^2E/E_2$ CI is negligible. The trajectories driven by the unshaped Gaussian pulse (not shown) behave similarly. Thus, the nonradiative relaxation mechanism to the ground state is the same regardless if the excitation is achieved using the unshaped Gaussian pulse or a pulse train. However, the excited state population dynamics while the pulses are acting is fundamentally different.

As discussed above, the dynamics induced by the pulse train is characterized by a sequence of excitations and de-excitations between the S_1 state and the higher-lying S_2

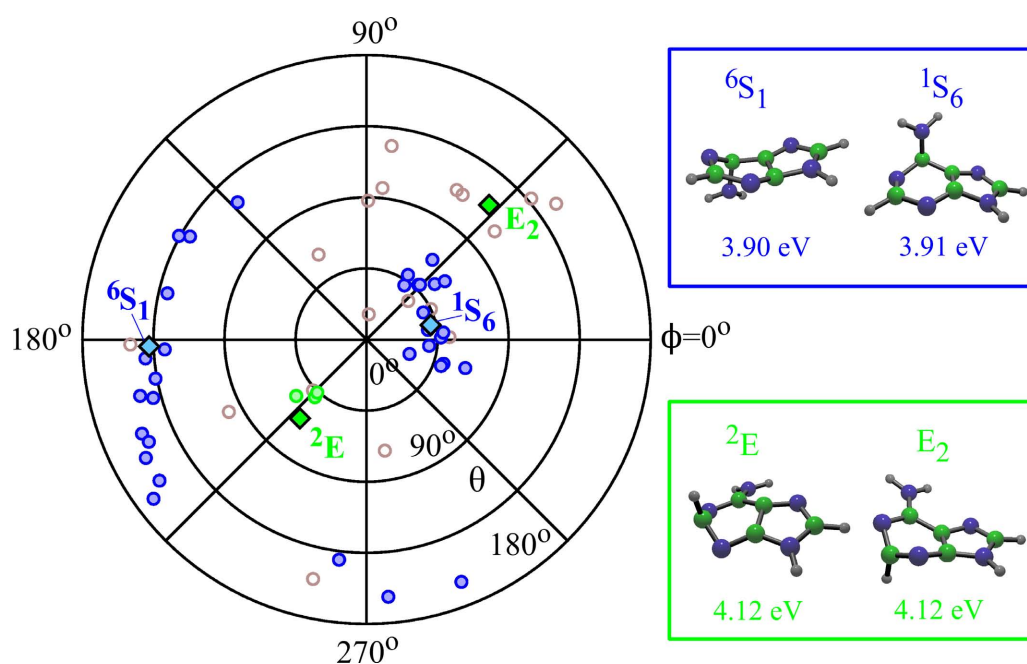


Figure 10.9: Distribution of Cremer-Pople parameters for the structures at final hops from S_1 to S_0 for dynamics induced by the pulse train of Fig. 10.7. The structures of the lowest-lying conical intersections of adenine are shown on the right. The individual structures are classified according to their similarity to the structure of a conical intersection. Blue circles: close to ${}^1S_6/{}^6S_1$, green circles: close to ${}^2E/E_2$, brown circles: structure not in the vicinity of a conical intersection.

and S_3 states. This can be quantified by analysing the hopping events between these states as a function of time as shown in Fig. 10.10. The highest number of hops between the states coincides with the presence of a subpulse. Immediately before the onset of a subpulse, almost the complete excited state population resides in S_1 (cf. Fig. 10.7). Therefore, first the hops from there up to S_2/S_3 occur and reach their highest number shortly before the field amplitude of the subpulse is maximal (cf. Fig. 10.10b)). With increasing occupation of S_2 and S_3 , also hops back to S_1 are induced (cf. Fig. 10.10c). The highest number of such events is reached a short time after the field maxima. When the subpulse ceases, the nonadiabatic coupling between the excited states still invokes hops from S_2 and S_3 down to S_1 , leading to rapid depopulation of these higher states (cf. Figs. 10.7 and 10.10c)). In contrast to this behaviour, the unshaped pulse only once excites the molecules, followed by a gradual relaxation from the bright states to the S_1 state, and further to the ground state (cf. Fig. 10.3).

Therefore, on average, a trajectory driven by the pulse train resides much longer in the higher excited states, which thus have a greater influence on the dynamics than in the case of the unshaped Gaussian pulse. This can be quantified by analysing the tendency of the trajectories to move towards a CI between the S_1 and S_0 states when being propagated in either of the excited states S_1 , S_2 , or S_3 . For this purpose, the temporal change of

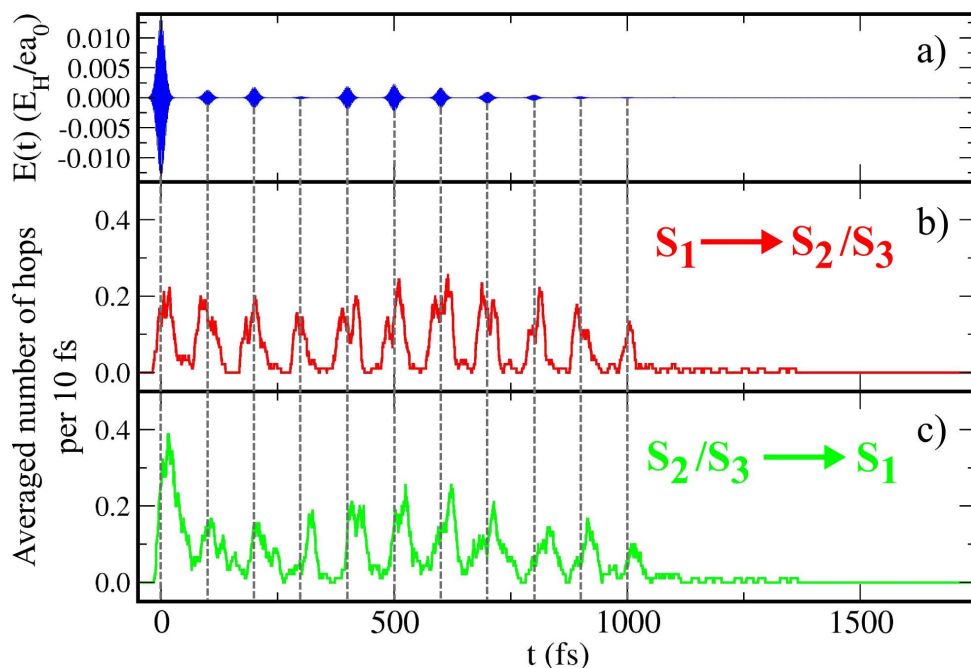


Figure 10.10: Time-averaged distribution of hopping events from the S_1 up to the S_2 and S_3 states (b) and back (c) for the dynamics induced by the pulse train of Fig. 10.7 (a). The subpulses of the train consistently repopulate the higher S_2 and S_3 states and thus decrease the time spent in S_1 where the trajectories would quickly move towards a conical intersection.

the S_1 - S_0 energy gap is used to monitor if a given trajectory moves towards a CI or not. This analysis has been performed for the trajectories driven by the pulse train for all time periods during which they resided in an excited state and is shown in Fig. 10.11. Evidently, when a trajectory is propagated in S_1 , in most cases the energy gap to the ground state becomes smaller (in average, by -0.7 eV), indicating that the dynamics is straightforwardly directed towards a CI. In contrast, the dynamics in S_2 and S_3 can lead almost in equal measure to an increase or to a decrease of the energy gap. In average, there is even a small bias towards the increase, as the average change is $+0.02$ eV for S_2 and $+0.1$ eV for S_3 . This means, the longer a trajectory is propagated in the S_2 or S_3 states, the more strongly impeded is the approach to nuclear configurations in the vicinity of an S_0/S_1 CI, which results in an elongated excited state lifetime. To achieve such more frequent occupation of the S_2 and S_3 states, it is not necessary, as could be surmised, to continuously irradiate the system. Instead, the above presented results show that a pulse train with temporally well separated weak features is sufficient to keep the population in excited states. This is mainly achieved by exploiting the different shapes of the S_2 and S_3 potential energy surfaces, thus hindering the direct approach to the CI geometries, which helps prevent the decay to the ground state for a longer time.

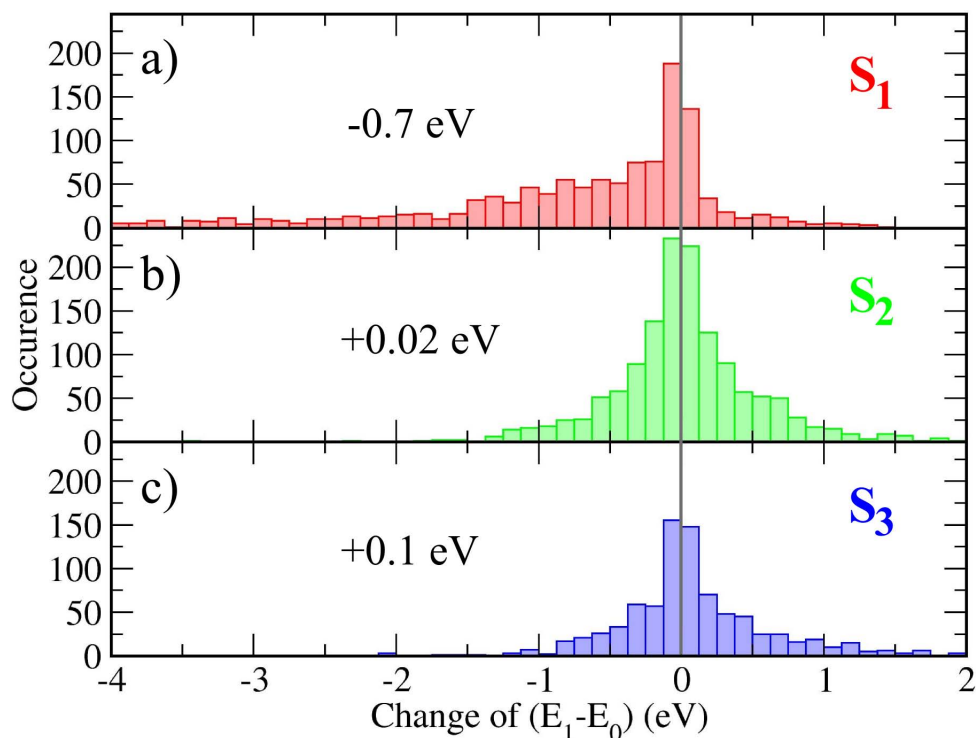


Figure 10.11: Change of the energy gap between S_0 and S_1 state for all time intervals when a trajectory resides in the states S_1 (a), S_2 (b) or S_3 (c) for the dynamics induced by the pulse train of Fig. 10.7. For the S_1 state the average value is negative (-0.7 eV), indicating straightforward motion towards a conical intersection. In contrast, the average value is slightly positive for the S_2 ($+0.02$ eV) and S_3 ($+0.1$ eV) states, which means that the trajectories depart from the vicinity of conical intersections.

10.5 Conclusions

It has been demonstrated how appropriately designed simple laser pulse trains can be used to manipulate the excited state dynamics of adenine in water so as to elongate the excited state lifetime. To this end, the combination of the FISH method with the QM/MM approach has been introduced in order to include the water environment in the laser driven dynamics simulations. This made it possible for the first time to fully simulate the light-induced coupled electron-nuclear dynamics of a molecule interacting with its solvent environment, thereby accounting for all degrees of freedom. Utilizing analytical phase modulation in the frequency domain with a limited set of parameters, a pulse train has been constructed which after initial excitation can keep the excited states in adenine populated for a longer time. The underlying mechanism is schematically illustrated in Fig. 10.12. It involves the sequential re-excitation from the first into higher excited states, competing with the nonradiative ultrafast decay back to the first excited state. In this way, the topography of higher potential energy surfaces in which the access to structures of conical intersections is hindered can be exploited in order to prevent fast decay to the

ground state. Such an elongation of the time period in which excited states are populated could represent a means for increasing the fluorescence yield in molecules that intrinsically exhibit ultrafast nonradiative relaxation. This may open fascinating new opportunities in the context of applications using fluorescence detection, such as fluorescent labelling in biosensing.

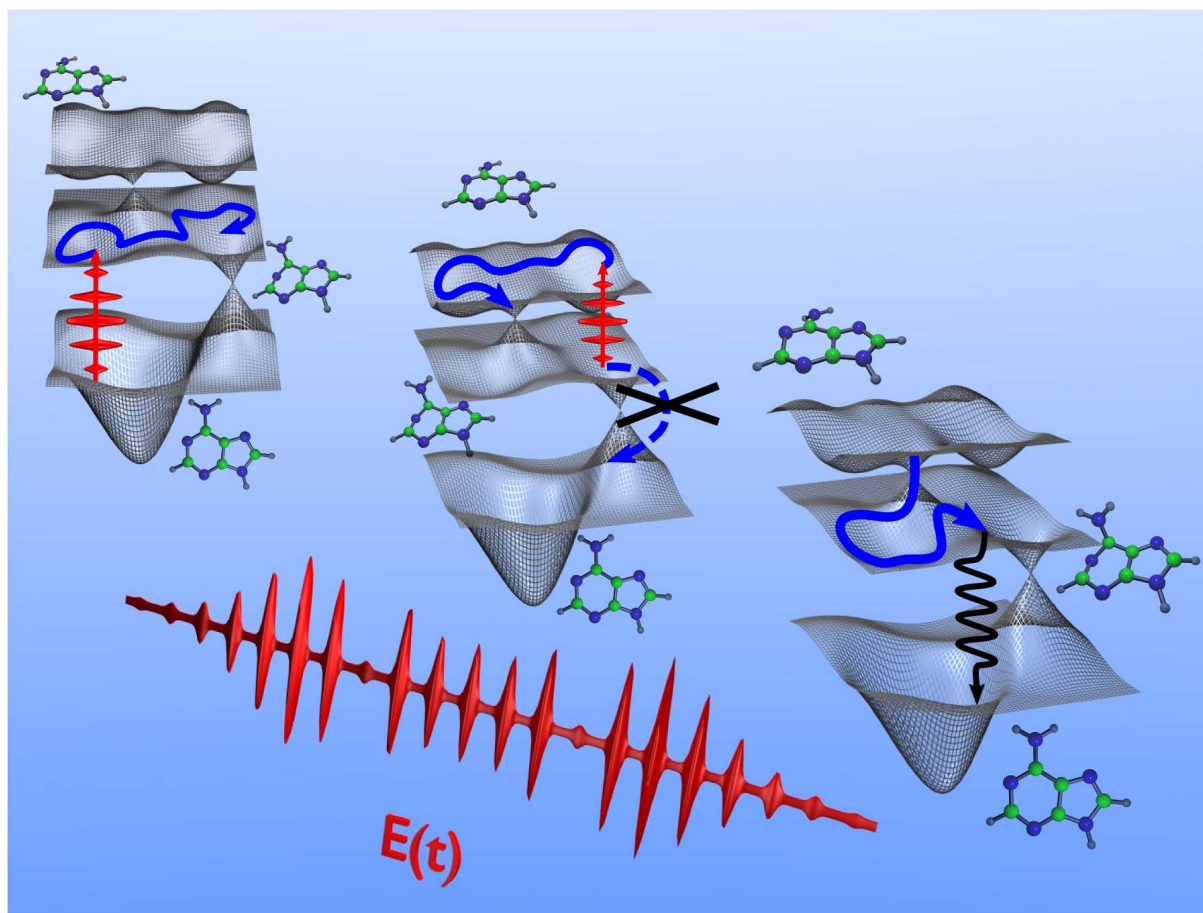


Figure 10.12: Schematic illustration of the laser-induced mechanism preventing immediate electronic state relaxation in adenine. After initial excitation (left part), the ensuing dynamics lead the system to conical intersections with the ground state. However, before these are reached, subsequent features of the laser pulse train lead to the population of higher excited states in which the direct access to structures near S_0/S_1 conical intersections is hampered (middle part). This may ultimately enhance the probability for radiative relaxation processes such as fluorescence (right part).

11 Revealing experimental control mechanisms: Optimal dynamic discrimination of flavins

11.1 Introduction

The capability of optimal control using shaped laser fields to selectively enhance or suppress a desired chemical or physical process such as formation of a specific reaction product, structural isomerization, selective quantum state population or ionization has been successfully demonstrated for a variety of examples in recent years, as discussed in Sec. 8. In these applications, the aim was to extremize a target function corresponding to a specific outcome in a molecular system. However, it is often desirable not only to drive the processes in a single system in a predefined way, but at the same time also to influence the system's environment such as to minimize any disturbing effects on the detection signal. Specifically, the detection of a molecule in the presence of structurally similar surrounding is an important task in analytical sciences. Conventional approaches to such problems can be based on high resolution spectroscopic or chromatographic techniques, aiming to utilize minute differences of the analytes in order to separate them and to create distinguishable detection signals. However, for molecules with almost identical response in the framework of a given analytical technique, such approaches come to their limits. As these methods are usually based on static molecular properties, it suggests itself to consider using the dynamical behaviour of the system as a new dimension for control. In this spirit, the optimal dynamic discrimination (ODD) technique has been theoretically proposed [421–423]. It is based on the idea to exploit minor differences in the dynamical properties of two almost identical quantum systems, the static properties of which do not allow for their discrimination, in order to create distinguishable detection signals and thus to significantly push the limits of optimal control. On the example of simple quantum mechanical few-level systems, the basic principles of ODD have been analysed in detail. It was found that optimized electric fields allowing for discrimination must drive one of the systems as efficiently as possible to the target state while keeping the other system's state as much as possible orthogonal to that state. This is achieved by exploiting different multistep pathways, starting from the initial state via various intermediate ones to the target state, thereby taking advantage of constructive or destructive interference between the pathways. In this way, efficient population of the target state may be achieved in one and avoided in the other of two similar systems [422]. For isolated systems of finite dimension, the fundamental question of controllability has been addressed, and based on a mathematical analysis, it has been shown that one can predict whether an arbitrarily given target state can be reached by excitation with optimized laser fields or not [424].

Under realistic experimental conditions, though, the studied system is in most cases not finite but interacts with its environment. Nevertheless, it could be demonstrated that the basic principles of ODD also hold in such cases, making ODD a significant concept for analytic applications. In pioneering studies, it has been shown that depletion of the analyte fluorescence can be used as a discriminating signal in solution [425–427]. This is achieved by employing a two-pulse pump-probe laser setup, in which one pulse prepares an excited state and the second one induces irreversible processes such as ionization or chemical degradation, thus decreasing the population of the excited state from which fluorescence could occur. In this way biological chromophores like tryptophan or riboflavin could be unambiguously discriminated from polycyclic organic pollutants such as naphthalene by different amounts of fluorescence depletion, although all species show only small differences in their static fluorescence spectra [425–427]. Based on these findings, the question can be raised how much the sensitivity of discrimination can be still pushed further, e.g. so as to discriminate between different types of biological samples such as different species of bacteria, which might in the future have a significant impact for novel health care applications and the protection against biological hazards. In this context, the use of optimally shaped laser fields instead of unshaped pulses has been considered. Specifically, on this account, the discrimination between the two molecules riboflavin (RBF) and flavin mononucleotide (FMN), which share the same chromophore (7,8-dimethyl isoalloxazine) and only differ in their side chain (ribityl for RBF, phosphorylated ribityl for FMN) has been investigated experimentally [66, 428]. The findings obtained in these studies represent the basis for the detailed theoretical analysis presented in this chapter of the thesis, with the aim to shed light on the molecular mechanisms underlying the ODD experiment for RBF and FMN.

The mixed quantum-classical coupled electron-nuclear dynamics in the framework of the FISH method offers a unique opportunity to directly employ experimentally obtained optimal laser fields in a simulation at the molecular level. This allows for the analysis of dynamical processes and for gaining mechanistic insight into the principle of ODD, which would not be possible based on experimental results alone. Therefore, the present chapter also serves to illustrate the utility of FISH to complement experimental optimal control in order to obtain a comprehensive picture of the control mechanism in complex molecular systems.

The remainder of this chapter is organized as follows: First, the basic photophysical properties of flavins are summarized in Sec. 11.2. The experimental results of the ODD between RBF and FMN are discussed in Sec. 11.3. Subsequently, the theoretical simulations of the ODD process using experimental pulses are presented and discussed in Sec. 11.4. Most of the results presented in Sec. 11.4 have been published in Refs. [67, 237, 429].

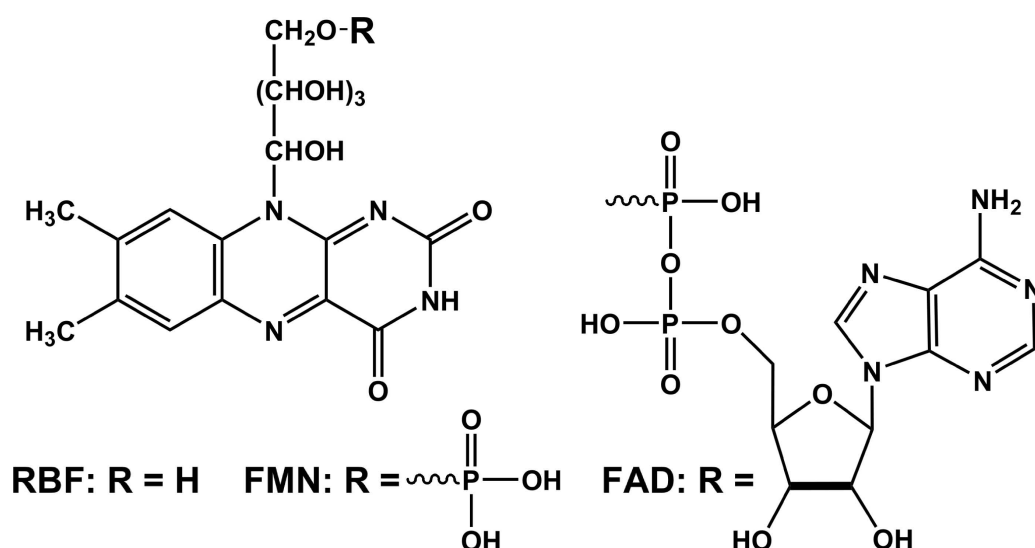


Figure 11.1: Chemical formulae of riboflavin (RBF), flavin mononucleotide (FMN) and flavin adenine dinucleotide (FAD).

11.2 Photophysical properties of flavins

Flavins [430] represent a family of chromophores fulfilling important biological functions as cofactors in a variety of enzymes [431], such as electron transferases [432,433], oxidases and oxygenases [434] or bluelight photoreceptors [435,436]. Their main function lies in the oxidation of substrate molecules, the transfer of electron and hydrogen equivalents as well as in their photochemical activity. All flavins are based on the same chromophore, the aromatic 7,8-dimethyl isoalloxazine ring system, which is responsible for the optical properties. However, they bear different side groups, such as a ribityl chain (derived from the sugar alcohol ribitol) in the case of riboflavin (RBF), a ribityl chain with terminal phosphate group in flavin mononucleotide (FMN), or a phosphorylated ribityl chain connected to an adenosine monophosphate molecule in flavin adenine dinucleotide (FAD). The chemical structures of these three molecules are depicted in Fig. 11.1. Their common chromophore enables them to exhibit different oxidation and protonation states [430]: The canonical neutral oxidized form can be reduced with one or two electrons (accompanied by protonation), leading to the radical semiquinone or the fully reduced hydroquinone form, respectively. All three forms can also be protonated or deprotonated, leading to at least nine different species that can be present in solution or protein environment and exhibit different absorption properties. In this way, the above mentioned variety of biological functions of flavins is achieved. Most remarkably, they are the only biological redox cofactors which can both undergo one and two electron reactions [437]. In biological systems such as proteins, the flavin cofactors present are FMN or FAD. The riboflavin molecule itself acts as a precursor for these in the human metabolism which has to be supplied by nutrition and therefore represents a vitamin (B₂). The structural, optical, and dynamical

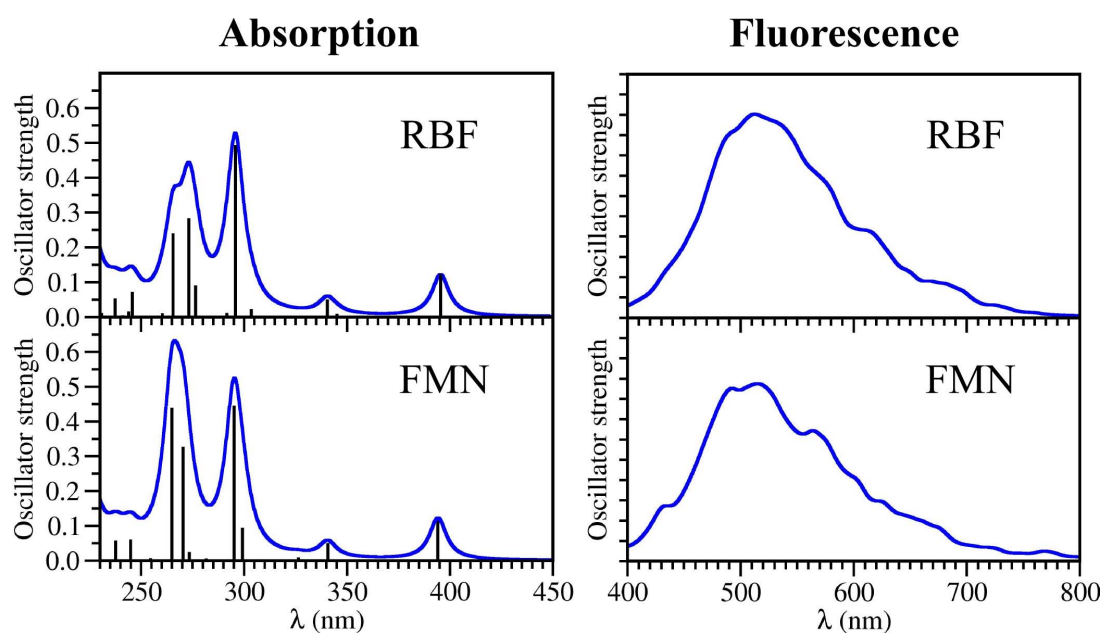


Figure 11.2: Calculated electronic absorption and fluorescence spectra for RBF (upper part) and FMN (lower part) obtained using the semiempirical PM3 CI method. The fluorescence spectra are obtained by broadening the individual transition lines of a Wigner ensemble of 500 structures.

properties of flavins have been intensively investigated both in protein environment and in the free molecules. In the following, the focus will be on the properties of bare RBF and FMN, which have been used in the ODD experiments and simulations described in the present chapter.

The common flavin species present both in solid phase and in aqueous solution is the oxidized one, which only in the presence of reducing reagents can be transformed to the semiquinone and hydroquinone species. Moreover, at neutral pH the uncharged forms are dominant and are in any case the main source of fluorescence, as the quantum yield of the charged species is very low [438,439]. Therefore, only the oxidized neutral flavins as depicted in Fig. 11.1 have been considered in the present chapter.

The electronic absorption spectra of both RBF and FMN in water are characterized by four broad bands centered at 440, 375, 270, and 220 nm, respectively (cf. Ref. [438,440] for RBF and Ref. [441] for FMN). The spectroscopic features in this wavelength regime are largely determined by the chromophoric isoalloxazine ring system common to all flavins. Therefore, the spectroscopical patterns of molecules as RBF or FMN which only differ in the structure of their side chain are essentially identical [66]. This can also be evidenced from the theoretical electronic absorption spectra of these two molecules calculated using the semiempirical PM3 CI method and shown in Fig. 11.2, which are, despite some shifts of bands, in reasonable agreement with the experimental ones. Similar results are obtained using higher-level quantum chemical methods such as time-dependent density functional

theory [442]. An analysis of the intense transitions shows that they are mainly composed of $\pi\pi^*$ excitations, with only small contributions of $n\pi^*$ character. The energies and electronic characters of the nine lowest excited electronic states for the lowest-energy optimized geometries of RBF and FMN are summarized in Appendix E.

Upon photoexcitation to the first excited electronic state, dynamical processes are initiated which have been the subject of several experimental and theoretical studies. Employing femtosecond transient absorption spectroscopy, it could be shown that in the initial stage of the dynamics, a coherent superposition between the bright $S_1(\pi\pi^*)$ state and a close-lying $n\pi^*$ state is formed. Moreover, within the sub-ps regime, coherent oscillations of the transient absorption signal are observed which can be attributed to low-lying vibrational modes [443]. This has been further confirmed by femtosecond stimulated Raman spectroscopy, clearly revealing the excitation of normal modes between 90 and 420 cm^{-1} after photoexcitation to the S_1 state [444]. These processes are accompanied by a red shift of the stimulated emission by $\approx 4000 \text{ cm}^{-1}$, which is mostly due to structural relaxation of RBF, and to a small part also to solvent effects. The low-lying vibrational modes of RBF have been in part also experimentally observed using far-infrared (terahertz) spectroscopy [445], and have been assigned utilizing quantum chemical calculations to torsions of the ribityl chain as well as to out-of plane and in-plane ring deformations [445, 446]. The vibrational relaxation proceeds on a subpicosecond time scale via intramolecular vibrational energy redistribution (IVR) as well as by vibrational cooling due to interaction with the solvent in the picosecond regime [444], as has been also established by time-resolved infrared spectroscopy [447]. Theoretical calculations of infrared spectra in the ground and first excited electronic state have allowed for the assignment of measured infrared peaks and for the analysis of differences between both states, which mostly involve slightly changed bond lengths in the isoalloxazine ring system, leading to shifts of the corresponding normal mode frequencies [447, 448]. Furthermore, vibronic absorption and emission spectra have been simulated, revealing that mainly progressions of in-plane and out-of-plane as well as various stretching modes within the ring system contribute to the vibrational structure of the emission and absorption bands [448]. Recently, also the nonadiabatic relaxation dynamics for RBF has been simulated using ab initio molecular dynamics combined with trajectory surface hopping [449]. In this way, the experimental red shift of the stimulated emission due to structural relaxation could be confirmed, and the occurrence of nonadiabatic transitions between states of $\pi\pi^*$ and $n\pi^*$ character on a 30 fs time scale could be established. Moreover, an analysis of the nuclear dynamics has revealed that, immediately after electronic excitation, mainly stretching modes of the ring system in the range between 1400-1700 cm^{-1} are excited. However, within less than 100 fs the vibrational energy is transferred to a multitude of other modes, in particular to those below 1000 cm^{-1} , which correspond to in-plane and out-of-plane motions of the

rings as well as to torsions of the ribityl side chain. Investigation of the influence of water on the dynamics has shown a stronger red shift of both absorption and emission maxima, as well as a slightly faster IVR [449].

No return of excited state population to the ground state has been observed in the picosecond time regime. Instead, the ground state is reached radiatively by fluorescence which takes place in water in the case of RBF with a time constant of ≈ 5 ns and a quantum yield of 0.26 [439] and for FMN with a time constant of 4.6 ns and the same quantum yield [450]. The shapes of the fluorescence spectra of RBF and FMN are also almost identical, as observed experimentally [439, 450] and shown theoretically in Fig. 11.2. Besides the fluorescence pathway, also intersystem crossing from the singlet to the triplet manifold takes place with reasonable quantum yield (≈ 0.4 in RBF), leading to phosphorescence on a time scale of several microseconds [440]. However, since the rate of intersystem crossing is sufficiently low ($7 \cdot 10^{-7} \text{s}^{-1}$ [440]), the triplet manifold is only negligibly populated within the picosecond time regime in which the laser pulses used for the optimal dynamic discrimination described in this chapter are acting. Therefore, only the dynamics within singlet states will be considered in the following.

11.3 Experimental ODD of RBF and FMN

The experimental ODD between RBF and FMN has been achieved by a two-pulse pump-probe sequence using an iteratively optimized 400 nm UV pump pulse and a time-delayed unshaped 800 nm IR probe pulse [66, 428]. The optimization target was to manipulate the fluorescence depletion induced by the pulse sequence, such as to generate a discriminating difference in the amount of depletion between RBF and FMN. For this purpose, the pump pulse was decomposed into 50 spectral parts corresponding to frequencies between 394.6 and 405.6 nm. Using a genetic algorithm, the spectral phases for each part were varied until the optimization goal was fulfilled, giving rise to optimized UV pulses of complex structure. The potential processes underlying the ODD control using such pulses are schematically presented in Fig. 11.3. Excitation with a shaped UV pulse leads to population of the S_1 state and induces ultrafast coupled electron-nuclear dynamics which can take slightly different pathways in both molecules. After a time delay Δt , the IR pulse further excites the molecules to higher electronic states in which irreversible processes such as ionization [451] or fragmentation [452] are likely to occur, but with different efficiency for each of the two molecules. This leads to a depopulation of the excited state manifold from which fluorescence could take place, and therefore the fluorescence yield is depleted for one of the species and not for the other. The optimization procedure has yielded a multitude of different pulses for both optimization targets, i.e. minimization or maximization of the fluorescence depletion ratio $D(FMN)/D(RBF)$. Characteristically,

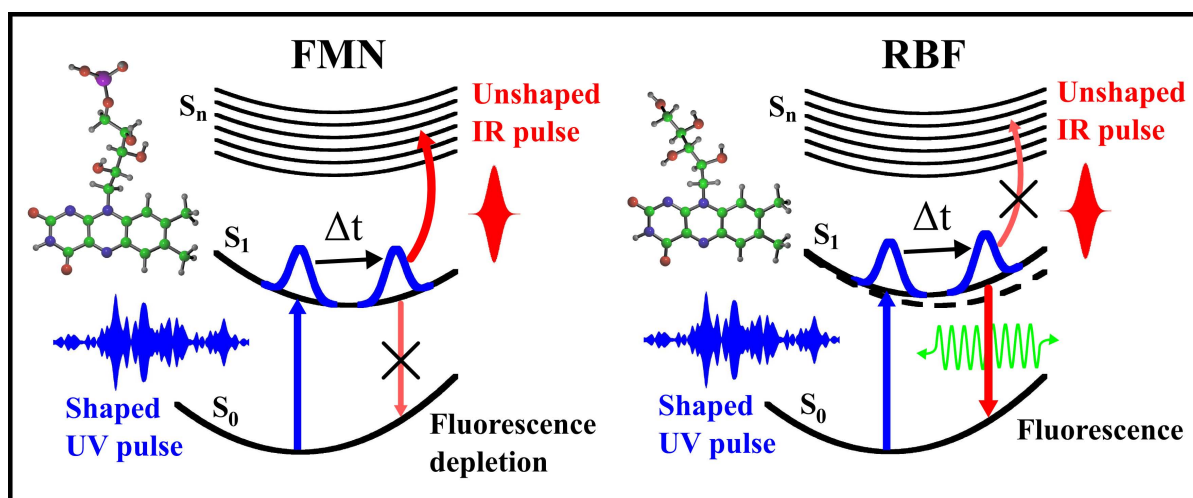


Figure 11.3: Schematic representation of the optimal dynamic discrimination between RBF and FMN. Irradiation with a shaped UV laser pulse leads to excitation to the S_1 state, as indicated by the blue arrow. After a time delay Δt , during which the molecules undergo dynamics in excited states, an unshaped IR pulse is applied. For one of the molecules (here FMN, left part of the Figure), this leads to further excitation to higher-lying states, where irreversible processes such as ionization can occur (red arrow), consequently the fluorescence gets depleted (crossed red arrow). By contrast, for the second molecule (here RBF, right part of the Figure), excitation to higher states is less favourable (crossed red arrow), and the fluorescence (green) will remain stronger than for the first molecule. With differently shaped UV pulses, also the reverse situation is possible.

it has been found that different temporal substructures are present, which are separated by time periods approximately equal to the oscillation periods of low-frequency normal modes located in the flavin's side chains. Therefore, the conclusion has been made that coherent vibrational dynamics of the side chain modes is largely responsible for efficient ODD. Moreover, by varying the time delay between pump and probe pulse, a typical temporal window of less than 1 ps has been identified, in which ODD is at all possible, while for larger delays of the probe pulse no discrimination was observed. This is consistent with the typical vibrational decoherence time scale of molecules in solution of less than 1-2 ps [34]. However, a detailed picture of the processes involved cannot be drawn based on experimental findings alone, which provides a strong motivation for the theoretical investigations presented in the remainder of this chapter. Beyond the possibility to discriminate between two molecular species, the existence of several distinct pairs of ODD pulses also offers an opportunity to use the different depletion signals as a means to determine the concentrations of both molecules in a given mixture [66,428]. In this way, a novel method of quantitative analysis could be established which would allow determination of a substance's concentration in the presence of a spectroscopically almost identical surrounding. Although the specific example of two flavin chromophores has been chosen to illustrate the applicability of the ODD concept, the results obtained are of general im-

portance, as they show the proof-of-principle. Therefore, ODD using shaped laser pulses represents a promising technique to push the limits of analytical applications beyond the current capabilities.

11.4 Simulation of ODD using experimentally shaped laser pulses

11.4.1 Computational

The simulation of ODD between FMN and RBF in the framework of the FISH method has been performed by using experimentally optimized pulses which maximize and minimize the fluorescence depletion ratio of both molecules, respectively.

For the multistate dynamics in the ground and the nine lowest excited singlet states (S_0 - S_9) the electronic structure is described employing the semiempirical PM3 CI method [188]. As the active space, 11 occupied and 6 virtual orbitals are used, taking into account all single excitations out of 12 reference configurations which have been identified as the leading configurations in the electronic states under consideration (cf. also Appendix, Tables E.1 and E.2). In this way, the spectroscopic properties of the two flavin molecules are reasonably accurately reproduced, as evidenced by the comparison with experimental data (cf. Sec. 11.2) as well as with theoretical results obtained using TDDFT [449, 453, 454]. The energies, forces, nonadiabatic couplings, and transition dipole moments needed for the molecular dynamics simulation are calculated “on the fly” accounting for all degrees of freedom. For the nonadiabatic couplings and transition dipole moments between all states the method developed by Thiel et al. is used [111].

The initial conditions (30 coordinates and momenta) for the simulation are generated by sampling a 10 ps long ground state trajectory at 300 K which was obtained by using the semiempirical PM3 method [188] for both molecules. The nuclear dynamics has been carried out using the Langevin equation of motion (Eq. (2.13)), which is integrated employing a modified version of the velocity Verlet algorithm [185]. For the atomic friction, an empirical coefficient of $\gamma = 91.0 \text{ ps}^{-1}$ for water environment is used [455]. In this way, dissipative effects on the nuclear motion are approximately accounted for, enabling the comparison of theoretical results with the experiment which was carried out in water. Moreover, in the case of long pulses, the dissipative effects also ensure that the excess of energy gained during the field-induced dynamics is released to the environment and not artificially accumulated in the molecule. Along the nuclear trajectories, the time-dependent Schrödinger equation (3.26) is numerically integrated in the manifold of all electronic states, taking into account both the field-induced as well as the nonadiabatic coupling. In order to determine in which state the trajectories are propagated, the hopping probabilities are calculated from the electronic state populations $\rho_{ii} = |c_i|^2$ using Eq. (3.32).

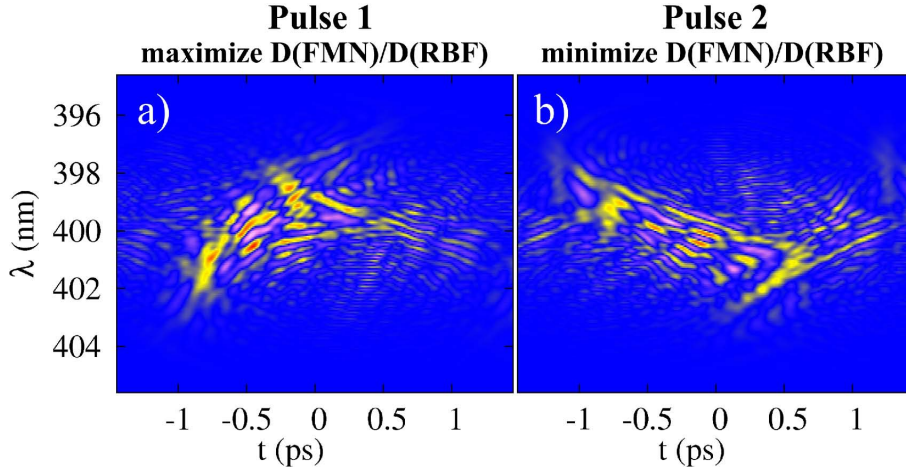


Figure 11.4: Wigner-Ville transforms of the shaped UV pulses for a) maximization of the depletion ratio $D(\text{FMN})/D(\text{RBF})$ (pulse 1) and b) minimization of that ratio (pulse 2). Analogous to the Wigner transform in the phase space, the Wigner-Ville transform is defined as $W(t, \omega) = 2\text{Re} \int_0^\infty d\tau e^{-i\omega\tau} E^*(t + \tau/2)E(t - \tau/2)$.

The laser fields obtained from experiment [66] are employed in the simulations according to Eq. (3.26). For the shaped UV pulses, 50 experimental spectral phases and amplitudes are used in order to reconstruct the field in the time domain according to

$$E(t) = \sum_n A_n \exp[i(\omega_n t + \phi_n)], \quad (11.1)$$

where A_n represents the spectral amplitude, ω_n is the frequency, and ϕ_n represents the spectral phase. The experimental frequencies correspond to wavelengths ($\lambda = \frac{2\pi c}{\omega}$) in the range between 394.6 nm and 405.6 nm and exhibit a temporal distribution as shown in Fig. 11.4. In the time domain, the reconstructed pulses have a duration of ≈ 5 ps and a maximum amplitude of $\approx 6 \cdot 10^{11}$ W cm $^{-2}$. The unshaped infrared probe pulse with a wavelength of 800 nm has a maximum amplitude of $\approx 3 \cdot 10^{12}$ W cm $^{-2}$ and a Gaussian envelope with a full width at half maximum of 100 fs.

Since the fluorescence depletion relies on irreversible processes such as ionization, these effects must be introduced approximately in the Schrödinger equation (3.26) for the electronic states. This can be modeled by adding an imaginary component $i\Gamma$ to the energy of the highest excited state S_9 which lies close to the experimentally determined ionization limit in water [451]. In this way, irreversible population decay from S_9 is introduced, leading to a non-conservation of the total population norm $\sum_i |c_i|^2$. Subsequently, the time-dependent coefficients along the trajectories are recalculated and a hopping probability from the S_9 state to the ionized state is introduced based on the decrease of the population norm. This leads to a trajectory-averaged ionized state population P_{ion} which represents the irreversible decrease of the excited state population from which fluores-

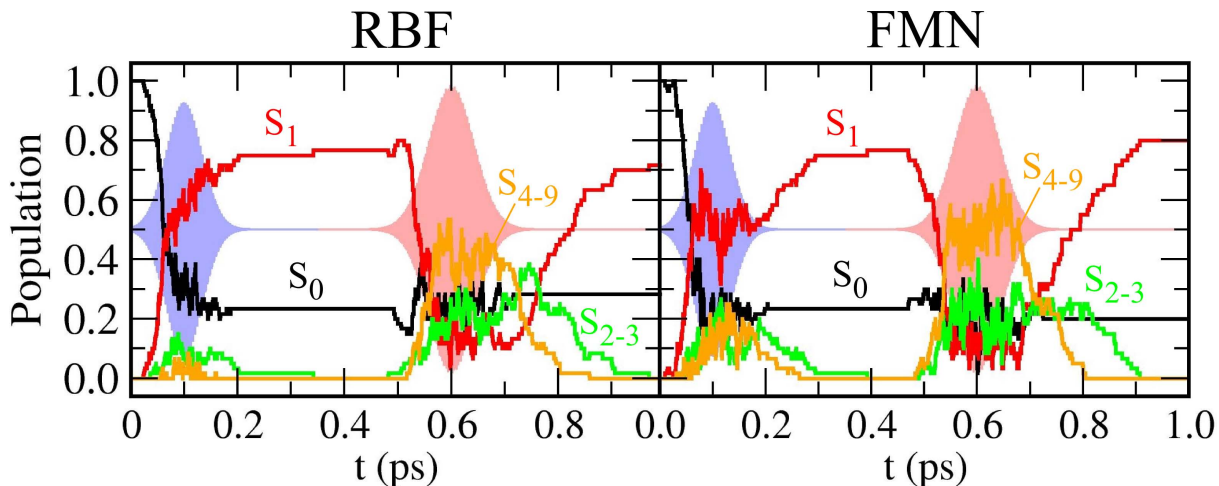


Figure 11.5: Electronic state population dynamics induced by an unshaped 400 nm UV pulse (light blue) followed by an unshaped 800 nm IR pulse (light red). Left panel: Time-dependent populations of the electronic states S_0 (black), S_1 (red), $S_2 - S_3$ (green) and $S_4 - S_9$ (orange) in RBF. Right panel: Time-dependent populations of the electronic states S_0 (black), S_1 (red), $S_2 - S_3$ (green) and $S_4 - S_9$ (orange) in FMN.

cence could occur, hence providing a direct measure for fluorescence depletion. In the experiment, the latter is determined by taking the difference between the two fluorescence intensities corresponding to the shaped UV pulse alone and to both the shaped UV pulse and the IR probe pulse, normalized to the intensity corresponding to the UV pulse alone. In order to calculate this depletion ratio from the theoretical simulation, the ionized populations P_{ion} are used to determine the fluorescence depletion D as

$$D = \frac{P_{ion}(UV + IR) - P_{ion}(UV)}{1 - P_{ion}(UV)}. \quad (11.2)$$

11.4.2 Results and Discussion

As outlined in Section 11.3, the experimental optimal dynamic discrimination has resulted in optimized pump-probe pulse pairs that utilize minute differences in the dynamics of the two almost identical molecules RBF and FMN to generate a measurable difference of the fluorescence depletion signal. Specifically, for the optimization target of maximizing the ratio $D(FMN)/D(RBF)$, about 12.6 % depletion has been achieved for FMN and about 8 % for RBF. For the target of minimizing the same ratio, the depletion values are essentially reversed, and in both cases this separation amounts to about 16 times the standard deviation of the experiments. By contrast, the use of unshaped laser pulses produces a depletion yield of ≈ 21 % for both molecules, thus illustrating the need for optimized fields in order to achieve discrimination [66].

In the experiment, the feasibility of this discrimination scheme could be impressively demonstrated [66]. However, in order to reveal the dynamical processes behind this out-

come on the molecular level, theoretical simulations are essential. Therefore, FISH simulations in the manifold of the electronic ground as well as nine excited states have been performed under the influence of both an unshaped UV/IR pulse sequence as well as of two experimentally obtained laser fields which have been optimized for maximizing or minimizing the ratio of fluorescence depletion between FMN and RBF. These experimental pulses are henceforth termed pulse 1 for maximizing and pulse 2 for minimizing the depletion ratio. As a starting point, the electronic state population dynamics induced by an unshaped UV/IR pulse pair is shown in Fig. 11.5 for both RBF and FMN. It becomes evident that the UV pulse is mainly responsible for excitation from the electronic ground state S_0 to the first excited state S_1 , while the IR pulse leads to further excitation to higher electronic states, the population of which rapidly decreases after this pulse has ended. No significant return to the ground state can be observed, which is consistent with the expected fluorescence of RBF and FMN. Small transient population differences are observable after UV excitation. Most remarkably, in the case of FMN the higher-lying states are populated with higher efficiency, but these differences disappear before the IR pulse sets in.

By contrast, the population dynamics induced by the optimized pulses 1 and 2 is very different due to their specific spectral and temporal structure, in particular their longer time duration and the temporal overlap between UV and IR parts, as depicted in Fig. 11.6. For both pulses and both molecules, the excitation process is initiated by transitions from the ground state to the first excited state S_1 . This is followed by further excitation to higher-lying states, in particular at $t \approx 0.5$ ps when the IR subpulse is acting. It can be seen that by comparing the effect of the two pulses on the two molecules, transient differences of the excited state populations are present. Furthermore, the population of the higher states $S_2 - S_9$ is systematically smaller for RBF than for FMN both for pulse 1 and pulse 2, similar to the dynamics driven by the unshaped pulses. However, all these differences vanish after the pulses have ceased ($t > +2.5$ ps), when the excited state population completely returns to S_1 , from which the fluorescence will occur. This underlines the need for including also such processes into the simulation which irreversibly decrease the excited state population and therefore lead to fluorescence depletion. These effects, which can be e.g. ionization or photodegradation, are in the present simulation approximately accounted for by allowing for irreversible population decay from the highest excited state, as described in section 11.4.1. The empirical decay parameter has been calibrated such that, as in the experiment, both molecules exhibit identical depletion values when irradiated with an unshaped UV/IR pulse pair. In this way, “ionized” state populations have been obtained which are shown in Fig. 11.7 (upper panel). From these quantities, it becomes clear that mainly the IR subpulse at +0.5 ps is responsible for ionization, although in the case of FMN ionized population occurs to

a minor extent already at earlier times. The ionization yield evoked by pulse 1 is larger than that due to pulse 2 in the case of FMN, whereas the reversed effect is observed for RBF. This already demonstrates that shaped laser pulses are capable to selectively and independently modulate the ionization efficiency of very similar molecules. From the ionized populations, the fluorescence depletion D has been calculated from the relative decrease of the excited state population due to the UV/IR pulse pairs vs. due to the UV pulse alone according to Eq. (11.2). This quantity is shown as a function of time in the lower panel of Fig. 11.7. Since the fluorescence occurs on a significantly longer time scale than the dynamics driven by the optimal laser pulses, depletion values at intermediate times < 2.5 ps should be interpreted as that amount of depletion which would be present if the laser pulse had immediately ended at the given time. The comparison to the measured depletion can be made from the final values at the end of the shaped pulses. It should be noted that, in order to connect the fluorescence depletion with the ionized populations, it has been assumed that no further population changes occur after the laser pulses have ceased. The final fluorescence depletion value obtained in this way under the action of

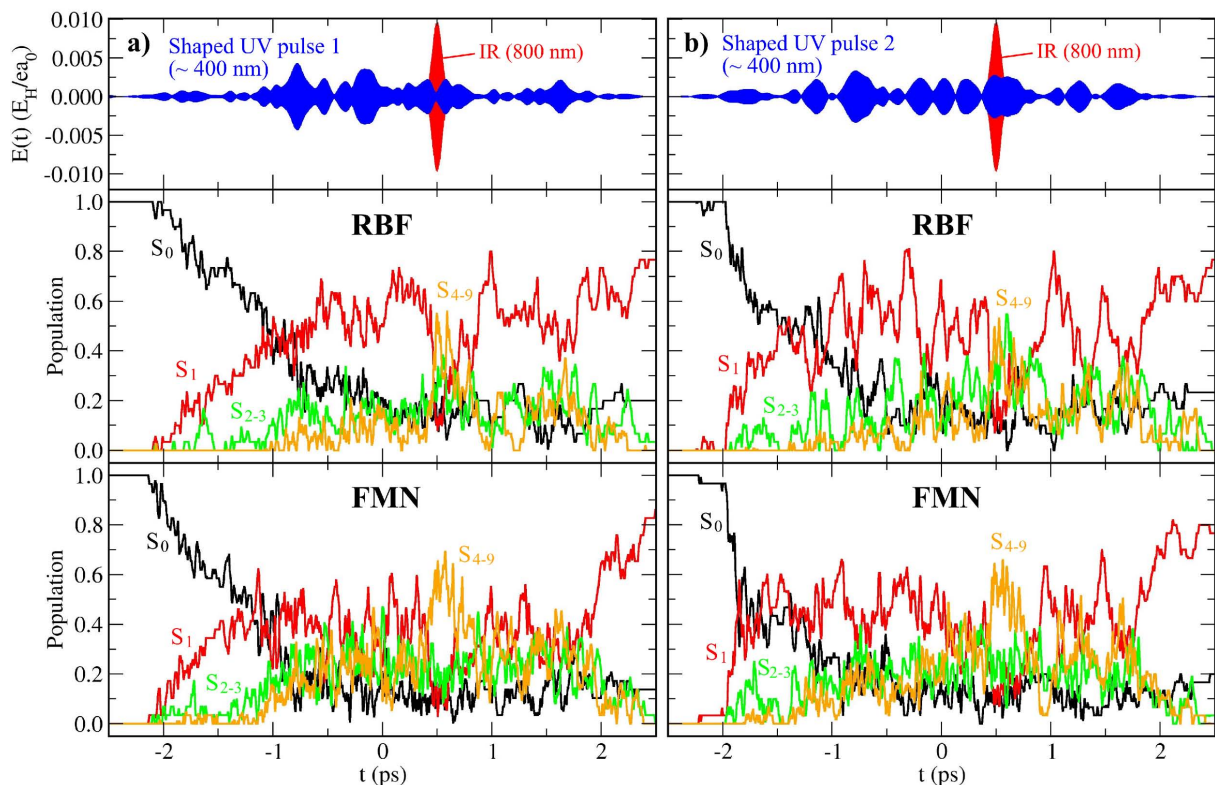


Figure 11.6: Upper panel: Temporal structure of the shaped UV pulses 1 (blue, left part) and 2 (blue, right part) as well as of the IR pulse (red). Middle panel: Time-dependent populations of the electronic states S_0 (black), S_1 (red), $S_2 - S_3$ (green) and $S_4 - S_9$ (orange) in RBF driven by the pulse sequences shown in the upper panel. Lower panel: Same as middle panel, but for FMN. For visual clarity, the populations have been time-averaged over periods of 10 fs.

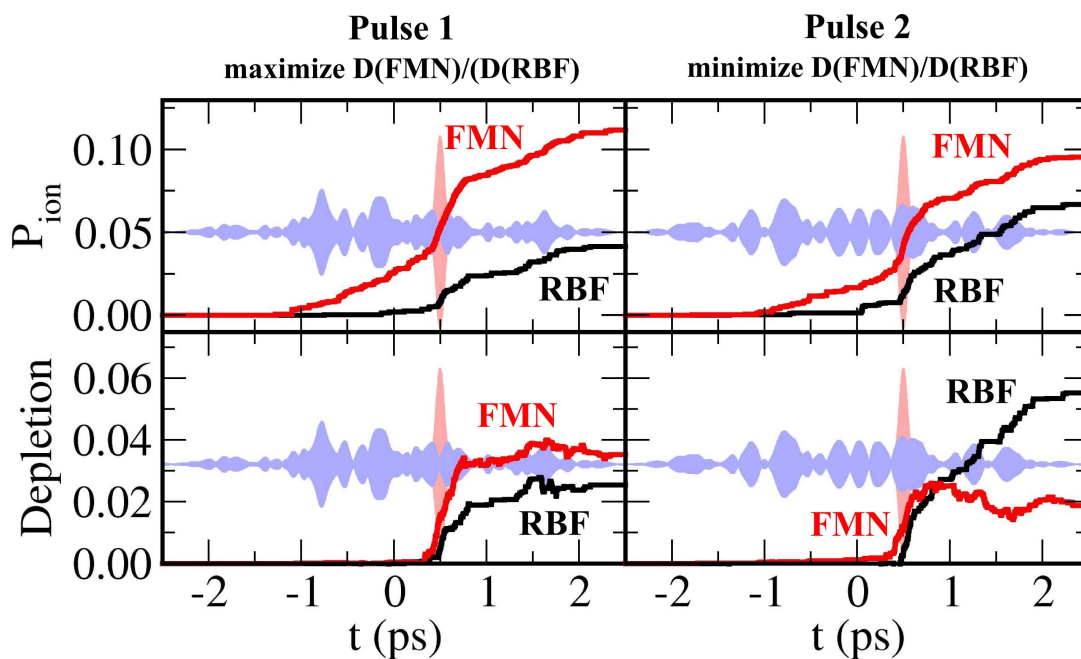


Figure 11.7: Upper panel: Ionized populations P_{ion} of RBF (black) and FMN (red) due to pulse 1 (left) and pulse 2 (right). Lower panel: Fluorescence depletion D of RBF (black) and FMN (red) due to pulse 1 (left) and pulse 2 (right). The laser pulses are indicated in the background in light blue (shaped pulses 1 and 2) and light red (unshaped IR pulse).

pulse 1 is larger for FMN than for RBF, while for pulse 2 the situation is opposite (cf. Fig. 11.7). The depletion ratios $D(FMN)/D(RBF)$ are calculated to be 1.4 for pulse 1 and 0.4 for pulse 2, which is in good agreement with the experimental values of 1.3 for pulse 1 and 0.7 for pulse 2 [66].

While this result has been obtained with an IR pulse time delay of 0.5 ps, the calculated depletion ratio shows a rapid loss of discrimination capability for larger time delays, as depicted in Fig. 11.8, similar to the experimental finding [66]. For time delays larger than 1 ps, the depletion ratios for both pulses approach 1.0, and discrimination is no longer possible. As discussed in Sec. 11.3, this corresponds to the time window of coherent dynamics in the liquid phase, thus emphasizing that the latter is necessary in order to achieve discrimination. It should also be noticed that the use of unshaped pulses does not allow for discrimination even for short time delays.

These results clearly confirm the experimental observations of ODD between very similar chromophores. However, beyond that, the theoretical simulations also offer a unique opportunity to gain an insight into the molecular mechanism responsible for discrimination. As outlined above, the amount of fluorescence depletion is directly related to the ionization yield, which depends on the efficiency of populating higher excited states above S_1 . Therefore, the transition dipole moments between S_1 and the higher states have been calculated along the trajectories driven by the laser pulses 1 and 2, and averaged over the whole ensemble. It becomes evident from Fig. 11.9a) and b) that pulse 1 induces

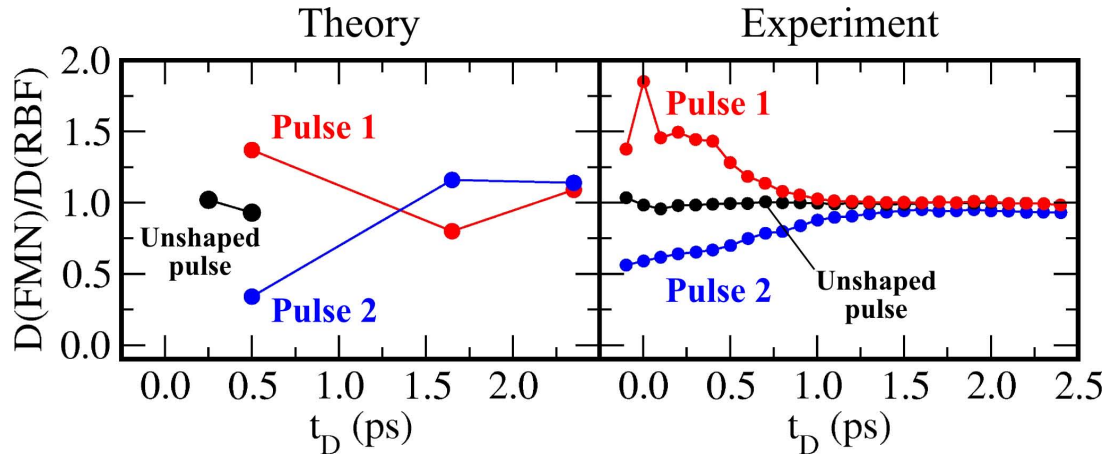


Figure 11.8: Fluorescence depletion ratio as a function of the IR pulse delay for unshaped UV pulse (black), pulse 1 (red) and pulse 2 (blue). For comparison, the experimental data from Ref. [66] are shown in the right panel.

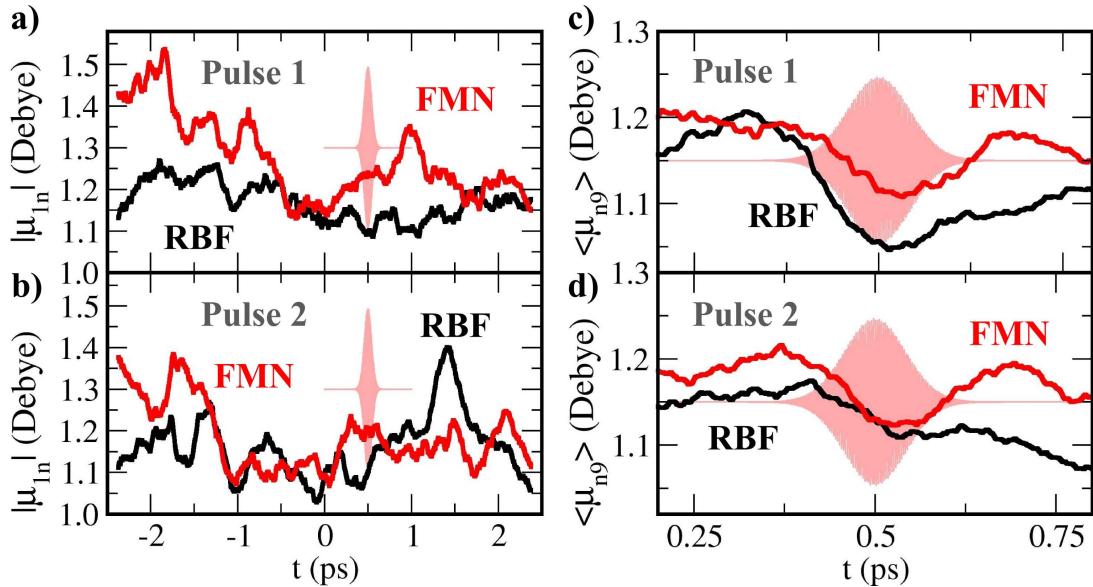


Figure 11.9: a), b): Average transition dipole moments for $S_1 \rightarrow S_2 - S_9$ transitions for the dynamics driven by pulse 1 (a) and 2 (b) for FMN (red) and RBF (black). The average is performed over the states $S_2 - S_9$ and over the ensemble of trajectories. c), d): Average transition dipole moments $\langle \mu_{n9} \rangle$ for $S_1 - S_8 \rightarrow S_9$ transitions weighted by the state populations as $\langle \mu_{n9} \rangle = \sum_n |c_n|^2 |\mu_{n9}|$, in the time window of the IR pulse (light red) for pulse 1 (c) and 2 (d).

dynamical pathways which exhibit systematically larger transition dipole moments for FMN than for RBF, indicating the stronger ionization and accordingly stronger fluorescence depletion in FMN. In contrast, for pulse 2 this behaviour is reversed at times after +0.5 ps, leading to higher transition dipole moments for RBF and thus in this case to a stronger fluorescence depletion compared to FMN. Since in the model used here the ionization only occurs from the highest excited state S_9 , also the efficiency of populating this particular state has been analysed by calculating the averaged transition dipole moments $\langle\mu_{n9}\rangle$ weighted by the populations of the respective states S_n , $n=1-8$, as presented in Fig. 11.9c) and d). The pulse 1 invokes larger differences between these quantities in favour of FMN, while for pulse 2, especially when the IR pulse is acting, only small differences between RBF and FMN are present. These findings obtained by analysing the transition dipole moments are clearly consistent with the ionization yields presented in Fig. 11.7.

In order to establish the connection between higher transition dipole moments and the structural changes during the dynamics, the averaged nuclear displacements have been analysed along the trajectories in terms of the ground state normal modes. In general, it has been found that the discriminating pulses induce conformational differences which are mainly localized in the polar side chains of both molecules. The normal modes most strongly involved typically lie in the low-frequency regime below 100 cm^{-1} . In Fig. 11.10, two prototype low-frequency modes of each molecule, exhibiting large displacements induced by pulses 1 and 2, are shown. The excitation of these modes differs considerably depending on which pulse is acting on the system: Pulse 1 invokes smaller deviations for the normal coordinate Q_2 in RBF, and also for Q_4 the deviation due to pulse 2 is transiently larger than that induced by pulse 1. For the case of FMN, there are larger deviations after a time of 0 ps for Q_2 and Q_9 due to pulse 1 compared to pulse 2. Similar observations can be made for other low-lying modes. Thus, the excitation of these modes leads to molecular conformations which exhibit systematically higher or lower transition dipole moments to higher excited states leading to ionization, depending on which of the two discriminating pulses is acting. Since RBF and FMN only differ in the side chain, differences in the dynamical behaviour can be expected to occur in this part of the molecules due to the interplay of the effect of the heavy phosphorus atom in FMN and the differences of the vibrational density of states in both molecules.

11.4.3 Conclusions

In the present study, FISH simulations in a manifold of 10 electronic states of RBF and FMN under the influence of experimentally shaped laser fields have been performed to obtain mechanistic insight into the processes leading to optimal dynamic discrimination. This represents the very first application of an experimentally optimized laser field in

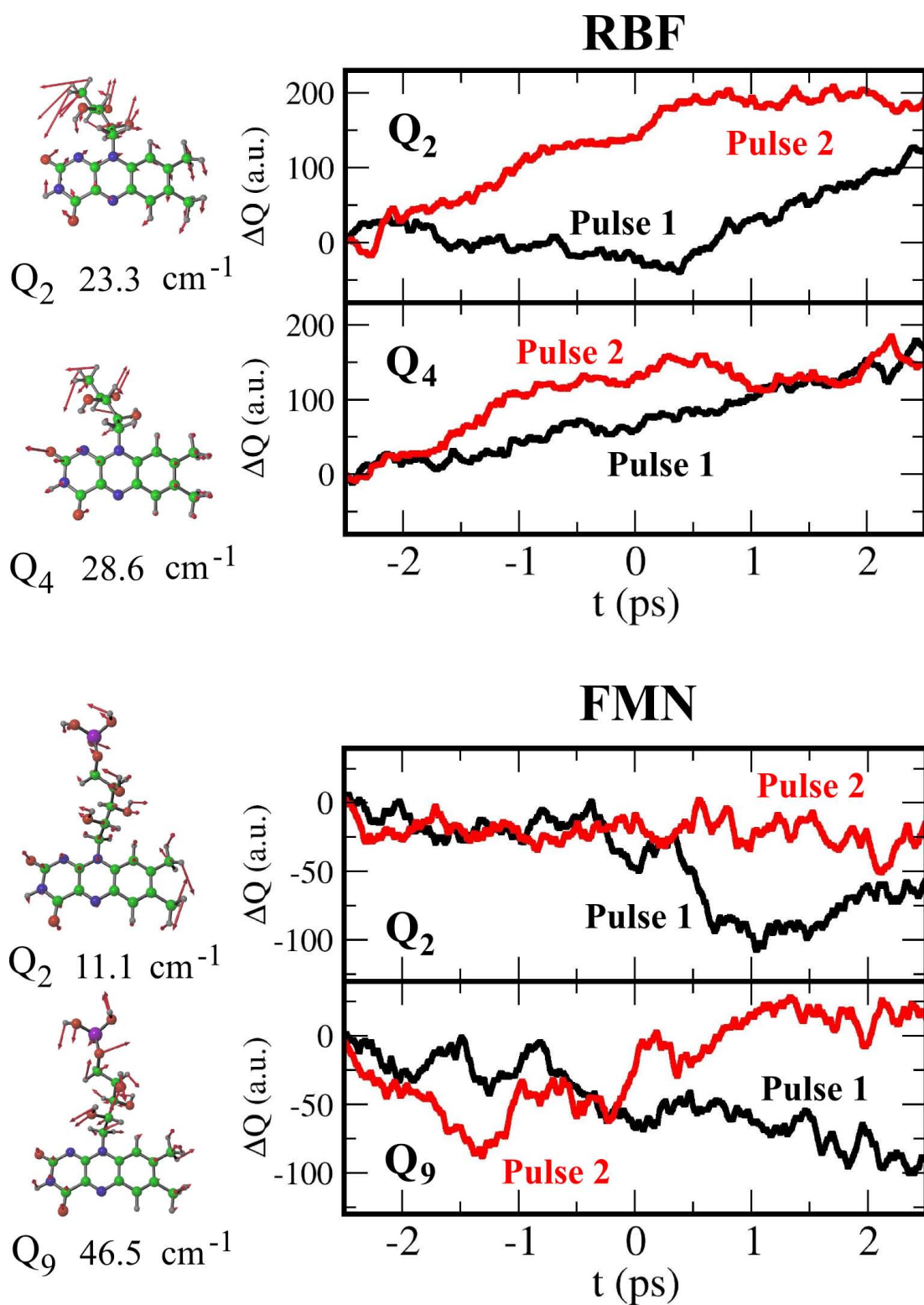


Figure 11.10: Selected averaged normal mode displacements for RBF (upper panel) and FMN (lower panel) induced by pulse 1 (black) and pulse 2 (red).

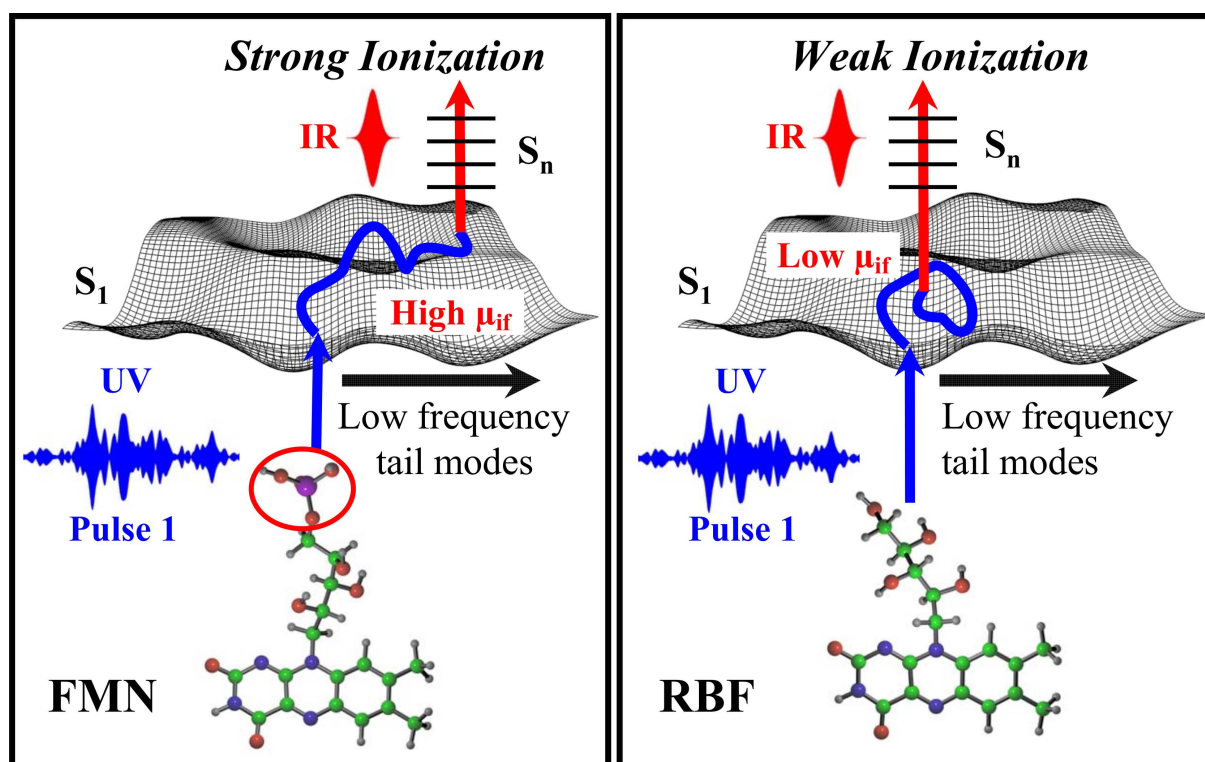


Figure 11.11: Schematic illustration of the optimal dynamic discrimination by shaped laser fields on the example of shaped pulse 1 maximizing the FMN/RBF fluorescence depletion ratio.

mixed quantum-classical dynamics simulations accounting for the full system complexity including environmental effects. The mechanism of the discrimination process found in this way can be summarized as depicted in Fig. 11.11: UV excitation of the molecule induces dynamical processes in excited states which mainly affect the low-frequency vibrational modes of the side chain. The discriminating pulse efficiently drives one of the molecules to regions of the potential energy surface where the transition dipole moments to higher excited states are large, such that the ionization and thus the fluorescence depletion are enhanced (pulse 1 for FMN, pulse 2 for RBF). The same pulse acting on the other molecule (RBF for pulse 1, FMN for pulse 2) suppresses the ionization (fluorescence depletion) by keeping it in regions of the potential energy surface with lower transition dipole moments. Thus, shaped pulses can take advantage of minute differences in the vibrational dynamics and exploit them to manipulate observables such as transition dipole moments, which eventually allows for selective molecular discrimination. This mechanism might represent a general toehold for the discrimination between similar molecules and therefore opens a promising perspective for using optimally shaped laser pulses in bioanalytical applications, in this way increasing the selectivity beyond the current capability.

Conclusion and Outlook

In the present thesis, a theoretical framework for the simulation and control of ultrafast coupled electron-nuclear dynamics in complex molecular systems has been presented and applied. As a methodological basis served the field-induced surface hopping method (FISH), which was extended for the description of complex systems including the solvent environment. The FISH method combines the classical description of the nuclei with the quantum mechanical treatment of the field-driven electronic dynamics, and thus represents a broadly applicable tool for the simulation of laser-driven multistate dynamics in complex systems. In particular, both the simulation of time-resolved spectroscopic observables as well as the active laser control of molecular processes can be performed in the frame of FISH.

Such investigations can be carried out under two complementary points of view. Firstly, theoretical studies can be performed for problems which have not been experimentally addressed so far. This allows for the prediction of new phenomena and may help establish the conditions for experimental observation, thus providing a strong impetus on the design of novel experiments. Besides that, theoretical simulations can also be utilized as a valuable device to supplement experimental findings, often providing a key to the molecular-level understanding of the studied processes. This approach is particularly convenient in the framework of FISH, since this method allows for the use of arbitrarily shaped electric fields, hence experimental laser pulses can be directly employed.

This broad applicational scope has permitted in the frame of this thesis the investigation of a number of intriguing problems in ultrafast spectroscopy and coherent control. With regard to spectroscopy, the FISH method has been extended in order to simulate experimental observables, with a particular focus set on time-resolved photoelectron spectra (TRPES), which represent a sensitive probe for the coupled electron-nuclear dynamics in molecular systems.

This new methodology has been employed to simulate the TRPES of small noble-metal clusters. Such systems are characterized by strongly size-dependent stationary and dynamical properties and are, due to their unique reactive and emissive properties, of large interest in the context of novel catalytic and photonic materials. In particular, the Ag_3 cluster was chosen as a representative system whose ground state dynamics has been already extensively studied previously. In contrast, knowledge about the excited state properties has been scarce so far. Performing FISH dynamics simulations and calculating the associated TRPES signal, the time scale of electronic relaxation from the initially populated states could be determined as about a picosecond, and the accompanying dynamics could be characterized by large-amplitude motions involving all degrees of freedom. The use of two different sets of initial conditions, both for the linear and the triangular struc-

ture of the system, revealed slight differences in the relaxation time scales, but overall, a similar electronic relaxation process leading to the lowest excited states without reaching the electronic ground state has been found. These results allow for proposing novel pump-probe experiments for the verification of the theoretical findings.

The second cluster system for which the relaxation dynamics and TRPES has been studied in this thesis is the anionic Au_7^- cluster, for which experimental TRPES data are available. While previous studies of the relaxation processes initiated after excitation to the lowest excited state have revealed a fast return to the ground state accompanied by a large structural rearrangement [62], the use of higher excitation energy leads to a completely different dynamics. The corresponding experimental TRPES data could be explained, using FISH simulations, as due to a bulk-like electronic relaxation in an electronic manifold of high state density, without the occurrence of large-amplitude nuclear motion. This finding has revealed the existence of different relaxation mechanisms in small clusters, depending on the initial excitation energy.

Beyond the simulation of time-resolved observables, the FISH approach provides also unique opportunities to simulate coherent control processes, which represents the main focus of the applications studied in this thesis. The accuracy of FISH for the control of strong-field electronic population dynamics has been assessed and validated against numerically exact quantum dynamics simulations on the example of selective electronic state population transfer in the K_2 molecule, which has recently been also realized experimentally [374]. In this system, it has been found that, due to subtle phase-matching conditions of the excitation field with the oscillations of the system's electronic coherence terms, selective population of close-lying excited states can be achieved. The very good agreement between the FISH and quantum dynamics simulations has provided a strong fundament for the use of FISH-based simulations in the context of optimal control. This has been exploited for studying applications of optimal control in complex molecular systems interacting with their environment.

For optimal laser control, precisely tuned field-induced excitation and deexcitation processes often play a decisive role. These are counteracted by the intrinsic molecular relaxation phenomena, such as internal conversion, which can, in certain molecules, proceed very fast through conical intersections between electronic states, thus preventing competing radiative processes such as fluorescence. Therefore, in this thesis the question was raised if optimal control may be used to suppress nonradiative relaxation in order to substantially elongate electronic lifetimes. Such a control strategy might be utilized for fluorescence enhancement in molecules with otherwise very small fluorescence quantum yield, which is of interest in the context of biosensing applications. In order to study this problem, the example of the nucleobase adenine embedded in a nanometer-sized droplet of water has been chosen. By employing an analytical pulse parameterization, a set of

pulse trains has been constructed, and the ability of each pulse train to achieve the optimization goal has been assessed. It has been concluded that the sequential population cycling in the excited state manifold, caused by the substructures of the pulse trains, is mainly responsible for an elongation of the excited state lifetimes. This is achieved by utilizing the topography of higher-lying excited-state potential energy surfaces, in which the motion of the adenine molecules towards conical intersections to the ground state is hindered and thus the nonradiative relaxation is retarded. These results represent the first application of theoretical pulse shaping in a full dimensional simulation in the condensed phase.

Besides this predictive aspect of FISH simulations for control applications, it has been also demonstrated in this thesis that laser pulses optimized experimentally can be straightforwardly employed in the simulations, thus allowing for the first time for molecular-level mechanistic insights into the experimentally achieved control of complex systems in the condensed phase. Specifically, this approach has been utilized in order to reveal the molecular mechanism underlying the method of optimal dynamic discrimination (ODD) of almost identical quantum systems. This technique has been previously proved experimentally to allow for the generation of distinctive signals for molecular systems that cannot be distinguished by common spectroscopic means [66]. It is based on initiating dynamical processes in excited states and subsequently probing the dynamics by a strong ionizing infrared laser pulse, which depletes the measured fluorescence yield. In the present thesis, the ODD of the two optically very similar biochromophores riboflavin and flavin mononucleotide has been studied. For these systems, experimental optimal control has succeeded to generate optimized laser pulses that give rise to distinguishable fluorescence depletion signals for the two molecules. FISH simulations of the dynamics induced by these pulses allowed for the identification of the control mechanism, which is based on utilizing minute differences of the transient dynamics in the two molecules. Thereby, one of them is driven to parts of the potential energy surfaces in which the ionization processes are enhanced, while the other molecule is lead to regions where these processes are suppressed. In this way, different ionization efficiencies are reflected in different amounts of fluorescence depletion, thus providing discriminating detection signals.

Altogether, in the present thesis the strength of the mixed quantum-classical FISH approach as a valuable novel tool for the simulation of light-driven nonadiabatic dynamics has been demonstrated. In particular, it could be shown that the applicability ranges from small diatomics up to complex biomolecules in the condensed phase, and both spectroscopic observables as well as optimal control can be simulated. Irrespective of the specific application, the FISH approach always allows for the study of two complementary aspects: The initial theoretical investigation of molecular systems, leading to the prediction of possible experimental outcomes or strategies, as well as the use of simulations as a

device for the interpretation of available experiments.

The results obtained from the investigations presented in this thesis allow for envisioning several lines of possible subsequent research. In the context of TRPES, the study of the time-resolved dynamics in more complex systems, such as biomolecules in solvent environment, is desirable. Moreover, the extension of the method for simulation of TRPES presented here to the simulation of both energy- and angle-resolved photoelectron anisotropy maps would represent an important advancement, and research effort in this direction is presently going on [456]. With regard to coherent control, it might be of interest to use adaptive pulse optimization in order to further improve the controllability of excited state lifetimes. Ultimately, this may lead to invoking fluorescence in otherwise non-fluorescent systems, which has application potential in the area of bioanalytics. Moreover, due to the recently accomplished demonstration that the FISH method is also capable to simulate multiphoton excitation processes [234], an extension of optimal control which exploits the interplay of different excitation regimes may be envisaged.

In summary, the results presented here provide a firm basis for further investigations along different directions of research in ultrafast spectroscopy and molecular optimal control, including both fundamental and application-oriented routes.

Part IV

Appendix

A Computational details and supplementary material for the model studies of Chapter 4

The model studies presented in Chapter 4 have been performed using one-dimensional potentials. In the following, the parameters of these potentials will be given. Throughout this chapter, atomic units are employed, i.e. Planck's constant \hbar equals unity, and the unit of mass is the electron mass m_e , the unit of length is the Bohr radius a_0 , the unit of energy is the Hartree E_H , and the unit of field strength is E_H/ea_0 with e as the elementary charge.

For all model systems presented here, the moving particle was assigned the reduced mass of Na_2 , $m=20953.888 m_e$. The quantum dynamics simulations were performed using the second-order difference propagator (cf. Sec. 1.1, Footnote 3) with a numerical grid of 256 points between 4 and 12 a_0 . The initial wavefunction was chosen as the lowest eigenfunction of a harmonic oscillator potential with $\omega = 9.551006 \cdot 10^{-4} E_H$, which is characterized by a similar curvature around the minimum as the ground state potential used Sec. A.1. In Sec. A.2 and A.3, this harmonic potential was directly employed as the ground state. For the FISH simulations, the Wigner distribution of the lowest harmonic oscillator eigenfunction was sampled at 0 K, and 200 (in Sec. A.3: 300) initial conditions were generated.

A.1 Forbidden hops and internal consistency (Sec. 4.1)

The system is composed of three Morse potentials of the form

$$V(R) = D (1 - e^{-\alpha(R-R_0)})^2 + D_0 \quad (\text{A.1})$$

with the parameters

V	$D(E_H)$	$\alpha(a_0^{-1})$	$R_0(a_0)$	$D_0(E_H)$
0	0.02707	0.4218	5.8	0.0
1	0.03574	0.2872	6.2	0.0665
2	0.02416	0.3338	6.3	0.1167

of which the D and α values were obtained by fitting the Na_2 potentials given in Ref. [457] to Morse functions. For the quantum dynamics simulation a time step of $2.42 \cdot 10^{-3}$ fs was used. For the FISH simulation, the initial Wigner ensemble was propagated twice using the velocity Verlet algorithm with a nuclear time step of 0.5 fs over a total propagation time of 200 fs. The electronic state coefficients were calculated using the fourth order

Runge Kutta method with a time step of $2 \cdot 10^{-4}$ fs. The field coupling was mediated by electronic transition dipole moments between the states 0 and 1 as well as between 1 and 2. The specific values were obtained by interpolation from the data given in Ref. [457]. The electric field was chosen as a sequence of two Gaussian pulses as

$$E(t) = \sum_{i=1}^2 E_i \exp \left[-\frac{4 \ln 2 (t - t_i)^2}{\Delta t_i^2} \right] \cos [\omega_i (t - t_i)], \quad (\text{A.2})$$

with the parameter values

Pulse	$E_i(\text{E}_\text{H}/ea_0)$	Δt_i (fs)	t_i (fs)	$\omega_i(\text{E}_\text{H})$
1	0.002	35	50	0.06703
2			90	0.05023

A.2 Quantum coherence in FISH (Sec. 4.2)

A.2.1 General settings

The classical trajectories in the FISH simulations were propagated using the velocity Verlet algorithm with a nuclear time step of 0.1 fs. The electronic coefficients were calculated using the fourth order Runge Kutta method with a time step of $4 \cdot 10^{-5}$ fs.

The field coupling was mediated for the two-state systems of A.2.2 and A.2.3 by a constant electronic transition dipole moment of $\mu_{01} = 3.6 ea_0$. For the three-state system described in paragraph A.2.4, in addition the transition dipole moment $\mu_{12} = 3.6 ea_0$ was employed. The electric field was chosen as a sequence of two Gaussian pulses as given in Eq. (A.2). In the following, the parameters specific to each model system will be summarized.

A.2.2 Model system for studying the influence of coherence magnitude

In order to construct the double well potential presented in Fig. 4.2, first, two harmonic potentials were considered

$$V(R) = \frac{k}{2} (R - R_0)^2 + V_0 \quad (\text{A.3})$$

with the parameters given as

V	$k(a_0^{-2})$	$R_0(a_0)$	$V_0(\text{E}_\text{H})$
0	0.01912	5.825	-0.01
1	0.04	7.825	0.0

In a second step, a 2×2 matrix was constructed for each point on a grid between 4 and 20 a_0 , with the diagonal elements given by the respective values of two above harmonic potentials, and the off-diagonal elements were set to a value of $V_{01} = 0.001 E_H$. The double well potential was then constructed from the lowest eigenvalues of all matrices as a function of the grid points, for intermediate points during the dynamics the values were interpolated. For the upper state potential, an exponential function given by

$$V = e^{-\alpha R} + V_0 \tag{A.4}$$

was used with the values $\alpha = 0.6 a_0^{-1}$ and $V_0 = -0.00914 E_H$.

The following additional settings were applied for the time propagation:

Propagation time (fs)	Quantum dynamics time step (fs)
120	$3.02 \cdot 10^{-3}$

The field was given according to Eq. (A.2) with the parameter values

Pulse	$E_i(E_H/ea_0)$	Δt_i (fs)	t_i (fs)	$\omega_i(E_H)$
1	varied	5	20	0.03122
2	0.002		80	0.0

where the amplitude of the first pulse was varied between 0.0005 and 0.004 E_H/ea_0 . The classical ensemble was propagated twice for the FISH simulations employing pulse 1 field strengths from 0.002 to 0.004 E_H/ea_0 .

A.2.3 Model system for studying the influence of coherence phase

This model system is composed of two harmonic potentials with parameters

V	$k(a_0^{-2})$	$R_0(a_0)$	$V_0(E_H)$
0	0.01912	5.825	0.0
1	0.005	6.3863	-0.0007876

The following additional settings were applied for the propagation:

Propagation time (fs)	Quantum dynamics time step (fs)
400	$6.05 \cdot 10^{-3}$

The field was given according to Eq. (A.2) with the parameter values

Pulse	$E_i(E_H/ea_0)$	Δt_i (fs)	t_i (fs)	$\omega_i(E_H)$
1	0.001	5	20	0.0
2			331	0.0

The whole ensemble was propagated twice.

A.2.4 Model system for studying pump-probe excitation

For this model system, the previous two harmonic potentials were supplemented by an additional one with the parameters

V	$k(a_0^{-2})$	$R_0(a_0)$	$V_0(E_H)$
2	0.005	6.3863	0.04921

The following additional settings were applied for the propagation:

Propagation time (fs)	Quantum dynamics time step (fs)
200	$6.05 \cdot 10^{-3}$

The field was given according to Eq. (A.2) with the parameter values

Pulse	$E_i(E_H/ea_0)$	Δt_i (fs)	t_i (fs)	$\omega_i(E_H)$
1	0.001	5	20	0.0
2	0.004		175.5	0.05

A.3 Field-induced excitation and distribution of vibronic energy (Sec. 4.3)

The employed potentials are of the harmonic form given in Eq. (A.3), with the parameters

V	$k(a_0^{-2})$	$R_0(a_0)$	$V_0(\text{E}_\text{H})$
0	0.01912	5.825	0.0
1	0.005	6.3863	-0.0007876
2	0.03	6.3863	-0.0047258

For the quantum dynamics simulation a time step of $6.05 \cdot 10^{-3}$ fs was used. For the FISH simulation, the initial Wigner ensemble was propagated twice using the fourth order Runge Kutta algorithm with a nuclear time step of 0.1 fs, over a total propagation time of 200 fs. The electronic coefficients were calculated using the fourth order Runge Kutta method with a time step of $4 \cdot 10^{-5}$ fs. The field coupling was mediated by a constant electronic transition dipole moment of $\mu_{01} = 3.6 ea_0$. The electric field was chosen as a Gaussian pulse as

$$E(t) = E_1 \exp \left[-\frac{4 \ln 2 (t - t_1)^2}{\Delta t_1^2} \right] \cos [\omega_1 (t - t_1)], \quad (\text{A.5})$$

with the parameter values

Pulse	Potentials	$E_1(\text{E}_\text{H}/ea_0)$	Δt_1 (fs)	t_1 (fs)	$\omega_1(\text{E}_\text{H})$
short	V_0+V_1/V_2	0.001	5	20	0.0
long	V_0+V_1	0.001	50	80	0.0
	V_0+V_2	0.002	50	80	0.0

In the following Fig. A.1 the total electronic state populations induced by these pulses are presented, supplementing the time-dependent vibrational state populations discussed in the main part of the thesis, Sec. 4.3.

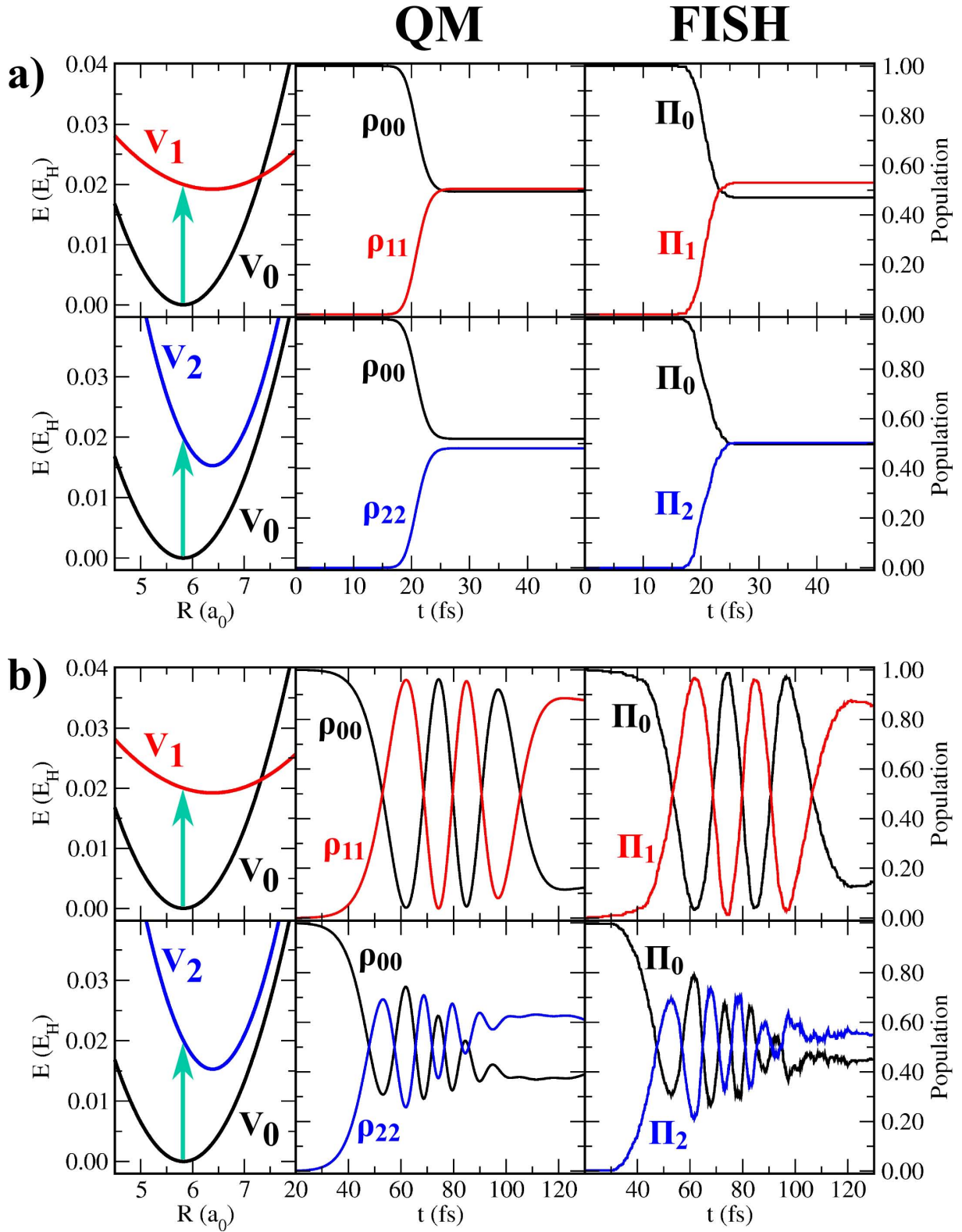


Figure A.1: Electronic state populations after excitation from V_0 to the shallow potential V_1 or to the step potential V_2 , respectively, using a resonant laser pulse of (a) 5 fs and (b) 50 fs duration (indicated as turquoise arrows).

B Field-induced surface hopping with decoherence correction

In order to remedy the problem of a non-decaying coherence magnitude, a modified FISH procedure including an empirical coherence decay correction is devised in the following. This approach is tested on the example of the double-well model system considered in Sec. 4.2 (cf. also Sec. A.2.2 above).

The method for introducing coherence decay is largely similar to the approach presented in Ref. [117], however some modifications are made to account for the specific case of field-induced excitation. The basic idea relies on the creation of Gaussian wavepackets in the coupled electronic states and modelling the coherence decay as a function of the overlap of these wavepackets. For this purpose, to each trajectory in a given state i a Gaussian g_i with fixed width σ is formally assigned. For the non-occupied states j , Gaussian wavepackets $g_{j,k}$ are created if either (i) between two time steps $n\Delta t$ ¹ the occupation probabilities $p_j = |c_j|^2$ increase by more than a threshold Δp_{min}^+ , or (ii) if the trajectory has just hopped out of the particular state j ². These Gaussians are assigned the current trajectory values for position and momentum³, as well as a weight factor, which in case (i) is given by the increase in probability as $w_k^{(j)} = p_j(t) - p_j(t - n\Delta t)$ and for case (ii) is chosen as $w_k^{(j)} = p_j(t)$. This weight is kept fixed for the rest of the dynamics. If more than one Gaussian are assigned to a particular state, their weighted sum $G_j = \sum_k b_k^{(j)} g_{j,k}$, with $b_k^{(j)} = N_j w_k^{(j)} / p_j$ is normalized, i.e. N_j is determined such that $\langle G_j | G_j \rangle = 1$. The Gaussians obtained in this way evolve in time governed by the forces corresponding to the assigned state for the current value of the position coordinate in the given trajectory. The coherence decay is then modelled in the following way: If the overlap $b_k^{(j)} \langle g_{j,k} | G_i \rangle$ of the Gaussian assigned to the current state i and the n 'th Gaussian assigned to another state j drops below a threshold S_{min} , then the respective Gaussian in state j is deleted, and the coefficients for the two states are modified according to

$$\begin{aligned} c_i &= c_i \sqrt{1 - \frac{w_k^{(j)}}{p_i}} \\ c_j &= c_j \sqrt{1 + \frac{w_k^{(j)}}{p_j}}. \end{aligned}$$

¹ Δt is the nuclear time step, n can be set larger than 1 if the correction procedure is not intended to be employed in every step.

²In the procedure outlined in Ref. [117], the case (ii) is not considered. However, this prevents the coherence decay after a successful state switch if the occupation probability of the old state does not increase. Yet irrespective of an increase or decrease of this probability, decoherence should be present for any pair of previously coupled states.

³In Ref. [117], the energy conservation condition for field-free electronic transitions is used instead, and the momentum is reduced accordingly. Formally negative momenta are replaced by a value of zero.

In addition, Gaussians can be also deleted without modifying the state coefficients if the occupation probabilities $p_j = |c_j|^2$ decrease by more than a threshold Δp_{min}^- . In this case, the Gaussians in the respective state are successively removed, beginning with the last created one, until the sum of the associated weights $b_n^{(j)}$ exceeds $|\Delta p_{min}^-|$. Moreover, after a surface hop, all previously existing Gaussians in the newly occupied state are removed either, and only a single one with weight 1 is formally considered, as outlined above.

This methodology has been applied for the double-well model system investigated in Sec. 4.2 with the computational settings as presented in Sec. A.2.2 above. In addition, the following parameters have been employed for the coherence correction:

n	$\sigma(a_0^{-2})$	Δp_{min}^+	Δp_{min}^-	S_{min}
5	0.05	10^{-4}	-10^{-4}	10^{-4}

In this way, the overcoherence in the studied example could be completely removed, leading to correct population dynamics as shown in Fig. 4.3.

C Electronic coherences in K_2

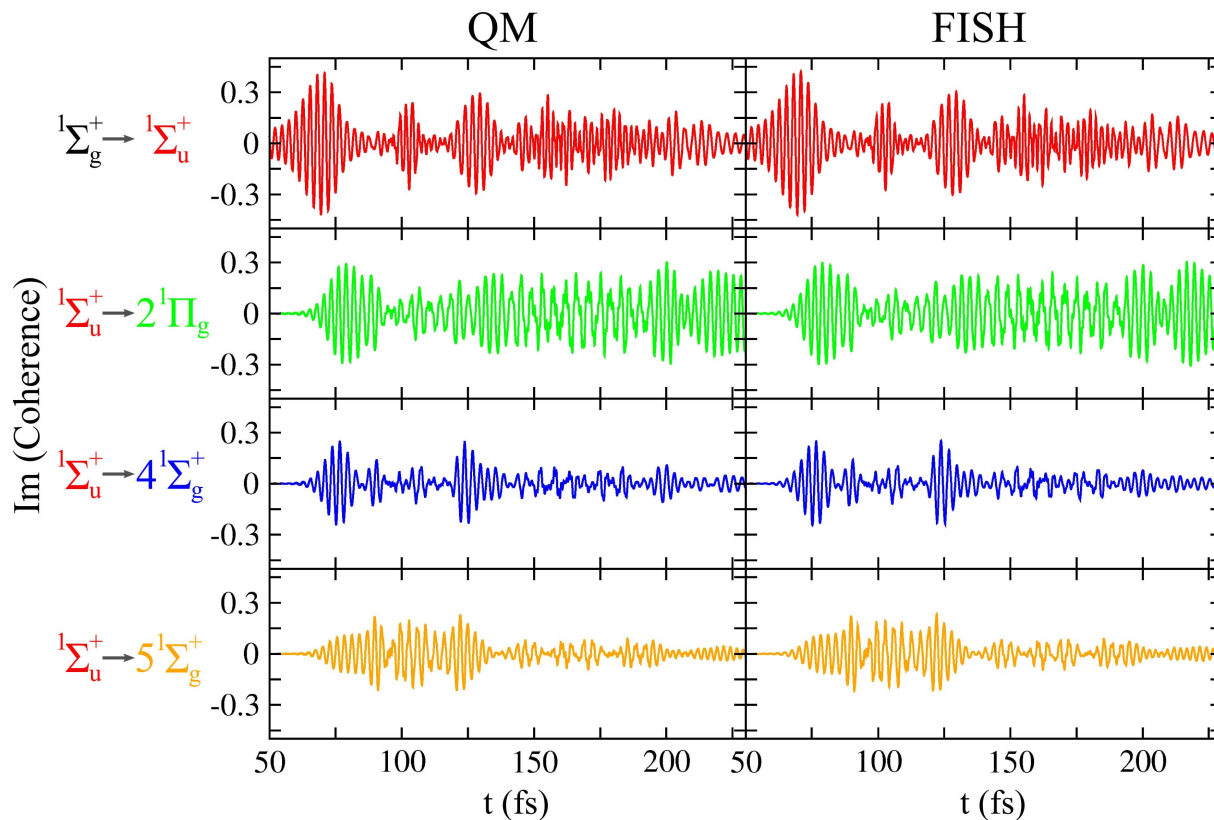


Figure C.1: Strong-field dynamics of K_2 driven by the optimized laser field shown in Fig. 9.5 and Table 9.1. Depicted are the imaginary parts of the electronic coherence for the pairs of states coupled by the laser field obtained both from full quantum dynamics and from FISH simulations. Both results agree excellently.

D FISH dynamics of adenine with electrostatic embedding

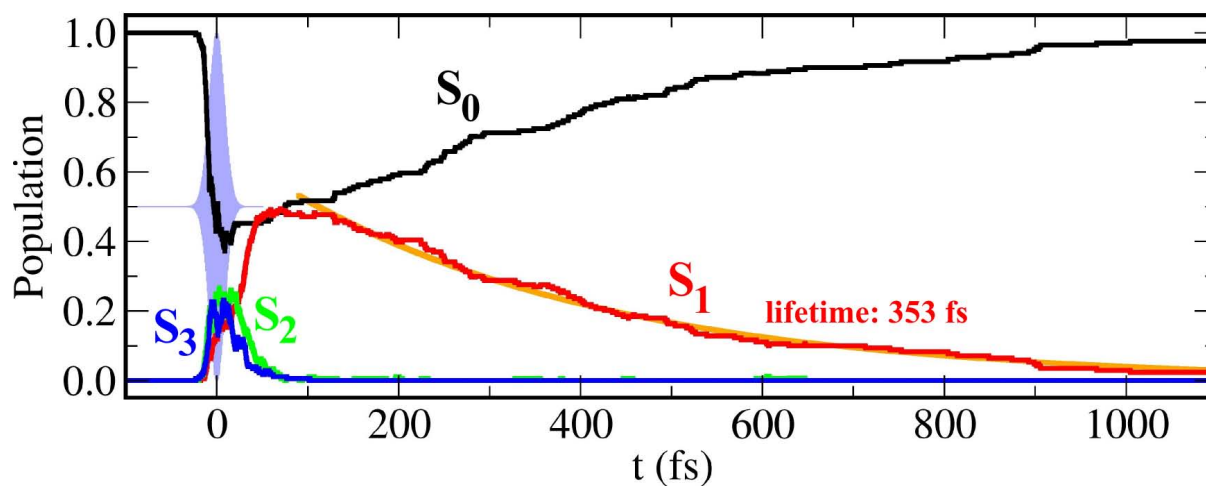


Figure D.1: Population dynamics of solvated adenine, obtained in the framework of the electrostatic embedding technique, induced by the fourier-limited laser pulse at 266 nm (indicated in light blue), showing almost complete return to the ground state after 1000 fs.

E Electronic structure of RBF and FMN

State	$\lambda(\text{nm})$	f_e	Configuration	$ C_i ^2(\%)$	Type of transition
1	395.4	0.119	H \rightarrow L	78	$\pi\pi^*$
2	345.1	0.005	H-3 \rightarrow L	63	$n\pi^*$
			H-5 \rightarrow L	14	$n\pi^*$
3	340.5	0.046	H \rightarrow L+1	48	$\pi\pi^*$
			H-1 \rightarrow L	32	$\pi\pi^*$
4	303.5	0.019	H \rightarrow L+3	83	$\pi \rightarrow$ side chain
			H \rightarrow L+2	20	$\pi\pi^*$
5	295.8	0.489	H-1 \rightarrow L+1	15	$\pi\pi^*$
			H \rightarrow L+1	15	$\pi\pi^*$
			H-1 \rightarrow L	12	$\pi\pi^*$
6	291.6	0.007	H-5 \rightarrow L	34	$n\pi^*$
			H-3 \rightarrow L+1	28	$n\pi^*$
7	276.4	0.086	H-2 \rightarrow L	72	$n\pi^*$
			H-6 \rightarrow L	25	$\pi\pi^*$
8	273.1	0.279	H-1 \rightarrow L	19	$\pi\pi^*$
			H \rightarrow L+1	13	$\pi\pi^*$
			H-1 \rightarrow L+1	12	$\pi\pi^*$
			H \rightarrow L+2	27	$\pi\pi^*$
9	265.5	0.236	H-1 \rightarrow L	17	$\pi\pi^*$
			H-6 \rightarrow L	15	$\pi\pi^*$

Table E.1: Excited electronic states of RBF obtained with semiempirical PM3-CI for the lowest energy optimized geometry. The acronyms H and L correspond to highest occupied and lowest unoccupied molecular orbital. The active space involves 11 occupied and 6 unoccupied molecular orbitals. Single excitations out of the closed-shell ground state determinant and of the following additional reference configurations are accounted for: H \rightarrow L, H \rightarrow L+1, H \rightarrow L+2, H \rightarrow L+3, H-1 \rightarrow L, H-2 \rightarrow L, H-3 \rightarrow L, H-5 \rightarrow L, H-6 \rightarrow L, H-10 \rightarrow L, H-3 \rightarrow L+1.

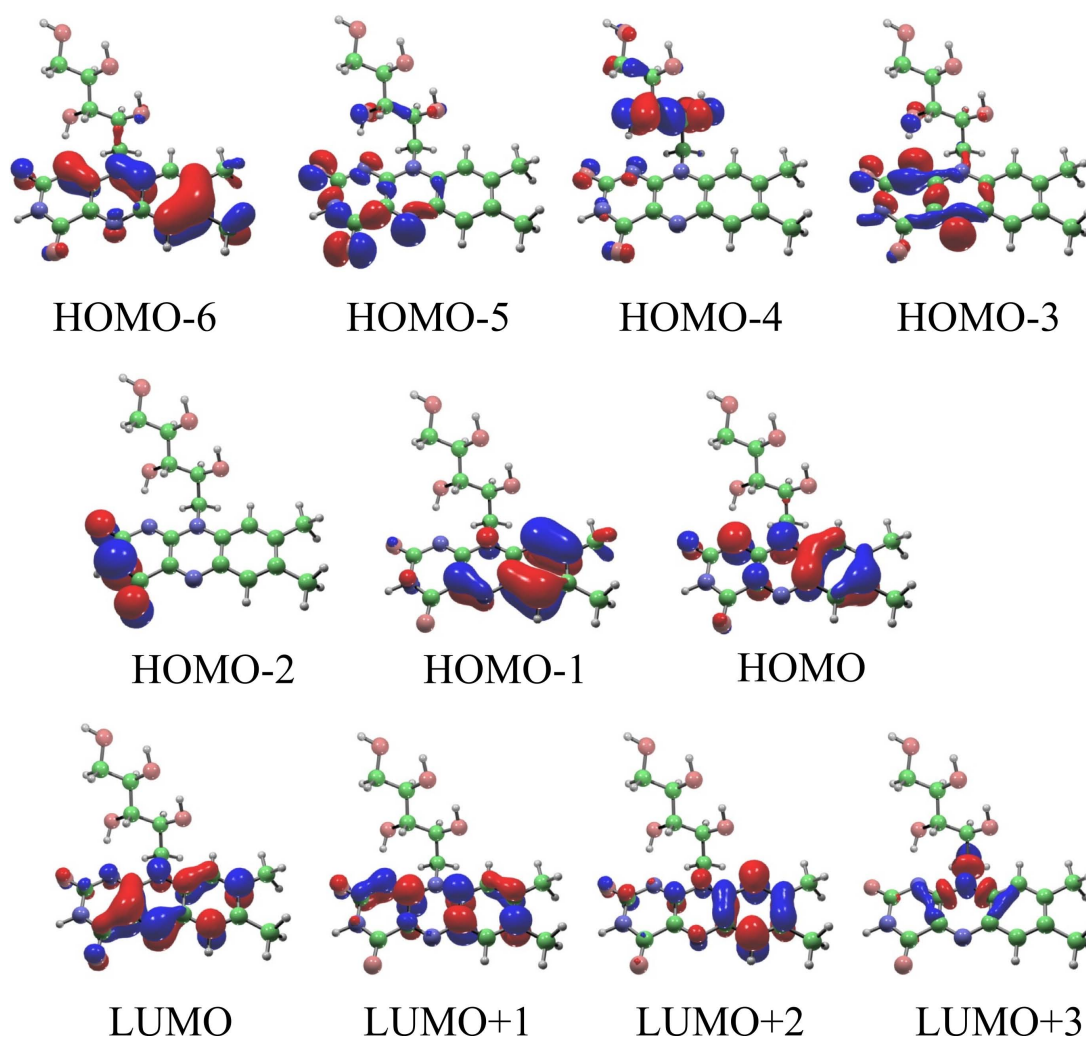


Figure E.1: Molecular orbitals of RBF obtained from semiempirical PM3-CI.

State	$\lambda(\text{nm})$	f_e	Configuration	$ C_i ^2(\%)$	Type of transition
1	394.2	0.120	H→L	78	$\pi\pi^*$
2	340.7	0.046	H→L+1	49	$\pi\pi^*$
			H-1→L	36	$\pi\pi^*$
3	326.4	0.005	H-3→L	70	$n\pi^*$
			H-5→L	14	$n\pi^*$
4	299.3	0.090	H→L+3	71	$\pi \rightarrow$ side chain
			H→L+3	18	$\pi \rightarrow$ side chain
5	295.1	0.441	H→L+2	16	$\pi\pi^*$
			H-1→L+1	14	$\pi\pi^*$
			H→L+1	13	$\pi\pi^*$
6	281.6	0.002	H-5→L	41	$n\pi^*$
			H-3→L+1	30	$n\pi^*$
7	273.5	0.021	H-2→L	30	$n\pi^*$
			H-1→L+1	16	$\pi\pi^*$
			H-6→L	15	$\pi\pi^*$
8	270.5	0.323	H-2→L	40	$n\pi^*$
			H-6→L	16	$\pi\pi^*$
9	265.0	0.435	H→L+2	23	$\pi\pi^*$
			H-1→L	23	$\pi\pi^*$
			H-6→L	10	$\pi\pi^*$

Table E.2: Excited electronic states of FMN obtained with semiempirical PM3-CI for the lowest energy optimized geometry. The acronyms H and L correspond to highest occupied and lowest unoccupied molecular orbital. The active space involves 11 occupied and 6 unoccupied molecular orbitals. Single excitations out of the closed-shell ground state determinant configuration and of the following additional reference configurations are accounted for: H→L, H→L+1, H→L+2, H→L+3, H-1→L, H-2→L, H-3→L, H-5→L, H-6→L, H-10→L, H-3→L+1.

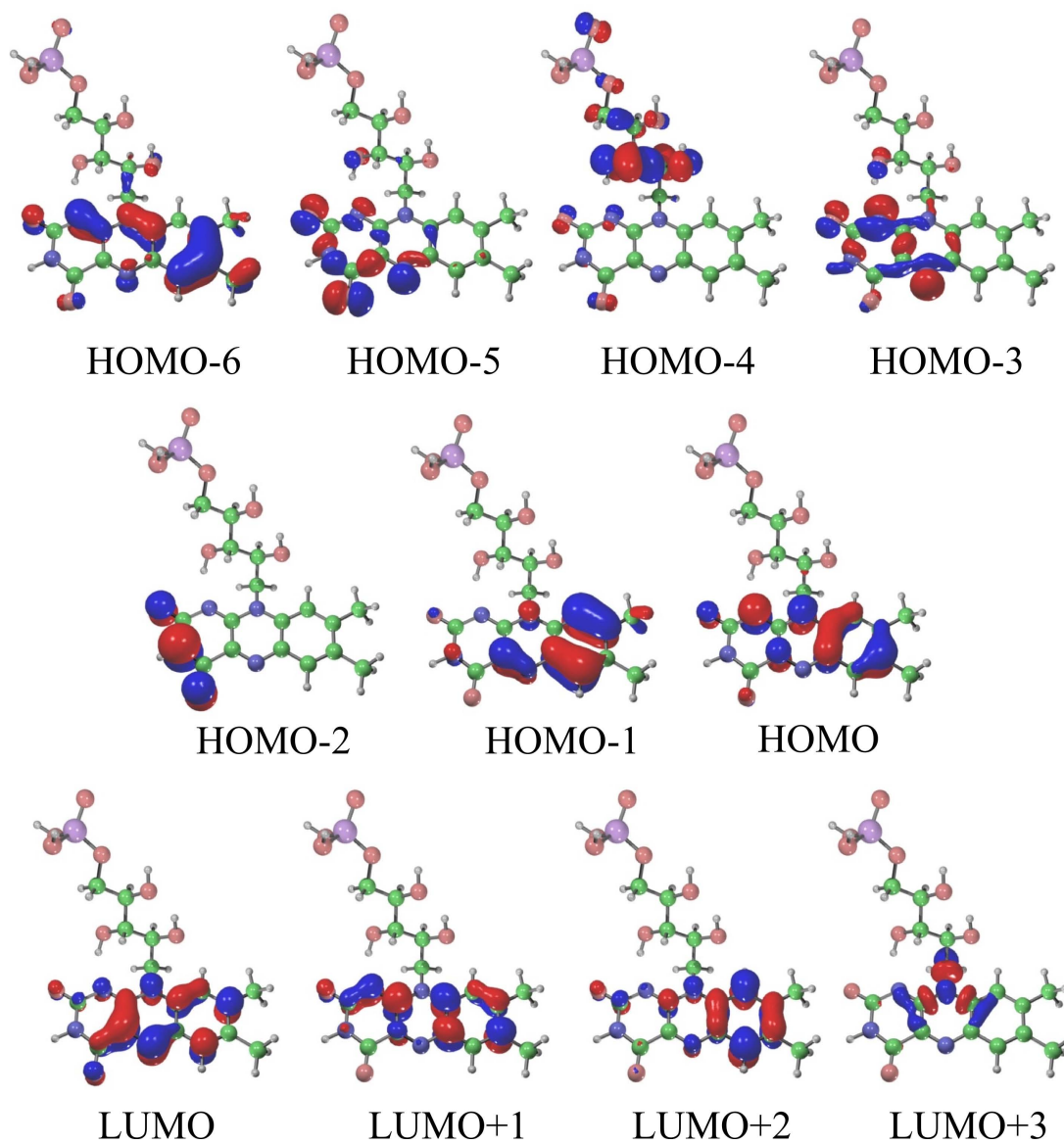


Figure E.2: Molecular orbitals of FMN obtained from semiempirical PM3-CI.

Bibliography

- [1] H. Hartridge and F. J. W. Roughton, Proc. Roy. Soc. London A **104**, 376 (1923).
- [2] B. Chance, J. Franklin Inst. **229**, 455, 613, 737 (1940).
- [3] S. Arrhenius, Z. Phys. Chem. **4**, 226 (1889).
- [4] G. Wedler, *Lehrbuch der Physikalischen Chemie*, VCH, Weinheim, 1987.
- [5] E. Schrödinger, Ann. Physik **79**, 361 (1926).
- [6] E. Schrödinger, Ann. Physik **79**, 489 (1926).
- [7] P. A. M. Dirac, *The principles of quantum mechanics*, 4th edition, Oxford Univ. Press, London, 1958.
- [8] P. A. M. Dirac, Proc. Roy. Soc. London A **123**, 714 (1929).
- [9] H. Eyring, J. Chem. Phys. **3**, 107 (1935).
- [10] M. G. Evans and M. Polanyi, Trans. Faraday Soc. **31**, 875 (1935).
- [11] M. Eigen, Discuss. Farad. Soc. **17**, 194 (1954).
- [12] R. G. W. Norrish and G. Porter, Nature **164**, 658 (1949).
- [13] G. Porter, Proc. Roy. Soc. London A **200**, 284 (1950).
- [14] A. H. Zewail, Pure Appl. Chem. **72**, 2219 (2000).
- [15] W. Sibbet, A. A. Lagatsky, and C. T. A. Brown, Opt. Express **20**, 6989 (2012).
- [16] A. H. Zewail, Faraday Discuss. Chem. Soc. **91**, 207 (1991).
- [17] M. F. Kling and M. J. J. Vrakking, Annu. Rev. Phys. Chem. **59**, 463 (2008).
- [18] F. Krausz and M. Ivanov, Rev. Mod. Phys. **81**, 163 (2009).
- [19] I. V. Hertel and W. Radloff, Rep. Prog. Phys. **69**, 1897 (2006).
- [20] D. J. Tannor and S. A. Rice, J. Chem. Phys. **83**, 5013 (1985).
- [21] P. Brumer and M. Shapiro, Chem. Phys. Lett. **126**, 541 (1986).
- [22] M. Shapiro and P. Brumer, J. Chem. Phys. **84**, 4103 (1986).
- [23] T. Baumert, T. Brixner, V. Seyfried, M. Strehle, and G. Gerber, Appl. Phys. B **65**, 779 (1997).
- [24] D. Meshulach, D. Yelin, and Y. Silberberg, Opt. Commun. **138**, 345 (1997).
- [25] D. Yelin, D. Meshulach, and Y. Silberberg, Opt. Lett. **22**, 1793 (1997).
- [26] E. Zeek, K. Maginnis, S. Backus, U. Russek, M. M. Murnane, G. Mourou, H. C. Kapteyn, and G. Vdovin, Opt. Lett. **24**, 493 (1999).
- [27] R. S. Judson and H. Rabitz, Phys. Rev. Lett. **62**, 1500 (1992).
- [28] T. Baumert, J. Helbing, and G. Gerber, Advances in Chemical Physics **101**, 47 (1997).
- [29] S. A. Rice and M. Zhao, *Optical Control of Molecular Dynamics*, John Wiley & Sons, Inc., New York, 2000.

- [30] P. W. Brumer and M. Shapiro, *Principles of the Quantum Control of Molecular Processes*, Wiley-VCH, Berlin, 2003.
- [31] T. Brixner and G. Gerber, *ChemPhysChem* **4**, 418 (2003).
- [32] M. Dantus and V. V. Lozovoy, *Chem. Rev.* **104**, 1813 (2004).
- [33] L. Wöste and O. Kühn, *Analysis and Control of Ultrafast Photoinduced Reactions*, Springer Series in Chemical Physics 87, 2007.
- [34] P. Nuernberger, G. Vogt, T. Brixner, and G. Gerber, *Phys. Chem. Chem. Phys.* **9**, 2470 (2007).
- [35] M. Born and R. Oppenheimer, *Ann. Physik (Leipzig)* **84**, 457 (1927).
- [36] W. Heitler and F. London, *Z. Phys.* **44**, 455 (1927).
- [37] H. Eyring and M. Polanyi, *Z. Phys. Chem. Abt. B* **12**, 279 (1931).
- [38] P. Ehrenfest, *Z. Phys.* **45**, 455 (1927).
- [39] J. O. Hirschfelder, H. Eyring, and B. Topley, *J. Chem. Phys.* **4**, 170 (1936).
- [40] M. Karplus, R. N. Porter, and R. D. Sharma, *J. Chem. Phys.* **43**, 3259 (1965).
- [41] S. Y. Wang and M. Karplus, *J. Am. Chem. Soc.* **95**, 8160 (1973).
- [42] A. Warshel and M. Karplus, *Chem. Phys. Lett.* **32**, 11 (1975).
- [43] C. Leforestier, *J. Chem. Phys.* **68**, 4406 (1978).
- [44] R. Car and M. Parrinello, *Phys. Rev. Lett.* **55**, 2471 (1985).
- [45] D. Marx and J. Hutter, *Ab initio Molecular Dynamics: Theory and Implementation*, in: *Modern Methods and Algorithms of Quantum Chemistry*, p. 329, Ed. J. Grotendorst, Forschungszentrum Jülich, 2000.
- [46] M. E. Tuckerman, *J. Phys.: Condens. Matter* **14**, R1297 (2002).
- [47] L. D. Landau, *Phys. Z. Sowj.* **2**, 46 (1932).
- [48] C. Zener, *Proc. Roy. Soc. (London) A* **137**, 696 (1932).
- [49] E. C. G. Stückelberg, *Helv. Phys. Acta* **5**, 369 (1932).
- [50] A. Bjerre and E. E. Nikitin, *Chem. Phys. Lett.* **1**, 179 (1967).
- [51] J. C. Tully and R. K. Preston, *J. Chem. Phys.* **55**, 562 (1971).
- [52] J. C. Tully, *J. Chem. Phys.* **93**, 1061 (1990).
- [53] D. Kohen, F. H. Stillinger, and J. C. Tully, *J. Chem. Phys.* **109**, 4713 (1998).
- [54] M. Barbatti, *WIREs Comput. Mol. Sci.* **1**, 620 (2011).
- [55] R. Mitrić, J. Petersen, and V. Bonačić-Koutecký, *Phys. Rev. A* **79**, 053416 (2009).
- [56] A. Stolow, A. E. Bragg, and D. M. Neumark, *Chem. Rev.* **104**, 1719 (2004).
- [57] A. Stolow and J. Underwood, *Adv. Chem. Phys.* **139**, 497 (2008).
- [58] G. Wu, P. Hockett, and A. Stolow, *Phys. Chem. Chem. Phys.* **13**, 18447 (2011).
- [59] R. Mitrić, J. Petersen, M. Wohlgemuth, U. Werner, V. Bonačić-Koutecký, L. Wöste, and J. Jortner, *J. Phys. Chem. A* **115**, 3755 (2011).

- [60] R. Mitrić, J. Petersen, M. Wohlgemuth, U. Werner, and V. Bonačić-Koutecký, *Phys. Chem. Chem. Phys.* **13**, 8690 (2011).
- [61] J. Stanzel, M. Neeb, W. Eberhardt, P. G. Lisinetskaya, J. Petersen, and R. Mitrić, *Phys. Rev. A* **85**, 013201 (2012).
- [62] J. Stanzel, F. Burmeister, M. Neeb, W. Eberhardt, R. Mitrić, C. Bürgel, and V. Bonačić-Koutecký, *J. Chem. Phys.* **127**, 164312 (2007).
- [63] J. Petersen and R. Mitrić, *Phys. Chem. Chem. Phys.* **14**, 8299 (2012).
- [64] J. Petersen, M. Wohlgemuth, B. Sellner, V. Bonačić-Koutecký, H. Lischka, and R. Mitrić, *Phys. Chem. Chem. Phys.* **14**, 4687 (2012).
- [65] C. E. Crespo-Hernandez, B. Cohen, P. M. Hare, and B. Kohler, *Chem. Rev.* **104**, 1977 (2004).
- [66] M. Roth, L. Guyon, J. Roslund, V. Boutou, F. Courvoisier, J.-P. Wolf, and H. Rabitz, *Phys. Rev. Lett.* **102**, 253001 (2009).
- [67] J. Petersen, R. Mitrić, V. Bonačić-Koutecký, J.-P. Wolf, J. Roslund, and H. Rabitz, *Phys. Rev. Lett.* **105**, 073003 (2010).
- [68] M. Born, *Nachr. Akad. Wiss. Göttingen*, Nr. 6 (1951).
- [69] M. Born and K. Huang, *Dynamical Theory of Crystal Lattices*, Oxford University Press, 1954.
- [70] D. Kosloff and R. Kosloff, *Comp. Phys. Comm.* **30**, 333 (1983).
- [71] A. Askar and A. S. Cakmak, *J. Chem. Phys.* **68**, 2794 (1978).
- [72] R. Kosloff, *J. Phys. Chem.* **92**, 2087 (1988).
- [73] P. Jungwirth and B. Gerber, *Chem. Rev.* **99**, 1583 (1999).
- [74] H.-D. Meyer, U. Manthe, and L. S. Cederbaum, *Chem. Phys. Lett.* **165**, 73 (1990).
- [75] Q. Meng, S. Faraji, O. Vendrell, and H.-D. Meyer, *J. Chem. Phys.* **137**, 134302 (2012).
- [76] E. J. Heller, *J. Chem. Phys.* **62**, 1544 (1975).
- [77] E. J. Heller, *J. Chem. Phys.* **75**, 2923 (1981).
- [78] E. Madelung, *Z. Phys.* **40**, 322 (1926).
- [79] D. Bohm, *Phys. Rev.* **85**, 166 (1952).
- [80] L. D. Landau, *Z. Phys.* **45**, 430 (1927).
- [81] J. von Neumann, *Mathematische Grundlagen der Quantenmechanik*, Springer-Verlag, Berlin, 1932.
- [82] E. Wigner, *Phys. Rev.* **40**, 749 (1932).
- [83] M. Hillery, R. F. O'Connell, M. O. Scully, and E. P. Wigner, *Phys. Rep.* **106**, 121 (1984).
- [84] G. A. Worth and L. S. Cederbaum, *Annu. Rev. Phys. Chem.* **55**, 127 (2004).
- [85] T.-S. Chu, Y. Zhang, and K.-L. Han, *Int. Rev. Phys. Chem.* **25**, 201 (2006).
- [86] N. F. Mott, *Proc. Cambridge Philos. Soc.* **27**, 553 (1931).
- [87] T. A. Niehaus, D. Heringer, B. Torralva, and T. Frauenheim, *Eur. Phys. J. D* **35**, 467 (2005).
- [88] D. A. Micha, *J. Chem. Phys.* **78**, 7138 (1983).

Bibliography

- [89] Z. Kirson, R. B. Gerber, A. Nitzan, and M. A. Ratner, *Surf. Sci.* **137**, 527 (1984).
- [90] S. I. Sawada, A. Nitzan, and H. Metiu, *Phys. Rev. B* **32**, 851 (1985).
- [91] K. C. Kulander, K. R. S. Devi, and S. E. Koonin, *Phys. Rev. A* **25**, 2968 (1982).
- [92] K. Runge, D. A. Micha, and E. Q. Feng, *Int. J. Quantum Chem. Suppl.* **24**, 781 (1990).
- [93] D. A. Micha and K. Runge, *Phys. Rev. A* **50**, 322 (1994).
- [94] D. A. Micha, *J. Phys. Chem. A* **103**, 7562 (1999).
- [95] X. Li, J. C. Tully, H. B. Schlegel, and M. J. Frisch, *J. Chem. Phys.* **123**, 084106 (2005).
- [96] S. Klein, M. J. Bearpark, B. R. Smith, M. A. Robb, M. Olivucci, and F. Bernardi, *Chem. Phys. Lett.* **292**, 259 (1998).
- [97] T. Kunert and R. Schmidt, *Eur. Phys. J. D* **25**, 15 (2003).
- [98] A. Castro, M. A. L. Marques, J. A. Alonso, G. F. Bertsch, and A. Rubio, *Eur. Phys. J. D* **28**, 211 (2004).
- [99] I. Tavernelli, U. F. Rörig, and U. Röthlisberger, *Mol. Phys.* **103**, 963 (2005).
- [100] Y. Tateyama, N. Oyama, T. Ohno, and Y. Miyamoto, *J. Chem. Phys.* **124**, 124507 (2006).
- [101] F. Wang, C. Y. Yam, L. H. Hu, and G. H. Chen, *J. Chem. Phys.* **135**, 044126 (2011).
- [102] N. L. Doltsinis and D. Marx, *J. Theor. Comp. Chem.* **1**, 319 (2002).
- [103] J. R. Stine and J. T. Muckerman, *J. Chem. Phys.* **65**, 3975 (1976).
- [104] N. C. Blais and D. G. Truhlar, *J. Chem. Phys.* **79**, 1334 (1983).
- [105] D. Papierowska-Kaminski, M. Persico, and V. Bonačić-Koutecký, *Chem. Phys. Lett.* **113**, 264 (1985).
- [106] J. C. Tully, *Faraday Discuss.* **110**, 407 (1998).
- [107] M. F. Herman, *J. Chem. Phys.* **81**, 754 (1984).
- [108] M. F. Herman, *J. Chem. Phys.* **81**, 764 (1984).
- [109] D. F. Coker and L. Xiao, *J. Chem. Phys.* **102**, 496 (1995).
- [110] S. Hammes-Schiffer and J. C. Tully, *J. Chem. Phys.* **101**, 4657 (1994).
- [111] E. Fabiano, T. W. Keal, and W. Thiel, *Chem. Phys.* **349**, 334 (2008).
- [112] U. Müller and G. Stock, *J. Chem. Phys.* **107**, 6230 (1997).
- [113] J.-Y. Fang and S. Hammes-Schiffer, *J. Phys. Chem. A* **103**, 9399 (1999).
- [114] C. Zhu, S. Nangia, A. Jasper, and D. G. Truhlar, *J. Chem. Phys.* **121**, 7658 (2004).
- [115] C. Zhu, A. Jasper, and D. G. Truhlar, *J. Chem. Theory Comput.* **1**, 527 (2005).
- [116] G. Granucci and M. Persico, *J. Chem. Phys.* **126**, 134114 (2007).
- [117] G. Granucci, M. Persico, and A. Zocante, *J. Chem. Phys.* **133**, 134111 (2010).
- [118] N. Shenvi, J. E. Subotnik, and Y. W., *J. Chem. Phys.* **134**, 144102 (2011).
- [119] J. E. Subotnik and N. Shenvi, *J. Chem. Phys.* **134**, 024105 (2011).

Bibliography

- [120] J. E. Subotnik, *J. Phys. Chem. A* **115**, 12083 (2011).
- [121] N. Shenvi, J. E. Subotnik, and W. Yang, *J. Chem. Phys.* **135**, 024101 (2011).
- [122] N. Shenvi and W. Yang, *J. Chem. Phys.* **137**, 22A528 (2012).
- [123] M. Barbatti, M. Ruckebauer, and H. Lischka, *J. Chem. Phys.* **122**, 174307 (2005).
- [124] R. Mitrić, V. Bonačić-Koutecký, J. Pittner, and H. Lischka, *J. Chem. Phys.* **125**, 024303 (2006).
- [125] E. Fabiano and W. Thiel, *J. Phys. Chem. A* **112**, 6859 (2008).
- [126] M. Barbatti and H. Lischka, *J. Am. Chem. Soc.* **130**, 6831 (2008).
- [127] U. Werner, R. Mitrić, T. Suzuki, and V. Bonačić-Koutecký, *Chem. Phys.* **349**, 319 (2008).
- [128] Z. Lan, E. Fabiano, and W. Thiel, *J. Phys. Chem. B* **113**, 3548 (2009).
- [129] N. L. Doltsinis and D. Marx, *Phys. Rev. Lett.* **88**, 166402 (2002).
- [130] C. F. Craig, W. R. Duncan, and O. V. Prezhdo, *Phys. Rev. Lett.* **95**, 163001 (2005).
- [131] E. Tapavicza, I. Tavernelli, and U. Röthlisberger, *Phys. Rev. Lett.* **98**, 023001 (2007).
- [132] R. Mitrić, U. Werner, and V. Bonačić-Koutecký, *J. Chem. Phys.* **129**, 164118 (2008).
- [133] G. Granucci, M. Persico, and A. Toniolo, *J. Chem. Phys.* **114**, 10608 (2001).
- [134] M. Barbatti, G. Granucci, M. Persico, M. Ruckebauer, M. Vazdar, M. Eckert-Maksić, and H. Lischka, *J. Photochem. Photobiol. A: Chem.* **190**, 228 (2007).
- [135] C. Ciminelli, G. Granucci, and M. Persico, *Chem. Phys.* **349**, 325 (2008).
- [136] Z. Lan, Y. Lu, E. Fabiano, and W. Thiel, *ChemPhysChem* **12**, 1989 (2011).
- [137] B. Heggen, Z.-G. Lan, and W. Thiel, *Phys. Chem. Chem. Phys.* **14**, 8137 (2012).
- [138] M. Ruckebauer, M. Barbatti, B. Sellner, T. Müller, and H. Lischka, *J. Phys. Chem. A* **114**, 12585 (2010).
- [139] W. C. Chung, S. Nanbu, and T. Ishida, *J. Phys. Chem. B* **116**, 8009 (2012).
- [140] T. Zelený, M. Ruckebauer, A. J. A. Aquino, T. Müller, F. Lankáš, T. Dršata, W. L. Hase, D. Nachtigallova, and H. Lischka, *J. Am. Chem. Soc.* **134**, 13662 (2012).
- [141] M. Wohlgenuth, R. Mitrić, and V. Bonačić-Koutecký, *J. Chem. Phys.* **135**, 054105 (2011).
- [142] I. Tavernelli, B. F. E. Cuchod, and U. Röthlisberger, *Chem. Phys.* **391**, 101 (2011).
- [143] S. Hammes-Schiffer, *J. Phys. Chem. A* **102**, 10443 (1998).
- [144] C. C. Martens and J.-Y. Fang, *J. Chem. Phys.* **106**, 4918 (1997).
- [145] R. Kapral and G. Ciccotti, *J. Chem. Phys.* **110**, 8919 (1999).
- [146] A. Donoso and C. C. Martens, *J. Phys. Chem. A* **102**, 4291 (1998).
- [147] A. Donoso and C. C. Martens, *J. Chem. Phys.* **112**, 3980 (2000).
- [148] E. Roman and C. C. Martens, *J. Chem. Phys.* **121**, 11572 (2004).
- [149] E. Roman and C. C. Martens, *J. Phys. Chem. A* **111**, 10256 (2007).
- [150] S. Nielsen, R. Kapral, and G. Ciccotti, *J. Chem. Phys.* **112**, 6543 (2000).

Bibliography

- [151] M. Santer, U. Manthe, and G. Stock, *J. Chem. Phys.* **114**, 2001 (2001).
- [152] C. C. Wan and J. Schofield, *J. Chem. Phys.* **112**, 4447 (2000).
- [153] K. Ando and M. Santer, *J. Chem. Phys.* **118**, 10399 (2003).
- [154] I. Horenko, C. Salzmann, B. Schmidt, and C. Schütte, *J. Chem. Phys.* **117**, 11075 (2002).
- [155] A. Donoso and C. C. Martens, *Phys. Rev. Lett.* **87**, 223202 (2001).
- [156] A. Donoso, Y. Zheng, and C. C. Martens, *J. Chem. Phys.* **119**, 5010 (2003).
- [157] P. A. M. Dirac, *Phys. Z. Sowj.* **3**, 64 (1933).
- [158] R. P. Feynman, *Rev. Mod. Phys.* **20**, 367 (1948).
- [159] W. H. Miller, *J. Phys. Chem.* **105**, 2942 (2001).
- [160] M. Thoss and H. Wang, *Annu. Rev. Phys. Chem.* **55**, 299 (2004).
- [161] P. Pechukas, *Phys. Rev.* **181**, 174 (1969).
- [162] F. Webster, P. J. Rossky, and R. A. Friesner, *J. Chem. Phys.* **100**, 4835 (1994).
- [163] G. Stock and M. Thoss, *Phys. Rev. Lett.* **78**, 578 (1997).
- [164] X. Sun and W. H. Miller, *J. Chem. Phys.* **106**, 916 (1997).
- [165] M. Thoss, W. H. Miller, and G. Stock, *J. Chem. Phys.* **112**, 10282 (2000).
- [166] T. J. Martinez, M. Ben-Nun, and G. Ashkenazi, *J. Chem. Phys.* **104**, 2847 (1996).
- [167] T. J. Martinez, M. Ben-Nun, and R. D. Levine, *J. Phys. Chem.* **100**, 7884 (1996).
- [168] M. Ben-Nun and T. J. Martinez, *J. Chem. Phys.* **108**, 7244 (1998).
- [169] M. Ben-Nun, J. Quenneville, and T. J. Martinez, *J. Phys. Chem. A* **104**, 5161 (2000).
- [170] T. J. Martinez and R. D. Levine, *J. Chem. Phys.* **105**, 6334 (1996).
- [171] M. Ben-Nun and T. J. Martinez, *J. Chem. Phys.* **112**, 6113 (2000).
- [172] K. K. Baeck and T. J. Martinez, *Chem. Phys. Lett.* **375**, 299 (2003).
- [173] A. Toniolo, S. Olsen, L. Manohar, and T. J. Martinez, *Farad. Discuss.* **127**, 149 (2004).
- [174] A. M. Virshup, C. Punwong, T. V. Pogorelov, B. A. Lindquist, C. Ko, and T. J. Martinez, *J. Phys. Chem. B* **113**, 3280 (2009).
- [175] B. G. Levine and T. J. Martinez, *J. Phys. Chem. A* **113**, 12815 (2009).
- [176] S. Olsen, K. Lamothe, and T. J. Martinez, *J. Am. Chem. Soc.* **132**, 1192 (2010).
- [177] H. Tao, T. K. Allison, T. W. Wright, A. M. Stooke, C. Khurmi, J. van Tilborg, Y. Liu, R. C. Falcone, A. Belkacem, and T. J. Martinez, *J. Chem. Phys.* **134**, 244306 (2011).
- [178] J. Kim, H. Tao, J. L. White, V. S. Petrović, T. J. Martinez, and P. H. Bucksbaum, *J. Phys. Chem. A* **116**, 2758 (2012).
- [179] S. Toxvaerd, *Phys. Rev. E* **47**, 343 (1992).
- [180] L. Verlet, *Phys. Rev.* **159**, 98 (1967).
- [181] W. C. Swope, H. C. Andersen, P. H. Berens, and K. R. Wilson, *J. Chem. Phys.* **76**, 637 (1982).

Bibliography

- [182] M. Abramowitz and I. A. Stegun, *Handbook of Mathematical Functions*, §25.5, Applied Mathematics Series, Vol. 55, National Bureau of Standards, Washington, 1972.
- [183] H. J. C. Berendsen, J. P. M. Postma, W. F. van Gunsteren, A. DiNola, and J. R. Haak, *J. Chem. Phys.* **81**, 3684 (1984).
- [184] F. Reif, *Statistische Physik und Theorie der Wärme*, Walter de Gruyter, Berlin, 1985.
- [185] W. F. van Gunsteren and H. J. C. Berendsen, *Molec. Phys.* **45**, 637 (1982).
- [186] A. Szabo and N. Ostlund, *Modern Quantum Chemistry*, McGraw-Hill, 1982.
- [187] F. Jensen, *Introduction to Computational Chemistry*, John Wiley & Sons, Chichester, 1999.
- [188] J. J. P. Stewart, *J. Comput. Chem.* **10**, 209 (1989).
- [189] M. J. S. Dewar, E. G. Zoebisch, E. F. Healy, and J. J. P. Stewart, *J. Am. Chem. Soc.* **107**, 3902 (1985).
- [190] W. Weber, *PhD thesis*, Universität Zürich (Switzerland), 1996.
- [191] W. Weber and W. Thiel, *Theor. Chem. Acc.* **103**, 495 (2000).
- [192] C. J. Cramer, *Essentials of Computational Chemistry*, John Wiley & Sons, Chichester, 2004.
- [193] A. Koslowski, M. E. Beck, and W. Thiel, *J. Comput. Chem.* **24**, 714 (2003).
- [194] P. Hohenberg and W. Kohn, *Phys. Rev.* **136**, 864 (1964).
- [195] L. H. Thomas, *Proc. Cambridge Philos. Soc.* **23**, 542 (1927).
- [196] E. Fermi, *Z. Phys.* **48**, 73 (1928).
- [197] P. A. M. Dirac, *Proc. Cambridge Philos. Soc.* **26**, 376 (1930).
- [198] W. Kohn and L. J. Sham, *Phys. Rev.* **140**, 1133 (1965).
- [199] C. F. von Weizsäcker, *Z. Phys.* **96**, 431 (1935).
- [200] J. P. Perdew, K. Burke, and M. Ernzerhof, *Phys. Rev. Lett.* **77**, 3865 (1996).
- [201] A. D. Becke, *J. Chem. Phys.* **98**, 5648 (1993).
- [202] C. Adamo and V. Barone, *J. Chem. Phys.* **110**, 6158 (1999).
- [203] S. Grimme, *WIREs Comput. Mol. Sci.* **1**, 211 (2011).
- [204] P. M. W. Gill and B. G. Johnson, *Chem. Phys. Lett.* **209**, 506 (1993).
- [205] J. M. Perez-Jorda, A. D. Becke, and E. San-Fabian, *J. Chem. Phys.* **100**, 6520 (1994).
- [206] E. Runge and E. K. U. Groß, *Phys. Rev. Lett.* **52**, 997 (1984).
- [207] A. Dreuw and M. Head-Gordon, *Chem. Rev.* **105**, 4009 (2005).
- [208] M. E. Casida, *All-Electron Local and Gradient-Corrected Density-Functional Calculations of $N\alpha_n$ Dipole Polarizabilities for $n=1-6$* , in: *Recent Advances in Density Functional Methods, Part I*, p. 155, Ed. D. P. Chong, World Scientific, Singapore, 1995.
- [209] K. Yabana and G. F. Bertsch, *Phys. Rev. B* **54**, 4484 (1996).
- [210] M. A. L. Marques, A. Castro, G. F. Bertsch, and A. Rubio, *Comp. Phys. Commun.* **151**, 60 (2003).
- [211] G. F. Bertsch and K. Yabana, "Density Functional Theory", Lecture Notes, 2001.

Bibliography

- [212] M. E. Casida, *J. Mol. Struct. THEOCHEM* **914**, 3 (2009).
- [213] P. Pulay, *Analytical derivative techniques and the calculation of vibrational spectra*, in: *Modern Electronic Structure Theory, Part II*, p. 1191, Ed. D. R. Yarkony, World Scientific, Singapore, 1995.
- [214] H. Hellmann, *Einführung in die Quantenchemie*, Deuticke, Leipzig/Wien, 1937.
- [215] R. P. Feynman, *Phys. Rev.* **56**, 340 (1939).
- [216] P. Pulay, *Mol. Phys.* **17**, 197 (1969).
- [217] N. C. Handy and H. F. Schaefer III, *J. Chem. Phys.* **81**, 5031 (1984).
- [218] S. Patchkovskii and W. Thiel, *Theor. Chem. Acc.* **98**, 1 (1997).
- [219] J. A. Pople, P. M. W. Gill, and B. G. Johnson, *Chem. Phys. Lett.* **199**, 577 (1992).
- [220] B. G. Johnson, P. M. W. Gill, and J. A. Pople, *J. Chem. Phys.* **98**, 5612 (1993).
- [221] B. G. Johnson and M. J. Frisch, *J. Chem. Phys.* **100**, 7429 (1994).
- [222] C. Van Caillie and R. D. Amos, *Chem. Phys. Lett.* **308**, 249 (1999).
- [223] C. Van Caillie and R. D. Amos, *Chem. Phys. Lett.* **317**, 159 (2000).
- [224] F. Furche and R. Ahlrichs, *J. Chem. Phys.* **117**, 7433 (2002).
- [225] B. H. Lengsfeld III, P. Saxe, and D. R. Yarkony, *J. Chem. Phys.* **81**, 4549 (1984).
- [226] M. Dupuis, *J. Chem. Phys.* **74**, 5758 (1981).
- [227] S. Matsika and D. R. Yarkony, *J. Phys. Chem. A* **106**, 2580 (2002).
- [228] A. Toniolo, M. Ben-Nun, and T. J. Martinez, *J. Phys. Chem. A* **106**, 4679 (2002).
- [229] U. Werner, R. Mitrić, and V. Bonačić-Koutecký, *J. Chem. Phys.* **132**, 174301 (2010).
- [230] A. Warshel and M. Levitt, *J. Mol. Biol.* **103**, 227 (1976).
- [231] M. J. Field, P. A. Bash, and M. Karplus, *J. Comput. Chem.* **11**, 700 (1990).
- [232] J. Gao, *Methods and Applications of Combined Quantum Mechanical and Molecular Mechanical Potentials*, *Reviews in Computational Chemistry Vol. 7*, p. 119, Ed. K. B. Lipkowsky and D. B. Boyd, Wiley, New York, 1995.
- [233] H. M. Senn and W. Thiel, *QM/MM Methods for Biological Systems*, in: *Atomistic Approaches in Modern Biology, Topics in Current Chemistry Vol. 268*, Ed. M. Reiher, Springer, Berlin, 2007.
- [234] M. I. S. Röhr, J. Petersen, M. Wohlgemuth, R. Mitrić, and V. Bonačić-Koutecký, *ChemPhysChem* **14**, 1377 (2013).
- [235] M. Wohlgemuth and R. Mitrić, (unpublished work).
- [236] M. Richter, P. Marquetand, J. Gonzalez-Vazquez, I. Sola, and L. Gonzalez, *J. Chem. Theory Comput.* **7**, 1253 (2011).
- [237] R. Mitrić, J. Petersen, and V. Bonačić-Koutecký, *Multistate Nonadiabatic Dynamics "on the Fly" in Complex Systems and Its Control by Laser Fields*, in: *Conical Intersections - Theory, Computation and Experiment*, p. 497, *Advanced Series in Physical Chemistry Vol. 17*, Eds. W. Domcke, D. R. Yarkony, H. Köppel, World Scientific, Singapore, 2011.
- [238] P. G. Lisinetskaya and R. Mitrić, *Phys. Rev. A* **83**, 033408 (2011).

Bibliography

- [239] D. E. Goldberg, *Genetic Algorithms in Search, Optimization, and Machine Learning*, Addison-Wesley, Reading, 1993.
- [240] I. Tavernelli, E. Tapavicza, and U. Röthlisberger, *J. Chem. Phys.* **130**, 124107 (2009).
- [241] M. J. Rosker, M. Dantus, and A. Zewail, *J. Chem. Phys.* **89**, 6113 (1988).
- [242] T. S. Rose, M. J. Rosker, and A. Zewail, *J. Chem. Phys.* **88**, 6672 (1988).
- [243] A. Mokhtari, P. Cong, J. L. Herek, and A. H. Zewail, *Nature* **348**, 225 (1990).
- [244] M. Dantus, R. M. Bowman, M. Gruebele, and A. H. Zewail, *J. Chem. Phys.* **91**, 7437 (1989).
- [245] M. Gruebele, G. Roberts, M. Dantus, R. M. Bowman, and A. H. Zewail, *Chem. Phys. Lett.* **166**, 459 (1990).
- [246] A. H. Zewail, *J. Phys. Chem. A* **104**, 5660 (2000).
- [247] T. Suzuki, *Annu. Rev. Phys. Chem.* **57**, 555 (2006).
- [248] N. Pontius, P. S. Bechthold, M. Neeb, and W. Eberhardt, *Phys. Rev. Lett.* **84**, 1132 (2000).
- [249] J. R. R. Verlet, A. E. Bragg, A. Kammrath, O. Cheshnovsky, and D. M. Neumark, *J. Chem. Phys.* **121**, 10015 (2004).
- [250] A. E. Bragg, J. R. R. Verlet, A. Kammrath, O. Cheshnovsky, and D. M. Neumark, *J. Chem. Phys.* **122**, 054314 (2005).
- [251] G. Lüttgens, N. Pontius, P. S. Bechthold, M. Neeb, and W. Eberhardt, *Phys. Rev. Lett.* **88**, 076102 (2002).
- [252] V. Blanchet, Z. Zgierski, T. Seideman, and A. Stolow, *Nature* **401**, 52 (1999).
- [253] V. Stert, P. Farmanara, and W. Radloff, *J. Chem. Phys.* **112**, 4460 (2000).
- [254] T. Horio, T. Fuji, Y.-I. Suzuki, and T. Suzuki, *J. Am. Chem. Soc.* **113**, 10392 (2009).
- [255] Y.-I. Suzuki, T. Fuji, T. Horio, and T. Suzuki, *J. Chem. Phys.* **132**, 174302 (2010).
- [256] S. Ullrich, T. Schultz, M. Z. Zgierski, and A. Stolow, *J. Am. Chem. Soc.* **126**, 2262 (2004).
- [257] C. Z. Bisgaard, H. Satzger, S. Ullrich, and A. Stolow, *ChemPhysChem* **10**, 101 (2009).
- [258] N. L. Evans and S. Ullrich, *J. Phys. Chem. A* **114**, 11225 (2010).
- [259] T. Schultz, J. Quenneville, B. G. Levine, A. Toniolo, T. J. Martinez, S. Lochbrunner, M. Schmitt, J. P. Schaffer, M. Z. Zgierski, and A. Stolow, *J. Am. Chem. Soc.* **125**, 8098 (2003).
- [260] O. Gefner, A. M. D. Lee, J. P. Shaffer, H. Reisler, S. V. Levchenko, A. I. Krylov, J. G. Underwood, H. Shi, A. L. L. East, D. M. Wardlaw, E. t. H. Chrysostom, C. C. Hayden, and A. Stolow, *Science* **311**, 219 (2006).
- [261] C. Z. Bisgaard, O. J. Clarkin, G. Wu, A. M. D. Lee, O. Gefner, C. C. Hayden, and A. Stolow, *Science* **323**, 1464 (2009).
- [262] T. Suzuki, *Int. Rev. Phys. Chem.* **31**, 265 (2012).
- [263] M. Seel and W. Domcke, *J. Chem. Phys.* **95**, 7806 (1991).
- [264] M. Braun, C. Meier, and V. Engel, *J. Chem. Phys.* **103**, 7907 (1995).
- [265] M. Braun, C. Meier, and V. Engel, *J. Chem. Phys.* **105**, 530 (1996).

Bibliography

- [266] S. Meyer, C. Meier, and V. Engel, *J. Chem. Phys.* **108**, 7631 (1998).
- [267] S. Diltthey, S. Hahn, and G. Stock, *J. Chem. Phys.* **112**, 4910 (2000).
- [268] S. Hahn and G. Stock, *Phys. Chem. Chem. Phys.* **3**, 2331 (2001).
- [269] T. Seideman, *J. Chem. Phys.* **107**, 7859 (1997).
- [270] Y. Arasaki, K. Takatsuka, K. Wang, and V. McKoy, *J. Chem. Phys.* **112**, 8871 (2000).
- [271] Y. Arasaki, K. Takatsuka, K. Wang, and V. McKoy, *J. Chem. Phys.* **119**, 7913 (2003).
- [272] T. Seideman, *Phys. Rev. A* **64**, 042504 (2001).
- [273] Y.-I. Suzuki, M. Stener, and T. Seideman, *J. Chem. Phys.* **118**, 4432 (2003).
- [274] Y. Arasaki and K. Takatsuka, *Chem. Phys.* **338**, 175 (2007).
- [275] M. T. do N. Varella, Y. Arasaki, H. Ushiyama, K. Takatsuka, K. Wang, and V. McKoy, *J. Chem. Phys.* **126**, 054303 (2007).
- [276] H. R. Hudock, B. G. Levine, A. L. Thompson, H. Satzger, D. Townsend, N. Gador, S. Ullrich, A. Stolow, and T. J. Martinez, *J. Phys. Chem. A* **111**, 8500 (2007).
- [277] H. R. Hudock and T. J. Martinez, *ChemPhysChem* **9**, 2486 (2008).
- [278] T. Fuji, Y.-I. Suzuki, T. Horio, T. Suzuki, R. Mitrić, U. Werner, and V. Bonačić-Koutecký, *J. Chem. Phys.* **133**, 234303 (2010).
- [279] C. Meier and V. Engel, *Chem. Phys. Lett.* **212**, 691 (1993).
- [280] Z. Li, J.-Y. Fang, and C. C. Martens, *J. Chem. Phys.* **104**, 6919 (1996).
- [281] M. Hartmann, J. Pittner, V. Bonačić-Koutecký, A. Heidenreich, and J. Jortner, *J. Chem. Phys.* **108**, 3096 (1998).
- [282] V. Bonačić-Koutecký, J. Pittner, M. Boiron, and P. Fantucci, *J. Chem. Phys.* **110**, 3876 (1999).
- [283] I. Rabin, W. Schulze, G. Ertl, C. Felix, C. Sieber, W. Harbich, and J. Buttet, *Chem. Phys. Lett.* **320**, 59 (2000).
- [284] S. Wolf, G. Sommerer, S. Rutz, E. Schreiber, T. Leisner, L. Wöste, and R. S. Berry, *Phys. Rev. Lett.* **74**, 4177 (1995).
- [285] D. W. Boo, Y. Ozaki, L. H. Andersen, and W. C. Lineberger, *J. Phys. Chem. A* **101**, 6688 (1997).
- [286] M. Niemietz, M. Engelke, Y. D. Kim, and G. Ganteför, *Phys. Rev. B* **75**, 085438 (2007).
- [287] M. Niemietz, P. Gerhardt, G. Ganteför, and Y. D. Kim, *Chem. Phys. Lett.* **380**, 99 (2003).
- [288] N. Pontius, G. Lüttgens, P. S. Bechthold, M. Neeb, and W. Eberhardt, *J. Chem. Phys.* **115**, 10479 (2001).
- [289] N. Pontius, M. Neeb, W. Eberhardt, G. Lüttgens, and P. S. Bechthold, *Phys. Rev. B* **67**, 035425 (2003).
- [290] A. Schäfer, C. Huber, and R. Ahlrichs, *J. Chem. Phys.* **100**, 5829 (1994).
- [291] D. Andrae, U. Haeussermann, M. Dolg, H. Stoll, and H. Preuss, *Theor. Chim. Acta* **77**, 123 (1990).
- [292] W. Huang, R. Pal, L.-M. Wang, X. C. Zeng, and L.-S. Wang, *J. Chem. Phys.* **132**, 054305 (2010).
- [293] P. G. Lisinetskaya, (personal communication).

Bibliography

- [294] J. Jortner and R. D. Levine, *Adv. Chem. Phys.* **47**, 1 (1981).
- [295] N. Bloembergen and A. H. Zewail, *J. Phys. Chem.* **88**, 5459 (1984).
- [296] T. Elsaesser and W. Kaiser, *Annu. Rev. Phys. Chem.* **42**, 83 (1991).
- [297] D. J. Nesbitt and R. W. Field, *J. Phys. Chem.* **100**, 12735 (1996).
- [298] M. Gruebele and R. Bigwood, *Int. Rev. Mod. Phys.* **17**, 91 (1998).
- [299] D. J. Tannor, R. Kosloff, and S. A. Rice, *J. Chem. Phys.* **85**, 5805 (1986).
- [300] D. J. Tannor and S. A. Rice, *Adv. Chem. Phys.* **70**, 441 (1988).
- [301] T. Baumert, R. Grosser, R. Thalweiser, and G. Gerber, *Phys. Rev. Lett.* **67**, 3753 (1991).
- [302] E. D. Potter, J. L. Herek, S. Pedersen, Q. Liu, and A. H. Zewail, *Nature (London)* **355**, 66 (1992).
- [303] P. Brumer and M. Shapiro, *Faraday Discuss. Chem. Soc.* **82**, 177 (1986).
- [304] M. Shapiro and P. Brumer, *Int. Rev. Phys. Chem.* **13**, 187 (1994).
- [305] H. G. Muller, P. H. Bucksbaum, D. W. Schumacher, and A. Zavriyev, *J. Phys. B* **23**, 2761 (1990).
- [306] C. Chen, Y. Yin, and D. S. Elliott, *Phys. Rev. Lett.* **64**, 507 (1990).
- [307] S. M. Park, R. J. Lu, and R. J. Gordon, *J. Chem. Phys.* **94**, 8622 (1991).
- [308] L. C. Zhu, V. Kleiman, X. N. Li, S. P. Lu, K. Trentelman, and R. J. Gordon, *Science* **270**, 77 (1995).
- [309] A. M. Weiner, *Rev. Sci. Instrum.* **71**, 1929 (2000).
- [310] G. Rodriguez and J. G. Eden, *Chem. Phys. Lett.* **205**, 371 (1993).
- [311] G. Rodriguez, P. C. John, and J. G. Eden, *J. Chem. Phys.* **103**, 10473 (1995).
- [312] H. Schworer, R. Pausch, M. Heid, V. Engel, and W. Kiefer, *J. Chem. Phys.* **107**, 9749 (1997).
- [313] C. Nicole, M. A. Bouchene, C. Meier, S. Magnier, E. Schreiber, and B. Girard, *J. Chem. Phys.* **111**, 7857 (1999).
- [314] R. Uberna, Z. Amitay, R. A. Loomis, and S. R. Leone, *Faraday Discuss.* **113**, 385 (1999).
- [315] G. Grègoire, M. Mons, I. Dimicoli, F. Piuze, E. Charron, C. Dedonder-Lardeux, C. Jouvot, S. Matenchard, D. Solgadi, and A. Suzor-Weiner, *Eur. Phys. J. D* **1**, 187 (1998).
- [316] R. de Vivie-Riedle, K. Kobe, J. Manz, W. Meyer, B. Reischl, S. Rutz, E. Schreiber, and L. Wöste, *J. Phys. Chem.* **100**, 7789 (1996).
- [317] U. Gaubatz, P. Rudecki, M. Becker, S. Schiemann, M. Külz, and K. Bergmann, *Chem. Phys. Lett.* **149**, 463 (1988).
- [318] U. Gaubatz, P. Rudecki, S. Schiemann, and K. Bergmann, *J. Chem. Phys.* **92**, 5363 (1990).
- [319] K. Bergmann, H. Theuer, and B. W. Shore, *Int. Rev. Mod. Phys.* **70**, 1003 (1998).
- [320] A. P. Peirce, M. A. Dahleh, and H. Rabitz, *Phys. Rev. A* **37**, 4950 (1988).
- [321] S. H. Shi, A. Woody, and H. Rabitz, *J. Chem. Phys.* **88**, 6870 (1988).
- [322] S. Shi and H. Rabitz, *Chem. Phys.* **139**, 185 (1989).
- [323] S. H. Shi and H. Rabitz, *J. Chem. Phys.* **92**, 364 (1990).

- [324] R. Kosloff, S. A. Rice, P. Gaspard, S. Tersigni, and D. J. Tannor, *Chem. Phys.* **139**, 201 (1989).
- [325] S. H. Tersigni, P. Gaspard, and S. A. Rice, *J. Chem. Phys.* **93**, 1670 (1990).
- [326] D. A. Coley, *An Introduction to Genetic Algorithms for Scientists and Engineers*, World Scientific, Singapore, 1999.
- [327] C. J. Bardeen, V. V. Yakovlev, K. R. Wilson, S. D. Carpenter, P. M. Weber, and W. S. Warren, *Chem. Phys. Lett.* **280**, 151 (1997).
- [328] A. Assion, T. Baumert, M. Bergt, T. Brixner, B. Kiefer, V. Seyfried, M. Strehle, and G. Gerber, *Science* **282**, 919 (1998).
- [329] C. Daniel, J. Full, L. González, E.-C. Kaposta, M. Krenz, C. Lupulescu, J. Manz, S. Minemoto, M. Oppel, P. Rosenda-Francisco, S. Vajda, and L. Wöste, *Chem. Phys.* **267**, 247 (2001).
- [330] C. Daniel, J. Full, L. Gonzalez, C. Lupulescu, J. Manz, A. Merli, S. Vajda, and L. Wöste, *Science* **299**, 536 (2003).
- [331] R. J. Levis, G. M. Menkir, and H. Rabitz, *Science* **292**, 709 (2001).
- [332] N. H. Damrauer, C. Dietl, G. Krampert, S. H. Lee, K. H. Jung, and G. Gerber, *Eur. Phys. J. D* **20**, 71 (2002).
- [333] V. I. Prokhorenko, A. M. Nagy, S. A. Waschuk, L. S. Brown, R. R. Birge, and R. J. D. Miller, *Science* **313**, 1257 (2006).
- [334] G. Vogt, P. Nuernberger, T. Brixner, and G. Gerber, *Chem. Phys. Lett.* **433**, 211 (2006).
- [335] G. Vogt, G. Krampert, P. Niklaus, P. Nuernberger, and G. Gerber, *Phys. Rev. Lett.* **94**, 068305 (2005).
- [336] J. L. Herek, W. Wohlleben, R. J. Cogdell, D. Zeidler, and M. Motzkus, *Nature* **417**, 553 (2002).
- [337] W. Wohlleben, T. Buckup, J. L. Herek, and M. Motzkus, *ChemPhysChem* **6**, 850 (2005).
- [338] T. C. Weinacht, J. L. White, and P. H. Bucksbaum, *J. Phys. Chem. A* **103**, 10166 (1999).
- [339] T. Hornung, R. Meier, and M. Motzkus, *Chem. Phys. Lett.* **326**, 445 (2000).
- [340] T. C. Weinacht, J. Ahn, and P. H. Bucksbaum, *Nature* **397**, 233 (1999).
- [341] R. Bartels, S. Backus, E. Zeek, L. Misoguti, G. Vdovin, I. P. Christov, M. M. Murnane, and H. C. Kapteyn, *Nature* **164** (2000).
- [342] M. Aeschlimann, M. Bauer, D. Bayer, T. Brixner, F. J. García de Abajo, W. Pfeiffer, M. Rohmer, C. Spindler, and F. Steeb, *Nature* **446**, 301 (2007).
- [343] S. Vajda, A. Bartelt, E.-C. Kaposta, T. Leisner, C. Lupulescu, S. Minemoto, P. Rosenda-Francisco, and L. Wöste, *Chem. Phys.* **267**, 231 (2001).
- [344] A. Bartelt, S. Minemoto, C. Lupulescu, S. Vajda, and L. Wöste, *Eur. Phys. J. D* **16**, 127 (2001).
- [345] B. Schäfer-Bung, R. Mitrić, V. Bonačić-Koutecký, A. Bartelt, C. Lupulescu, A. Lindinger, S. Vajda, S. M. Weber, and L. Wöste, *J. Phys. Chem. A* **108**, 4175 (2004).
- [346] A. Lindinger, C. Lupulescu, M. Plewicky, F. Vetter, A. Merli, S. M. Weber, and L. Wöste, *Phys. Rev. Lett.* **93**, 033001 (2004).
- [347] A. Baltuska, T. Udem, M. Uiberacker, M. Hentschel, E. Goulielmakis, C. Gohle, R. Holzwarth, V. S. Yakovlev, A. Scrinzi, T. W. Hänsch, and F. Krausz, *Nature* **421**, 611 (2003).

- [348] E. Goulielmakis, V. S. Yakovlev, A. L. Cavalieri, M. Uiberacker, V. Pervak, A. Apolonski, R. Kienberger, U. Kleineberg, and F. Krausz, *Science* **317**, 769 (2007).
- [349] C. Winterfeldt, C. Spielmann, and G. Gerber, *Rev. Mod. Phys.* **80**, 117 (2008).
- [350] M. Wollenhaupt and T. Baumert, *Faraday Discuss.* **153**, 9 (2011).
- [351] M. A. Montgomery, R. R. Meglen, and N. H. Damrauer, *J. Phys. Chem. A* **110**, 6391 (2006).
- [352] A. Bartelt, A. Lindinger, C. Lupulescu, S. Vajda, and L. Wöste, *Phys. Chem. Chem. Phys.* **5**, 3610 (2003).
- [353] A. F. Bartelt, T. Feurer, and L. Wöste, *Chem. Phys.* **318**, 207 (2005).
- [354] G. Vogt, P. Nuernberger, R. Selle, F. Dimler, T. Brixner, and G. Gerber, *Phys. Rev. A* **74**, 033413 (2006).
- [355] G. Cerullo, C. J. Bardeen, Q. Wang, and C. V. Shank, *Chem. Phys. Lett.* **262**, 362 (1996).
- [356] C. J. Bardeen, Q. Wang, and C. V. Shank, *J. Phys. Chem. A* **102**, 2759 (1998).
- [357] C. J. Bardeen, V. V. Yakovlev, J. A. Squier, and K. R. Wilson, *J. Am. Chem. Soc.* **120**, 13023 (1998).
- [358] K. Misawa and T. Kobayashi, *J. Chem. Phys.* **113**, 7546 (2000).
- [359] H. A. Rabitz, M. Hsieh, and C. Rosenthal, *Science* **303**, 1998 (2004).
- [360] R. Chakrabarti and H. Rabitz, *Int. Rev. Phys. Chem.* **26**, 671 (2007).
- [361] C. Brif, R. Chakrabarti, and H. Rabitz, *New J. Phys.* **12**, 075008 (2010).
- [362] M. Wollenhaupt, A. Präkelt, C. Sarpe-Tudoran, D. Liese, and T. Baumert, *J. Mod. Opt.* **52**, 2187 (2005).
- [363] T. Bayer, M. Wollenhaupt, and T. Baumert, *J. Phys. B: At. Mol. Opt. Phys.* **41**, 074007 (2008).
- [364] P. Marquetand, P. Nuernberger, G. Vogt, T. Brixner, and V. Engel, *Europhys. Lett.* **80**, 53001 (2007).
- [365] J. Roslund and H. Rabitz, *Phys. Rev. A* **80**, 013408 (2009).
- [366] A. N. Pechen and D. J. Tannor, *Phys. Rev. Lett.* **106**, 120402 (2011).
- [367] H. Rabitz, T.-S. Ho, and R. Long, *Phys. Rev. Lett.* **108**, 198901 (2012).
- [368] A. N. Pechen and D. J. Tannor, *Phys. Rev. Lett.* **108**, 198902 (2012).
- [369] V. Bonačić-Koutecký and R. Mitić, *Chem. Rev.* **105**, 11 (2005).
- [370] M. Wollenhaupt, A. Präkelt, C. Sarpe-Tudoran, D. Liese, and T. Baumert, *J. Opt. B: Quantum Semiclass. Opt.* **7**, S270 (2005).
- [371] M. Wollenhaupt, D. Liese, A. Präkelt, C. Sarpe-Tudoran, and T. Baumert, *Chem. Phys. Lett.* **419**, 184 (2006).
- [372] T. Bayer, M. Wollenhaupt, C. Sarpe-Tudoran, and T. Baumert, *Phys. Rev. Lett.* **102**, 023004 (2009).
- [373] M. Wollenhaupt and T. Baumert, *J. Photochem. Photobiol. A: Chem.* **180**, 248 (2006).

Bibliography

- [374] T. Bayer, H. Braun, C. Sarpe, R. Siemering, P. von den Hoff, R. de Vivie-Riedle, T. Baumert, and M. Wollenhaupt, *Phys. Rev. Lett.* **110**, 123003 (2013).
- [375] H.-J. Werner and P. J. Knowles, *J. Chem. Phys.* **89**, 5803 (1988).
- [376] P. J. Knowles and H.-J. Werner, *Chem. Phys. Lett.* **145**, 514 (1988).
- [377] P. J. Knowles and H.-J. Werner, *Theor. Chim. Acta* **84**, 95 (1992).
- [378] H.-J. Werner et al., Molpro, version 2010.1, a package of ab initio programs, 2010, see <http://www.molpro.net>.
- [379] H.-J. Werner and P. J. Knowles, *J. Chem. Phys.* **82**, 5053 (1985).
- [380] P. J. Knowles and H.-J. Werner, *Chem. Phys. Lett.* **115**, 259 (1985).
- [381] J. C. Barthelat and P. Durand, *Theor. Chim. Acta* **38**, 283 (1975).
- [382] S. Magnier and P. Millié, *Phys. Rev. A* **54**, 204 (1996).
- [383] W. Müller and W. Meyer, *J. Chem. Phys.* **80**, 3311 (1984).
- [384] S. Magnier, M. Aubert-Frécon, and A. R. Allouche, *J. Chem. Phys.* **121**, 1771 (2004).
- [385] J. Köhler, M. Wollenhaupt, T. Bayer, C. Sarpe, and T. Baumert, *Opt. Express* **19**, 11638 (2011).
- [386] M. Sukharev and T. Seideman, *Phys. Rev. Lett.* **93**, 093004 (2004).
- [387] P. S. Christopher, M. Shapiro, and P. Brumer, *J. Chem. Phys.* **123**, 064313 (2005).
- [388] P. S. Christopher, M. Shapiro, and P. Brumer, *J. Chem. Phys.* **125**, 124310 (2006).
- [389] M. Daniels and W. Hauswirth, *Science* **171**, 675 (1971).
- [390] A. Reuther, H. Iglev, R. Laenen, and A. Laubereau, *Chem. Phys. Lett.* **325**, 360 (2000).
- [391] J.-M. L. Pecourt, J. Peon, and B. Kohler, *J. Am. Chem. Soc.* **122**, 9348 (2000).
- [392] J. Peon and A. H. Zewail, *Chem. Phys. Lett.* **348**, 255 (2001).
- [393] H. Kang, K. T. Lee, B. Jung, Y. J. Ko, and S. K. Kim, *J. Am. Chem. Soc.* **124**, 12958 (2002).
- [394] B. Cohen, P. M. Hare, and B. Kohler, *J. Am. Chem. Soc.* **125**, 13594 (2003).
- [395] D. C. Lührs, J. Viallon, and I. Fischer, *Phys. Chem. Chem. Phys.* **3**, 1827 (2001).
- [396] T. Pancur, N. K. Schwalb, F. Renth, and F. Temps, *Chem. Phys.* **313**, 199 (2005).
- [397] B. A. West, J. M. Womick, and A. M. Moran, *J. Phys. Chem. A* **115**, 8630 (2011).
- [398] D. Porezag, T. Frauenheim, T. Kohler, G. Seifert, and R. Kaschner, *Phys. Rev. B* **51**, 12947 (1995).
- [399] G. Seifert, D. Porezag, and T. Frauenheim, *Int. J. Quant. Chem.* **58**, 185 (1996).
- [400] M. Elstner, D. Porezag, G. Jungnickel, J. Elsner, M. Haugk, T. Frauenheim, S. Suhai, and G. Seifert, *Phys. Rev. B* **58**, 7260 (1998).
- [401] T. Frauenheim, G. Seifert, M. Elstner, T. Niehaus, C. Köhler, M. Amkreutz, M. Sternberg, Z. Hájnal, A. Di Carlo, and S. Suhai, *J. Phys.: Condens. Matter* **14**, 3015 (2002).
- [402] T. Niehaus, S. Suhai, F. Della Salla, P. Lugli, M. Elstner, and G. Seifert, *Phys. Rev. B* **63**, 5108 (2001).

Bibliography

- [403] R. Mitrić, U. Werner, M. Wohlgenuth, G. Seifert, and V. Bonačić-Koutecký, *J. Phys. Chem. A* **113**, 12700 (2009).
- [404] J. W. Ponder and F. M. Richards, *J. Comput. Chem.* **8**, 1061 (1987).
- [405] W. L. Jorgensen, D. S. Maxwell, and J. Tirado-Rives, *J. Am. Chem. Soc.* **117**, 11225 (1996).
- [406] W. L. Jorgensen and N. A. McDonald, *J. Mol. Struct.: THEOCHEM* **424**, 145 (1998).
- [407] N. A. McDonald and W. L. Jorgensen, *J. Phys. Chem. B* **102**, 8049 (1998).
- [408] R. C. Rizzo and W. L. Jorgensen, *J. Am. Chem. Soc.* **121**, 4827 (1999).
- [409] W. L. Jorgensen, J. P. Ulmschneider, and J. Tirado-Rives, *J. Phys. Chem. B* **108**, 16264 (2004).
- [410] W. L. Jorgensen, J. Chandrasekhar, J. D. Madura, R. W. Impey, and M. L. Klein, *J. Chem. Phys.* **79**, 926 (1983).
- [411] S. Patchkovskii, A. Koslowski, and W. Thiel, *Theor. Chem. Acc.* **114**, 84 (2005).
- [412] W. Thiel, MNDO program, Max-Planck-Institut für Kohlenforschung, Mühlheim, Germany, 2007.
- [413] L. B. Clark and I. Tinoco, *J. Am. Chem. Soc.* **87**, 11 (1965).
- [414] W. Voelter, R. Records, E. Bunnenberg, and C. Djerassi, *J. Am. Chem. Soc.* **90**, 6163 (1968).
- [415] A. Fucaloro and L. S. Forter, *J. Am. Chem. Soc.* **93**, 1378 (1971).
- [416] C. M. Marian, *J. Chem. Phys.* **122**, 104314 (2005).
- [417] L. Serrano-Andres, M. Merchan, and A. Borin, *Proc. Natl. Acad. Sci.* **103**, 8691 (2006).
- [418] T. Fleig, S. Knecht, and C. Hättig, *J. Phys. Chem. A* **111**, 5491 (2007).
- [419] D. Cremer and J. A. Pople, *J. Am. Chem. Soc.* **97**, 1354 (1975).
- [420] J. C. A. Boeyens, *J. Chem. Crystallogr.* **8**, 317 (1978).
- [421] B. Li, G. Turinici, V. Ramakrishna, and H. Rabitz, *J. Phys. Chem. B* **106**, 8125 (2002).
- [422] A. Mitra and H. Rabitz, *J. Phys. Chem. A* **108**, 4778 (2004).
- [423] B. Li, H. Rabitz, and J.-P. Wolf, *J. Chem. Phys.* **122**, 154103 (2005).
- [424] G. Turinici, V. Ramakrishna, B. Li, and H. Rabitz, *J. Phys. A: Math. Gen.* **37**, 273 (2004).
- [425] F. Courvoisier, V. Boutou, V. Wood, A. Bartelt, M. Roth, H. Rabitz, and J.-P. Wolf, *Appl. Phys. Lett.* **87**, 063901 (2005).
- [426] F. Courvoisier, V. Boutou, L. Guyon, M. Roth, H. Rabitz, and J.-P. Wolf, *J. Photochem. Photobiol. A: Chem.* **180**, 300 (2006).
- [427] F. Courvoisier, L. Bonacina, V. Boutou, L. Guyon, C. Bonnet, B. Thuillier, J. Extermann, M. Roth, H. Rabitz, and J.-P. Wolf, *Farad. Discuss.* **137**, 37 (2008).
- [428] J. Roslund, M. Roth, L. Guyon, V. Boutou, F. Courvoisier, J.-P. Wolf, and H. Rabitz, *J. Chem. Phys.* **134**, 034511 (2011).
- [429] R. Mitrić, J. Petersen, U. Werner, and V. Bonačić-Koutecký, *Theoretical Methods for Nonadiabatic Dynamics "on the fly" in Complex Systems and its Control by Laser Fields*, in: *Advances in the Theory of Quantum Systems in Chemistry and Physics*, p. 299, *Progress in Theoretical Chemistry and Physics* Vol. 22, Eds. P. E. Hoggan, E. J. Brändas, J. Maruani, P. Piecuch, G. Delgado-Barrio, Springer, Berlin, 2012.

- [430] P. F. Heelis, *Chem. Soc. Rev.* **11**, 15 (1982).
- [431] P. Hemmerich, V. Massey, and H. Fenner, *FEBS Lett.* **84**, 5 (1977).
- [432] J. Sancho, *Cell. Mol. Life Sci.* **63**, 855 (2006).
- [433] H. S. Toogood, D. Leys, and N. S. Scrutton, *FEBS Journal* **274**, 5481 (2007).
- [434] M. W. Fraaije and W. J. H. van Berkel, *Flavin-Containing Oxidative Biocatalysts*, in: *Biocatalysis in the Pharmaceutical and Biotechnology Industries*, p. 181, Ed. R. N. Patel, CRC Press, Boca Raton, Florida, 2006.
- [435] M. A. van der Horst and K. J. Hellingwerf, *Acc. Chem. Res.* **37**, 13 (2004).
- [436] A. Losi, *Photochem. Photobiol.* **83**, 1283 (2007).
- [437] A. M. Edwards, *General Properties of Flavins*, in: *Flavins: Photochemistry and Photobiology*, p. 1, Eds. A. M. Edwards and E. Silva, Elsevier, Amsterdam, Netherlands, 2006.
- [438] K. H. Dudley, A. Ehrenberg, P. Hemmerich, and F. Müller, *Helv. Chim. Acta* **47**, 1354 (1964).
- [439] P. Drössler, W. Holzer, A. Penzkofer, and P. Hegemann, *Chem. Phys.* **282**, 429 (2002).
- [440] S. D. M. Islam, A. Penzkofer, and P. Hegemann, *Chem. Phys.* **291**, 97 (2003).
- [441] Y. Nishimura and M. Tsuboi, *Chem. Phys. Lett.* **59**, 210 (1978).
- [442] E. Sikorska, I. Khmelinskii, A. Komasa, J. Koput, L. F. V. Ferreira, J. R. Herance, J. L. Bourdelande, S. L. Williams, D. R. Worrall, M. Insińska-Rat, and M. Sikorski, *Chem. Phys.* **314**, 239 (2005).
- [443] A. Weigel, A. L. Dobryakov, M. Veiga, and J. L. P. Lustres, *J. Phys. Chem. A* **112**, 12054 (2008).
- [444] A. Weigel, A. Dobryakov, B. Klaumünzer, M. Sajadi, P. Saalfrank, and N. P. Ernsting, *J. Phys. Chem. B* **115**, 3656 (2011).
- [445] M. Takahashi, Y. Ishikawa, J. Nishizawa, and H. Ito, *Chem. Phys. Lett.* **401**, 475 (2005).
- [446] R. A. Copeland and T. G. Spiro, *J. Phys. Chem.* **90**, 6648 (1986).
- [447] M. M. N. Wolf, C. Schumann, R. Gross, T. Domratcheva, and R. Diller, *J. Phys. Chem. B* **112**, 13424 (2008).
- [448] B. Klaumünzer, D. Kröhner, and P. Saalfrank, *J. Phys. Chem. B* **114**, 10826 (2010).
- [449] B. Klaumünzer, D. Kröhner, H. Lischka, and P. Saalfrank, *Phys. Chem. Chem. Phys.* **14**, 8693 (2012).
- [450] T. A. Schüttrigkeit, C. K. Kompa, M. Salomon, W. Rüdiger, and M. E. Michel-Beyerle, *Chem. Phys.* **294**, 501 (2003).
- [451] N. Getoff, S. Solar, and D. B. McCormick, *Science* **201**, 616 (1978).
- [452] L. Guyon, T. Tabarin, B. Thuillier, R. Antoine, M. Broyer, V. Boutou, J.-P. Wolf, and P. Dugourd, *J. Chem. Phys.* **128**, 075103 (2008).
- [453] C. Neiss, P. Saalfrank, M. Parac, and J. Grimme, *J. Phys. Chem. A* **107**, 140 (2003).
- [454] S. Salzmann, J. Tatchen, and C. M. Marian, *J. Photochem. Photobiol. A* **198**, 221 (2008).
- [455] S. Yun-Yu, W. Lu, and W. F. van Gunsteren, *Molec. Simul.* **1**, 369 (1988).
- [456] A. Humeniuk, M. Wohlgemuth, T. Suzuki, and R. Mitrić, *J. Chem. Phys.* (submitted).
- [457] I. R. Sola, J. Santamaria, and V. S. Malinovsky, *Phys. Rev. A* **61**, 043413 (2000).

Summary

In the present thesis, a general approach for the simulation and control of laser-driven coupled electron-nuclear dynamics in complex molecular systems is developed on the basis of the field-induced surface-hopping method (FISH). In particular, the latter is generalized to incorporate the molecular environment and to include arbitrary laser pulse forms parameterized in the spectral domain. Moreover, a thorough analysis and validation of the method is provided.

This theoretical framework is utilized for application-oriented studies in the fields of ultrafast spectroscopy and optimal control, involving two complementary aspects: The simulation and interpretation of available experiments, providing a molecular-level understanding of the experimental observations, and the theoretical prediction of molecular processes, eventually stimulating novel experiments.

In order to simulate time-resolved spectroscopic observables, in particular time-resolved photoelectron spectra, an extension of the FISH method is devised. This approach is illustrated on the example of nonradiative relaxation of small noble metal clusters, providing both theoretical predictions as well as analysing experimental data and revealing the underlying molecular mechanisms.

The main emphasis of the thesis, however, lies on the quantum control in complex systems. To assess the applicability of the FISH approach in the context of coherent control, the method is validated on the example of selective electronic state population in the potassium dimer. For this purpose, the comparison with numerically exact quantum dynamics simulations is made, and excellent agreement is found. This provides a basis for studying much more complex systems, enabling the investigation of two challenging applications of condensed-phase control.

The first of these is motivated by the well-known finding that in many molecular systems, initial electronic excitation is rapidly followed by ultrafast relaxation processes which may lead the system back to the electronic ground state. This is ultimately responsible for the vanishingly small fluorescence quantum yields observed e.g. in certain biomolecules such as nucleobases. Therefore, the photodynamics of the adenine molecule in aqueous environment is studied under the influence of theoretically designed laser pulse trains with the aim to assess their capability to counteract the ultrafast electronic relaxation and to elongate the electronic lifetimes. It is shown that substantially longer lifetimes are achievable using such pulse trains, which act by keeping higher-lying electronic states populated, where the direct access of the molecules towards conical intersections to the electronic ground state is hindered.

Besides the predictive potential of control simulations using FISH, this thesis also provides the demonstration that experimentally optimized laser pulses can be straightforwardly employed in theoretical simulations, thus allowing for molecular-level mechanistic insights into the experimentally achieved control. This approach is utilized to reveal the mechanism of the optimal dynamic discrimination between the two spectroscopically nearly identical molecules riboflavin and flavin mononucleotide. It is shown that the measured discriminating signals are caused by transiently different dynamics induced by the shaped laser pulses, which drive the two molecules to different parts of their potential energy surfaces where the efficiency to generate the detection signal is enhanced in one case and diminished in the other.

Altogether, in the present thesis a new general methodology for simulation and control of light-driven dynamics in complex systems is introduced and applied. The results presented here demonstrate the unique potential of this approach for obtaining molecular-level insights into the ultrafast processes in complex molecular systems, which is beyond the reach of previously available methods. This provides a firm basis for further investigations along different directions of research in ultrafast spectroscopy and molecular optimal control, including both fundamental and application-oriented routes.

Zusammenfassung

Im Rahmen dieser Dissertation wurde ein allgemeines Verfahren für die Simulation und Kontrolle der lasergetriebenen gekoppelten Kern-Elektronendynamik in komplexen molekularen Systemen entwickelt, das auf der feldinduzierten Surface-Hopping-Methode (FISH) beruht. Insbesondere wurde diese für die Einbeziehung der molekularen Umgebung verallgemeinert, und die Verwendung spektral parametrisierter Laserpulse wurde ermöglicht. Darüber hinaus wurde eine grundlegende Analyse und Validierung der Methode vorgenommen.

Die so geschaffene theoretische Methodologie wurde verwendet, um anwendungsorientierte Untersuchungen auf den Gebieten der ultraschnellen Spektroskopie und der optimalen Kontrolle durchzuführen. Grundsätzlich können dabei zwei komplementäre Aspekte im Fokus stehen: Einerseits die Simulation und Interpretation bereits vorliegender experimenteller Ergebnisse, wodurch ein tieferes Verständnis experimenteller Beobachtungen auf molekularer Ebene ermöglicht wird; zum anderen die theoretische Vorhersage molekularer Prozesse, die einen Anstoß für die Durchführung neuer Experimente geben kann.

Für die Simulation zeitaufgelöster spektroskopischer Observabler, insbesondere zeitaufgelöster Photoelektronenspektren, wurde eine Erweiterung der FISH-Methode ausgearbeitet und am Beispiel der nichtradiativen Relaxation kleiner Edelmetallcluster illustriert. Für deren Verhalten konnten sowohl theoretische Vorhersagen getroffen, als auch experimentelle Daten analysiert und die zugrunde liegenden molekularen Mechanismen aufgeklärt werden.

Das Hauptaugenmerk der Dissertation liegt jedoch auf dem Gebiet der Quantenkontrolle in komplexen Systemen. Um die Anwendbarkeit der FISH-Methode für die kohärente Kontrolle zu belegen, wurde sie am Beispiel der selektiven Besetzung elektronischer Zustände im Kalium-Dimer durch Vergleich mit exakten quantendynamischen Rechnungen validiert. Dabei wurde hervorragende Übereinstimmung zwischen den Ergebnissen beider Methoden gefunden. Dies bildet eine Grundlage für die Untersuchung weitaus komplexerer Systeme, wie der im folgenden umrissenen Anwendungen aus dem Bereich der Kontrolle in der kondensierten Phase.

Zunächst wurde eine Problematik untersucht, die durch die bekannte Tatsache motiviert wurde, dass in vielen Molekülen auf die lichtinduzierte elektronische Anregung ultraschnelle Relaxationsprozesse folgen, die das System zurück in den Grundzustand bringen. Diese sind die Hauptursache für die verschwindend geringen Fluoreszenz-Quantenausbeuten in bestimmten Biomolekülen, wie z.B. Nucleobasen. Daher wurde im Rahmen dieser Arbeit die Photodynamik des Adeninmoleküls in wässriger Umgebung unter dem Einfluss theoretisch konstruierter Laserpulszüge untersucht, mit dem Ziel, deren Fähigkeit auszuwerten, der ultraschnellen elektronischen Relaxation entgegenzuwirken und die elektronischen Lebensdauern zu verlängern. Es wurde gezeigt, dass wesentlich längere Lebensdauern durch solche Pulszüge hervorgerufen werden können. Dies basiert auf der Besetzung höherer elektronisch angeregter Zustände, in denen der direkte Zugang der Moleküle zu konischen Durchschneidungen mit dem elektronischen Grundzustand erschwert ist.

Neben dem Potential theoretischer Vorhersagen durch Simulationen optimaler Kontrolle mittels FISH wurde in dieser Dissertation auch gezeigt, dass experimentell optimierte Laserpulse unmittelbar in Simulationen angewandt werden können, wodurch die Möglichkeit zu grundlegenden mechanistischen Einblicken in die experimentell erzielte optimale Kontrolle auf molekularer Ebene gegeben wird. Dieser Ansatz wurde genutzt, um den Mechanismus der optimalen dynamischen Diskriminierung der zwei spektroskopisch fast identischen Moleküle Riboflavin und Flavin-Mononucleotid aufzuklären. Es wurde gezeigt, dass die gemessenen Diskriminierungs-Signale auf transienten Unterschieden der Dynamik beider Moleküle beruhen, die durch die optimierten Laserpulse hervorgerufen werden. Diese führen eines der Moleküle in Bereiche seiner Potentialenergiefläche, in denen das Detektionssignal effizient generiert werden kann,

während das andere Molekül in Bereiche geleitet wird, in denen das Detektionssignal nur mit geringer Effizienz entsteht.

Insgesamt wurde in dieser Dissertation eine neue, allgemeine Methodologie für die Simulation und Kontrolle lichtgetriebener Dynamik in komplexen Systemen eingeführt und angewandt. Die hier vorgestellten Ergebnisse demonstrieren das einmalige Potential dieses Ansatzes für den Gewinn tiefer Einblicke in ultraschnelle Prozesse auf molekularer Ebene, was über die Anwendungsbreite bisher verfügbarer Methoden hinaus geht. Dies stellt eine feste Grundlage für weitere Forschungsarbeiten entlang unterschiedlicher Richtungen in der ultraschnellen Spektroskopie und molekularen optimalen Kontrolle dar und ermöglicht sowohl grundlegende als auch anwendungsorientierte Folgeuntersuchungen.

Vorveröffentlichungen von Teilen der Dissertation

Zeitschriften

1. J. Petersen, R. Mitrić, V. Bonačić-Koutecký, J.-P. Wolf, J. Roslund, H. Rabitz:
"How shaped light discriminates nearly identical biochromophores",
Phys. Rev. Lett. **105**, 073003 (2010).
2. R. Mitrić, J. Petersen, M. Wohlgemuth, U. Werner, V. Bonačić-Koutecký, L. Wöste, J. Jortner:
"Time-resolved femtosecond photoelectron spectroscopy by field-induced surface hopping",
J. Phys. Chem. A **115**, 3755 (2011).
3. R. Mitrić, J. Petersen, M. Wohlgemuth, U. Werner, V. Bonačić-Koutecký:
"Field-induced surface hopping method for probing transition state nonadiabatic dynamics of Ag₃",
Phys. Chem. Chem. Phys. **13**, 8690 (2011).
4. J. Stanzel, M. Neeb, W. Eberhardt, P. G. Lisinetskaya, J. Petersen, R. Mitrić:
"Switching from molecular to bulklike dynamics in electronic relaxation of a small gold cluster",
Phys. Rev. A **85**, 013201 (2012).
5. J. Petersen, M. Wohlgemuth, B. Sellner, V. Bonačić-Koutecký, H. Lischka, R. Mitrić:
"Laser pulse trains for controlling excited state dynamics of adenine in water",
Phys. Chem. Chem. Phys. **14**, 4687 (2012).
6. J. Petersen, R. Mitrić:
"Electronic coherence within the semiclassical field-induced surface hopping method: Strong field quantum control in K₂",
Phys. Chem. Chem. Phys. **14**, 8299 (2012).

Buchkapitel

1. R. Mitrić, J. Petersen, V. Bonačić-Koutecký:
"Multistate Nonadiabatic Dynamics *on the fly* in Complex Systems and its Control by Laser Fields",
Conical Intersections - Theory, Computation and Experiment, Advanced Series in Physical Chemistry Vol. 17, W. Domcke, D. R. Yarkony und H. Köppel (Hrsg.), World Scientific, 2011, ISBN: 978-981-4313-44-5.
2. R. Mitrić, J. Petersen, U. Werner, V. Bonačić-Koutecký:
"Theoretical Methods for Nonadiabatic Dynamics 'on the fly' in Complex Systems and its Control by Laser Fields",
Advances in the Theory of Quantum Systems in Chemistry and Physics, Series: Progress in Theoretical Chemistry and Physics, Vol. 22, P. E. Hoggan, E. J. Brändas, J. Maruani, P. Piecuch, G. Delgado-Barrio (Hrsg.), Springer, 2012, ISBN: 978-94-007-2075-6.

Lebenslauf Jens Petersen

Der Lebenslauf ist in der Online-Version aus Gründen des Datenschutzes nicht enthalten

Vollständige Publikationsliste

Zeitschriften

1. I. Compagnon, T. Tabarin, R. Antoine, M. Broyer, P. Dugourd, R. Mitrić, J. Petersen, V. Bonačić-Koutecký:
"Spectroscopy of isolated, mass selected tryptophan-Ag₃ complexes: A model for photoabsorption enhancement in nanoparticle-biomolecule hybrid systems",
J. Chem. Phys. **125**, 164326 (2006).
2. T. Tabarin, R. Antoine, I. Compagnon, M. Broyer, P. Dugourd, R. Mitrić, J. Petersen, V. Bonačić-Koutecký:
"Optical Absorption of Isolated Silver Cluster-Tryptophan: A Joint Experimental and Theoretical Study",
Eur. Phys. J. D **43**, 275 (2007).
3. R. Mitrić, J. Petersen, A. Kulesza, V. Bonačić-Koutecký, T. Tabarin, I. Compagnon, R. Antoine, M. Broyer, P. Dugourd:
"Photoabsorption and Photofragmentation of Silver Cluster-Tryptophan Hybrid Systems",
J. Chem. Phys. **127**, 134301 (2007).
4. R. Mitrić, J. Petersen, A. Kulesza, V. Bonačić-Koutecký, T. Tabarin, I. Compagnon, R. Antoine, M. Broyer, P. Dugourd:
"Absorption Properties of Cationic Silver Cluster-Tryptophan Complexes: A Model for Photoabsorption and Photoemission Enhancement in Nanoparticle-Biomolecule Systems",
Chem. Phys. **343**, 372 (2008).
5. G. Scholz, R. König, J. Petersen, B. Angelow, I. Dörfel, E. Kemnitz:
"Mechanical activation of α -AlF₃: changes in structure and reactivity",
Chem. Mater. **20**, 5406 (2008).
6. R. Mitrić, J. Petersen, V. Bonačić-Koutecký:
"Laser field-induced surface hopping method for the simulation and control of ultrafast photodynamics",
Phys. Rev. A **79**, 053416 (2009).

7. J. Petersen, R. Mitrić, V. Bonačić-Koutecký, J.-P. Wolf, J. Roslund, H. Rabitz:
"How shaped light discriminates nearly identical biochromophores",
Phys. Rev. Lett. **105**, 073003 (2010).
8. R. Mitrić, J. Petersen, M. Wohlgenuth, U. Werner, V. Bonačić-Koutecký, L. Wöste, J. Jortner:
"Time-resolved femtosecond photoelectron spectroscopy by field-induced surface hopping",
J. Phys. Chem. A **115**, 3755 (2011).
9. R. Mitrić, J. Petersen, M. Wohlgenuth, U. Werner, V. Bonačić-Koutecký:
"Field-induced surface hopping method for probing transition state nonadiabatic dynamics of Ag₃",
Phys. Chem. Chem. Phys. **13**, 8690 (2011).
10. R. Mitrić, J. Petersen, A. Kulesza, M. I. S. Röhr, V. Bonačić-Koutecký, C. Brunet, R. Antoine, P. Dugourd, M. Broyer, R. A. J. O'Hair:
"Gas-phase synthesis and vibronic action spectroscopy of Ag₂H⁺",
J. Phys. Chem. Lett. **2**, 548 (2011).
11. C. Brunet, R. Antoine, M. Broyer, P. Dugourd, A. Kulesza, J. Petersen, M. I. S. Röhr, R. Mitrić, V. Bonačić-Koutecký, R. A. J. O'Hair:
"Structural and photochemical properties of organosilver reactive intermediates MeAg₂⁺ and PhAg₂⁺",
J. Phys. Chem. A **115**, 9120 (2011).
12. J. Stanzel, M. Neeb, W. Eberhardt, P. G. Lisinetskaya, J. Petersen, R. Mitrić:
"Switching from molecular to bulklike dynamics in electronic relaxation of a small gold cluster",
Phys. Rev. A **85**, 013201 (2012).
13. J. Petersen, M. Wohlgenuth, B. Sellner, V. Bonačić-Koutecký, H. Lischka, R. Mitrić:
"Laser pulse trains for controlling excited state dynamics of adenine in water",
Phys. Chem. Chem. Phys. **14**, 4687 (2012).
14. J. Petersen, R. Mitrić:
"Electronic coherence within the semiclassical field-induced surface hopping method: Strong field quantum control in K₂",
Phys. Chem. Chem. Phys. **14**, 8299 (2012).
15. M. I. S. Röhr, J. Petersen, C. Brunet, R. Antoine, M. Broyer, P. Dugourd, V. Bonačić-Koutecký, R. A. J. O'Hair, R. Mitrić:
"Synthesis and Spectroscopic Characterization of Diphenylargentate, [(C₆H₅)₂Ag]⁻",
J. Phys. Chem. Lett. **3**, 1197 (2012).
16. G. Tomasello, M. Wohlgenuth, J. Petersen, R. Mitrić:
"Photodynamics of Free and Solvated Tyrosine",
J. Phys. Chem. B **116**, 8762 (2012).
17. M. I. S. Röhr, J. Petersen, M. Wohlgenuth, R. Mitrić, V. Bonačić-Koutecký:
"Nonlinear Absorption Dynamics Using Field-Induced Surface Hopping: Zinc Porphyrin in Water",
ChemPhysChem **14**, 1377 (2013).

Buchkapitel

1. V. Bonačić-Koutecký, R. Mitrić, C. Bürgel, J. Petersen:
"Tailoring functionality of clusters and their complexes with biomolecules by size, structures and lasers",
Nanoclusters - A Bridge across Disciplines, P. Jena und A. W. Castleman (Hrsg.), Elsevier B.V., Amsterdam 2010, ISBN: 978-0-444-53440-8.
2. R. Mitrić, J. Petersen, V. Bonačić-Koutecký:
"Multistate Nonadiabatic Dynamics *on the fly* in Complex Systems and its Control by Laser Fields",
Conical Intersections - Theory, Computation and Experiment, Advanced Series in Physical Chemistry Vol. 17, W. Domcke, D. R. Yarkony und H. Köppel (Hrsg.), World Scientific, 2011, ISBN: 978-981-4313-44-5.
3. R. Mitrić, J. Petersen, U. Werner, V. Bonačić-Koutecký:
"Theoretical Methods for Nonadiabatic Dynamics 'on the fly' in Complex Systems and its Control by Laser Fields",
Advances in the Theory of Quantum Systems in Chemistry and Physics, Series: Progress in Theoretical Chemistry and Physics, Vol. 22, P. E. Hoggan, E. J. Brändas, J. Maruani, P. Piecuch, G. Delgado-Barrio (Hrsg.), Springer, 2012, ISBN: 978-94-007-2075-6.

Selbstständigkeitserklärung

Hiermit erkläre ich, Jens Petersen, geboren am 24.10.1983 in Berlin, diese Dissertation selbstständig und nur unter Verwendung der angegebenen Hilfen und Hilfsmittel angefertigt zu haben. Die Arbeit wurde weder in einem früheren Promotionsverfahren angenommen noch als ungenügend beurteilt. Ich erkläre die Kenntnisnahme der dem Verfahren zugrunde liegenden Promotionsordnung des Fachbereichs Physik der Freien Universität Berlin vom 05.02.2010.

Berlin, den 04.06.2013

Jens Petersen